



Highly photoconductive oxide films functionalized with GeSi nanoparticles

Muhammad Taha Sultan

Doctor of Philosophy

November 2019

Applied Physics

Reykjavík University

Ph.D. Dissertation



Highly photoconductive oxide films functionalized with GeSi nanoparticles

Dissertation submitted to the School of Science and Engineering
at Reykjavík University in partial fulfillment of
the requirements for the degree of
Doctor of Philosophy (Ph.D.) in Applied Physics

November 2019

Thesis Committee:

Halldór Guðfinnur Svavarsson, Professor, and Supervisor
Reykjavík University, Reykjavík, Iceland

Jon Tomas Gudmundsson, Professor, co-supervisor
University of Iceland, Reykjavík, Iceland
KTH Royal Institute of Technology, Sweden

Andrei Manolescu, Professor
Reykjavík University, Reykjavík, Iceland

Thesis Examiner:

Marin Alexe, Professor
University of Warwick, UK

Copyright
Muhammad Taha Sultan
November 2019

Highly photoconductive oxide films functionalized with GeSi nanoparticles

Muhammad Taha Sultan

November 2019

Abstract

Growth of self-assembled quantum dots is of great interest due to their potential quantum confinement effect and numerous applications in optoelectronics and nano-sized structures. Semiconducting Si, Ge and SiGe nanocrystals (NCs), embedded in a dielectric-oxide matrix have for instance been found to exhibit strong quantum confinement. For SiGe nano-based structures in addition to strong quantum confinement effect they offer the advantage of fine tuneability of energy-band structure via quantum confinement, strain engineering and varying the Si/Ge ratio.

Among the most common methods to obtain NCs embedded in oxide systems is deposition with magnetron sputtering, followed by subsequent anneal treatments. However, the device performance obtained are lower in production line than obtained for research devices. This has mainly been attributed to the thermal treatment used, which causes strain accumulation within the structure, dislocations and dangling bonds, clustering and phase separation of Ge in $\text{Si}_{1-x}\text{Ge}_x$ system, diffusion and formation of unwanted insulating oxide. All of these side-effects cause degradation of optical and electrical properties of the fabricated structures.

In this study, structures comprising of $\text{SiO}_2/\text{SiGe}/\text{SiO}_2$ and $\text{TiO}_2/\text{SiGe}/\text{TiO}_2$ were fabricated by utilizing radio frequency (rfMS), direct current (dcMS) and/or high power impulse magnetron sputtering (HiPIMS). The structures were then subjected to thermal and/or hydrogen (H_2) plasma treatment. Their photocurrent intensity was increased by up to several orders of magnitude along with wider spectral coverage into near infra-red regime by controlling the sputter discharge and anneal parameters. Moreover, as a proof of concept, a control over the HiPIMS discharge parameters have exhibited the possibility of obtaining as-grown crystalline structures, consisting of SiGe NCs without the need of annealing, along with a viable control over the size of NCs. The annealing of such structure prepared via HiPIMS method, have shown an interesting self-organization of periodically arranged columnar SiGe NCs. Exposure to hydrogen plasma of both as-grown samples and annealed samples ensued amplification in photoconductivity by neutralization of dangling bonds and passivation of non-radiative defects in the oxide matrix and/or at SiGe/matrix interfaces.

Highly photoconductive oxide films functionalized with GeSi nanoparticles

Muhammad Taha Sultan

November 2019

Útdráttur

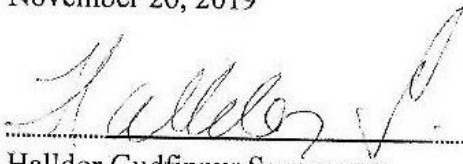
Ræktun sjálfsamsettra skammtapunkta er mjög áhugavert rannsóknaverkefni vegna margvíslegra notkunarmöguleika í ljósnæmum rafeindatækjum og ýmsum örsmáum skynjurum. Hálfleiðandi Si, Ge og SiGe örnir í þunnhúðum úr torleiðiefnum (einkum málmoxíðum) hafa til dæmis reynst hafa sterka skammtaeiginleika. Sökum skammtahrifa má fínstillast þá ljós-öldulengd sem þarf til að gera þá leiðandi með því að stýra stærð örnanna, hlutfalli milli Si og Ge og álagi sem þeir verða fyrir í þunnhúðinni.

Algengasta leiðin til að búa til ofangreind kerfi er þunnhúðun með segulspættun og hitameðhöndlun í kjölfarið. Hefðbundin hitameðferð veldur hinsvegar ákveðnum skemmdum í $\text{Si}_{1-x}\text{Ge}_x$ kerfinu, s.s. lausum efnatengjum, efnis-aðskilnaði, myndun þyrpinga og útsveimi. Þessar aukaverkanir rýra ljós- og rafeiginleika efnisins. Framleiðslu aðferðir sem valda ekki slíkum skemmdum geta því haft mikla þýðingu.

Í þessari rannsókn voru riðspennu (rfMS)-, jafnspennu (dcMS) - og háaflpúlsuð segulspættun (HiPIMS) aðferðir notaðar til að rækta lög af $\text{SiO}_2/\text{SiGe}/\text{SiO}_2$ og $\text{TiO}_2/\text{SiGe}/\text{TiO}_2$ kerfum. Í kjölfarið var mildum hita- og vetnis rafgasmeðferðum beitt til að framkalla SiGe og Ge örnir í húðinni sem sýndu breytilega ljósnæmni. Með þessum hætti tókst að auka ljósnæmnina um nokkrar stærðargráður auk þess sem næmnisvið litrófsins var víkkað. Önnur megin niðurstaða er að með notkun HiPIMS aðferðarinnar tóks að útbúa sýni með háa ljósnæmni án þess að hitameðhöndla þau. Meðhöndlun með vetnis-rafgasi leiddi til mikillar (stærðargráðu) aukningar á ljósnæmni húðanna, bæði fyrir og eftir hitameðhöndlun.

The undersigned hereby certify that they recommend to the School of Science and Engineering at Reykjavík University for acceptance this Dissertation entitled **Highly photoconductive oxide films functionalized with GeSi nanoparticles** submitted by **Muhammad Taha Sultan** in partial fulfillment of the requirements for the degree of **Doctor of Philosophy (Ph.D.) in Applied Physics**.

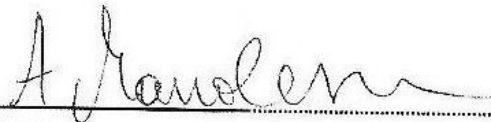
.....
November 26, 2019



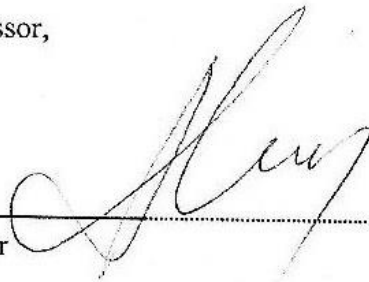
.....
Halldor Gudfinnur Svavarsson,
Supervisor, Professor,
Reykjavík University



.....
Jon Tomas Gudmundsson,
Co-Supervisor, Professor,
Science Institute, University of Iceland



.....
Andrei Manolescu,
Co-Supervisor, Professor,
Reykjavík University

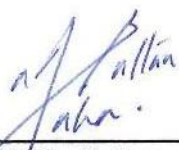


.....
Marin Alexe, Examiner
Professor,
University of Warwick, UK

The undersigned hereby grants permission to the Reykjavík University Library to reproduce single copies of this Dissertation entitled **Highly photoconductive oxide films functionalized with GeSi nanoparticles** and to lend or sell such copies for private, scholarly or scientific research purposes only.

The author reserves all other publication and other rights in association with the copyright in the Dissertation, and except as herein-before provided, neither the Dissertation nor any substantial portion thereof may be printed or otherwise reproduced in any material form whatsoever without the author's prior written permission.

Date: 26-11-2019

A handwritten signature in blue ink, appearing to read 'Muhammad Taha Sultan', is written over a horizontal dotted line.

Muhammad Taha Sultan
Doctor of Philosophy

Impact: *The project is designated as a successful project by M-ERA.NET consortium and is included in the abstracts brochure of (EU) M-Era.NET program.*

*With no words that can narrate I dedicate all my humble effort to
my parents*

***Sultan Mehmood and Rehana Sultan**, they were the compass
who guide me, inspired me to reach great heights and my comfort
when I occasionally falter.*

&

*To my wife **Maham** for her tremendous support, and
companionship*

&

To my family

Talha, Talal, Huzaiifa

Faiza, Shazil

Acknowledgments

Firstly, I would like to express my sincere gratitude to my advisor Prof. Halldór Guðfinnur Svavarsson for the continuous support of my Ph.D study and related research, for his patience, motivation, and most of all friendliness, aspiring guidance, and immense knowledge and without whose kind consideration and constant feedback this work would not have been possible.

Besides my advisor, I would like to thank the Prof. Jón Tómas Guðmundsson, for his insightful suggestions and encouragement that widen my research vision from various perspectives. He not only kept my moral high but also accounted my abilities for a much better outcome.

Further, I would like to present my deepest gratitude to Prof. Andrei Manolescu for his never ending, precious and unfailing support and assistance and providing me with the facilities being required and conducive conditions for my project. Your advice on both research as well as on my career have been invaluable.

Moreover, I gratefully acknowledge the support from Prof. Magdalena Lidia Ciurea in carrying out my project, the support I received from the collaborative work I undertook and without whose guidance it would not be possible to learn the insights of project and for being always so helpful and providing me with assistance throughout my dissertation.

Moreover, my special thanks to our other Romanian partner from Magurele especially Prof. Valentin Serban Teodorescu and researchers Catalin Palade, Ana-Maria Lepadatu, Adrian Slav and Ionel Stavarache for their contributions and their thoughtful suggestions and providing me with a great time being in their city and institute. I am sincerely grateful to them for sharing their truthful and illuminating views on a number of issues related to the project.

I would like to end with a special mention to VRIII colleges and professors, Tryggvi Kr. Tryggvason, Fridrik Magnus, Arni Sigurdur Ingason, Unnar Arnalds, Einar Baldur, Einar Örn, Snorri Ingvarsson, Hamid and Movaffaq. It was fantastic to have the opportunity to work majority of my research in your facility. Thank you for having me in your office for discussion and providing me best of the answer. I would say...What a cracking place to work!

I thank my fellow lab mates Ragnar, Kibbi, David and Kristbjorg for the stimulating discussions, and for all the fun we have had in the last years.

At last I would like to thank my uncles Akhtar and Azhar Mehmood for being there for my family in need, they sum up the strength for me, while I can be here with no stress.

I appreciatively acknowledge the funding by RANNIS, through the M-ERA NET program.

Preface

This dissertation is the original work of the author, Muhammad Taha Sultan. A major portion of the thesis is based upon 7 refereed journal papers, 5 refereed conference papers and 4 other refereed conference contributions (printed abstracts), published or submitted for publication (or under revision) during the course of Ph.D. study. The papers (published or accepted) appear as per their submitted version at the end of the thesis. The overall list of journal and conference papers throughout this study is listed below.

Published ISI Journal papers:

1. **Sultan M T**, Manolescu A, Gudmundsson J T, Torfason K, Alexandru Nemnes G, Stavarache I, Logofatu C, Teodorescu V S, Ciurea M L and Svavarsson H G 2019 Enhanced photoconductivity of SiGe nanocrystals in SiO₂ driven by mild annealing *Appl. Surf. Sci.* **469** 870–8
2. **Sultan M T**, Gudmundsson J T, Manolescu A, Stoica T, Ciurea M L and Svavarsson H G 2019 Enhanced photoconductivity of embedded SiGe nanoparticles by hydrogenation *Appl. Surf. Sci.* **479** 403–9
3. **Sultan M T**, Manolescu A, Gudmundsson J T, Stoica T, Ciurea M L and Svavarsson H G 2019 Efficacy of annealing and fabrication parameters on photo-response of SiGe in TiO₂ matrix *Nanotechnology.* **30** 365604
4. **Sultan M T**, Teodorescu V S, Manolescu A, Gudmundsson J T, Ciurea M L and Svavarsson H G 2019 Fabrication and characterization of Si_{1-x}Ge_x nanocrystals in as-grown and annealed structures: A comparative study *Beilstein Journal of Nanotechnology* **10** 1873-82.

Submitted ISI journal papers

5. **Sultan M T**, Gudmundsson J T, Manolescu A, V S Teodorescu, M L Ciurea and Svavarsson H G Obtaining SiGe nano-crystallites between crystalline TiO₂ layers by HiPIMS without annealing. (submitted for publication, under revision)
6. Stavarache I, Constantin L, **Sultan M T**, Manolescu A, Svavarsson H G, Teodorescu V S, Ciurea M L SiGe nanocrystals in SiO₂ with high photosensitivity from VIS to SWIR. (submitted for publication, under revision)
7. **Sultan M T**, Gudmundsson J T, Manolescu A and Svavarsson H G, Structural and photoluminescence study of self-assembled Si_{1-x}Ge_x nanoislands over HiPIMS sputtered TiO₂ layer. (In manuscript)

Refereed conference papers:

1. Slav A, Palade C, Stavarache I, Teodorescu V S, Ciurea M L, Muller R, Dinescu A, **Sultan M T**, Manolescu A, Gudmundsson J T and Svavarsson H G 2017 Influence of preparation conditions on structure and photosensing properties of GeSi/TiO₂ multilayers *2017 International Semiconductor Conference (CAS) (IEEE)* pp 63–6.
2. **Sultan M T**, Gudmundsson J T, Manolescu A, Ciurea M L, Palade C, Maraloiu A V and Svavarsson H G 2018 Enhanced Photoconductivity of SiGe-Trilayer Stack by Retrenching Annealing Conditions *2018 International Semiconductor Conference (CAS) (IEEE)* pp 61–4.
3. **Sultan M T**, Gudmundsson J T, Manolescu A, Ciureai M L and Svavarsson H G 2018 The Effect of H₂/Ar Plasma Treatment Over Photoconductivity of SiGe Nanoparticles Sandwiched Between Silicon Oxide Matrix *2018 International Semiconductor Conference (CAS) (IEEE)* pp 257–60.
4. Palade C, Slav A, Cojocaru O, Teodorescu V S, Lazanu S, Stoica T, **Sultan M T**, Svavarsson H G and Ciurea M L 2018 Enhanced Photocurrent in GeSi NCs / TiO₂Multilayers *2018 International Semiconductor Conference (CAS) (IEEE)* pp 73–6.
5. Palade C, Stavarache I, Lepadatu A -M, Slav A, Lazanu S, Stoica T, Teodorescu V S, Ciurea M L, Comanescu F, Dinescu A, Müller R, Stan G, Enuica A, **Sultan M T**, Manolescu A, Svavarsson H G 2019 New advanced materials based on SiGeSn nanocrystals in oxides for SWIR photodetectors and non-volatile memory devices *June 12-14 EuroNanoForum 2019*.

Other refereed conference contributions: printed abstract

1. DINAMO (Discussions on Nano and Mesoscopic Optics) 2017 in ICELAND May 14-19, 2017, Siglufjordur, Iceland.
2. **Sultan M T**, Gudmundsson J T, Manolescu A, Ciurea M L, Svavarsson H G 2019 Growth of SiGe nanocrystals in SiO₂ matrix by incorporating HiPIMS: On the way to crystallization bypassing the need of annealing International Workshop on Thinfilms for Electronics, Electro-optics, Energy and Sensors (SPIE event), Reykjavik, Iceland, June 2019
3. Svavarsson H G, **Sultan M T**, Gudmundsson J T, Manolescu A, Ciurea M L, 2019 Effect of H₂/Ar plasma exposure: influence of short and protracted intervals International Workshop on Thin-films for Electronics, Electro-optics, Energy and Sensors (SPIE event), Reykjavik, Iceland, June 2019
4. Palade C, Stavarache I, Lepadatu A -M, Slav A, Lazanu S, Stoica T, Teodorescu V S, Ciurea M L, Comanescu F, Dinescu A, Müller R, Stan G, Enuica A, **Sultan M T**, Manolescu A, Svavarsson H G 2019 New advanced materials based on SiGeSn nanocrystals in oxides for SWIR photodetectors and non-volatile memory devices June 12-14 EuroNanoForum 2019

Table of Content

Acknowledgments	xvii
Preface	xix
List of Figures	3
List of Tables	7
List of Abbreviations	8
List of Symbols	9
1 Introduction	1
2 Theoretical frame of reference	5
2.1 Semiconductors.....	5
2.2 Quantum dots and quantum confinement	8
2.3 Exciton Bohr radius	9
2.4 Low-dimensional nanostructures	10
2.4.1 Si-NCs	10
2.4.2 Fundamental properties of SiGe NCs.....	11
2.4.3 SiGe nanostructures.....	15
2.4.4 Embedded SiGe-NCs	20
2.4.5 Hydrogen plasma treatment	29
2.4.6 Photoconductivity.....	31
3 Experimental Equipment and Methods	35
3.1 Principles of sputtering	36
3.2 Magnetron sputtering (MS)	37
3.2.1 Direct current magnetron sputtering (dcMS)	39
3.2.2 Radio frequency magnetron sputtering (rfMS)	41
3.2.3 High power impulse magnetron sputtering (HiPIMS)	42
3.3 Annealing.....	49
3.4 Hydrogenation	50
4 Characterization techniques	53

4.1	X-ray diffraction	53
4.1.1	Theoretical perspective and basic principal	54
4.1.2	Grazing incidence X-ray diffraction	55
4.1.3	X-ray Reflectometry (XRR).....	56
4.2	Atomic Force Microscopy (AFM).....	56
4.2.1	Working Modes.....	57
4.3	Scanning electron microscopy (SEM)	58
4.4	Photocurrent (spectral) analysis.....	60
5	Summary of papers	63
6	Summary.....	67
	Bibliography.....	69
	Appendix	86

List of Figures

- Figure 1.** Schematic expression of the bandgap of (a) insulator, (b) semiconductor and (c) conductors. CB and VB corresponds to conduction and valence band, respectively..... 6
- Figure 2.** Schematic presentation of (a) direct and (b) indirect bandgap in semiconductors.... 7
- Figure 3.** The diamond crystal structure of silicon. 7
- Figure 4.** Low dimensional structure 3D – 0D, along with density of states vs. energy for bulk materials, quantum well, quantum wire and dots (i.e. 3D to 0D, respectively) [71]..... 8
- Figure 5.** Illustration of the change in energy levels as a function of crystal size. The quantum dot materials shows the individual energy levels which can be calculated using the particle-in-a-box model [77]. As the crystal grows bigger, it approaches the bulk semiconductor state with energy bands separated by the bandgap energy..... 10
- Figure 6.** Binary phase diagram of the Si-Ge..... 13
- Figure 7.** Sample illustration of $\text{Si}_{1-x}\text{Ge}_x$ pseudomorphic growth and misfit dislocations [2]. 13
- Figure 8.** The critical $\text{Si}_{1-x}\text{Ge}_x$ thickness as a function of germanium percentage [113]. 14
- Figure 9.** The bandgap as a function of germanium percentage for unstrained (diamonds), strained undoped (circles), and strained heavily doped $\text{Si}_{1-x}\text{Ge}_x$ (squares) [2]. 15
- Figure 10.** A schematic kinetic phase diagram (at anneal temperature of 500 °C) showing the growth regimes of $\text{Si}_{1-x}\text{Ge}_x$ layers as a function of the deposited thickness h and misfit m due to strain ϵ on (a) Si (111) and (b) Si (001) substrate. After Berbezier *et al.*[6]..... 17
- Figure 11.** AFM images of 200 nm thick homoepitaxial SiGe layers deposited on Si (001) surfaces with a miscut of 1.16° in [100] direction (arrows). Films were deposited at 0.8 \AA/s and substrate temperatures of 450, 490, and 550 °C (from left to right). Insets depict the 2D Fourier transforms. From Berbezier *et al.* [6]). 18
- Figure 12.** $5 \times 5 \mu\text{m}^2$ AFM image of SiGe over p-type Si(001)-substrate annealed at 600 °C for 1 hr. 18
- Figure 13.** (a) AFM image of $\text{Si}_{1-x}\text{Ge}_x$ as-grown “hut” and “domes” islands with $x = 0.4$ and $h \sim 5 \text{ nm}$; (b) GIXRD spectrum of the sample. From Berbezier *et al.* [6]..... 19
- Figure 14.** AFM image of TiO_2/SiGe over p-type Si-substrate annealed at 1000 °C. The dotted white circles shows merging of small domes to (form) super domes. 20
- Figure 15.** AFM images of bimodal distribution of “domes” in $\text{Si}_{1-x}\text{Ge}_x$, $x = 0.5$ and $h \sim 5 \text{ nm}$. Larger domes are dislocated and smaller ones are coherent (From Berbezier *et al.* [6]). (b) $13 \times 13 \mu\text{m}^2$ AFM image of SiGe over p-type Si(001)-substrate annealed at 700 °C for 1 hr..... 21
- Figure 16.** Structures annealed at (a) 700 °C for 7 hr (b) 750 °C for 10 hr and (c, d) 800 °C for 7 hr showing the evolution of SiGe nanoislands coalescence (domes). 22
- Figure 17.** TEM low-magnification image showing the contrast due to the shearing defects appearing in the SiGe crystallites, of a sample annealed at 600 °C for 1 min. (b) HRTEM image showing the lens-like shape of SiGe crystallites as a result of of shearing defects. The arrows indicate the shearing planes. (c) Sequence of

- microtwin bands, observed in a very thin area of the XTEM specimen (MLs with 200 nm thick SiGe), where the SiGe NCs are not superposed in the specimen thickness. 23
- Figure 18.** Cross section TEM images of: (a) $\text{TiO}_2/\text{SiGe}/\text{TiO}_2$ structure over Si substrate, annealed at 650 °C for 2 h. The figure shows the SiGe phase separation and formation of segregated Ge nanoparticles and the inter-diffusion of oxygen from oxide matrix and/or ambient atmosphere resulting formation of SiO_x insulating layer, (b) double stack $(\text{TiO}_2/\text{SiGe}/\text{TiO}_2)\times 2$, annealed at 800 °C. A formation of SiO_2 layer after annealing was observed, deteriorating the interface integrity and the thickness of which increases while going from bottom to top of the structure [165]. 23
- Figure 19.** GiXRD diffractogram of a sample annealed at 650 °C for (a) 2 hr and (b) 5 min, where vertical dashed and dotted lines correspond to standard tabulated positions for cubic Ge ($2\theta = 27.45^\circ; 45.59^\circ; 54.04^\circ$ — ASTM 01-079-0001), cubic Si ($28.45^\circ; 47.31^\circ; 56.13^\circ$ — ASTM 01-070-5680) and to TiO_2 anatase [JCPDS 21-1272] [36]. 26
- Figure 20.** XTEM cross-sectional image of the $\text{TiO}_2/\text{SiGe}/\text{TiO}_2$ annealed at 650 °C for 2 hr (similar structure as in **Fig. 19(a)**), showing segregation of Ge NPs and formation of insulating SiO_2 layer. (b) TEM image of structure $\text{TiO}_2/\text{SiGe}/\text{TiO}_2$ annealed at 650 °C for 5 min with SiGe layer having SiGe spherical nanoparticles without formation of any SiO_2 layer at the interface. 27
- Figure 21.** GiXRD diffractogram of as-deposited Ge (20 nm) deposited via HiPIMS at varying repetition frequency (100–300 Hz) for fixed applied voltage (470 V) and pulse width (200 μs). A comparison to structure obtained by dcMS deposition at 40W is given with the red line. The arrow points to SiGe (110) peak positioned between the Si and Ge tabulated ones i.e. ASTM 01-079-0001 for cubic Ge and for cubic Si, ASTM 01-070-5680. 27
- Figure 22.** Structural evolution analysis by GiXRD diffractogram for TiO_2 deposited via HiPIMS. The discharge parameters are listed in paper V. The labels R, A and B denote rutile, anatase and X-ray amorphous nature of TiO_2 thin films (~80 nm). The plots labelled ‘e’ and ‘j’ are pure anatase and rutile phase, respectively, while the ones in between contains both phases. The JCPDS card no. 21-1272 and JCPDS card no. 21-1276 for anatase and rutile phase respectively. 28
- Figure 23.** GiXRD diffractograms of (a) as-deposited (asd) Ge only along with as-deposited structure (MLs) of $\text{SiO}_2/\text{SiGe}/\text{SiO}_2$ deposited via HiPIMS, where vertical dashed lines correspond to standard tabulated positions for cubic Ge ($2\theta=27.45^\circ; 45.59^\circ; 54.04^\circ$ - ASTM 01–079-0001) and cubic Si ($28.45^\circ; 47.31^\circ; 56.13^\circ$ - ASTM 01–070-5680). (b) $\text{TiO}_2/\text{SiGe}/\text{TiO}_2$ structures, where the TiO_2 film (lower blue-line) is deposited with HiPIMS at 300 Hz repetition frequency and cathode voltage of 755 V with average power of 468 W forming anatase phase (HHD-A) and the second TiO_2 film (upper black-line) was sputtered at 340 Hz at 813 V with average power of 545 W resulting in rutile phase (i.e. HHD-R). The vertical short-dashed and dotted lines corresponds to standard TiO_2 anatase (JCPDS card no. 21-1272) and rutile (JCPDS card no. 21-1276) phases, respectively. 29
- Figure 24.** (a) XTEM images of $\text{SiO}_2/\text{SiGe}/\text{SiO}_2$ structure with 20 nm SiGe layer after 600 °C annealing for 1 min. (b) Magnified image from (a) showing columnar morphology of SiGe crystallites covered with a shell structure of amorphous SiGeO layer of ~2 nm. The crystallites have a periodicity of ~12.5 nm. (c) TEM

image of sample TiO ₂ /SiGe/TiO ₂ with SiGe layer showing presence of columnar formation of SiGe nanoparticles (~10 nm) having a gap between them of ~5–6 nm.....	29
Figure 25. A schematic of the photocurrent measurement setup with intended structural scheme consisting of Si-wafer/ buffer-SiO ₂ (200 nm)/ SiO ₂ /SiGe/SiO ₂ with coplanar Al contacts on top of the structure [29].....	32
Figure 26. A schematic showing rise and decay curves of photoconductivity for n-type silicon.	32
Figure 27. The current vs. time response plot for structures (TiO ₂ /SiGe/TiO ₂) (a, b) deposited via dcMS method and annealed at 650 °C for 2 h and 5 min, respectively, and (c) deposited via HiPIMS method in as-grown state with out any pre-/post-annealing. The applied bias (U) is 2 V for (a) and 1 V for plots in (b) and (c).	33
Figure 28. A schematic of a structure deposited over p-type Si-substrate. First there is a SiO ₂ buffer layer and on top of that we have the active layers of either TiO ₂ /SiGe/TiO ₂ or SiO ₂ /SiGe/SiO ₂	35
Figure 29. Processes initiated by the impact of highly energetic particles on the target surface.	36
Figure 30. Pictorial representation of difference between (a) conventional dc sputtering and (b) MS. In a non-magnetron sputtering system, the plasma is not confined and electrons and Ar ions propagate through space, and may collide with the substrate. While, in MS, the plasma is confined in an area where the magnetic field is present and strong.....	39
Figure 31. Process schematic of direct current magnetron sputtering (dcMS).....	40
Figure 32. Hysteresis curve in reactive sputtering because of target poisoning [235].	42
Figure 33. (a) Plot of peak power density at the target versus duty cycle for different magnetron discharges (Gudmundsson <i>et al.</i> [233]). (b) Power versus time in direct current magnetron sputtering (dcMS) and high-power impulse magnetron sputtering (HiPIMS), respectively.	43
Figure 34. Discharge voltage V _d as a function of the O ₂ flow during reactive dcMS and HiPIMS of a Ce target. For the HiPIMS process, pulsing frequencies of 1 and 4 kHz are shown. The average discharge power was 70W and the argon partial pressure was 0.65 Pa at a pumping speed of 25 l/s (Gudmundsson <i>et al.</i> [233]). ...	45
Figure 35. (a) The discharge current for various oxygen flow rates for Ar/O ₂ discharge with titanium target. The discharge pressure is roughly 0.6 Pa, the repetition frequency 50 Hz, and the pulse voltage is 600 V. (b) The discharge current for various repetition frequencies for Ar/O ₂ discharge with titanium target. The discharge pressure is roughly 0.6 Pa, the oxygen flow rate 2 sccm, and the pulse voltage is 600 V. After Magnus <i>et al.</i> [251].....	46
Figure 36. The discharge current for various oxygen flow rates, for the Ar/O ₂ discharge with titanium target. The pulse length is 200 μs, pulse voltage is 670 V and the discharge pressure is approximately 7.5 Pa. The discontinuous lines shows the current waveform for non-reactive sputtering.....	46
Figure 37. Schematic illustration of the HiPIMS discharge current divided into five different phases. The bottom two curves display an approximately 300 μs long current pulse, where the current decays after an initial peak at around 80 μs mainly due to depletion of the working gas, followed by a current plateau. The	

top two curves illustrate the onset of self-sputtering, where the current may reach a second maximum before the pulse is switched off. The middle curve displays an intermediate state due to partial self-sputtering. The Π_{ss} is a self-sputtering parameter. After Gudmundsson <i>et al.</i> [233].....	47
Figure 38. Schematic 3D view of the sputter chamber: (ssubstrate holder (SH); load lock (LL); temperature controller (TC); Ar and oxygen inlet (1 and 2); turbo pump (TP); target shutter (Sht.) and axis manipulator (AM).	48
Figure 39. A close view inside the RTA processor.....	49
Figure 40. Schematic of the cylindrical inductively coupled discharge H ₂ /Ar utilized for hydrogenation. The inset shows a schematic of structure i.e. Sip/SiO ₂ /SiGe/SiO ₂ and is also employed for Sip/SiO ₂ /TiO ₂ /SiGe/TiO ₂	51
Figure 41. Home-built hydrogenation setup. The left end of the tube is connected to pumping system, whereas right end is a close end with a gate to insert samples. .	51
Figure 42. Illustration of the 2θ deviation, which causes a phase shift resulting in either constructive (left figure) or destructive (right figure) interferences.....	54
Figure 43. Illustration of constructive interference when Braggs law is satisfied.	55
Figure 44. (a) The geometry in grazing incidence diffraction is characterized by a small angle α that is kept constant during the measurement. (b) XRR experiment from the viewpoint of the sample reference frame. From Birkholz <i>et al.</i> [257].	55
Figure 45. The relationship between force and distance. From Maghsoudy-Louyeh <i>et al.</i> [264]	56
Figure 46. Schematic working principal of AFM.	57
Figure 47. The working principle of AFM in contact mode, where the tip contacts the sample surface with a small cantilever deflection and the feedback loop keeps the deflection constant [266].	58
Figure 48. The Principle working mechanism of atomic force microscopy in tapping mode.	58
Figure 49. Basic construction of SEM.	60
Figure 50. Construction of Everhart-Thorney (SE) detector [271].....	60

List of Tables

Table 1. Exciton Bohr diameter along with E_G for various semiconductors.....	11
--	----

List of Abbreviations

0D	Zero dimensional
1D	One dimensional
2D	Two dimensional
3D	Three dimensional
NCs/NPs	Nano-crystals/ nanoparticles
QDs	Quantum dots
NWs	Nanowires
Pb-defects	Non-radiative defects
E _G	Bandgap
DOS	Density of states
VB	Valence band
CB	Conduction band
HUMO	Highest occupied molecular orbital
LUMO	Lowest unoccupied molecular orbital
SPV	Surface photo-voltage
NIR	Near infra red
Vis.	Visible
MFP	Mean free path
MFC	Mass flow controller
TE	Thermionic emission
CL	Condensor lens
OL	Objective lens
QTH	Quartz tungsten-halogen
SE	Secondary electron
BE	Backscattered electrons
e ⁻ - h ⁺	Electron - hole
CT	Critical thickness
TB	Thermal budget
S-K	Stranski–Krastanov
Si _p - substrate	p-type silicon substrate
GiXRD	Grazing incidence X-Ray diffraction
TEM	Transmission electron microscope
SEM	Scanning electron microscope
STEM	Scanning transmission electron microscope
AFM	Atomic force microscope
XRR	X-ray reflectometry
dcMS	Direct current magnetron sputtering
rfms	Radio-frequency magnetron sputtering
HiPIMS	High power impulse magnetron sputtering
CFA	Conventional furnace annealing
RTA	Rapid thermal annealing
PVD	Physical Vapou deposition
IPVD	Ionized physical vapour deposition
ECR	Electron cyclotron resonance

List of Symbols

Notation	Description
I_p	Photocurrent
U	voltage
\bar{E}	Average ion energy
λ_{fp}	Mean free path
V_c	Cathode fall voltage
Y	Sputter yield
γ_{SEE}	Secondary electron emission coefficient
∇	Gradient
x	Ge fraction in $S_{1-x}Ge_x$
λ	Wavelength
k_α	Characteristic X-rays (electron transitions to the innermost K shell from L shell)
k_β	Characteristic X-rays (electron transitions to the innermost K shell from M shell)
μ	Absorbtion coefficient (in GiXRD)
E_{Γ_1}	Energy separation in conduction band
a_B	Eciton Bohr radius
ϵ_0	vacuum permittivity
m_e^*	Effective mass of electron
m_h^*	Effective mass of hole
\hbar^2	Planck's constant,
$E_G(x)$	Bandgap as a function of Ge fraction
$\Delta\sigma$	Photo-conductivity
q	Electronic charge
Δn	Density of electrons
Δp	Density of holes
δ	dispersion
β	Absorption (in XRR)
k	Spring constant
z_d	Deflection in z-direction(axis)

Chapter 1

1 Introduction

The compatibility of silicon (Si) with germanium (Ge) and their transition from two-dimensional structure to nano-crystallites (NCs) or nanoparticles has grasped the interest of numerous researchers. Employment of SiGe nanocrystals (NCs) hetero-structures have heightened the applications of monolithic Si-based devices because of their high light emission efficiency. The lattice mismatch of 4.2 % between Si and Ge [1–3], formerly a stumbling block, has turned-out to materialize the advantage of such system in quantum electronic and optoelectronic devices, by tailoring the bandgap of the system via quantum confinement, strain engineering and/or varying Ge ratio [1,4–6].

One of the objectives in fabricating such structures is to increase the efficiency of photoconductive devices by widening the spectral sensitivity interval from visible to near infrared with the aim towards applications in photovoltaics [7], optoelectronics [8,9], photodetectors [10], and optical-telecommunications [9]. A considerable effort has been devoted to the clarification of their self-assembly, and whether nanoparticles with dense arrays can be achieved with better control and reliability of their size and properties. These structures have drawn interest especially because of their potential bandgap-tuning by quantization to the optimal power and energies for conversion efficiency and enhancement of optical properties [11–13]. SiGe nanostructures embedded in dielectric/ oxide matrices are potential elements for application in optoelectronic devices.

Being an indirect bandgap semiconductor, Si has relatively poor light absorption [14–17]. Mixing Si with Ge results in reduced bandgap and increased absorption coefficient at longer wavelengths. The bandgap can be further reduced by introducing strain in the $\text{Si}_{1-x}\text{Ge}_x$ system [1,4–6]. Ge is also an indirect bandgap material but with much smaller energy difference between the indirect and direct bandgaps than in the case of Si (136 meV for Ge vs 2.4 eV for Si) [18]. Introducing a tensile strain in the crystal lattice additionally reduces the energy difference between the direct and indirect bandgaps because the direct bandgap shrinks faster than the indirect one. Thus, the bandgap of the SiGe nanocrystals (NCs) can also be adjusted to enhance energy conversion efficiency and optical properties by utilizing strain engineering [11,12,19–21].

For this purpose, significant work has been carried out to fabricate structures having SiGe NCs embedded in oxide matrices such as SiO_2 [22–29], Al_2O_3 [30,31], HfO_2 [31], SiN_3 and TiO_2 [11,32–36]. Of these, SiO_2 and TiO_2 have gained considerable interest due to many reasons. SiO_2 remains amorphous while providing lateral confinement upto high anneal temperature and is compatible with the well-established Si technology [37]. TiO_2 have shown potential candidacy in optics for being cost effective, it is thermodynamically stable, has dense structure, and has high dielectric constant and refractive index [33,38–40]. In bulk form, TiO_2 exhibits three polymorphs i.e., two tetragonal (anatase and rutile) and one

orthorhombic (brookite) [38,41,42]. Out of these, only anatase and rutile have been observed in thin film form, having bandgap energy of 3.2 and 3.0 eV, respectively [38,39,42,43]. The rutile phase is thermodynamically stable and has slightly extended photo-response in the visible range as compared to the anatase phase. The electron-hole rates in TiO₂ films are affected by the direct (rutile) and indirect (anatase) nature of the bandgaps. Therefore higher carrier recombination rates are observed for rutile having an exponential decay profile for electrons and holes, while anatase has longer charge-carrier lifetime and non-exponential decay profile [44,45]. The rutile phase is the densest of the three structures (4.25 g/cm³) [38,46] is transparent upto high end of visible spectral range [45,47] and has high refractive index [47,48] (up to 2.75 at 550 nm). Hence, rutile is broadly utilized for optical coatings, optoelectronic and semiconductor electronics [49]. Its high dielectric constant also makes it a desirable candidate in microelectronic devices [38,43,47,50]. The anatase phase however, is known to exhibit photocatalytic activity superior to that of the rutile phase [45,50].

Formation of SiGe nanocrystals (NCs) in oxide matrix via deposition by magnetron sputtering and subsequent annealing is a widely applied approach [23,24,31,32,51–62] as it gives good control over optical properties by varying the Ge atomic fraction, the size and shape of the NCs and the crystallinity of the NCs. However, a common drawback of the annealing step is a strain relaxation (resulting in dislocation nucleation or intermixing at the SiGe/matrix interface) in the structure, creating dislocations, point defects, dangling bonds, Ge clustering and altered interface morphology. All these phenomena are well known to degrade the optoelectronic and electrical properties of the structure. Additionally, issues commonly observed with fabrication of such structures include inhomogeneity at the matrix/nanoparticle interfaces [16,63,64]. The interface of such structure has been a matter of concern in studying the optical response as it may give rise to dangling bonds acting as electrically active interface traps (known as P_b-type defects) [51,63]. These interface traps produce scattering centers, which can affect the mobility of charge carriers, thus altering the transport properties [63,65]. Moreover, sharp interfaces with an abrupt change in the dielectric constant or thermal expansion coefficients, gives rise to surface polarization effect due to the local field built up (which assumes a crucial role for systems characterized by strong charge inhomogeneity) or strain development in the structure (influencing the size and shape of the NCs, thus resulting in alteration of the bandgap energy).

With the aim to enhance optical and electrical properties, SiGe nanoparticles are sandwiched within oxide matrix, several different approaches were adopted in this work for the fabrication and treatment of the structures:

- controlling annealing parameters, with the aim to avoid: diffusion of oxygen and/or formation of insulating SiO₂ layer, strain development in the structure and large variation in the SiGe ratio due to phase separation in the SiGe nanoparticles.
- use of the HiPIMS method, in order to obtain nano-crystallites already at as-grown state.
- employing hydrogen plasma treatment over as-grown or annealed structures, thus passivating the shallow and deep-level traps, defects in form of dangling bonds and/or non-radiative centers (P_b-defects), along with reduction of the fixed positive oxide charges and formation of relaxed amorphous oxides.

The objective of this study is to obtain oxide films (TiO₂, SiO₂) functionalized with Si_{1-x}Ge_x nanoparticles (NPs), photosensitive in the 0.6-1.2 μm spectral range. Novel solutions for obtaining a new advanced material with targeted photoconductive (PHC) properties were

derived. The innovative results achieved in the project are: functionalized oxide films with $\text{Si}_{1-x}\text{Ge}_x$ NPs where the spectral range of sensitivity is controlled by engineering NPs sizes, composition and concentration; fabrication of PHC-SiGe film-based demonstrator with the targeted PHC properties. At present, for evaluating different slippery road conditions, InGaAs and Si photodetectors (commercial) are used. The PHCG-SiGe based oxide films have improved sensitivity beyond the $\lambda > 1.1 \mu\text{m}$ Si edge, require less expensive technology and are less raw material demanding than the currently available photodetectors.

Chapter 2

2 Theoretical frame of reference

2.1 Semiconductors

Semiconductors are a class of material having electrical conductivity between those of conductors and insulators. Here an insulator is a material that does not conduct electrical current under normal conditions. Most good insulators are compounds rather than single-element materials and have very high electrical resistivity. A conductor is a material that easily conducts electrical current. Most of the metals are good conductors. Silicon and germanium are the best known elemental semiconductors. As the name suggests elemental semiconductors are formed from a single chemical element which itself acts as a semiconductor by origin. Si and Ge both belong to group IV in the periodic table of elements, on the border of the line separating metals and nonmetals. They have cubic lattice structure with varying lattice parameters. The basic properties of Si and Ge will be discussed in later paragraphs.

In contrast to elemental semiconductors, compound semiconductors are composed of two or more elements. GaAs and InP are common examples of the latter. These compound semiconductors provide an example of group III-V semiconductors, where one element in the semiconductor belongs to group III of the periodic table and the other to group V. The chemical bonds in III-V semiconductors are much similar to that for elemental semiconductor (i.e. number of electrons and protons is equal), this is because there is one electron deficiency for the group III elements which is compensated by one extra electron in the group V element. Similar explanation goes for compound semiconductors of II-IV. However in this case group II element is deficient by two electrons which is compensated by two extra electrons in group IV elements. Details about the compound semiconductors will not be further entertained here.

Semiconductors are also classified on the basis of their band structure as:

- Direct bandgap semiconductor
- Indirect bandgap semiconductor

Before describing the (energy) band structures of semiconductors, it is crucial to understand the electron configuration in crystals. Each electron of an atom has its unique set of so-called quantum numbers, defining their energy and position. When numbers of atoms approach each other to form a solid, their outermost electrons (valence electrons) start to interact with each other. As dictated by Pauli's exclusive principle, no two electrons of the same atom or system can have the same set of quantum numbers. Thus, the sharp (discrete) energy-levels of the atoms overlap to form a bundle or band of energy levels, so-called energy band. Upon further approach of the atoms, the energy band splits into two energy bands corresponding to bundles of bonding and antibonding molecular orbitals. In particular, the lower energy bands corresponding to bonding are referred to as valence band and is regarded as

a linear combination of all bonding orbitals formed between constituent pairs of atoms in the crystal. In contrast, the linear combination of all anti-bonding orbitals having the higher energies are referred to as conduction band. A resultant consequence of the electronic structure with bonding and anti-bonding orbitals is the appearance of bandgap or energy gap (E_g), the size of which depends on the binding energy of the crystals and on the widths of the valance and conduction band.

For an insulator this gap is quite large. Excitation of electrons from the valence to conduction band requires large amount of energy and only very few mobile carriers will ever be present within an insulator at moderate temperatures. For conductors (classical metals) the bands i.e. valance and conduction band do overlap and little or no energy is required to generate mobile carriers. Thus in between insulators and conductors are semiconductors having a bandgap that is relatively small and is between those of metals and insulators (See **Fig. 1**).

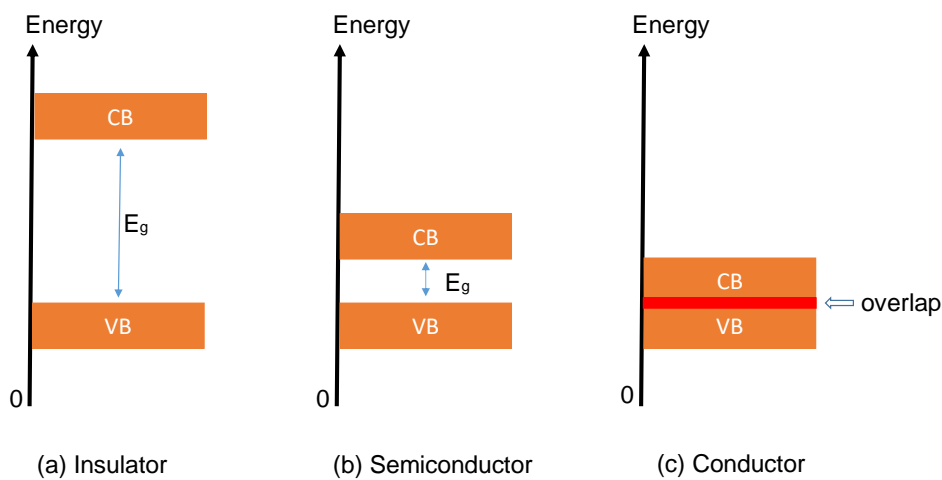


Figure 1. Schematic expression of the bandgap of (a) insulator, (b) semiconductor and (c) conductors. CB and VB corresponds to conduction and valence band, respectively.

Thus the bandgap of semiconductors i.e. direct and indirect bandgap can be explained by the band structure, where the electrons in solids have a wave like character represented by a wave vector \vec{k} . Thus for crystalline materials a simple energy band diagram can be constructed as E vs. \vec{k} , that presents the valence and conduction band.

In lattices, the band structure takes complex 3-dimensional shape. Semiconductors having their lowest laying minima of the conduction band directly above the highest maxima of the valence bands (thus at the same wave-vector) are referred to as direct bandgap semiconductors. Similarly, if the lowest laying minima of the conduction band does not appear at the same wavevector as the highest maxima of the valence band, the semiconductor is said to be with indirect bandgap. In a direct bandgap semiconductor the electron can be excited from the valence band (VB) to the conduction band (CB) directly without any change in its momentum at $k = 0$; for instance by thermal excitation or by optical absorption. On the contrary in an indirect bandgap semiconductor the minimum in the conduction band does not occur at $k = 0$, and thus there is a need for change in momentum. In this case excitation of electron from the VB to CB requires interaction with the crystal lattice in order to satisfy the principle of momentum conservation. A schematic representation of direct and indirect nature of bandgaps is shown in **Fig. 2**. The nature of bandgaps in semiconductors is of technological significance for optoelectronic applications.

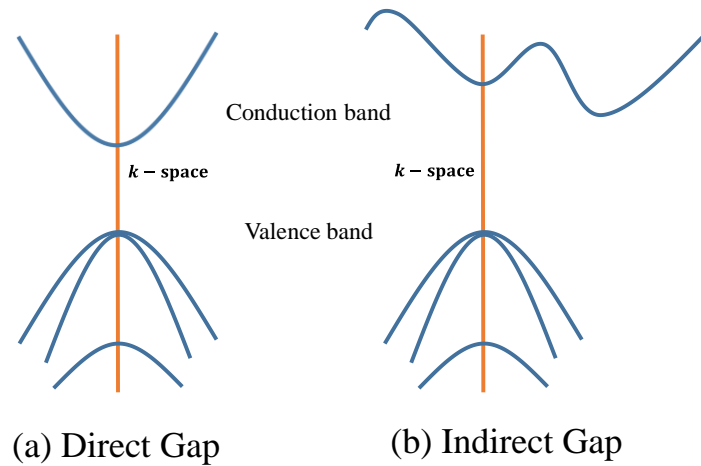


Figure 2. Schematic presentation of (a) direct and (b) indirect bandgap in semiconductors.

Silicon

Silicon (Si) is the world's most perceived material in modern electronic and optics, mainly due to its abundance, low cost, incoherent toxicity and maturity in the purification process and device fabrication [66]. However, unlike most of the II – VI group nanoparticles (which have direct bandgap transitions), bulk Si possesses indirect energy-gap which makes it less efficient in light emission. The emission and absorption of photon in this case requires in addition to energy a change in lattice vibration (i.e. phonon assisted excitation). Such limitation makes the use of bulk Si in optoelectronic application limited [67]. In addition, the bandgap of Si is too small to interact effectively in the visible spectrum. It could be anticipated that if the gap could be tuned, it could give Si larger role in optoelectronic applications. Low-dimensional Si structures and NCs exhibit distinctive properties different to bulk-Si, and their bandgap can be tuned by altering the size, crystallinity and shape of the NCs (more detailed discussion will be given in succeeding chapter). Since 1990, when Canham [68] observed room temperature photoluminescence in porous Si in the visible range, silicon-clusters, nanoparticles (NPs/NCs) and quantum dots (QDs) have tantalized many research on experimental, theoretical and computational basis.

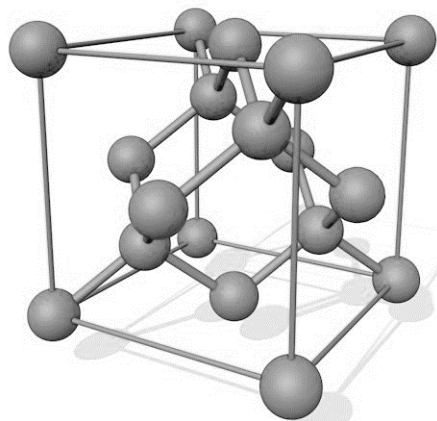


Figure 3. The diamond crystal structure of silicon.

Silicon crystallizes in a diamond structure on a face-centered cubic (FCC) Bravais lattice displaced by one quarter of the body diagonal ($a_0/4 (1, 1, 1)$) as visualized in **Fig. 3**. Other materials that possess a diamond structure when crystallized include for example, Ge, Sn and C. The lattice constant a_0 for Si is 5.431 Å. The indirect bandgap of Si is 1.12 eV at 300 K.

Germanium

Germanium (Ge) is an elemental semiconductor (metalloid) in group IV in the periodic table, just like Si. It was discovered in 1885 in Freiberg, Germany, and is greyish-white in color and has physical and chemical properties similar to that of Si. Like silicon, Ge has a diamond structure with a lattice parameter $a_0 = 5.658 \text{ \AA}$. Although Si is superior to Ge in respect to mechanical properties, chemical stability and formation of stable oxides, Ge has its own advantages. These advantages includes higher carrier mobility and lattice constant closer to that of the III – IV group materials providing more coherency when such materials are matched together.

Ge is an indirect bandgap material with $E_g = 0.66 \text{ eV}$. However, it has direct bandgap of 0.8 eV (E_{Γ_1}) (i.e. only 0.14 eV above the indirect bandgap [18]), which results in the aforementioned increase in carrier mobility and also provides the possibility of transformation from indirect to direct bandgap material upon application of strain.

2.2 Quantum dots and quantum confinement

Semiconductor quantum dots (QDs) are nano-sized inclusions that have smaller bandgap than its bulk counterpart. This difference in bandgap acts as a potential barrier for carriers, thus confining them inside the dot itself. This shrinkage in size at a nanometer scale makes the carriers occupy only discrete levels, and the transition between these levels in the conduction and valence band requires either the absorption or emission of photon at optical energies [69].

Semiconductor QDs have a crystal structure with diameter of few nanometers consisting of $\sim 10^3 - 10^9$ atoms. Quantum dots can be created by spatially confining the materials in three dimensions [70]. The dimensionality refers to the degree of freedom in term of direction in which the carriers within a material are free. In case of bulk semiconductor the carriers (electrons and holes) are free in all three directions, hence 3D structure. Now if we consider or spatially confine the bulk material in one direction we have a thin film (also referred to as quantum well). Further, if we now confine the thin film we are left with a 1D system also known as nanowires (NWs). Eventually when a material is confined in all three directions, we have a 0D structures i.e. QDs or nanoparticles/ nanocrystals (NPs/NCs). A schematic illustration of confinement from bulk to 0D structure is shown in Fig. 4.

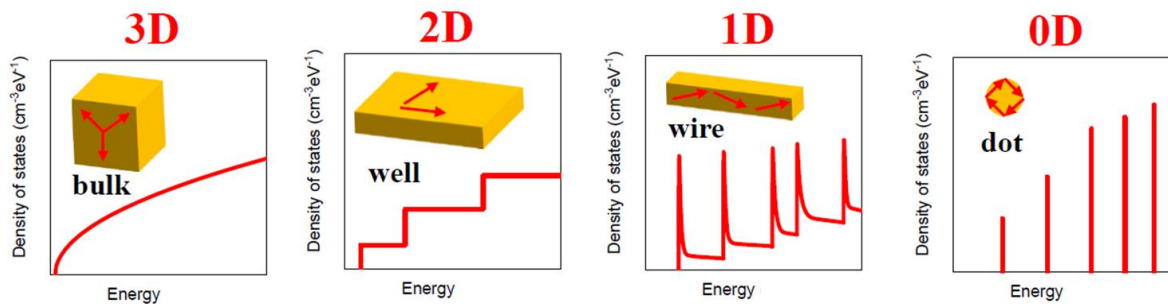


Figure 4. Low dimensional structure 3D – 0D, along with density of states vs. energy for bulk materials, quantum well, quantum wire and dots (i.e. 3D to 0D, respectively) [71].

For a semiconductor structure which is brought down to nanoscale, with low number of atoms, the quantized energy level become perceptible and distinct, and the quantum confinement effects plays a vital role in determining the properties of the material. Therefore, any addition or removal of atoms from the nanostructure (QD) significantly changes the energy levels within the bandgap thus making the bandgap size dependent [72–74]. The plot

in **Fig. 4** can emphasize the importance of the spatial confinement of carriers, for density of states (DOS) for respective structures from bulk to low-dimensional structures. As can be seen, the charge carriers in the 0D structures are restricted to a particular set of quantized energy states rather than a continuous band of allowable energies as in case of bulk materials [75]. There are several properties of QDs that make such structures intriguing for the purpose of science and technology. For example the possibility of bandgap tuning, discrete energy levels, high carrier mobility, long relaxation time and light absorption and emitting efficiency superior to that of their respective bulk counter parts [76].

2.3 Exciton Bohr radius

A photon of energy greater or equal to the bandgap is capable of making an electron-hole pair by exciting an electron from the VB to CB, leaving an empty hole in its place. Such electron - hole ($e^- - h^+$) pair as an entity is called exciton. The average exciton size (called exciton Bohr radius) is smaller than the size of the QD, creating an energy confinement as the exciton is squeezed into the material. The Bohr radius of exciton is given by:

$$a_B = \frac{4\pi\epsilon_0\epsilon_\infty\hbar^2}{m_0e^2} \left(\frac{1}{m_e^*} + \frac{1}{m_h^*} \right) \quad (1)$$

Where, a_B is the Bohr radius, ϵ_0 is the permittivity of free space, \hbar is the reduced Planck's constant, m_0 is the electron rest mass, e is the elementary charge, and m_e^* and m_h^* are the effective masses of electrons and holes, respectively. In contrast to bulk materials, QDs do not form continuous valance and conduction bands. Instead they create discrete electronic states (energy levels); the bigger the QDs the smaller the bandgap will be. (**Fig. 5**). In brief, for QD the confinement of an electron in nanometer crystalline materials requires that its wave-function vanish outside the crystallite. The magnitude of the confinement energy can be determined by the equation:

$$E_{\text{conf}} = \frac{\hbar^2\pi^2}{2a^2} \left(\frac{1}{m_e^*} + \frac{1}{m_h^*} \right) = \frac{\hbar^2\pi^2}{2m_0a^2} \quad (2)$$

where, m_0 is the reduced mass of the exciton system, and a is the radius of the quantum dot.

Table 1. Exciton Bohr diameter along with E_g for various semiconductors.

<i>Semiconductors</i>	<i>Exciton Bohr diameter</i> (Å)	E_g (eV)
<i>Si</i>	37 (longitudinal)	1.12
	90 (transverse)	
<i>Ge</i>	50 (longitudinal)	0.67
	200 (transverse)	
<i>GaAs</i>	280	1.43
<i>CdSe</i>	106	1.74
<i>CuCl</i>	13	3.4
<i>ZnSe</i>	84	2.58
<i>CdTe</i>	150	1.50

The effect of changing size on the bandgap of the QD's depends on the confinement regime. This regime is a function of how the size of the quantum dot compares to the exciton Bohr radius a_B , which can be calculated for a specific material using **Equation (1)**. If the quantum dot radius is of the same order of magnitude as the exciton Bohr radius, it is said to

be in the “weak confinement regime”. Quantum dots in the “strong confinement regime”, which are smaller than the exciton Bohr radius, are however of more interest. In this regime, confinement effects dominate and energy levels do not yet form a continuous spectrum, and the optical and electronic properties can be easily controlled.

The nature of the $e^- - h^+$ bond, in some aspects analogous to that of the hydrogen atom, in which a single electron is bound to a single proton by Coulombic attraction. In similar fashion this applies to the behavior of exciton, as the electron orbits the hole and a set of hydrogen-like states are created, and therefore the Schrödinger wave equation is easily adaptable in order to solve the energy states in a quantum dot. Furthermore, similar to that of Bohr’s model where electrons orbit the nucleus, the same notion is applied to QDs not just complying with the energy states but also to that of carrier orbit dimension. Thus, akin to an electron orbiting the nucleus with a dimension called Bohr radius, so does the e^- orbiting a h^+ . In a QD exciton, the exciton Bohr radius is a critical dimension over which the size confinement of the materials is evaluated. **Table 1** summarizes some of the semiconductors exciton Bohr radius [78–80]. Thus for instance in the case of Ge the exciton Bohr radius is 50 \AA , this means in order to obtain a quantum confinement the size of Ge NCs needs to be approximately 50 \AA or lower.

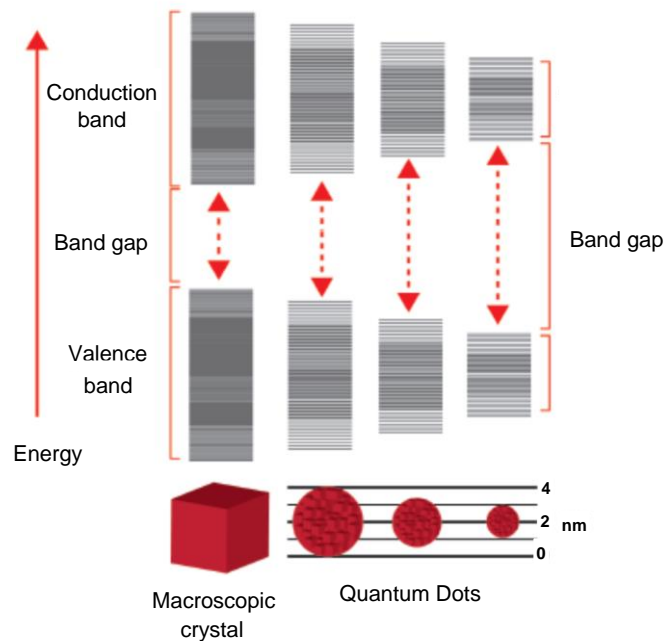


Figure 5. Illustration of the change in energy levels as a function of crystal size. The quantum dot materials shows the individual energy levels which can be calculated using the particle-in-a-box model [77]. As the crystal grows bigger, it approaches the bulk semiconductor state with energy bands separated by the bandgap energy.

2.4 Low-dimensional nanostructures

2.4.1 Si-NCs

Silicon is the mainstay in semiconductor technology with its application in micro and nanoelectronics but it has been considered unsuitable for applications in optoelectronics owing to its indirect energy bandgap. This is until the discovery by Cahm and Cullis *et*

al. [68,81,82], showing the possibility of light emission in porous-Si. These low-dimensional Si-based structures have grasped interest of numerous researchers, with studies still under way aimed at increasing the room temperature light emission from systems such as Si-NCs, porous-Si, and superlattice structures embedded with Si NCs [62,83–85]. These recent developments have shed the focus on the fabrication of low dimensional NCs. Due to the exceeding small region of space in such systems, it has been given its name as ‘dots’ [86], thus eventually called Si quantum dots. In fact, these are also referred as artificial atoms as to reflect the importance of quantization observed in their properties [86]. It is believed that light emission in Si QDs/NCs structures is originated from the quantum confinement phenomena and from the defects or interface states present between Si-NCs and surrounding medium [56,87,88].

A fundamental consequence of quantum confinement of electronic wave-function in Si-NCs, is that these nanoparticles exhibit bandgap energy which is found to depend on the size of the NCs [89]. Another consequence of the quantum size effect in Si-NCs smaller than exciton-Bohr radius, is the spatial confinement of charge carries, i.e. there exists a significant overlap and a spread of the wave functions in k-space for the electrons and holes in NCs. Thus, quantum confinement in such systems results in efficient light emission with energy corresponding to the bandgap determined by the size of Si-NCs [90,91]. This allows for unique applications in the fields of optoelectronics, semiconductor memories and photovoltaics [92].

Among the various schemes employed for the synthesis of systems containing Si nanocrystals, structures with embedded Si-NCs in oxide matrices are of significant interest as the available growth techniques allow good control over the size and crystallinity of NCs, their distribution and density [11,21,32,34,83,87,91–97], along with very fast optical transition, and multiple carrier generation[98]. This results in potential applications of such systems in light emitters [84,87,92,99,100], photodetectors [98,101,102], solar cells [55,56,99,100], semiconductor memories [92] and silicon based lasers [21,55]. Systems with NCs embedded in a thin layer of dielectric/oxide matrix offer the possibility to tune the bandgap by controlling the size of the NCs.

2.4.2 Fundamental properties of SiGe NCs

The distinctive properties that awarded Si its leading position in the electronic world and devices includes:

- A bandgap of 1.12 eV allows operation to temperatures several hundred degrees higher than for Ge.
- A stable oxide, SiO₂, which tends to act as a passivating mask in device manufacturing; thus preserving device functionality and surfaces.
- An extremely low-density of surface states at interfaces especially at the SiO₂-Si interface.

In contrast, the oxide of Ge is not stable and the interface density of states is too high for the operation of a metal-oxide-semiconductor field effect transistors (MOSFET) [103][16]. In addition, the rapid improvements in Si technology, i.e., doubling the number of devices per chip and their speed approximately every 18 months, as postulated by Moore’s Law, have been in progress for the past 40 years. However, the dimensions have become so small that the device scaling is in jeopardy. Improvements based not only on dimensionality but also on

fundamental properties have to be realized. The mobility of electrons and holes is one such critical property and is ultimately related to the band structure. For instance, the band structures of Si has six equivalent CB minima and three VB maxima, all at the center of the Brillouin zone and application of stress to its structure profoundly affects the bandgap. Thus, in this situation, the six CB minima in Si are affected by the intervalley scattering and the degeneracy of VB is lifted. The changes in band structure lead to changes in mobility, where the holes will reside in the lower or the higher effective mass band, depending on the sign of the stress. While, the electron mobility rises with stress because the intervalley scattering becomes smaller and the hole mobility increases when the effective mass becomes smaller. In order to overcome such strain-effect, one approach is the formation of SiGe alloy graded composition, or a deposition of relaxed $\text{Si}_{1-x}\text{Ge}_x$ epitaxial layer on a silicon wafer [6,17,52,104] where the value of x can be varied (as discussed later in this chapter). A variation in x will cause a variation in the lattice constant accordingly. Experimentation with $\text{Si}_{1-x}\text{Ge}_x$ epilayers, both strained and relaxed, started in the 1980s led to commercial devices [6,103]. Bandgap engineering for increased mobility of electrons and holes through strain, caused by the addition of germanium, has brought this element back full circle into mainstream electronic device technology. However, the outlook for Ge may be even brighter. The reader with an interest in this topic is referred to an excellent recent review by Hiller *et al.* [62].

In the past two decades, much effort has been devoted to the study of Ge-NCs due to their wide range of applications in new integrated optoelectronic devices and highly-efficient solar cells [105]. Compared with Si-NCs, Ge-NCs exhibit strong visible photoluminescence and electroluminescence, which are suitable for fabrication of light-emitting devices [106–109]. The hole and electron mobilities of bulk Ge are 4.2 and 2.6 times higher than those of Si [31,110], so that the nanostructured germanium is very promising for the development of high-speed devices. Also, the low energy bandgap of Ge (0.66 eV) can increase the quantum confinement effects inside Ge-NCs for promoting multiple exciton generation in third generation solar cells [105].

As an indirect bandgap semiconductor, Si has relatively poor light absorption. However mixing it with Ge results in reduced bandgap and increased absorption coefficient at longer wavelengths. A further reduction in the bandgap can be obtained by introducing strain in the $\text{Si}_{1-x}\text{Ge}_x$ system [60]. As already mentioned, Ge is also an indirect bandgap material but with much smaller energy difference between the indirect and direct bandgaps than in the case of Si (136 meV for Ge vs 2.4 eV for Si) [3,111]. An introduction of a tensile strain in the crystal lattice additionally reduces the energy difference between the direct and indirect bandgaps because the direct bandgap shrinks faster than the indirect one. Thus, the bandgap of the SiGe nanocrystals (NCs) can be adjusted to enhance energy conversion efficiency and optical properties by utilizing strain engineering [11,12].

Physical properties of Si and Ge

Si and Ge having similar lattice structure (diamond) are completely miscible over the full range of composition [2,112,113] and hence can be formed into alloy of $\text{Si}_{1-x}\text{Ge}_x$ with Ge fraction ranging from 0 – 100 %. The phase diagram in a binary system for Si-Ge is shown in Fig. 6.

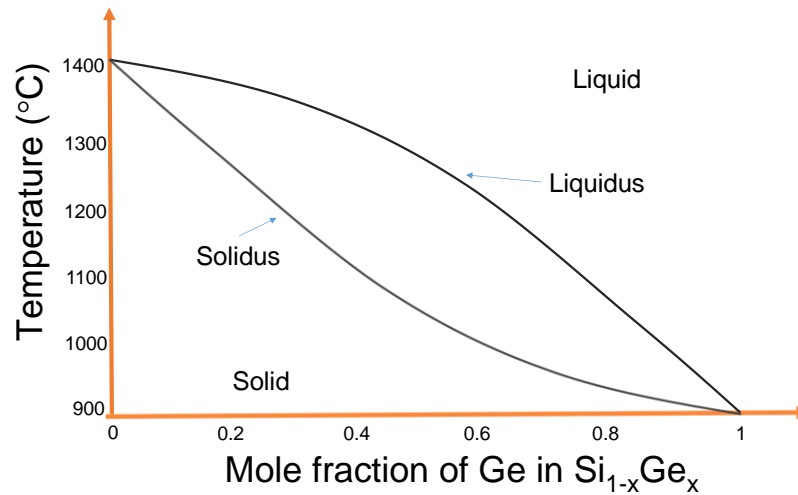


Figure 6. Binary phase diagram of the Si-Ge.

Furthermore, since Si and Ge have a different lattice constants, the misfit or lattice mismatch for $\text{Si}_{1-x}\text{Ge}_x$ with respect to Si accounts for 4.2 %. The SiGe lattice constant is given by Vegard's rule [2]:

$$a_{\text{Si}_{1-x}\text{Ge}_x} = a_{\text{Si}} - x (a_{\text{Ge}} - a_{\text{Si}}) \quad (3)$$

However, for the lattice constant of bulk relaxed SiGe alloy, a small deviation from the Vegard's rule is observed and the lattice constant is given by Kasper and Lyutovich [113] as:

$$a_{\text{Si}_{1-x}\text{Ge}_x} = 0.5431 + 0.01992x + 0.002733x^2 \quad (4)$$

When the SiGe layer is grown over the Si-substrate, the lattice mismatch at the interface of these two materials has to be accommodated either by compression of SiGe layer such that it fits the lattice constant of Si-substrate or by the formation of misfit dislocations at the interface [2,112] (shown schematically in the Fig. 7). The dislocation-free strained SiGe in the former case is called “pseudomorphic” whereas, in the latter case the SiGe layer is relaxed (unstrained) with consequent formation of in plane misfit dislocation to accommodate the lattice mismatch.

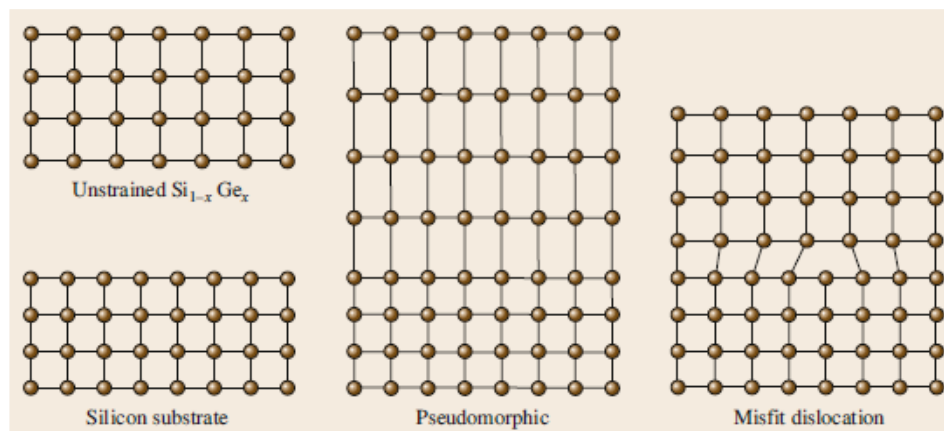


Figure 7. Sample illustration of $\text{Si}_{1-x}\text{Ge}_x$ pseudomorphic growth and misfit dislocations [2].

Critical thickness

For $\text{Si}_{1-x}\text{Ge}_x$, the critical thickness (CT) can be defined as the thickness that can be grown before the strain relaxation occurs via formation of misfit dislocation i.e. the thickness above which a large amount of energy would be required to grown elastically strained (hetero) layer in coherence with the substrate[2,6]. The critical thickness as discussed by Haddera *et al.* and Berbezier and Ronda [2,6] was found to depend on the Ge fraction in the $\text{Si}_{1-x}\text{Ge}_x$ layer.

The two most widely used critical thickness derivations in literature are those by Matthews and Blakeslee [114,115] and People and Bean [116]. According to Matthews and Blakeslee, the derivation for critical thickness was made on the basis of mechanical equilibrium of the threading dislocations. However for some hetero-layers which were grown at low temperatures, the critical thickness explained by Matthews and Blakeslee was exceeded. This inconsistency was later explained by People and Bean who re-calculated the CT, assuming that the misfit dislocation formation was dependent solely on the energy balance. Here the discrepancy between the two models can be described by a gradual strain relaxation process in the $\text{Si}_{1-x}\text{Ge}_x$ layers as shown in Fig. 8 [2,113]. The layers with thickness below the Mathews can be considered as strained while layers with thickness above People and Blakeslee can be considered relaxed. The strained layers are usually termed as *stable* as they do not relax during any subsequent annealing [14]. The layer lying between these two curves are referred to as metastable. Although these layers are free of dislocations after the growth process, they are susceptible to relaxation by forming dislocation [117] and other form of instabilities (explained in [6,14]) during high temperature annealing.

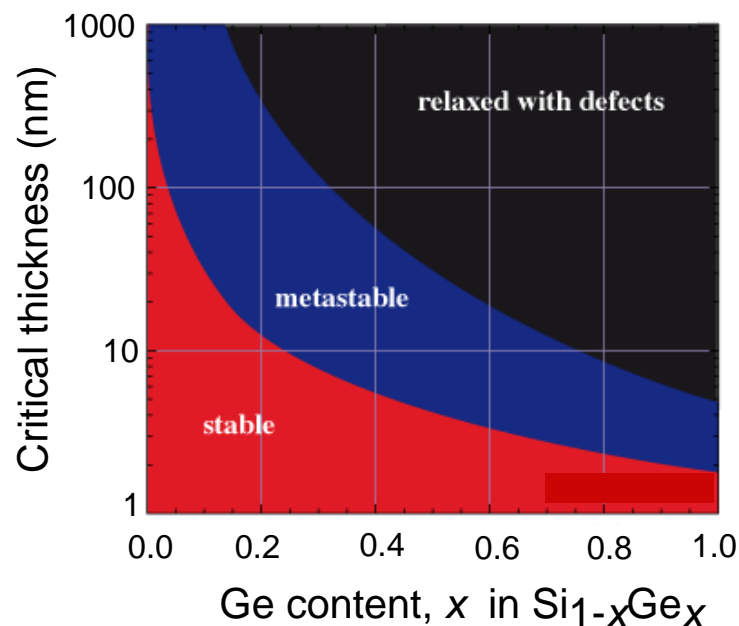


Figure 8. The critical $\text{Si}_{1-x}\text{Ge}_x$ thickness as a function of germanium percentage [113].

Band structure

$\text{Si}_{1-x}\text{Ge}_x$ has a smaller bandgap than silicon, partly because of the lattice constant, which is larger, and because of lattice-mismatch induced strain [2]. Fig. 9 shows the variation in bandgap as a function of Ge fraction for both strained and unstrained $\text{Si}_{1-x}\text{Ge}_x$. It is to mention here that the bandgap is strongly depend on the type and magnitude of strain, which is further affected by the type and orientation of the substrate [6]. Thus, the data provided in Fig. 9 are for a Si (001) substrate. It is evident form the figure that the strain have an immense effect on the bandgap, and that the bandgap narrowing increases with increased Ge fraction. For the

unstrained $\text{Si}_{1-x}\text{Ge}_x$ the variation in bandgap (E_g) as a function of Ge fraction can be determined by following equation [2,113]:

$$E_g(x) = \begin{cases} 1.17 - 0.47x + 0.24x^2, & x < 0.85 \\ 5.88 - 9.58x + 4.43x^2, & x > 0.85 \end{cases} \quad (5)$$

Whereas for strained layers the following equation is appropriate:

$$E_g(x) = 1.17 - 0.94x + 0.34x^2 \quad (6)$$

The above equations are suitable over the entire range of Ge fraction.

From above descriptions, it is worth noting that the band structure of hetero-devices is important in the operation design, and performance of electronic devices. For the case of $\text{Si}_{1-x}\text{Ge}_x$, the strain can lift the degeneracy of the degenerated bands and alter the band alignment at the hetero-interface of the two materials. It is important to understand that the nature of strain in such structure comprises of two important components i.e. ‘*hydrostatic*’ strain and ‘*uniaxial or biaxial*’ strain [113,118,119]. The former type of strain will change the position of the band while the latter type will split the degeneracy of the band. . At last, it can be concluded that not only the bandgaps are important for the hetero-layers, but the alignments of bands at the interface is also crucial for the device consideration. A detailed study of strain in structure (comprising of SiGe-NCs in an oxide matrix) and its effect over the spectral response are highlighted in chapter 5 Results and discussion.

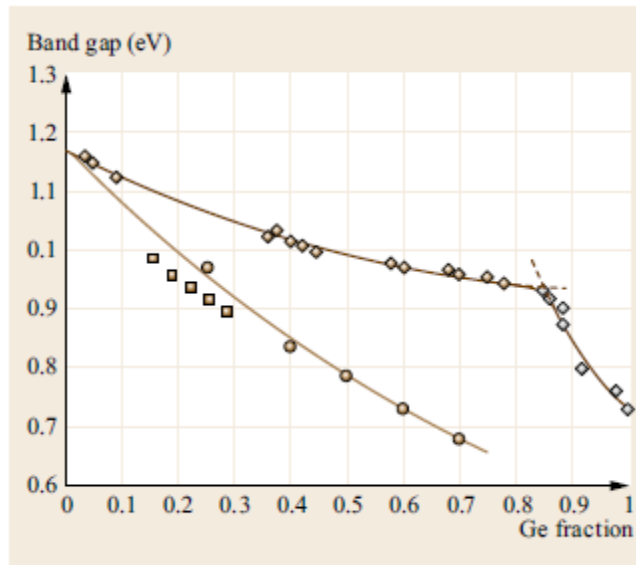


Figure 9. The bandgap as a function of germanium percentage for unstrained (diamonds), strained undoped (circles), and strained heavily doped $\text{Si}_{1-x}\text{Ge}_x$ (squares) [2].

2.4.3 SiGe nanostructures

Down-the-line nano- is the principal theme in all discipline of science from both industrial and academic applied research perspective due to their structural and physical behaviors they adopt at nanoscale, in comparison to their bulk form. In semiconductors the interest in their nanoscale dimensions stems fundamentally from the fact that at such small scale the properties alters due to quantum length scale which are affected by the size and shape of the nanostructure.

Although the micro and nanoelectronics industry is governed by group-IV semiconductors such as Si and Ge, they have not been as popular in the area of optoelectronics due to nature of their indirect bandgap. It was since the advent of nanotechnology by Canham as mentioned earlier, these semiconductors have been the substantial matter of subject in research, as it has opened vast variety of new possibilities for their application in micro and optoelectronics, bio-imaging, photodetectors and with the foremost advantage of being compatible with the actual and already existing device technology [120,121].

The future of nanoelectronic devices rely on structures having features of \sim less than 10 nm, for which many new quantum device concepts have been proposed [14]. Still the bottleneck of these proposed devices depends on the composition, complexity of structure, morphology, the self-assembly of the nanostructures, the dopant and their concertation, and/or their fabrication on virtual substrate. Thus, the understanding and control of growth processes is essential in improving the device performance.

SiGe nanostructures/hetero-structure have emerged during last few decades as a viable system for device technology industrially, due to their self-assembly, low cost and a simple design. Self-assembly of nano-objects is one of the emerging fields of research because of potential applications in different areas, for which the local physical properties can be tailored at the atomic scale, such as to govern the optical and electronic properties [14]. Most common methods to produce these nanostructures include NCs embedded in a matrix or grown over the substrate or a film in form of nanoislands. Such matrix embedded NCs have long term stability and are already well established for use with deposition techniques commonly integrated in standard nanoelectronics fabrication lines [14]. However, although these materials and process techniques are quite mature, the device characteristic are different in production line compared to those demonstrated by the devices in research practice [6,122]. This has been attributed to high temperature thermal annealing which additionally implicates a huge thermal budget (TB)). Here the thermal budget is defined as $TB = \int T dt$, and is a quantity of particular relevance without any physical meaning [56]. Several definition of TB employ the product of temperature T and time t. Thus, it is possible to use statement corresponding to low thermal budget even at high temperature for which the time of process is very short. However, the other definition of TB takes into account the product of diffusivity and time, thus defining the unwanted diffusivity and degradation of interface [54]. Moreover, the thermal budget has a significant impact on the dopant distribution profile and diffusion length which are not a linear function of temperature and time [56]. Thereby, rather high TB complicates the process integration into sensitive devices [55] and also delays the energy efficient production and pay back of these devices, as it is assumed to have detrimental effect on strain relaxation, dopant redistribution, clustering of Ge in SiGe and degrading interface morphology [14,29,36,65,123,124].

Formation of Si_{1-x}Ge_x nanodots/islands

In SiGe system, nanoislands may result due to relaxation of elastic strain after formation of wetting layer by Stranski–Krastanov (S-K) mode where the formation of QDs is governed by competition between thermodynamics and kinetics [125]. The classical stages of nanoislands formation involves nucleation and subsequent growth of islands by coarsening (including Ostwald ripening and diffusion mechanism). The growth scheme of SiGe islands involves more detailed evaluation not accounted for by S-K method [1].

- Monolayer formation by layer by layer mode with formation of dimer vacancies.
- 3D islands start to form after roughening of an initial layer via mass transfer by surface diffusion as a result of strain or morphological instability.

As the coverage keeps on increasing, various transition in metastable morphologies from pyramid to square based and to dome-shaped islands occurs. Moreover, several other parameters including surface anisotropy, which involves surface orientation and hetero-epitaxy, involving different materials and alloying plays a vital role in altering the growth mode of islands and their properties [1,5,125,126]. Misfit between the islands and their substrate, subsequently influence the shape of the islands as they grow. The strain can be relieved through the introduction of dislocation or islands in metastable state this is circumvent by the high energetic cost of dislocation formation e.g. during the creation of dome shaped Ge island on Si substrate [1,5,18,58,117,127]. Alternatively, strain can be relieved by transition from square morphology to rectangular or dome shaped islands [6].

Different substrates exhibit different growth modes and nanoislands morphologies depending on the orientation as well, for e.g. (001) and (111) orientation of Si-substrate. A graphical representation and a detailed study over the formation of nanoislands was carried out in this study [1,6,14]. For the case of Si-(111) substrate, only two growth regimes are distinguished i.e. 2D layer by layer growth at low thickness and strain equivalent to Ge content, while a S-K growth mode at higher thickness and strain (**Fig.10a**). Where as in the case of Si(001) (used in our studies) the evolution of SiGe can be categorized into four different regimes that corresponds to different surface morphology and strain relaxation processes [6,128,129] (**Fig.10b**). Only a brief discussion about the growth and structural changes of SiGe over Si-(001) substrates is given here. A thorough review can be found elsewhere [1,6].

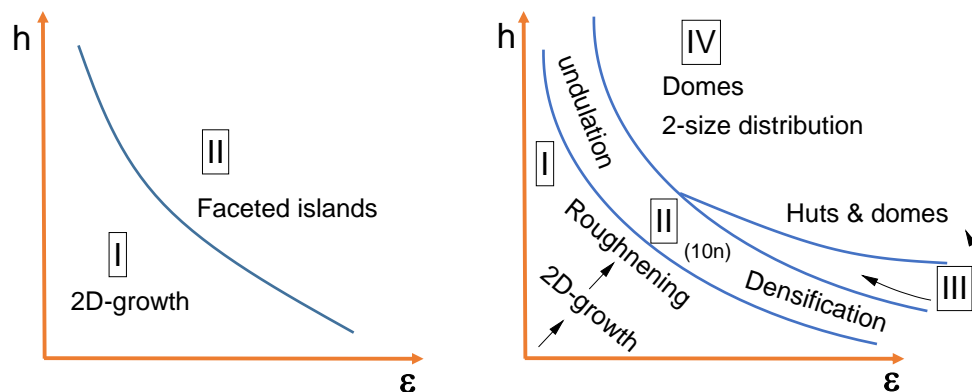


Figure 10. A schematic kinetic phase diagram (at anneal temperature of 500 °C) showing the growth regimes of $\text{Si}_{1-x}\text{Ge}_x$ layers as a function of the deposited thickness h and misfit m due to strain ϵ on (a) Si (111) and (b) Si (001) substrate. After Berbezier *et al.*[6].

- *Regime I*: layer-by-layer growth accompanied by a gradual increase of surface roughness;
- *Regime II*: ripple-like islands (or undulations) that exhibit a broad distribution in size and in shape at low (h,ϵ) and square base islands (called “huts” islands) at higher misfits;
- *Regime III*: coexistence of “huts” and “domes” islands. The two island groups are characterized by different aspect ratios and faceting;
- *Regime IV*: bimodal size distribution of domes that correspond to dislocated and coherent structures respectively.

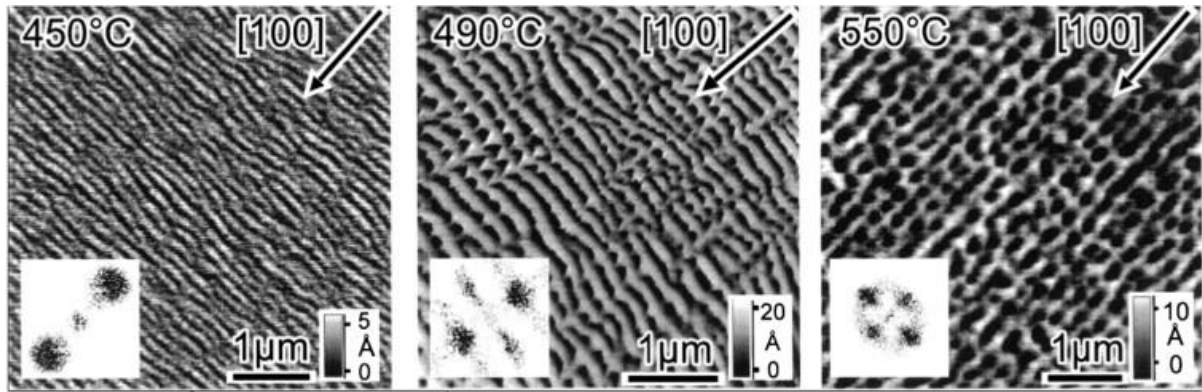


Figure 11. AFM images of 200 nm thick homoepitaxial SiGe layers deposited on Si (001) surfaces with a miscut of 1.16° in [100] direction (arrows). Films were deposited at 0.8 \AA/s and substrate temperatures of 450, 490, and 550 °C (from left to right). Insets depict the 2D Fourier transforms. From Berbezier *et al.* [6].

In regime I (with low deposition thickness or Ge content) the growth mode can be categorized by a flat surface which gradually roughens during growth by formation of kinks and dimer vacancies [130] and other steps formations [131] that in turn relaxes strain [1]. Another possible mechanism of strain relaxation in this regime is the intermixing of SiGe. Regime II is associated with the formation of ripple like islands (also named undulations) [6,14] that show a broad size and shape distribution. An example of such feature is shown in **Fig. 11**. These structures shows an interesting feature that is their elongation in a direction at 45° from the $(2 \cdot n)$ reconstruction which continuously increases with the deposited thickness up to formation of long undulated regions.

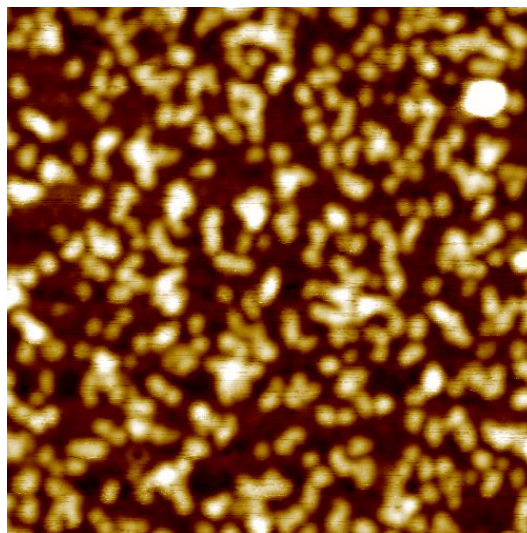


Figure 12. $5 \times 5 \mu\text{m}^2$ AFM image of SiGe over p-type Si(001)-substrate annealed at 600 °C for 1 hr.

However, these undulations present very low aspect ratios for h/l of ~ 0.05 and a slope of $\sim 5^\circ$. Additionally, there is a possibility at some growth temperatures and alloy compositions that islands can evolve from these undulations [14]. The island formation can be followed by formation of pre-pyramid islands that form with no nucleation barriers. For the higher Ge content or higher deposited thickness, these undulated regions (or pre-pyramids) transform into faceted islands (called “huts”) over a rough wetting layer (**Fig. 12**). These islands adopt a rectangular shape which have their sides oriented along the $\langle 100 \rangle$ direction and the four sides correspond to (105) facets with aspect ratio of ~ 0.1 [6,14]. Two possible mechanism

for hut formation has been proposed in the study by Berbezier *et al.* [6]: one in which the transformation is thermally activated nucleation process and the other is barrier less formation of faceted huts which are formed through transforming pre-pyramids. It is also deduced that there is a possibility of strain relaxation taking place in hut islands by intermixing of Si and Ge, resulting in lateral and as well as longitudinal variation in compositions [14].

For the higher strain energy regime, i.e. regime III (related to higher deposited thickness and Ge content) there is a coexistence of huts and domes islands (Fig. 13) [129]. The two island geometries are categorized by aspect ratio of ~ 0.15 and ~ 0.04 for huts and domes, respectively. Huts present a pyramidal shape with (105) facets while domes present a rounded shape with large (113) and (111) facets [1,5,14]. It is also important to mention here that the relative density of huts and domes vary with the experimental conditions, i.e. domes are being favored in the higher stress regime and huts in the lower stress regime. Further, the strain relaxation in such morphologies i.e. huts and domes, are measured to be approximately 25 and 65%, respectively. Moreover, the shape and size distribution of the respective islands depends on the temperature and the deposited thickness. At this point we won't be going into further discussion as it is out of the project's scope but the topic is discussed in detail elsewhere [1,5,14]. However, strain and inter-diffusion are the essential parameters that influence the island growth, their coarsening and stability. For instance at growth temperature of 500°C, domes and pyramids present average Ge concentration of 60- 70% and 30 – 40% respectively, thus pointing out that the pyramids (or huts) are more Si intermixed than those of domes [6,14].

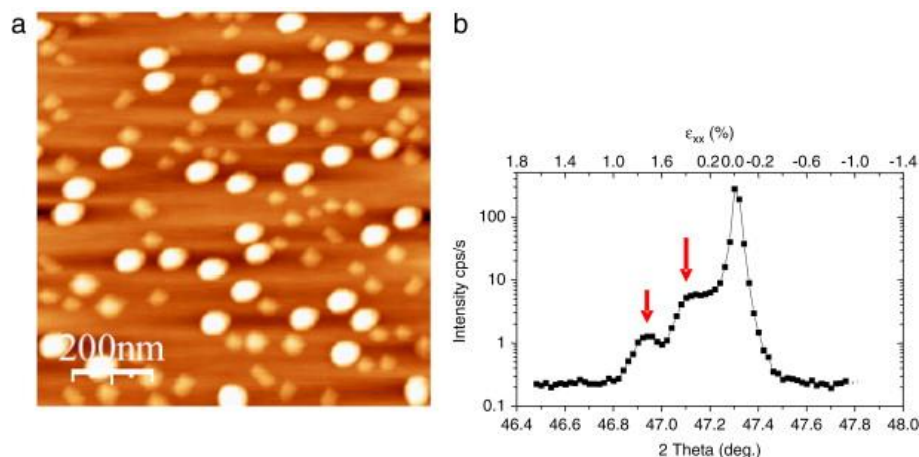


Figure 13. (a) AFM image of $\text{Si}_{1-x}\text{Ge}_x$ as-grown “hut” and “domes” islands with $x = 0.4$ and $h \sim 5$ nm; (b) GIXRD spectrum of the sample. From Berbezier *et al.* [6].

Regime IV is associated with high strain energy where the onset of plastic relaxation is due to the misfit dislocation [6,14]. In this regime, a bimodal distribution domes that correspond to dislocated and coherent islands are formed. The coherent domes are similar to those that are observed in regime III whereas dislocated domes (also called super domes) are formed by merging of coherent islands. Such a merging was observed in our structure of TiO_2/SiGe over a p-type Si-substrate which was annealed at 1000 °C (Fig. 14). In superdomes, the strain relaxation is up to 85% [132]. The superdomes can be seen in Fig. 15 where they are visible around the small islands. Moreover, the superdomes are less intermixed than those of the coherent domes because once the dislocation are introduced the superdomes or dislocated islands become more relaxed.

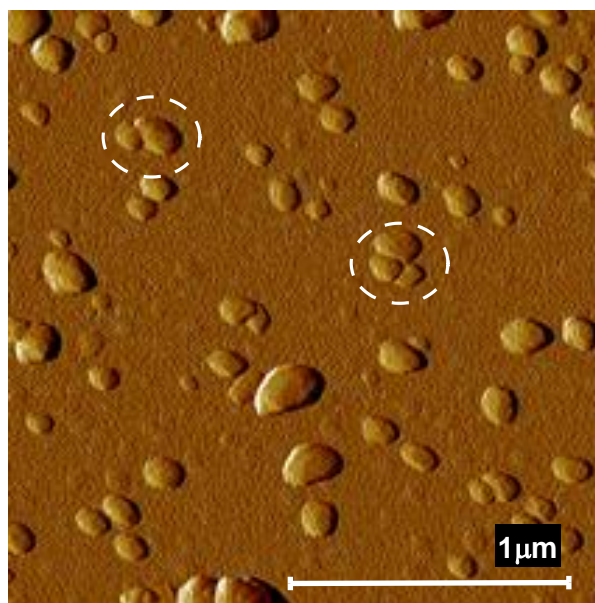


Figure 14. AFM image of TiO_2/SiGe over p-type Si-substrate annealed at 1000 °C. The dotted white circles shows merging of small domes to (form) super domes.

If the growth proceeds further to the bimodal distribution of domes, the large dislocated islands will extend further and coalesce to form a relaxed 2D layer, as can be seen for our case samples (**Fig. 16**) with multitudinous dislocations. In **Fig. 16(a)**, one can still see the presence of domes, which further coalesced completely later when annealed at higher temperatures (**Fig. 16(b-d)**). This is one of the common ways to grow a relaxed buffer layer [14]. However, Volmer-Weber growth mode takes place in case of nanoislands formation over oxide surface and has been studied in detail in article VII.

2.4.4 Embedded SiGe-NCs

The terminology, nanocrystal (NC) is used in the literature for small crystallites or nanoparticles (NPs) with typical size range from few to tens of nm. As explained earlier, the NCs with size less than the exciton Bohr radius are usually referred to as quantum dots (QDs) [31,133]. These QDs and NPs present strong quantum confinement effect and therefore possess a great advantage as their size, density, shape and crystallinity can be tailored [21,64,119,134–141] leading to different properties and consequently to a large variety of applications.

The potential applications of structures containing Si(/Ge) NCs includes nonvolatile memory devices [133,142,143], solar cells [76,144,145], efficient light emitters [81,133,146,147] and optical sensors [11,84,148,149] For instance, the electrical, optical, and photoconductive properties of structure containing Si(/Ge) NPs can be altered by tailoring their size, density, shape, crystalline structure, surrounding dielectric matrix (e.g. SiO_2 and TiO_2), and additionally by controlling the localized states formed at the interfaces between NCs and the matrix [19–21,51,52,61,63,138,140,141,150]. Furthermore, the presence and/or development of internal/ imposed strains (tensile or compressive) can significantly influence the properties [19–21,51,52,63,135]. One possible route to obtain nanostructured films for targeted applications is to prepare Ge and Si NCs or their alloy embedded in dielectrics by using magnetron sputtering deposition followed by annealing for film nanostructuring, i.e. for NCs formation, showing quantum confinement. Besides magnetron sputtering, which is the most used deposition method, other methods such as ion implantation [146,151,152],

chemical vapor deposition (CVD) [15,123,153–155], sol-gel [146,156,157], molecular beam epitaxy (MBE) [31,146,158] etc., are used for the preparation of oxide matrix with embedded NCs of Ge and Si.

In comparison to elemental Si and Ge, $\text{Si}_{1-x}\text{Ge}_x$ alloy offers additional possibilities for tailoring the NCs physical and chemical properties as a function of the Ge fraction [17,30,37,52,60,63]. SiGe alloy is also an interesting material for high temperature thermoelectric devices[17]. In particular, the use of Ge and Ge-rich $\text{Si}_{1-x}\text{Ge}_x$ alloys as channel materials in MOSFETs is promising for the improvement of the electrical performances of devices, due to their high electron and hole mobilities [16,57,60], which together with their lower processing temperatures (as compared to Si-devices) enables their integration within matrices having high dielectric constant [16]. $\text{Si}_{1-x}\text{Ge}_x$ nanocrystals provide an advantage of fine tuning the electronic band structure, which plays a detrimental role in the charging/discharging and retention properties of the memory element [60]. In order to fabricate high performance devices with SiGe nanocrystals, it is necessary to know and control their structural and electrical properties [159,160] which depend on several factors including particle size, shape, surface condition, atomic composition, and compositional uniformity [17,30,37,51,52,60]. Apart from NCs in an oxide matrix, other structures can be thought to exist in such systems when taking surface effects and kinetics into consideration. There have been several theoretical and experimental studies indicating that a core-shell structure can be obtained and are more stable than a homogenous structure [51,52,60]. In addition, a composition gradient in the SiGe nanocrystals or a core-shell NCs can possibly arise by high temperature treatment of SiGe nanocrystals in an oxide matrix on Si where several effects may contribute to the end results. Moreover, there is a flux to and from the particles resulting in Oswald ripening, which will be influenced by the different surface energies of small and large NPs as well as the bond on Si(/Ge) NPs surface. These fluxes may be further coupled to flux from the substrate involving epitaxial growth on the substrate and an additional possibility of particle flux that can react with species from the ambient during annealing or sputtering, forming some new oxide or compounds [60,161].

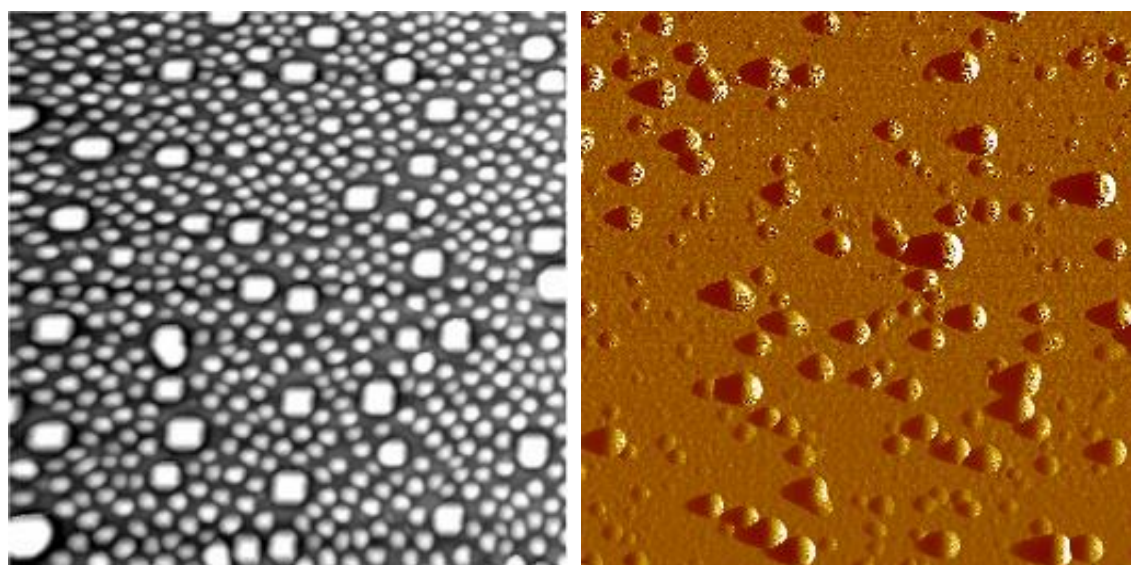


Figure 15. AFM images of bimodal distribution of “domes” in $\text{Si}_{1-x}\text{Ge}_x$, $x = 0.5$ and $h \sim 5$ nm. Larger domes are dislocated and smaller ones are coherent (From Berbezier *et al.* [6]). (b) $13 \times 13 \mu\text{m}^2$ AFM image of SiGe over p-type Si(001)-substrate annealed at 700°C for 1 hr.

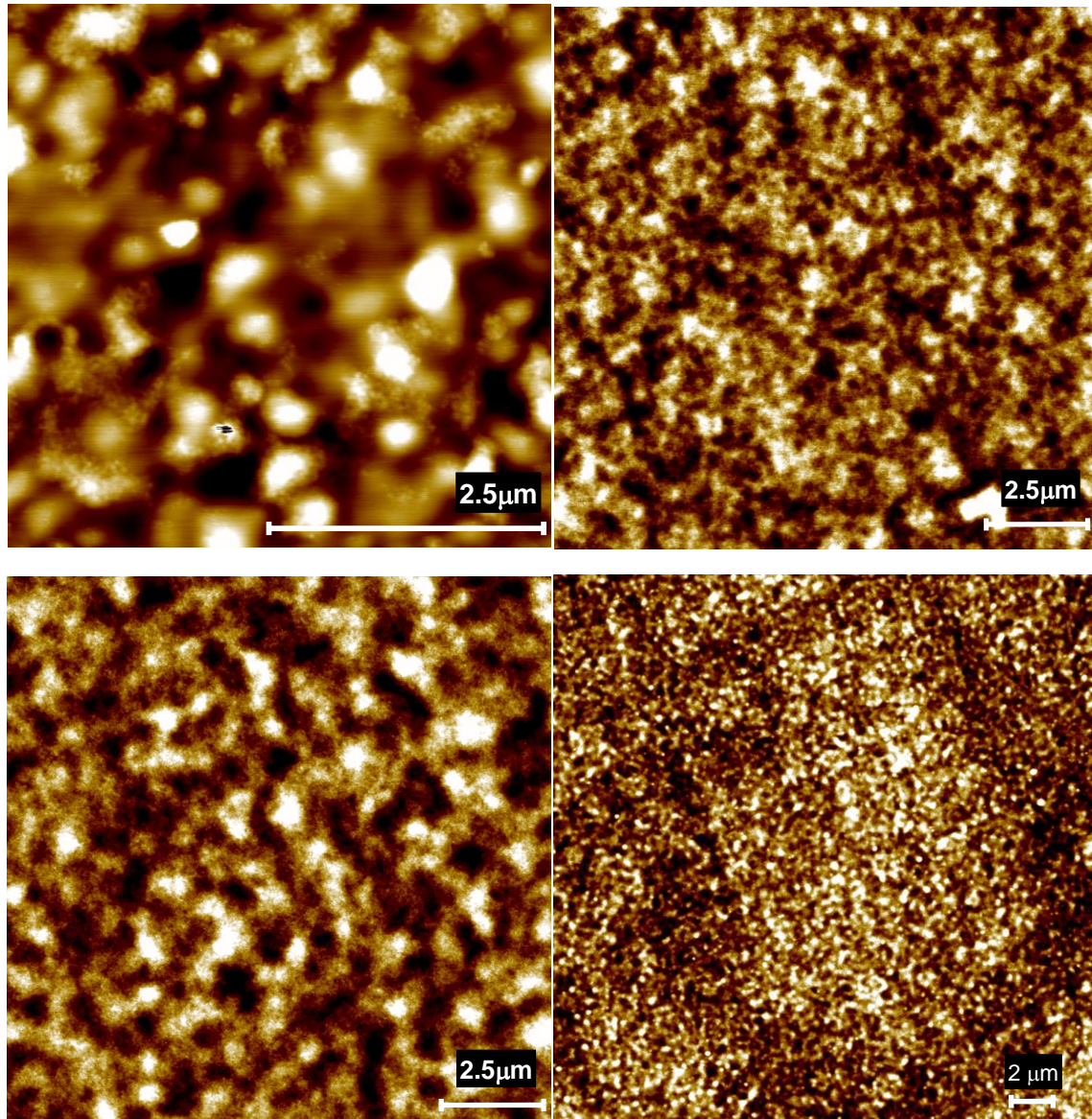


Figure 16. Structures annealed at (a) 700 °C for 7 hr (b) 750 °C for 10 hr and (c, d) 800 °C for 7 hr showing the evolution of SiGe nanoislands coalescence (domes).

Challenges

For the last few decades, $\text{Si}_{1-x}\text{Ge}_x$ hetero-structures have evolved as a viable system for device technology with its industrial production for integrated circuit. Still for the majority of the present and future devices, the improvement of these devices needs a better understating and control of the fabrication processes. One of the challenges faced by the modern day technology is the fabrication of high quality films incorporating nanoparticles with improved optoelectronic properties for sensitive functional devices. Common methods to fabricate such structures incorporates various physical and chemical methods followed by subsequent annealing. Even though the Si-Ge materials are quite mature in the field of research; the obtained device characteristics in the production line are much weaker than those demonstrated for research devices. This is due to the high TB as explained earlier, which is assumed to have a detrimental effect on strain relaxation (by dislocation nucleation or by intermixing at interfaces (Fig. 17), dopant redistribution, Ge clustering (Fig. 18(a)), inter-diffusion of oxygen from the (oxide) matrix or atmosphere towards the NCs' interface (Fig. 18), phase separation of SiGe (Fig. 18(a)), blunting and degradation of the interfaces [56,60,61,63,162–165]. Besides the NCs size and density, the alteration in defects density

and/or change in interface quality can influence the optical and optoelectronic properties. All these phenomena are well-known to degrade the electrical and optical properties of the structures and device characteristics.

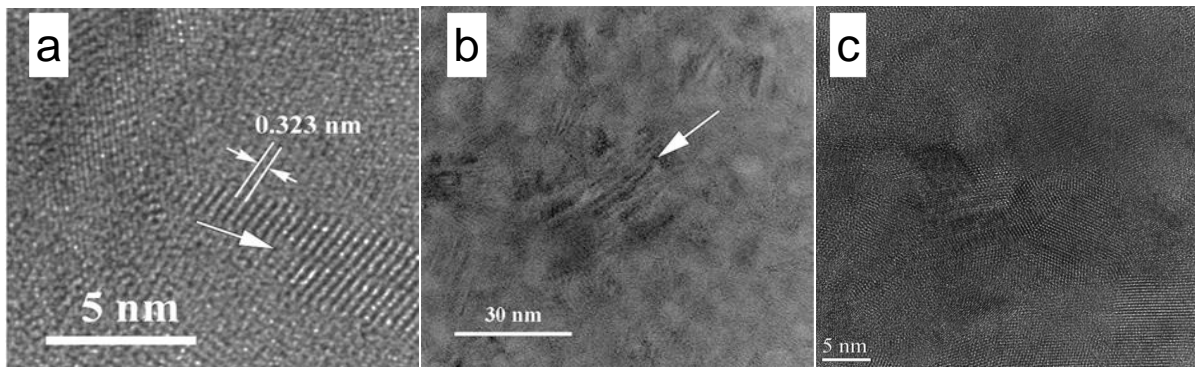


Figure 17. TEM low-magnification image showing the contrast due to the shearing defects appearing in the SiGe crystallites, of a sample annealed at 600 °C for 1 min. (b) HRTEM image showing the lens-like shape of SiGe crystallites as a result of shearing defects. The arrows indicate the shearing planes. (c) Sequence of microtwin bands, observed in a very thin area of the XTEM specimen (MLs with 200 nm thick SiGe), where the SiGe NCs are not superposed in the specimen thickness.

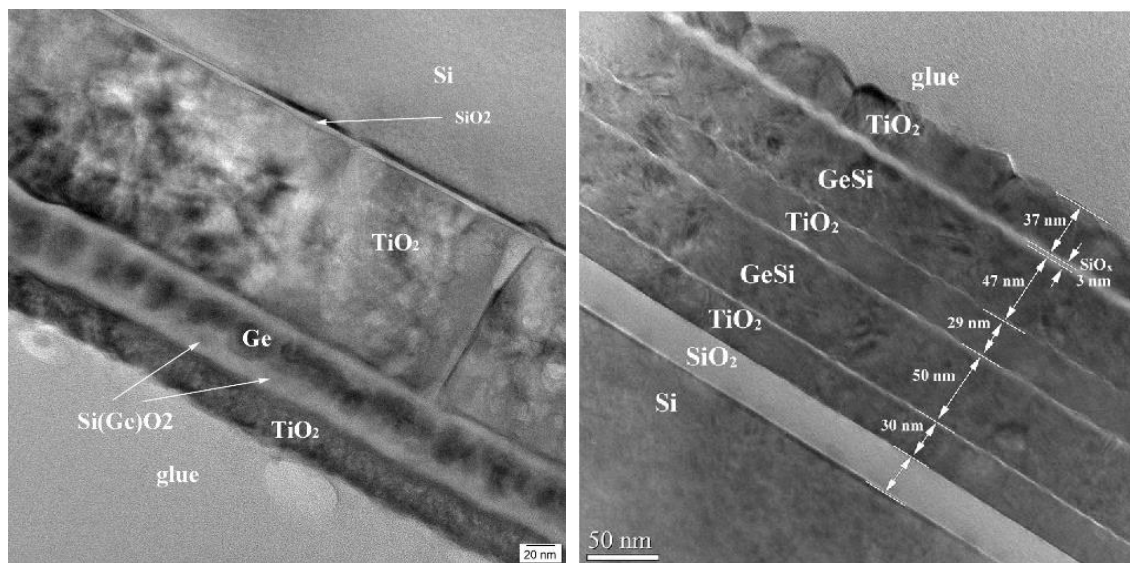


Figure 18. Cross section TEM images of: (a) $\text{TiO}_2/\text{SiGe}/\text{TiO}_2$ structure over Si substrate, annealed at 650 °C for 2 h. The figure shows the SiGe phase separation and formation of segregated Ge nanoparticles and the inter-diffusion of oxygen from oxide matrix and/or ambient atmosphere resulting formation of SiO_x insulating layer, (b) double stack $(\text{TiO}_2/\text{SiGe}/\text{TiO}_2) \times 2$, annealed at 800 °C. A formation of SiO_2 layer after annealing was observed, deteriorating the interface integrity and the thickness of which increases while going from bottom to top of the structure [165].

In systems with NCs embedded in an oxide matrix, a common issue encountered is the effect of surrounding matrix over the NCs and strain formation in the structure [19,21,140,166]. This is due to different thermal expansion coefficients of the matrix and the NCs and density gradient of the matrix [19,21,167,168]. Moreover, the lattice mismatch of 4.2% between Si and Ge plays a vital role [6,18] in inducing strain. Taking into account the above criteria, it can be deduced that when two differently ordered structures with different dielectric constants are merged, one of them will deform to accommodate the reconstruction

of other at the interface [21], resulting in strain accumulation. Several studies have been conducted on Si, Ge and SiGe NCs embedded in oxide matrices, to determine the effect of strain [19–21,141,166] and post-annealing [24,30,51,52,57,169,170] on the NCs' size, shape and degree of crystallinity. The effect of the type of strain (compressive or tensile) and diffusivity of Si, Ge and oxygen (O) in such systems has also been studied in respect to its optical and electrical properties [23,24,32,60,61,122,135,162,163]. Moreover, various studies have been devoted to the morphology of the interface between oxide matrices and nanocrystals [16,63,64]. For instance in a study by Zatoryb *et al.* [21] it was shown that the NCs shape and crystallinity is effected by the degree of matrix ordering, i.e. the ordering of the oxide matrix determines the size of expanding NCs. Furthermore, in a study by Ciurea *et al.* [135] it is shown that the size of NCs can be controlled by the oxide thickness. In addition, the degree of matrix ordering can produce strain in the structure especially at nanocrystals/matrix interface [21]. These strains causes the NCs to deform which also in turn alters the bandgap. It is well documented that NCs are under large stress when embedded in an oxide matrix [19–21,141] and that the magnitude of either compressive or tensile stress varies with NCs size. According to a study by Zatoryb *et al.* [19] small nanocrystals are under compressive stress, the magnitude of which depends upon the matrix ordering. Consequently, large compressive stress will be exerted over NCs if the matrix forms an ordered structure, resisting them to expand freely [21].

Various groups have studied the effect of strain in relation to the energy band gap (E_g) of systems (often Si-NCs embedded in SiO_2 matrix), where the magnitude and the type of strain can alter the valence and/or conduction states, energy gap and the carrier dynamics. Guerra *et al.* [140] have shown that strain over the NCs depends on the degree of oxidation, which in turn determines the shift in the highest occupied molecular orbitals (HOMO) and the lowest unoccupied molecular orbitals (LUMO) gaps thus resulting in variation of E_g (where the E_g is defined as the difference in energy between HOMO, i.e. valence band and the LUMO, i.e. conduction band). The variation in E_g as a function of hydrostatic and non-hydrostatic strain was also studied in another work by Peng *et al.* [118,171]. As explained earlier in this section, the non-hydrostatic strain was shown to have impact in altering the E_g by splitting of degenerated orbitals due to breaking of its tetrahedral bond symmetry. This study is complemented by the work of Sun *et al.* [119], where shear strain was shown to distort the crystal symmetry, leading to degeneracy lifting. Furthermore, an enhancement in quantum confinement along with variation in bandgap is also effected by the degree of strain over the NCs exerted by the surrounding oxide matrix [138]. Thus, as stated here earlier and elsewhere [172,173], the presence of strain creates defects and/ or local deformation in structure and/or NCs. These defects/ distorted regions (especially at the interface) acts as traps reducing the charge carrier concentration, and is eventually compensated by a reduction in recombination rates. Concurrently, the interface of such structure has been a matter of concern in studying optical response as it may give rise to dangling bonds acting as electrically active interface traps (known as P_b -type defects). These interface traps produce scattering centers, which can affect the mobility of charge carriers, thus altering the transport properties [65]. Moreover, as mentioned any presence of sharp interfaces with an abrupt change in the dielectric constant or thermal expansion coefficients, gives rise to a surface polarization effect due to the local field built up (which assumes a crucial role for systems characterized by strong charge inhomogeneity). Thus, size and surface chemistry of the NCs and oxygen-related bonds are the factors determining the photocurrent spectra. It is well understood that annealing results in the formation of dangling bonds in the structures either at the interface of the nanocrystals or in the surrounding matrix results in alteration of interface quality [155,174,175]. Furthermore, for interface quality, it has been theoretically shown [176] that Si-O-Si bonds are formed when a Si-nanoparticle is oxidized [177]. It is likely that these relatively weak Si-O-Si and Si-Si bonds will break due to stress at the NCs/oxide-matrix interface. Thus,

distorted bonds will either result in dangling bonds or eventually form a Si = O bridge since it does not require large additional amount of energy or deformation to form [178,179]. These dangling bonds which act as electrically active recombination centers for charge carriers and can alter the optical properties of the structure, by contributing to oxide positive charges (depending on the location of the bond) and interface states [174] and may deteriorate the optical properties of the structure. It is also thought that in the case of increased annealing temperature, a formation of Si=O bonds, along with an increase in the number of dangling bonds may be possible. Increased number of dangling bonds increases the number of localized states in the band-structure along with an increase in non-radiative centers (Pb)[90,180]. This result in energy-width broadening of localized states with annealing temperature, resulting in bandgap alteration. One solution to reduce the concentration of these dangling bonds and/or non-radiative defects, is passivating the structure via hydrogen plasma treatment often referred to as hydrogenation [28,174,180].

Reason out

In the past decades, nanostructured materials have been the focus of many research groups due to their improved structural, optical and electrical properties, appropriate for various practical applications. The properties of SiGe-NCs incorporated into oxide matrix can be strongly influenced by difficulties related to the control of the technological parameters of the deposition and/or to the inevitable formation of defects regardless of the preparation methods.

Structuring of SiGe-NCs embedded into oxide matrix has been achieved so far by thermal annealing after deposition of thin SiGe layers, or by thermal oxidation of SiGe layers, at high temperature, in excess of 700 °C or higher [162,181]. This temperature is lower than needed to obtain Si-NCs (which occur typically around 1100 °C), but is still too high to be appropriate for processing structures and devices on flexible or glass substrates. Moreover, a commonly observed downside of annealing such a structure is the inter-diffusion of oxygen from the (oxide) matrix towards the NCs' interface. This results in blunting and degradation of the interfaces, deteriorating the structure and/or forming insulating SiO₂ at the matrix/NCs interfaces as discussed earlier. Thus, to preserve the functionality of incorporated Si-based electronics, a low processing temperature is required [29,36,56,122]. This is the present challenge to be solved in order to benefit from the advantages in terms of reducing manufacturing cost and much broader range of applications [182,183].

Therefore, it is crucial to lower the temperature required for structuring of NCs in an oxide matrix as to use these materials in Si-based optoelectronics devices, where low processing temperature is highly desirable to preserve the functionality of the accompanying Si electronics. In this study, the above-mentioned issues associated with treatment of structure were dealt by:

- reducing the thermal budget by reducing the time and/or temperature,
- fabricating crystalline structures in as-grown states,
- hydrogen passivation of deep level states and traps.

The following paragraphs will give a quick overview of how the issues were dealt with.

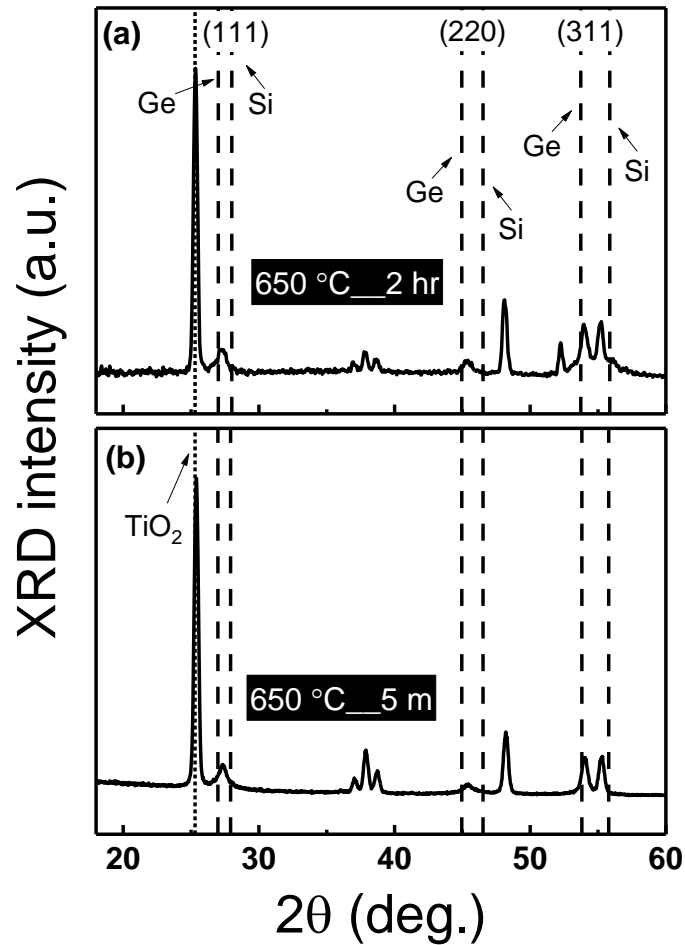


Figure 19. GiXRD diffractogram of a sample annealed at 650 °C for (a) 2 hr and (b) 5 min, where vertical dashed and dotted lines correspond to standard tabulated positions for cubic Ge ($2\theta = 27.45^\circ; 45.59^\circ; 54.04^\circ$ — ASTM 01-079-0001), cubic Si ($28.45^\circ; 47.31^\circ; 56.13^\circ$ — ASTM 01-070-5680) and to TiO₂ anatase (JCPDS 21-1272) [36].

Fig. 19(a, b) shows the GiXRD diffractogram analysis of samples consisting of TiO₂/SiGe/TiO₂ over a p-type Si-substrate having 200 nm of buffer SiO₂ layer, which were annealed at 650 °C for 2 h in contrast to that annealed for only 5 min, respectively [36]. The results obtained elaborate that lowering the anneal temperature still results in crystalline structure without any formation of SiO₂ insulating layer or deterioration of interface quality. As also can be seen by TEM analysis in **Fig. 20**, where the structure showed no formation of SiO₂ insulating layer in contrast to the one which was annealed for 2 h. A similar behavior was observed in a structure having SiO₂ as a dielectric matrix instead of TiO₂. In addition, the low budget annealed structure showed photo-response threshold up to NIR regime.

For the second approach, a modern variation of magnetron sputtering i.e. high power impulse magnetron sputtering (HiPIMS) was utilized to fabricate samples, resulting in crystalline structure without the need of anneal treatment. **Fig. 21** shows the GiXRD analysis of thin-films of Ge and TiO₂ (**Fig. 22**) grown over Si- substrates using HiPIMS method. A schematic evolution of Ge crystallites within amorphous Ge layer and advancement of TiO₂ structure form amorphous to anatase, which further leads to structure having both anatase and rutile phase and finally appearance of rutile peaks. The mentioned characteristics were obtained by varying the HiPIMS discharge parameters.

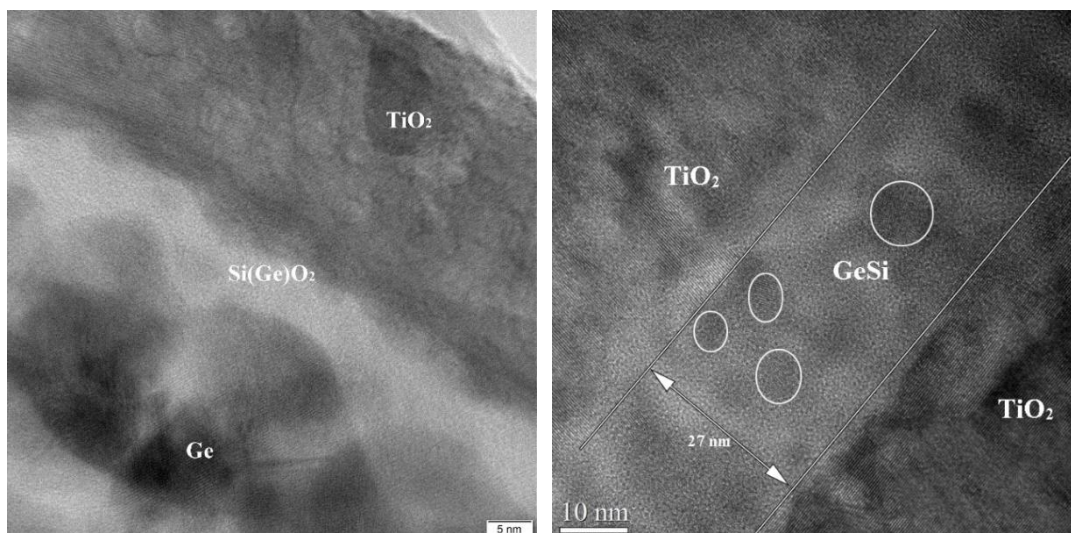


Figure 20. XTEM cross-sectional image of the $\text{TiO}_2/\text{SiGe}/\text{TiO}_2$ annealed at 650°C for 2 hr (similar structure as in **Fig. 19(a)**), showing segregation of Ge NPs and formation of insulating SiO_2 layer. (b) TEM image of structure $\text{TiO}_2/\text{SiGe}/\text{TiO}_2$ annealed at 650°C for 5 min with SiGe layer having SiGe spherical nanoparticles without formation of any SiO_2 layer at the interface.

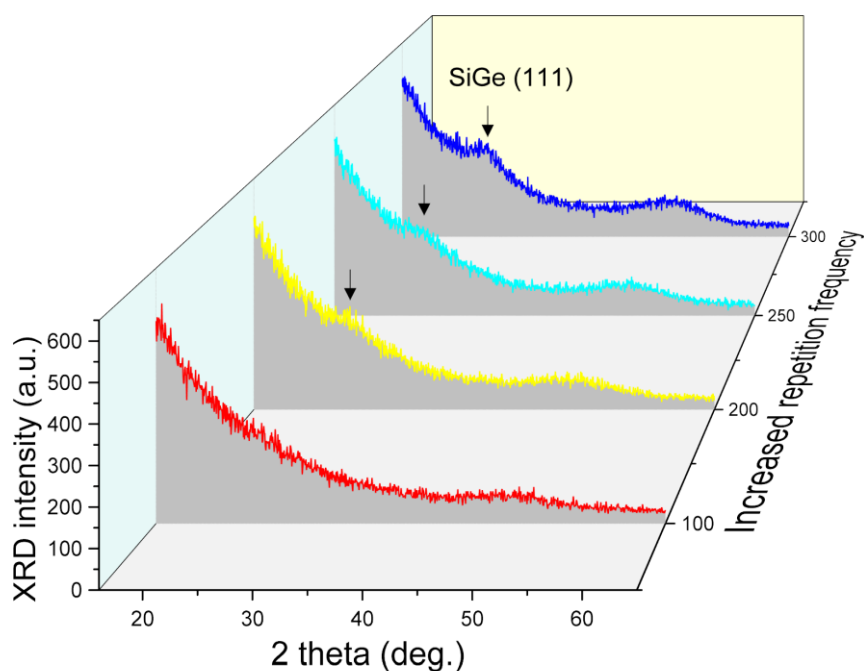


Figure 21. GiXRD diffractogram of as-deposited Ge (20 nm) deposited via HiPIMS at varying repetition frequency (100–300 Hz) for fixed applied voltage (470 V) and pulse width (200 μs). A comparison to structure obtained by dcMS deposition at 40W is given with the red line. The arrow points to SiGe (110) peak positioned between the Si and Ge tabulated ones i.e. ASTM 01-079-0001 for cubic Ge and for cubic Si, ASTM 01-070-5680.

The GiXRD diffractogram of structures comprising of SiO_2 and/or TiO_2 matrices having small SiGe crystallites sandwiched between, are shown in **Fig. 23**. One can explicitly see the presence of crystallites by the appearance of broad peaks in **Fig. 23(a)**, marked by vertical dashed lines position between the Si and Ge tabulated ones, and as well as presence of either anatase or rutile peaks in **Fig. 23(b)**. The results will further be discussed in chapter 5 and 6 in terms of their morphological evolution and their resulting effect over enhanced

photoconductive properties.

In addition, a peculiar behavior of these as-grown crystalline structures is the formation of columnar self-assembly of SiGe crystallite having a definite periodicity as evident in **Fig. 24** and is assigned to be due to implication of HiPIMS technique that results in formation of a good wetting layer and further that, the presence of small crystallites have acted as seed/catalyst for the formation of columnar structure.

The third method employed to improve the photoconductive response of our structure comprises of exposing the fabricated structures either in as-grown or annealed state, to an rf- H_2 plasma treatment process. The plasma treatment resulted in up to 2 order of magnitude increase in photocurrent intensity after exposure [28]. The basics of hydrogen plasma treatment (hydrogenation) is discussed below, while the setup and results are discussed in chapter 4 and 5.

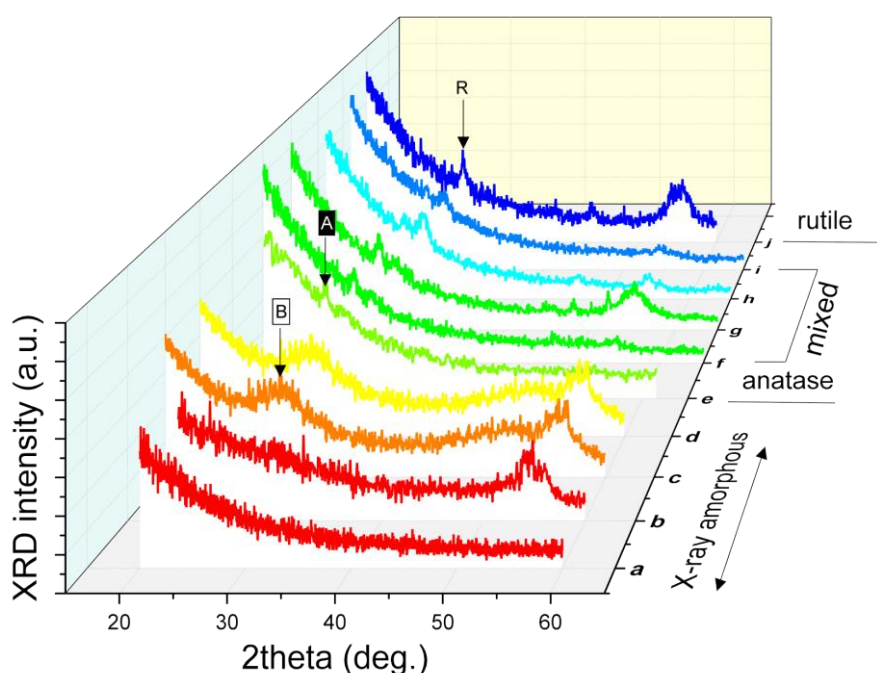


Figure 22. Structural evolution analysis by GiXRD diffractogram for TiO_2 deposited via HiPIMS. The discharge parameters are listed in paper V. The labels R, A and B denote rutile, anatase and X-ray amorphous nature of TiO_2 thin films (~ 80 nm). The plots labelled ‘e’ and ‘j’ are pure anatase and rutile phase, respectively, while the ones in between contains both phases. The JCPDS card no. 21-1272 and JCPDS card no. 21-1276 for anatase and rutile phase respectively.

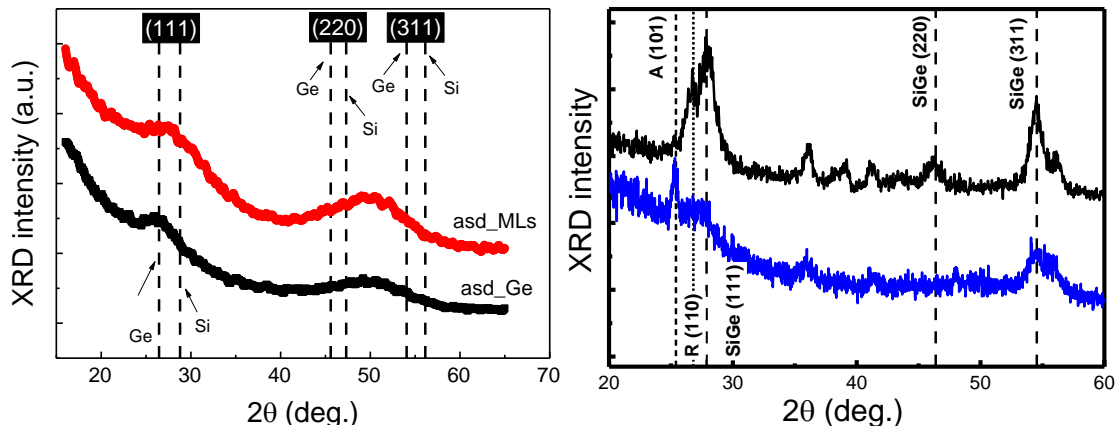


Figure 23. GiXRD diffractograms of (a) as-deposited (asd) Ge only along with as-deposited structure (MLs) of $\text{SiO}_2/\text{SiGe}/\text{SiO}_2$ deposited via HiPIMS, where vertical dashed lines correspond to standard tabulated positions for cubic Ge ($2\theta=27.45^\circ$; 45.59° ; 54.04° - ASTM 01-079-0001) and cubic Si (28.45° ; 47.31° ; 56.13° - ASTM 01-070-5680). (b) $\text{TiO}_2/\text{SiGe}/\text{TiO}_2$ structures, where the TiO_2 film (lower blue-line) is deposited with HiPIMS at 300 Hz repetition frequency and cathode voltage of 755 V with average power of 468 W forming anatase phase (HHD-A) and the second TiO_2 film (upper black-line) was sputtered at 340 Hz at 813 V with average power of 545 W resulting in rutile phase (i.e. HHD-R). The vertical short-dashed and dotted lines corresponds to standard TiO_2 anatase (JCPDS card no. 21-1272) and rutile (JCPDS card no. 21-1276) phases, respectively.

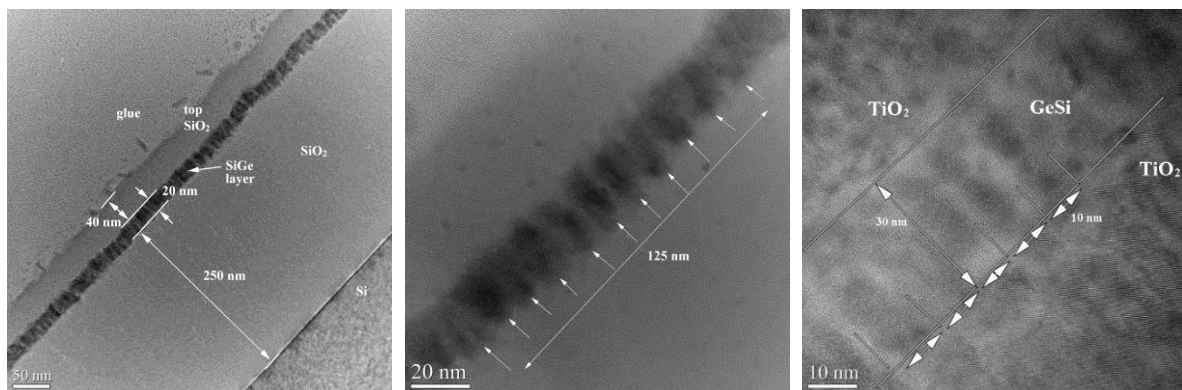


Figure 24. (a) XTEM images of $\text{SiO}_2/\text{SiGe}/\text{SiO}_2$ structure with 20 nm SiGe layer after 600°C annealing for 1 min. (b) Magnified image from (a) showing columnar morphology of SiGe crystallites covered with a shell structure of amorphous SiGeO layer of ~ 2 nm. The crystallites have a periodicity of ~ 12.5 nm. (c) TEM image of sample $\text{TiO}_2/\text{SiGe}/\text{TiO}_2$ with SiGe layer showing presence of columnar formation of SiGe nanoparticles (~ 10 nm) having a gap between them of ~ 5 – 6 nm.

2.4.5 Hydrogen plasma treatment

The notion of H_2 plasma

As processing steps in microelectronics manufacturing become more demanding and with shrinking devices sizes and large processing areas, understanding the plasma processes becomes essential in achieving better process control and optimization. Plasma-hydrogenation is known to effectively passivate defects in polycrystalline-Si thin films. It has been suggested that discharge operation conditions that promotes dissociation of H_2 to form neutral H and H^+ ion are important to achieve higher [184] process rates for plasma-

hydrogenation. It has been demonstrated that the rate of hydrogen introduced on to the device surface profoundly influences processing time and shortens the passivation process from several hours to few minutes. The use of an inductively coupled plasma source like electron cyclotron resonance (ECR) discharges tends to provide higher plasma-density than does conventional parallel-plate like capacitively coupled discharge [185].

The effectiveness of hydrogen passivation associated with the ion energy distribution at varying partial pressures has been studied extensively through the years. Cielaszyk *et al.* [186] found that $[H^+]/[H_2^+]$ ion density ratio depends on the neutral gas pressure ranging from 0.254 to 2.25 mTorr in hydrogen ECR discharge. They hypothesized that H and H^+ were accountable for the effective hydrogenation. It is believed in this case that the atomic hydrogen diffuses through the solid material more readily than the molecular hydrogen, resulting in higher flux of either ionized atomic hydrogen or neutrals reaching the surface thus resulting in higher rates of hydrogenation. In addition, it has been signified that even though the H^+ ions have lower concentration than the neutral H atoms in the plasma; the flux of H^+ ions will be higher due to acceleration of ions towards the substrate by electrostatic fields in the plasma. It is because of this acceleration that the ions reach the surface with greater kinetic energy than the neutral atoms, making them more likely to adsorb on the surface once they reach. In addition, H^+ ions with higher energy are more likely to adhere to the surface and become available for diffusion and that the energetic H_2^+ ions will dissociate into H and H^+ on impact.

In studies by Gudmundsson *et al.* [184,187], the main effectiveness from the hydrogen plasma was attributed to the presence of H_3^+ and H_2^+ ions. In order to impel the ionization of H_2 , argon gas (Ar) is introduced into the hydrogen plasma during hydrogenation [187]. It was established that the electron density increased with increasing fractional Ar pressure and that the $[H_3^+]/[H_2^+]$ ratio did not change when Ar was added. The addition of Ar gas into the H_2 plasma effectively enhance the ionization of H_2 . The reason is that in pure H_2 plasma, the generation of H_2^+ is inadequate due to small electron impact ionization cross-section of H_2 . The excitation of Ar atom to the metastable state i.e. Ar^* in electron collision, requires 11.6 eV whereas, ionization of H_2 to H_2^+ requires 15.9 eV. This reaction then promotes *Penning ionization*, given as:



Some of the H_2^+ will react with H_2 to generate H_3^+ . The hydrogenation time is reduced by operating at higher plasma density. In all aforementioned studies, it was concluded that the density of H^+ ions grew with decreasing pressure and that the density of H_3^+ and H_2^+ grew with increasing pressure. Therefore, increase in partial pressure of either H_2 or Ar increases the $[H_3^+]/[H_2^+]$ ratio as well as the total ion density [184]. Thus, this increased concentration of H_3^+ and H_2^+ implies that higher number of these ions will reach the surface where they on impact will dissociate into H and H^+ that diffuse into the surface, resulting in more effective hydrogenation.

The Acquisition from hydrogenation

With the aim to obtain enhanced optical and electrical properties of Si(/Ge) nanoparticles in question, various approaches to gain a control over the NCs size and its distribution have been proposed. These approach encompasses; incorporating barrier or buffer layer [24,99,188], exploiting growth or post annealing temperatures [24,25,122,189], doping [152,190], super-lattice structure [17,117,189] and varying the Ge fraction in $Si_{1-x}Ge_x$ [52,62,191]. However, another common and better approach is the exposure of hydrogen plasma as a post-fabrication process. It has been well established that an exposure to hydrogen

plasma can passivate deep-levels, shallow defects and traps in many semiconductors [180,192–195]. Moreover, hydrogenation works efficiently on structures containing nanoparticles in amorphous/oxide matrix [196] where an increase in photoluminescence (PL) intensity has been achieved for InAs/GaAs [197,198] quantum dots (QDs), Si or SiGe QDs [174,199] and InAs QDs [200] due to hydrogenation. As explained earlier, regarding the formation of P_b defects and dangling bonds, hydrogenation tends to passivate these non-radiative centers (P_b) located at or in close proximity of NCs. In addition, it has been demonstrated by several researchers [174,184,186,200] that introducing atomic hydrogen in semiconductor structures results in reduction of Si dangling bonds thus increasing the durability of devices incorporating such structures [180].

Furthermore, the ionized hydrogen plays a crucial role in the hydrogenation of the oxide/NCs interface, resulting in reduction of positive fixed charges in the dielectric, i.e. SiO_2 and TiO_2 in our study [177,201]. In addition, there is a considerable decrease in electron trapping within the oxide matrix as a result of hydrogen plasma treatment due to reduction of structural defects in the oxide matrix resulting in ordering of the SiO_2 amorphous network [180]. More precisely, hydrogenation supports the formation of relaxed amorphous oxide matrix with less defect concentration and better (maximal) binding energy. Hence improving the quality of the interface. Also room temperature H_2 plasma treatment reduces structural defect concentration in oxide matrices, along with subsurface semiconducting layers and surface states concentration on the interfaces [202]. One important highlight of such treatment is that no significant alteration of NCs size is observed [28,201]. During plasma treatment the passivation can be of two types: one in which atomic hydrogen chemically bonds with defects at interfaces or with dangling bonds present. In this case the passivation proceeds through neutralization of dangling bonds, by breaking of strained Si-Si bonds and/or bonds of Si-O-Si in SiO_2 matrix for instance, where charged carrier can be trapped. The excess atomic hydrogen enters these strained bonds and breaks them into Si-H and Si-OH [180,201]. Additionally, hydrogenation prevents formation of the Si-O bond and can passivate $\text{O}_3\equiv\text{Si}$ - and $\text{O}_3\equiv\text{Si-O}$ - dangling bonds [180]. While in latter case, the hydrogen acts as a radical stimulus, which causes relaxation of mechanical stresses or defect transformation after which it escapes the structure. These configurational change results in relaxation of oxide network with minimal potential energy [180,203].

2.4.6 Photoconductivity

Photoconduction can be defined as the increase in conductivity of a material resulting from the absorption of optical photons most notably in the study of semiconductors and insulators [204,205]. The basic processes that govern the generation of the photocurrent are the generation of free electrons and holes through the absorption of incident photons while illumination and their transport through the material under the influence of an applied electric field, and consequently their recombination [204–206]. Furthermore, the wavelength of light source necessary to create the photo-excited/generated carriers is determined predominantly by the bandgap of the material. The study of any of the above-mentioned aspects as a function of illumination intensity and optical power, temperature and applied field strength, will provide insights into the structure optical and electronic properties.

When a thin film semiconducting structure is illuminated, e^-h^+ pairs are generated, contributing to the overall conductivity of the film/structure. The two major terms, which help to define the conductive behavior of a structure, are the carrier density and the mobility of the respective carriers. Thus, photoconductive measurement (as in our study) uses a constant (monochromatic) light source to generate equal number/densities of free electrons

and holes ($n = p$) that leads to a change in the conductivity and is given by:

$$\Delta\sigma = q(\mu_n\Delta n + \mu_p\Delta p) \quad (8)$$

Where, q is the charge of an electron and Δn and Δp are the increase in the the electron and hole density, and μ_n and μ_p are the mobilities of electrons and holes, respectively. The experimental setup will be discussed in chapter 4. A basic scheme of the experimental set-up is shown in Fig. 25.

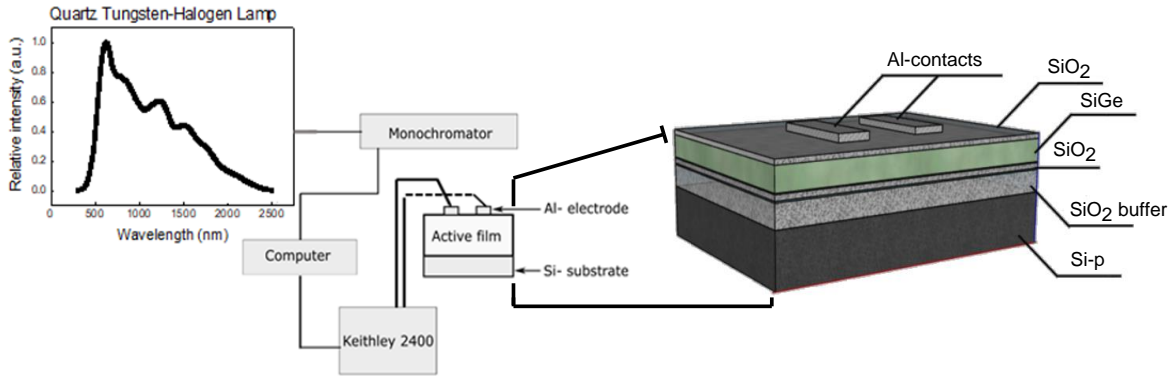


Figure 25. A schematic of the photocurrent measurement setup with intended structural scheme consisting of Si-wafer/ buffer-SiO₂ (200 nm)/ SiO₂/SiGe/SiO₂ with co-planar Al contacts on top of the structure [29].

Generally, for thin films, coplanar electrodes (for ohmic contacts) are typically deposited by electronic-beam evaporation through a shadow mask onto the film surface. The structures are then measured using a setup(explained later in Chapter 4) consisting of a source supplying constant applied bias to the structure, along with a light source and monochromator shining onto sample surface, resulting in increased current. The measured current in such setups is called photocurrent, as it arises from generation and availability of photo-excited carriers such as to maintain charge neutrality across the contacts. For materials with defects and other imperfections a significant fraction of photo-generated carriers may become trapped at localized states in the semiconductor (band tails and/or defects), therefore not all electrons and holes contributes equally to the photoconductivity. Often recombination of electrons and holes occurs between these trapped carries and a free carrier of opposite sign or even between closely trapped carriers. This causes reduction in free carrier density and hence reduces the photoconductive response of the structure.

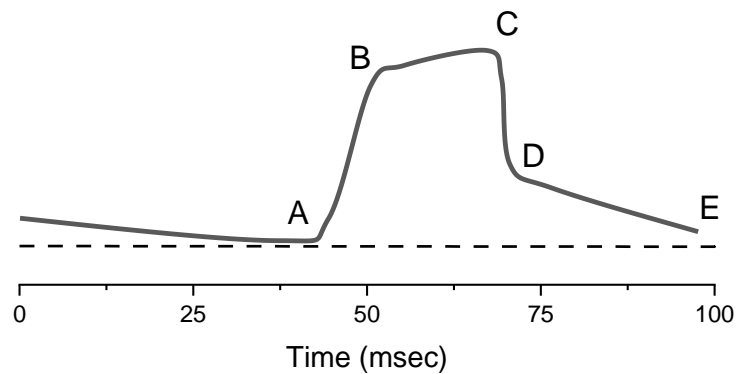


Figure 26. A schematic showing rise and decay curves of photoconductivity for n-type silicon.

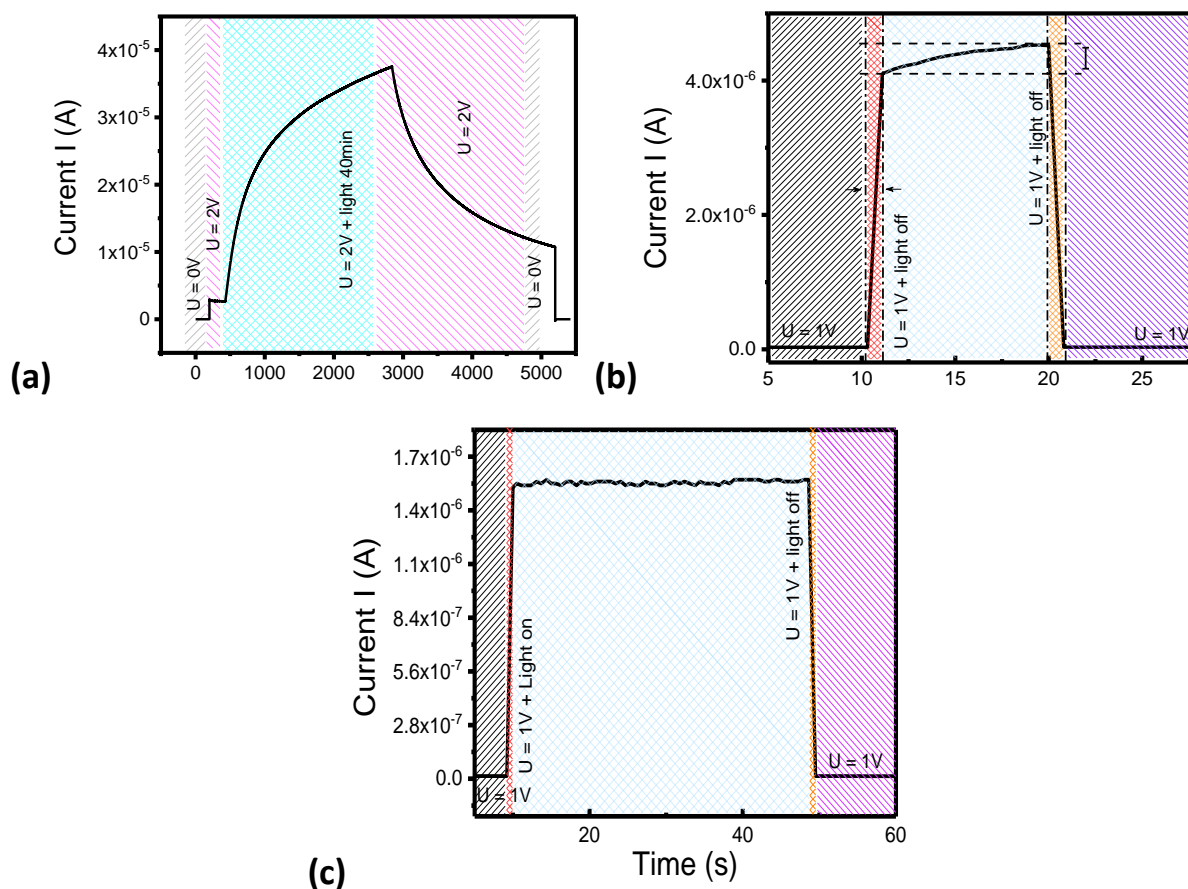


Figure 27. The current vs. time response plot for structures $(\text{TiO}_2/\text{SiGe}/\text{TiO}_2)$ (a, b) deposited via dcMS method and annealed at 650°C for 2 h and 5 min, respectively, and (c) deposited via HiPIMS method in as-grown state with out any pre-/post-annealing. The applied bias (U) is 2 V for (a) and 1 V for plots in (b) and (c).

This trapping of carriers tends to have pronounced influence over the dynamics of carrier transport in material and more specifically on the photo-generated carrier decay time. When a photoconductive material is illuminated, carriers are excited, which results in an increased conductivity. When illumination is turned off, the production of carriers will stop and carriers in excited states will start to fall to their ground states. This rate of de-excitation can give insight into materials trapping sites. For instance the decay time in photoconductive experiment of n-type silicon [207] have been carried out. Fig. 26 shows a typical rise and fall (decay) curve illustrating a general effect of trapping sites. The sample is illuminated at point A generating electrons and holes resulting in increase of photoconductivity to point B. From point B to C the hole trapping takes place causing the overall conductivity rate to decrease. At point C the light is turned off and a decay is observed relating to the recombination of excess e^- and h^+ up to point D. After which the shallow traps got emptied thus resulting in a slower decay rate from point D to E. Examples of measurements are shown in Fig. 27.

Chapter 3

3 Experimental Equipment and Methods

Multilayer structure of SiGe layer sandwiched between the oxide matrices (i.e. TiO_2 or SiO_2) were deposited on a polished $10 \times 10 \text{ mm}^2$ p-type Si (100) substrates. Prior to deposition, the substrates were etched with 2M HF for 120 s to remove native oxide. A 200 nm SiO_2 buffer layer was deposited prior to deposition of the active layers. A typical construction of the structure is shown in Fig. 28.

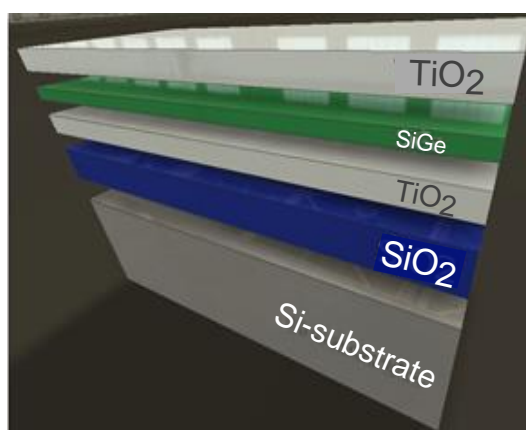


Figure 28. A schematic of a structure deposited over p-type Si-substrate. First there is a SiO_2 buffer layer and on top of that we have the active layers of either $\text{TiO}_2/\text{SiGe}/\text{TiO}_2$ or $\text{SiO}_2/\text{SiGe}/\text{SiO}_2$.

The intermediate SiGe layer was obtained by various approaches. In the initial approach, co-deposition from the individual targets of Si and Ge (having 6N purity) was carried out via direct current magnetron sputtering (dcMS) technique. In the second approach the co-deposition was carried out by using two separate sputter techniques i.e. dcMS for the Si-target and high power impulse magnetron sputtering (HiPIMS) for the Ge-target. In the third approach the SiGe layer was deposited from a custom build target consisting of Si and Ge pieces in (45: 55 ratio) placed over a 2" Si p-type substrates using a thermal paste. In case of the SiO_2 and TiO_2 deposition, various sputter techniques were utilized depending upon the desired quality of the film. The sputter techniques included dcMS, radio-frequency magnetron sputtering (rfMS) and HiPIMS. All the above fabrication techniques with their theories and working principal are discussed later in this section

The structure, after fabrication were then treated as per desired and if needed be. Either the structure were characterized in their as-grown state or they subsequently underwent annealing procedures by using conventional furnace annealing (CFA) or rapid thermal annealing (RTA). The annealing procedure was carried out in order to study its effect on the crystallite size and interface morphology, and spectral sensitivity. The structures in their as-grown or annealed states were then later hydrogenated to further increase the spectral sensitivity of the structures. The principle of hydrogenation is reviewed briefly in chapters 1 and 3. Details regarding annealing and hydrogenation is explored in subsequent chapter.

3.1 Principles of sputtering

Wide varieties of methods are available to deposit materials such as metals, ceramics, and plastics onto a surface (substrate) in thin film form. Among these available techniques is a physical vapor deposition (PVD) which can include processes such as evaporation, sublimation or ionic [208–210] impingement on a target facilitate the transfer of material atom by atom from one or more sources to the surface of a growing film being deposited onto a substrate. Sputtering is a physical vapor deposition (PVD) [208,211] process used for depositing materials onto a substrate, by ejecting atoms from such materials and condensing the ejected atoms onto a substrate in a high vacuum environment. Sputtering, is increasingly widely used to produce thin coatings. If the sputtering is due to positive-ion bombardment, it is referred to as cathodic sputtering, where the ions are derived from a low-pressure gas discharge [208].

There are several PVD methods for producing coatings in a vacuum environment and these can be separated into two main groups: (i) those involving thermal evaporation techniques, where the material is heated in vacuum until its vapor pressure is greater than the ambient pressure; and (ii) those involving ionic sputtering methods, where high-energy ions strike a solid and knock off atoms from the surface [208,212]. Ionic sputtering techniques include diode sputtering, ion-beam sputtering and magnetron sputtering [209,210,213,214].

In principle the ejection of an atom from the top surface of a material i.e. target, by bombardment with energetic particles is called sputtering. These ejected or sputtered atoms can be condensed on a substrate to form a thin film. There are several other processes associated with bombardment of a target material by energetic ions: ejection of secondary electrons (SE), ion reflection at the target surface and ion implantation where an ion is buried in the target, radiation damage and emission of X-rays and photons [213,215]. The processes are illustrated in [Fig. 29](#).

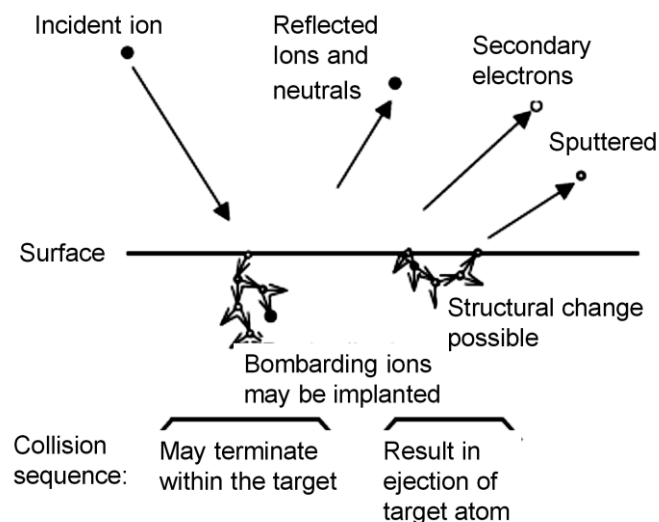


Figure 29. Processes initiated by the impact of highly energetic particles on the target surface.

The basics of the sputtering process is as follows. A target, or source of the material desired to be deposited, is bombarded with energetic ions, typically ionized inert gas such as Argon (Ar^+). The forceful collision of these ions onto the target ejects target atoms into the space. These ejected atoms then travel some distance until they reach the substrate and start to condense into a film. As more and more atoms coalesce on the substrate, they begin to bind to each other at the atomic level, forming a tightly bound atomic layer. One or more

layers of such atoms can be created, depending on the sputtering time, allowing for production of precisely layered thin-film structures. Although the basic idea of operation is seemingly simple, the actual mechanisms at play are quite complex. Electrically neutral Ar atoms are introduced into a vacuum chamber at a pressure of 1 to 10 mTorr. A dc-voltage is placed between the target and substrate which leads to ionization of some of the Argon atoms and creates a plasma, hot gas-like phase consisting of neutral atoms, ions and electrons, within the chamber. In a simple dc diode sputter device the secondary electrons that are ejected from the cathode surface maintain the discharge. This plasma is also known as a glow discharge due to the light emitted. These Ar ions are now charged and are accelerated toward the cathode target [216]. Their collision with the cathode target ejects target atoms, which travel to the substrate and eventually freeze there. Electrons released during Argon ionization are accelerated to the anode substrate, subsequently colliding with additional Argon atoms, creating more ions and free electrons in the process continuing the cycle [216–219]. A schematic of sputtering process is shown in [Fig. 30](#) and [31](#).

To obtain sputtering as a useful coating process a number of criteria must be met. Firstly, ions of sufficient energy must be created and directed towards the surface of a cathode target to eject atoms from the material. Secondly, ejected atoms must be able to move freely towards the object to be coated with little impedance to their movement. This is why sputter coating is a vacuum process: low pressures are required (i) to maintain high ion energies and (ii) to prevent too many atom-gas collisions after ejection from the target. The concept of mean free path (MFP) is useful here [210]. This is the average distance that atoms can travel without colliding with another gas atom. Above this pressure material undergoes many gas collisions and deposition rates are very low. Material can also be deflected straight back onto the target and this reduces deposition rates further. However, the discharge is set up in a way to accelerate the positive ions to the target to cause sputtering. The average ion energy is given by:

$$\bar{E} = \frac{2\lambda_{fp}}{L} qV_c \quad (9)$$

Where, L is the separation between the cathode and anode, λ_{fp} is mean free path of the sputtering ion, V_c is the cathode fall voltage and q is the electron charge. In addition to pressure, the target substrate distance determines the scattering of the sputtered particles on their way to the substrate and hence also the amount of energy that they deposit on the substrate. Sputtering is further characterized by the sputter yield Y that is the ratio of the number of ejected atoms and the number of incoming energetic particles, which are predominantly ions. According to the theory of Sigmund [221], the sputter yield near threshold, i.e. at low ion energy, is given by:

$$Y = \frac{3\alpha}{4\pi^2} \frac{M_1 M_2}{(M_1 + M_2)^2} \frac{E}{U_s} \quad (10)$$

Where, E the energy of the projectile and M_1 and M_2 the masses of the projectile and the target atom (in a.m.u). U_s is the surface binding energy and α is a dimensionless constant depending on the mass ratio and the ion energy. At low energy and mass ratios $M_2/M_1 < 1$, α is approximately 0.2.

3.2 Magnetron sputtering (MS)

Sputtering as a phenomenon was first observed back in the 1850s but remained mostly dormant until around the 1930s when diode sputtering was first used to any significant extent as a commercial coating [208,222,223] Conventional dc diode sputtering suffers from relatively low deposition rates, in many applications too low to make the process economic,

and was only used in applications where the special benefits of sputtered films were justified. In the 1960s-1970s, a magnetically enhanced variant of diode sputtering emerged, the so-called 'magnetron sputtering' (MS). MS in particular, shows how the application of simple physical principles has led to a successful commercial technology. Magnetron sputtering is a high-rate vacuum coating technique for depositing metals, alloys and compounds onto a wide range of materials. It exhibits several important advantages over other vacuum coating techniques and has led to the development of a number of commercial applications ranging from microelectronics fabrication through to simple decorative coatings. Magnetron sputtering has emerged to complement other vacuum coating techniques such as thermal evaporation and electron-beam evaporation. However, these techniques show certain disadvantages. In particular, alloys and refractory metals cause problems because of differences in alloy constituent vapor pressures and their high melting points (the need to run sources very hot thereby affecting your coated articles). In addition, compounds can dissociate into their chemical constituents at the low evaporation pressures used. Magnetron sputtering overcomes these problems and has many other advantages. The primary advantages are the high deposition rates, ease of sputtering any metal, alloy or compound, high-purity films, extremely high adhesion of films, excellent coverage of steps and small features, ability to coat heat-sensitive substrates, ease of automation, and excellent uniformity on large-area substrates, e.g. architectural glass [210,217,219].

The basic idea: The magnetron uses the principle of applying a specially shaped magnetic field to a sputter target. The principle is that the cathode surface is immersed in a magnetic field such that an electron trap is created in the cathode target vicinity are created so that $E \times B$ drift electron currents close in on themselves [208,219,221]. The principle was discovered as far back as the 1930s by Penning [224] but has only been used in the magnetron coating context for about fifty years. In essence, the operation of a magnetron sputter source relies on the fact that primary and secondary electrons are trapped in a localized region close to the cathode/ target into an endless 'racetrack'. In this manner, their chance of experiencing an ionizing collision with a working gas atom is vastly increased and so the ionization efficiency is increased too. This causes the impedance of the plasma to drop and the magnetron source operates at much lower voltages than dc diode sputter systems (500-600 V as compared with several kV). This greater ionization efficiency leads directly to an increase in the ion current density onto the target, which is proportional to the erosion rate of the target. The common feature is that electron drift is controlled and electrons are trapped. The planar magnetron sputtering discharge is a much-favored design because of its physical simplicity and the ability to extend the cathode to virtually any size required. Large cathodes are particularly suited to continuous processing. Sources are easy to fabricate into circular, rectangular or any complex shape: the only criterion is that an endless racetrack must exist. It is most straightforward to consider the construction of planar magnetron sputtering discharges. **Fig. 30** shows a basic difference in process of a magnetron sputter in contrast to conventional dc diode sputter process.

Electromagnets or permanent magnets may be used but for simplicity of design, permanent magnets are commonly used. These can be of several different possible geometries but the essential feature is that the magnetic field-lines forms a tunnel shape in front of the target surface. In order to achieve an efficient electron trap, field strength in the range of 20 mT are used. With the increase in field strength the efficiency of electron trapping increases, high-magnetic-field systems will generally operate at lower pressures, enabling operation well down into the low-pressure region.

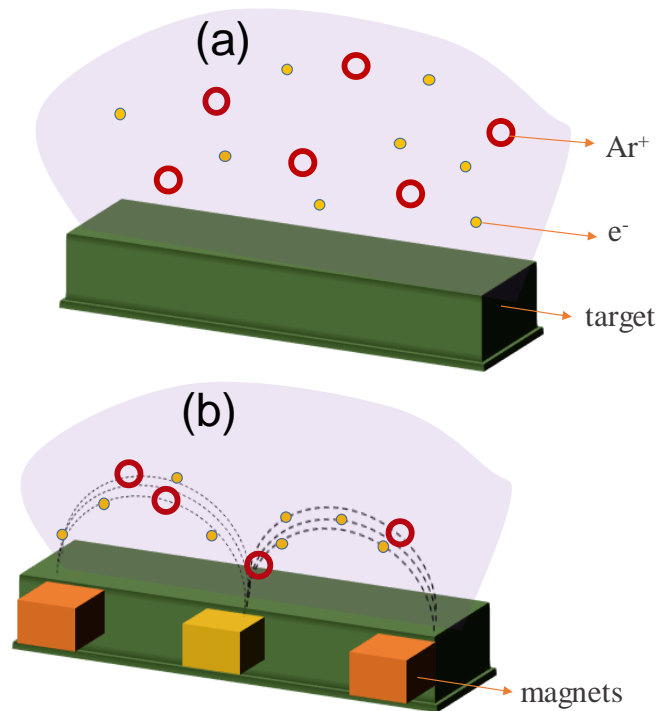


Figure 30. Pictorial representation of difference between (a) conventional dc sputtering and (b) MS. In a non-magnetron sputtering system, the plasma is not confined and electrons and Ar ions propagate through space, and may collide with the substrate. While, in MS, the plasma is confined in an area where the magnetic field is present and strong.

The advantage of this is that the plasma is confined to an area near the target, without causing damages to the thin film being formed. In addition, electrons travel for a longer distance, increasing the probability of further ionizing Ar atoms. This tends to generate a stable plasma with high density of ions. More ions mean more ejected atoms from the target, therefore, increasing the efficiency of the sputtering process [210,217–219,221]. The faster ejection rate, and hence deposition rate, minimizes impurities to form in the thin-film, and the increased distance between the plasma and substrate minimizes damage caused by stray electrons and Ar ions.

3.2.1 Direct current magnetron sputtering (dcMS)

The degree of ionization for a typical self-sustaining DC glow discharge is approximately $\sim 10^{-4}$, while the the number of secondary electrons emitted at the cathode per incident ion when bombarded with ~ 100 eV Ar^+ , is about 0.1 for most metals [228]. Thus, in order to sustain the plasma discharge it is necessary to have a high probability of collisions between electrons and neutral gas atoms. In case of too low working gas pressure, the probability of collision is smaller due to a large electron λ_{fp} , causing loss of electrons to the chamber walls and the presence of inadequate number of ionized gas atoms. Whereas, if the pressure is too high, frequent collisions will restrict the electrons from acquiring sufficient energy to ionize gas atoms, which will eventually suppress the discharge. This means that the ion-generation rates will be low and high voltages will be needed to sustain the plasma.

These issues can be overcome by using permanent magnets arranged in an appropriate configuration in close vicinity of the the cathode (Figs. 30 and 31). The magnetic field lines B penetrates the target and form a closed path on its front surface. The electrons generated, will initially execute a helical motion along the magnetic field that is normal to the target.

The electrons are forced to drift in an orbit back to the target as they encounter region with parallel component of the magnetic field. This phenomenon will make the electrons follow cycloidal trajectories near the target along the space confined by the magnetic field lines. Therefore, in the presence of the magnetic field, the secondary electrons make more ionizing collisions in close vicinity of the target and thereby increasing the flux of bombarding ions, resulting in higher deposition rates.

The dcMS often operates at a cathode potential of some hundreds of volts, giving a maximum power densities of a few tens of W/cm^2 . The targets in dcMS mode are directly conducting electricity and are subject to I^2R losses and may be operated up to current density of approximately $4 - 60 \text{ mA}/\text{cm}^2$ averaged over the target [208]. Deposition rates are quite high or $20\text{-}130 \text{ nm}\cdot\text{min}^{-1}/\text{Wcm}^{-2}$ [225], while the sputtering yield may range from ~ 0.5 to ~ 5 (at a given 300 eV Ar bombardment), which increases with increasing ion energy, but eventually saturates at higher energy due to ion implantation in the target [226]. The majority of the sputtered particles have energies of up to 10 eV , but individual particles may have energy as high as $\sim 50 \text{ eV}$ [227].

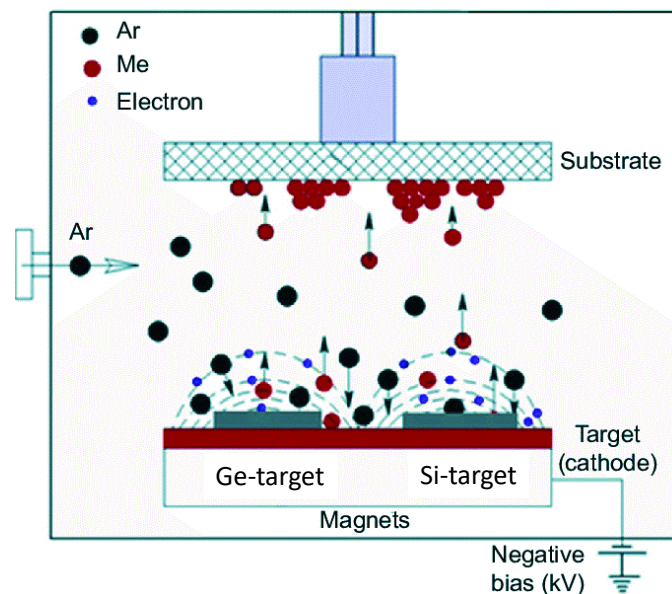


Figure 31. Process schematic of direct current magnetron sputtering (dcMS).

The dcMS is the least costly of the magnetron processes because dc-power supplies are lower cost and simpler to manufacture than rfMS. As described previously a cathodic discharge plasma is generated by dc power, in which a target material to be deposited is connected to the negative terminal of a power supply. The basic principle is elaborated in paragraphs above. At first when the dc-voltage is applied to the electrodes, initially small amount of charge carriers present in the working gas (typically Ar) create a small current. As the inelastic collisions occur in the gas more electron-ion pairs are created, and thus the current-density increases. The generated Ar^+ ions bombard the target surface, resulting in the generation of secondary electrons (SE) from the cathode surface and sputtering of target atoms on the substrate. In addition the SE present, are simultaneously accelerated away from the cathode and thus further increases the ionization of the working gas by inelastic collisions. This results in charge multiplication causing the current to increase rapidly. At higher applied voltages the number of Ar^+ ions produced by collisions per secondary electrons are sufficiently high to regenerate more SE, making the discharge to be self-sustaining and glowing due to excitation of gas atoms [208,214,217]. Note however that the magnetron sputtering discharge is not only sustained by SE emission, there is always a rather significant

contribution due to Ohmic heating within the magnetic trap [256].

Generally, the deposition rate in a dcMS deposition system is proportional to the dc-power dissipated. The significantly increased deposition rate attainable by dcMS in contrast to simple dc diode sputtering is very desirable as for instance, the impurity level in the deposited samples will be lowered due to a higher flux of incoming atoms with respect to impurity atoms onto the substrate. Most importantly, a high deposition rate of dcMS makes it attractive for industrial applications. However, a common drawback of dcMS is the creation of the “race track” i.e. the erosion of the target surface. This is due to the high density of electrons, which is confined by the magnetic field and thus the plasma is not uniformly distributed across the target surface. This irregular erosion of target area, results in a typical material utilization of only 20–30%. However, optimizing the shape and balancing of the magnetic field and altering magnetron configurations can be utilized to overcome such issues [208,217,219]. Another drawback is that up to 80% of the energy applied to the sputtering target is transformed to heat, and to avoid melting and destroying the target, the magnetron assembly requires efficient cooling [225].

3.2.2 Radio frequency magnetron sputtering (rfMS)

One major drawback of using dcMS is that it is not applicable for depositing from insulating targets, as no current can flow through it. One solution to this impediment is to use an alternating current at high frequency. Radio frequency MS (rfMS) has been developed to insure the deposition of dielectric/ insulating materials. When rf-power is applied to a target it creates a capacitively coupled discharge and a dc-self biaspotential develops over the target surface. For the rfMS, the frequency of 13.56 MHz is normally used; which tends to make ions and electrons having considerably different motilities in the alternating field [210]. That is they physically cover varying distances during each half cycle. In a capacitively coupled system, no net charge can be transferred so the electrode biases negatively to compensate, creating negative dc voltage on the target surface. Due to this capacitively coupling, the target material does not need to be a conductor and can be an insulating material for that sake. Because a dc-self bias is present, the surface ion bombardment still occurs and therefore it is possible to sputter ceramic or insulating materials as well as metallic materials. However, rfMS requires an impedance matching unit to ensure that the maximum power is absorbed into the plasma discharge. Furthermore, the higher complexity of rf-generators implies that these power sources are more expensive to purchase compared to dc-power supplies. Further limitations include that the dielectric materials are often difficult to fabricate and obtaining large targets can be an issue. In addition, sputtering of ceramics could pose an issue as magnetron sputtering puts a significant thermal load on the cathode surface and owing to the uneven nature of the ion bombardment, the heat flow varies across the target surface [210,229]. Since ceramic materials often have very low thermal conductivity along with low intrinsic shock resistance; the excessive heating may cause unwanted failures. A major disadvantage of rfMS is a very low deposition rate. All in all, the rfMS of compound targets is still an attractive technique and has found application in wide range of fabrication processes.

Reactive sputtering

Many dielectric materials which would be considered too insulating to be sputtered by conventional dcMS, can often be deposited by dcMS using a reactive gas atmosphere in conjunction with noble working gas. In that case, the target will still be metallic. Such reactive sputtering is, however, significantly more complex than metal sputtering or sputtering from compound targets. Argon gas is introduced as the carrier gas but additional minute quantities

of a reactive gas is brought to the chamber. This can be any gas which have a tendency to react with the target atoms to form the desired compound. Oxygen and nitrogen are commonly used, to deposit oxides and nitrides, respectively, but other gases can also be used as long as the reaction byproducts can be appropriately handled. However, the desired compound is formed both at the cathode target and at the substrate, depending on power and surface reactivity. This can result in different mode of operation i.e. metallic mode or poisoned mode [216,218,230] and will be further discussed later in this chapter. By controlling the reactive gas flow rate it is possible to control the stoichiometry of the growing film. The process suffers from one important drawback, namely target 'poisoning' [216,218,230]. A poisoned target refers to a metal target where there is enough compound formation on the surface for it to act as a compound target, with corresponding collection of positive charges on the substrate, frequent arcing, and low deposition rate [231,232]. Once a target is poisoned, the gas flow rate should be reduced such that there is insufficient reactive gas to react fully with the target; this region is commonly known as metallic mode sputtering. It should be noted that the reactive gas flow required to induce metallic mode sputtering might be much lower than that to induce a poisoned target, leading to the well-known hysteresis curves [210,216,233,234] inherent to reactive sputtering, as shown in **Fig. 32**. One way of avoiding the hysteresis is to increase the pumping speed to such an extent that reactive species requires more time to poison the target [58].

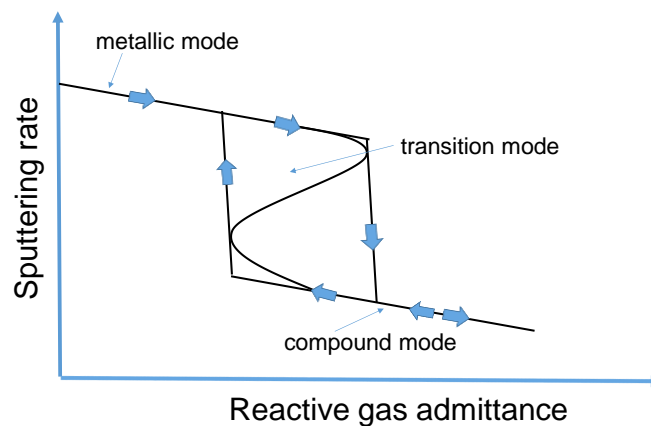


Figure 32. Hysteresis curve in reactive sputtering because of target poisoning [235].

3.2.3 High power impulse magnetron sputtering (HiPIMS)

Over the last few decades, several studies have been carried out in order to increase the plasma density [233,234,236–238] as it influences the ionization of the sputtered materials and consequently the deposition rate. Several applications require a higher degree of ionization of the sputtered species, since the ion flux reaching the substrate is known to have a significant influence on the overall quality of the film [233]. One way of achieving increased plasma density is by applying higher power to the target. However, increased power density at the target can cause overheating and may gradually melt the target. Hence, the power density is restricted by a maximum power which can be delivered to the target without damaging the target. To overcome the issue, ionized physical vapor deposition (IPVD) has been achieved by applying a high power unipolar pulse of low frequency and low duty cycle to the cathode/ target in order to generate highly dense plasma [234,236,237]. This technique is referred as high power pulsed magnetron sputtering (HPPMS). The essential advantage of HPPMS techniques is that it uses the same magnetron sputtering equipment, assembly and chamber, except for the power supply [233,234]. Thus, making this technique applicable to

full-scale industrial size deposition systems, independent of the target geometry, with relative ease. There are a few variations of the HPPMS technique of which the most common is high impulse power magnetron sputtering (HiPIMS) [233,234,238]. In HiPIMS a pulse of very high amplitude, i.e. an impulse, is applied to the cathode and a long pause exists between the pulses.

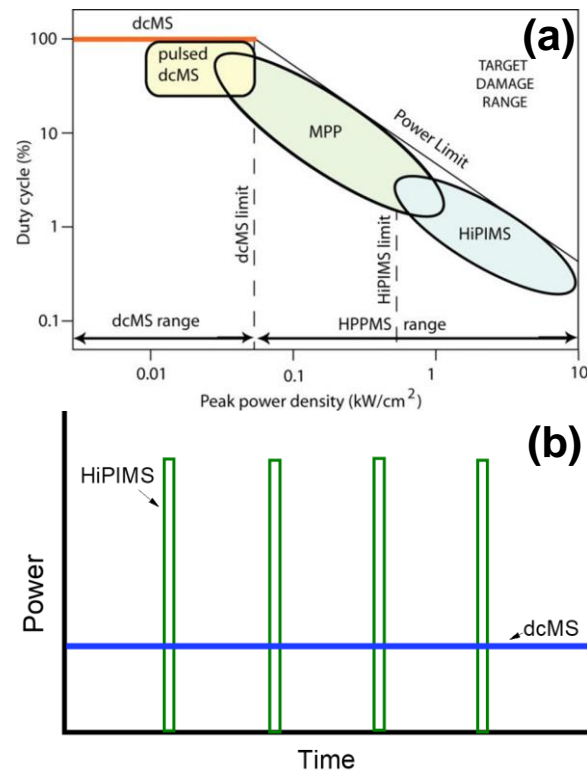


Figure 33. (a) Plot of peak power density at the target versus duty cycle for different magnetron discharges (Gudmundsson *et al.* [233]). (b) Power versus time in direct current magnetron sputtering (dcMS) and high-power impulse magnetron sputtering (HiPIMS), respectively.

Thorough reviews on IPVD (with focus on HiPIMS) techniques and their applications has been given by for instance Helmersson *et al.* [234], Sarakinos *et al.* [239], Anders [240], a thorough overview of the modulated pulsed power magnetron sputtering (MPPMS) technique by Lin *et al.* [241], Lundin and Sarakinos [242], Alami *et al.* [243,244], Gudmundsson [238,245] and Gudmundsson *et al.* [233]. In addition, the effect of magnetic field configuration over the discharge has been studied [246–248]. The HiPIMS discharge is a relatively new addition to plasma based sputtering systems [233]. HiPIMS differs from dcMS in the important respect that self-sputtering quickly becomes the dominant sputter mechanism. In HiPIMS, high power is applied to the cathode in short unipolar pulses at low duty cycle and repetition frequency while maintaining the average power about ~ 2 orders of magnitude lower than the peak power [233,245]. This results in a high plasma density with higher ionization fraction of the sputtered vapor. This increase in the ionization fraction allows good control over film quality by controlling the energy and direction of the deposited species. This depicts a major difference and a significant advantage of HiPIMS over dcMS where the sputtered material consists mainly of neutral species. A typical HiPIMS discharge can operate with a cathode voltage in the range of 500–2000 V, current densities of up to 3–4 A/cm², peak power densities in the range of 0.5–10 kW/cm², repetition frequency in the range of 0.05–50 KHz, and duty cycle in the range of 0.5%–5% [233,249]. The peak power is 2–3 orders of magnitude higher than in typical dcMS discharge while the average power is the same. In addition, the range of parameters available are much wider in the pulsed system

than for the dcMS and rfMS methods. That is, the discharge pulsing gives a much greater flexibility due to additional control parameters i.e. pulse width, duty cycle, and repetition frequency. A simple graphical representation for differentiation between HiPIMS and dcMS in terms of duty cycle and power vs. time is shown in **Fig. 33(a, b)**, along with a pictorial representation of deposited film morphologies **Fig. 33(a)**. An experimental demonstration of results and discussion are given in subsequent sections, thus complementing the HiPIMS method.

The Physics Behind - in brief

A discharge current and voltage characteristics gives a fundamental insight into the discharge physics of the HiPIMS process. Several studies have been reported over the discharge characteristics of HiPIMS either for reactive or non-reactive discharge. A typical current-voltage waveform for non-reactive sputtering (**Fig. 35(a)**, red curve) can be described by a rise in current to a peak value which then drops followed by a relatively stable plateau [245]. The drop in intensity is due to strong gas compression and a consequent large flux of atoms from the cathode. The collision of sputtered atoms with the Ar (as working gas) causes heating and expansion of the working gas, and is well-known characteristic of the discharge called as '*gas-rarefaction*' [233,245,250]. This therefore replaces the working gas atoms with the sputtered atoms in the vicinity of the cathode (target) to some extents as the pulse evolves. If the plasma density becomes high enough, a major fraction of the sputtered atoms will experience electrons impact ionization, which are then attracted back to the target in order to participate in the sputtering process. This process is known as '*self-sputtering*' [233,245] and is responsible for the increase in discharge current before a stable plateau is achieved. The viability of the self-sputtering process relies on various parameters such as the working gas, the sputter yield, the SE emission yield, and the target voltage [233].

However, in reactive sputtering case, the discharge current waveform can be quite different when working in different modes i.e., either poisoned, transition or metals mode, which depends on the reactive gas and the target material [233,245]. For reactive sputtering, a reactive gas (such as O₂ and N₂ etc.) along with noble working-gas (such as Ar) is introduced to synthesize a compound film. In HiPIMS discharge, the dissociation probability of molecular gases tends to increase due to the presence of higher electron density. However, the presence of reactive gas can also lead to the formation of compound material on the target surface. This is often referred to as target poisoning [230]. Due to this target poisoning the reactive sputtering process is unstable, and generally exhibits a hysteresis behavior. For instance, the curves [233] in **Fig. 34** presents a discharge voltage vs. oxygen flow rate while sputtering a Ce target in an Ar/O₂ discharge is shown for both dcMS and HiPIMS, respectively. The upper part of each curve refers to metal mode sputtering and the lower part of each curve to oxide/ compound mode sputtering. While the middle part can be attributed as transition mode. A hysteresis is already observed in the dcMS case. This hysteresis effect originates due to reaction of target with the reactive gases. Sputtering at low reactive gas flows, where there is no significant reaction with the sputtering target, is referred to as metal mode, while for high flows of reactive gas, when a compound has formed on the target, is referred to as compound mode or poisoned mode sputtering. The hysteresis occurs if the effective etching rate of the compound is lower than for the pure metal, which is commonly the case due to a lower sputter yield of the compound. Further the unstable or transition region of dcMS is much wider than in the case of HiPIMS.

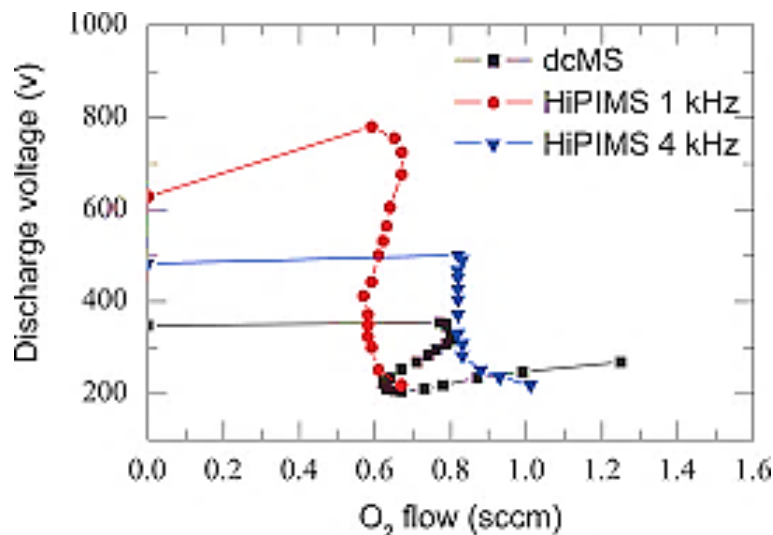


Figure 34. Discharge voltage V_d as a function of the O_2 flow during reactive dcMS and HiPIMS of a Ce target. For the HiPIMS process, pulsing frequencies of 1 and 4 kHz are shown. The average discharge power was 70W and the argon partial pressure was 0.65 Pa at a pumping speed of 25 l/s (Gudmundsson *et al.* [233]).

A typical discharge current waveform in the case of reactive sputtering in metal [251] (Fig. 35(a)), green and blue line) follows as an increase in current to a peak value, followed by a drop due to gas compression and rarefaction and then an increase to a stable plateau where the discharge is dominated by self-sputtering. Several studies of discharge characteristics of reactive HiPIMS sputtering have shown a striking feature observed where the form of discharge current waveform changes along with the peak current values, as the reactive gas flow rate changes.

Such a change in the current waveform in a reactive HiPIMS discharge has also been reported for Ti target in Ar/ O_2 mixture by Stranák *et al.* [252], for Ru target in Ar/ O_2 mixture by Benzeggouta *et al.* [253] for Ti target in Ar/ N_2 mixture by Magnus *et al.* [254], and for Al target in Ar/ N_2 mixture by Moreira *et al.* [255].

Fig. 35(a) shows the discharge characteristics. One can see a decrease in peak current (initial rise/ peak in current) when oxygen is added and then a decrease when flow-rates is increased. However, with first addition of oxygen (2 sccm) the discharge remains in the metal mode, while the plasma density decreases, due to higher energy loss per electron-ion pair created. When the flow is increased further to 5.6 sccm, a transition to compound mode is observed. Further, a delay in an onset of initial peak is seen with reduced intensity, which is then continued with a transition to self-sputtering as indicated by a steeper slope of current. This steeper rise of current is typically associated with transition of discharge from metal mode to compound mode.

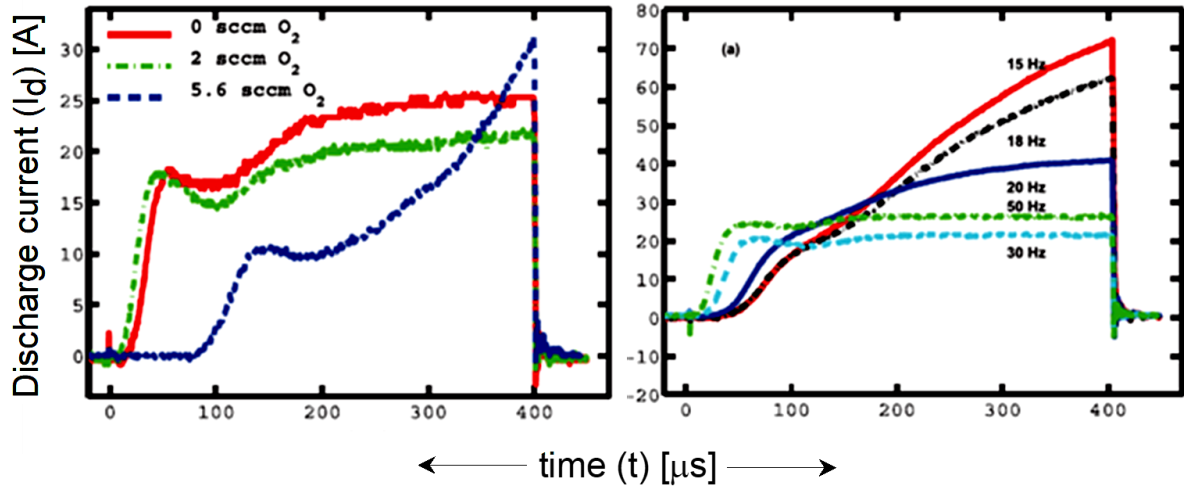


Figure 35. (a) The discharge current for various oxygen flow rates for Ar/O₂ discharge with titanium target. The discharge pressure is roughly 0.6 Pa, the repetition frequency 50 Hz, and the pulse voltage is 600 V. (b) The discharge current for various repetition frequencies for Ar/O₂ discharge with titanium target. The discharge pressure is roughly 0.6 Pa, the oxygen flow rate 2 sccm, and the pulse voltage is 600 V. After Magnus *et al.* [251].

In similar study [251] on the effect of varying repetition frequency for the Ti in Ar/O₂ discharge (**Fig. 35(b)**) a familiar waveform was observed at lower repetition frequency. However, as the repetition frequency is reduced the current discharge waveform transit in to a different waveform similar to that observed for the discharge where the oxygen flow was higher. This implies oxidation takes place due to long pause between the pulses, i.e. as the time between the pulses increase there is more time available for target to be poisoned. The above mentioned increase in discharge current is attributed to working gas recycling as the target gets poisoned and the sputter yield drops significantly [256].

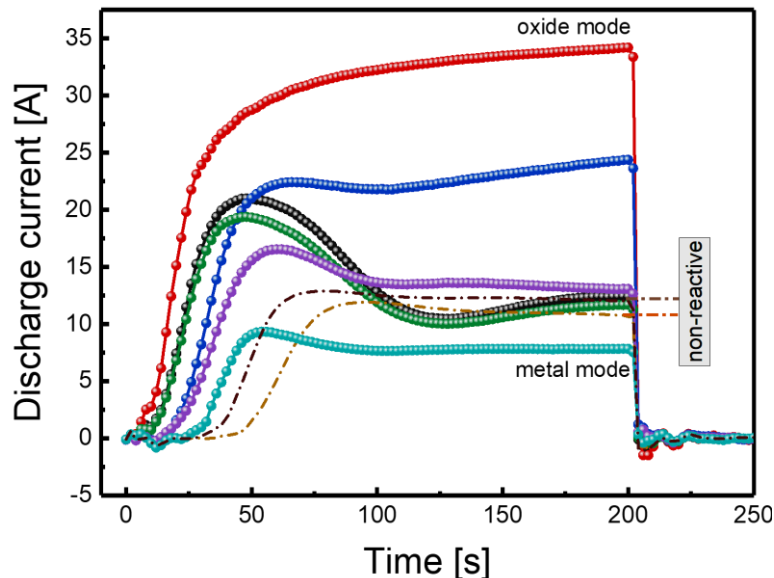


Figure 36. The discharge current for various oxygen flow rates, for the Ar/O₂ discharge with titanium target. The pulse length is 200 μ s, pulse voltage is 670 V and the discharge pressure is approximately 7.5 Pa. The discontinuous lines shows the current waveform for non-reactive sputtering.

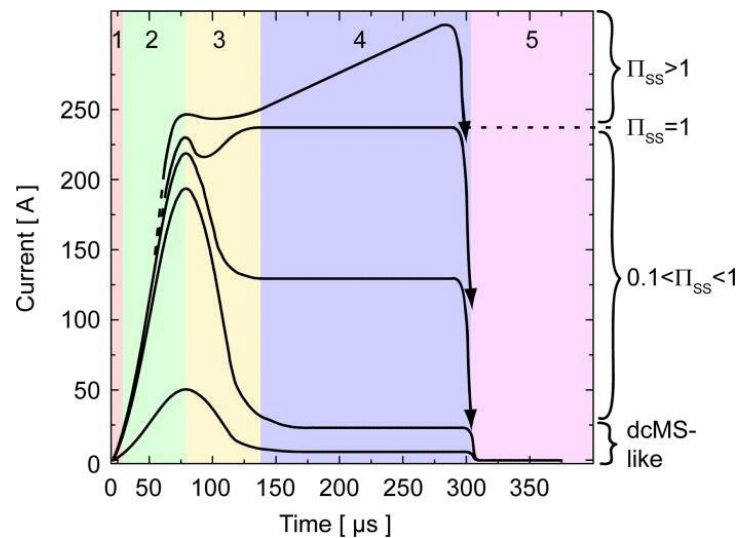


Figure 37. Schematic illustration of the HiPIMS discharge current divided into five different phases. The bottom two curves display an approximately 300 μs long current pulse, where the current decays after an initial peak at around 80 μs mainly due to depletion of the working gas, followed by a current plateau. The top two curves illustrate the onset of self-sputtering, where the current may reach a second maximum before the pulse is switched off. The middle curve displays an intermediate state due to partial self-sputtering. The Π_{ss} is a self-sputtering parameter. After Gudmundsson *et al.* [233].

Few typical discharge current waveform for titanium in Ar/O₂ discharge are shown in Fig. 36, where the O₂ flow rate is varied by keeping the pulse voltage (~ 670 V) and pulse length (200 μs) constant. Such characteristic behavior of discharge can be explained in a good manner [233] where the typical pulse shapes of the discharge current are described by using a model in Fig. 37. The curves in Fig. 37 suitably categorized according to the degree of self-sputtering during the plateau (or so called runaway phase i.e. region 4).

The sputter system

Two different sputter system were utilized in our study. The cross-sectional drawing of the first sputter chamber is shown in Fig. 38. The chamber is equipped with 6 magnetron assemblies (two 2 and four 3 inches) MAK Planar Magnetron Sputter Source, MeiVac, with Nd/FeB magnets. Each magnetron assembly consist of a cooling system and pressurized air shutter system that can be controlled manually or by using homemade LabVIEW software. The targets or magnetron assemblies are aligned at an angle of 45° facing the substrate holder assembly on top in the middle of chamber. The substrate holder assembly is equipped with a holder stage, a Molybdenum-heater (controlled via SM 400-AR-8 power supply by Delta Elektronika), a K-type thermocouple and 3-axis substrate holder manipulator in x, y and z directions. The substrate assembly can be rotated 360° in both clock and counter-clock wise directions. The sample holder itself is a stainless steel plate.

To insert the samples in the main chamber, the substrate holder (SH) is first placed in a load-lock over a magnetic arm that slide the sample holder into the chamber after acquiring 10⁻⁴ Pa pressure. Only after which the gate valve is allowed to open to slide the samples into the main chamber over the sample holder assembly. Both load-lock and main chamber are equipped with separate turbo pumps. Two gas inlets, one for working gas (Ar) and second for reactive gas (O₂, N₂ or H₂) are present. The gas flow rate is adjusted by mass flow controllers (MFC, Area FC-D980C). A butterfly valve controlled via electronics (MKS, 600 Series Pressure controller) precisely is used to adjust the pressure inside chamber. Before deposition, the chamber is pumped down to 10⁻⁷ Pa.

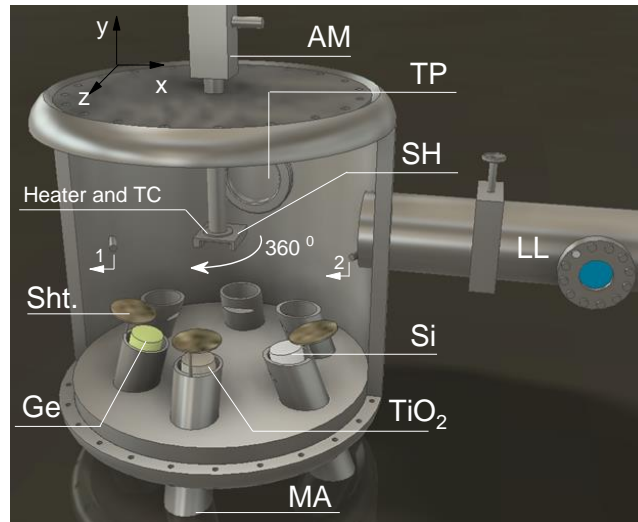


Figure 38. Schematic 3D view of the sputter chamber: (s)substrate holder (SH); load lock (LL); temperature controller (TC); Ar and oxygen inlet (1 and 2); turbo pump (TP); target shutter (Sht.) and axis manipulator (AM).

The second sputter chamber is equipped with 5 magnetron (2'') assemblies each equipped with a cooling system. The shutter system is basically a huge circular plate with a rectangular chimney that can be placed directly over the target to be sputtered. The SH assembly consist of a horizontal arm mounted on a vertical assembly, that can be rotated 360° such as to maneuver the sample directly on top of the target or so to say the chimney. Two SH position are available on each of the arm. The SH sits directly over the targets at a distance of 12 cm. A feedthrough is present to assist SH biasing up to - 60 V. A rough pump followed by cryogenic pump system is used to lower the pressure ($\sim 10^{-6}$ Pa). A butterfly valve is used to adjust the pressure manually. The gas inlets are for Ar and O₂ only, along with N₂ inlet for purging. All the magnetrons assemblies i.e. their water cooling guides are facilitatet with N₂ purging; so as to clean the water guides (inlet and outlet) after deposition. However, it is neither possible to co-sputter the targets nor rotate the sample holder itself while sputtering, since the sample is directly on top of the target.

The Power supplies utilized

For dcMS, deposition was carried out in a constant- power mode using Advanced Energy MDX500 power supply. For the HiPIMS setup, the power was supplied by SPIK1000A pulse unit (Melec GmbH) operating in unipolar negative mode at a constant voltage, which in turn was charged by a dc power supply (ADL GS30). The discharge current and voltage were monitored using a combined current transformer and a voltage divider unit (Melec GmbH) and the data was recorded with a digital storage oscilloscope (Agilent 54624A). In case of sputtering via rfMS, radio frequency CESAR© 136 radio frequency (rf) power generator (13.56 MHz) source coupled with impedance matching unit was used to initiate the plasma. The magnetrons were either equipped with N or HN-connectors, that connects to the power supplies.

3.3 Annealing

After fabrication, the samples (if required) underwent annealing procedure using either conventional furnace annealing (CFA) or rapid thermal annealing (RTA).

RTA

A JipelecTM JetFirst 200, shown in **Fig. 39** is used for RTA processing. The setup is equipped with 12 sets of flash lamps, Ar, O₂, N₂ and H₂ gases and mass-flow controllers, along with a cooling system, turbo pump ($\sim 10^{-5}$ mbar), three thermocouples, a pyrometer and other electronics. A clean Si-wafer is used as a sample stage with thermocouple just touching. Prior to use the chamber is pumped down to avoid any contamination, and during use a slight overpressure of N₂ is maintained to avoid oxidation.

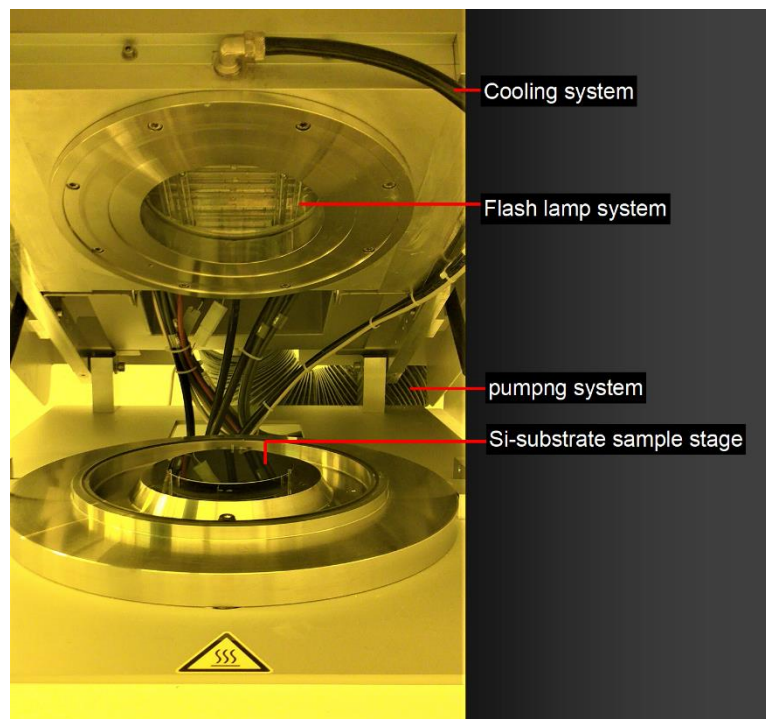


Figure 39. A close view inside the RTA processor.

CFA

A Heraeus D-6450 Hanau anneal furnace with maximum temperature achievable of 1300 °C was used. For annealing, first an alumina tube was inserted into the furnace which is then brought to desired temperature and is held there for ~ 30 -60 min in order to stabilize. The sample is then inserted to the center region of the alumina tube, using a homemade sliding rod. A slight overpressure of N₂ gas of 5N purity was applied to avoid oxidation of the samples. After the desired time of heating the sample is retracted from the alumina tube and allowed to cool down to room temperature, while N₂ overpressure still being kept.

3.4 Hydrogenation

Basic principal

As already mentioned in Chapter 2, an inductively coupled discharge is one of the simplest methods to create a high density plasma, which is an essential requirement to obtain an effective means of passivation. The high plasma density is achieved when the discharge is operated in an electromagnetic mode, where an rf-coil induces an azimuthal electric field within the plasma that further maintains the discharge. Low pressure (< 50 mTorr) is generally utilized for inductive discharges. Samples are placed inside a quartz tube that is located inside the inductive coil. The coil is typically separate from a plasma by a quartz tube walls. The inductive coil is driven by a current at 13.56 MHz using an rf-supply attached to an impedance matching unit. The inductively transfer of power and the absence of electrodes leads to low voltages across the plasma sheaths and the wall surfaces (i.e. quartz tube wall). Therefore, the discharge can operate at high processing rate and at the same time avoiding any damage and/or contamination that may have occurred due to high-energy ion bombardment [184,187].

Assembly

A schematic and a photograph of the setup is shown in **Figs. 40** and **41**. A 290 mm long cylindrical quartz tube was used with an inside diameter of 34 mm, with one end connected to a pumping system and the other end closed. The close end is made accessible to place the sample inside. The structures to be exposed were first placed over a long rectangular piece of Si- substrate to ease the introduction and draw out the samples. The quartz tube was placed inside a circular inductive coil (41/2 turns) with inside diameter of 54 mm, prepared from 85 cm long and 10mm thick copper tube. The gas mixture consist of H_2/Ar (~70/ 30 %). The flow rates ($q_{Ar} = 4$ sccm, $q_{H_2} = 14$ sccm) were controlled via mass flow controllers and the throttle valves was adjusted to the required pressure using butterfly valve close to the pumping system. During the hydrogenation, the total gas pressure was varied in the range of 0.6–20 mTorr. Radio frequency CESAR© 136 radio frequency (rf) power generator (13.56 MHz) source coupled with impedance matching unit was used to generate the plasma. The driving frequency of the discharge of 13.56 MHz belongs to the industrial, scientific and medical (ISM) radio bands, which are, are radio bands reserved internationally for the use of radio frequency (RF) energy for industrial, scientific and medical purposes other than telecommunications. The ISM bands were first established at the International Telecommunications Conference of the International Telecommunication Union in Atlantic City, in 1947. So this choice of driving frequency is dictated by these regulations. Plasma oscillations are rapid oscillations of the electron density in conducting media such as plasmas. The frequency of these oscillations are commonly described by the plasma frequency. The plasma frequency is proportional to the square root of the plasma electron density. For an inductively coupled discharge like the one used here the plasma frequency is of the order of 9 GHz, so it is significantly higher than the driving frequency.

Color-changing temperature stripes, placed inside the quartz tube, were utilized to determine the rise in temperature during hydrogenation.

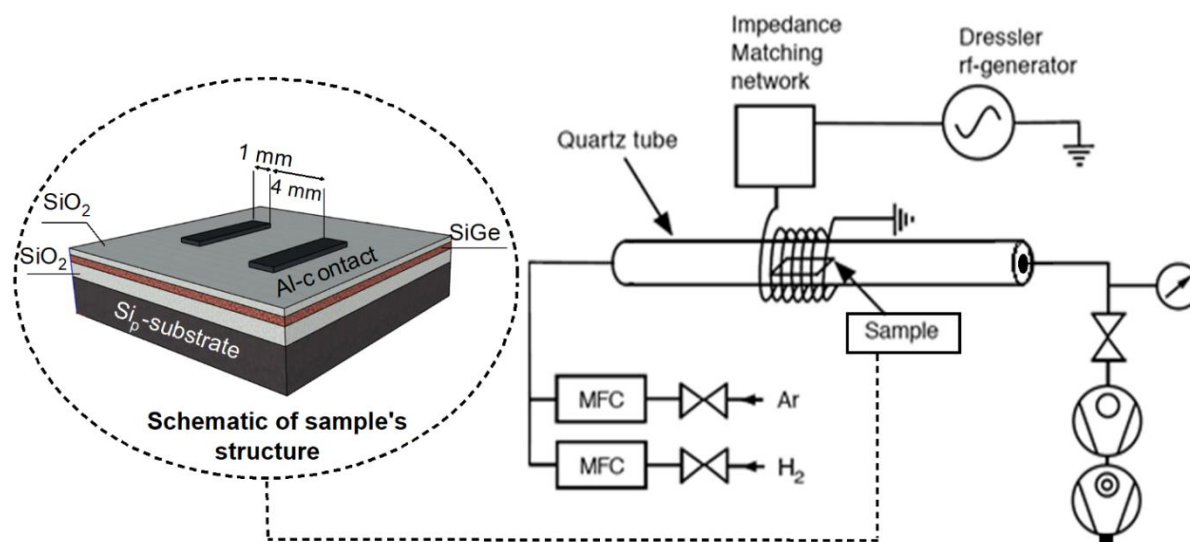


Figure 40. Schematic of the cylindrical inductively coupled discharge H_2/Ar utilized for hydrogenation. The inset shows a schematic of structure i.e. $\text{Si}_p/\text{SiO}_2/\text{SiGe}/\text{SiO}_2$ and is also employed for $\text{Si}_p/\text{SiO}_2/\text{TiO}_2/\text{SiGe}/\text{TiO}_2$.

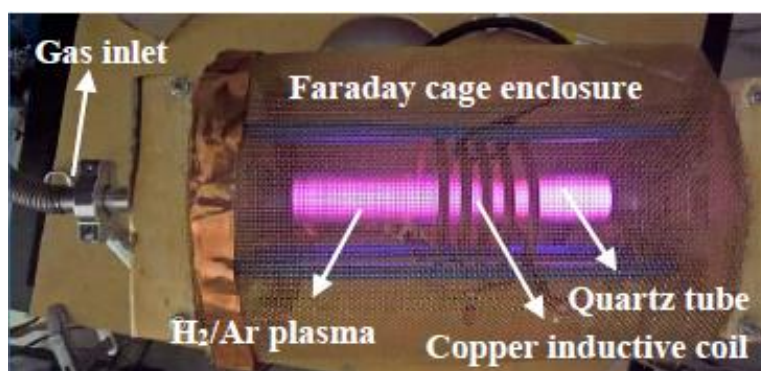


Figure 41. Home-built hydrogenation setup. The left end of the tube is connected to pumping system, whereas right end is a close end with a gate to insert samples. .

Chapter 4

4 Characterization techniques

The chapter gives a brief overview of characterization techniques employed for structural investigation, surface analysis, electrical and optical measurements. After the fabrication and anneal (and/or hydrogenation) treatment procedures as mentioned in previous chapter, the structures were characterized by following methods:

- Grazing incidence X-Ray diffraction (GiXRD)
- X-ray reflectometry (XRR)
- Atomic force microscopy (AFM)
- Scanning electron microscopy (SEM)
- Energy-dispersive X-ray spectroscopy (EDS)
- Transmission electron microscopy (TEM)
- Scanning transmission electron microscopy (STEM)
- Photocurrent (PC) spectral analysis

Each of the above mentioned characterization methods (except TEM, EDX and STEM analysis) are discussed successively in this chapter. The TEM, EDX and STEM analysis along with respective sample preparation was carried out by our Romanian partner, while SEM analysis were carried out at Innovation Center Iceland (NMI).

4.1 X-ray diffraction

X-ray reflectometry was applied to determine the layer thickness, film mass density and surface roughness. Whereas, for the structural investigation of the fabricated MLs was carried out by grazing incidence XRD (GIXRD) via Philips X'pert diffractometer ($\text{CuK}\alpha$, 0.15406 nm and having the precision of 0.0001°). For GiXRD and XRR scans $2 \times \text{Ge}$ (220) asymmetrical hybrid monochromator utilizing line focus, a divergence slit ($1/32^\circ$, $1/16^\circ$, $1/4^\circ$, $1/2^\circ$, 1°) and a parallel plate collimator (0.27°) was used. The measurement run was made with a step size of ranging from 0.0008 to 0.005° and time per step of $0.5 - 2.0$ s.

4.1.1 Theoretical perspective and basic principal

Max von Laue, in 1912, discovered that crystalline substances act as three-dimensional diffraction gratings for X-ray wavelengths similar to the spacing of planes in a crystal lattice. X-ray diffraction is based on constructive interference of monochromatic X-rays in a crystalline sample [257,258]. XRD signal is due to an elastic scattering of monochromatic X-ray by core electrons of atoms in a sample. The regularly spaced atoms in a crystal lattice causes the X-rays to be diffracted, producing the well-known XRD patterns, analogous to diffraction of visible light by gratings. The principal is based on that an electron in an alternating electromagnetic field will oscillate at the same frequency as that of the field. Thus, when an X-ray beam hits an atom, the electrons around the atom start to oscillate with the same frequency as the incoming beam. Almost in all directions, we will have destructive interference, that is, the combining waves are out of phase and there is no resultant energy leaving the solid sample [258]. An illustration of constructive and destructive interference is shown in **Fig. 42**. However the atoms in a crystalline form are arranged in a regular pattern, and as a result in few directions we will have constructive interference (**Fig. 42** and **43**). This implies that the waves will be in phase and there will be well defined X-ray beams leaving the sample in various directions [257]. Hence, a diffracted beam may be described as a beam composed of a large number of scattered rays mutually reinforcing one another. However, the intensities of obtained peaks (reflections) are determined by the distribution of the electrons in the unit cell. Since, the electron density is highest around an atom. The intensities depend on the kind of atoms and where they are located in the unit cell. Plane going through areas with high electron density will reflect strongly, whereas, plane waves passing through low electron density will give weak intensities.

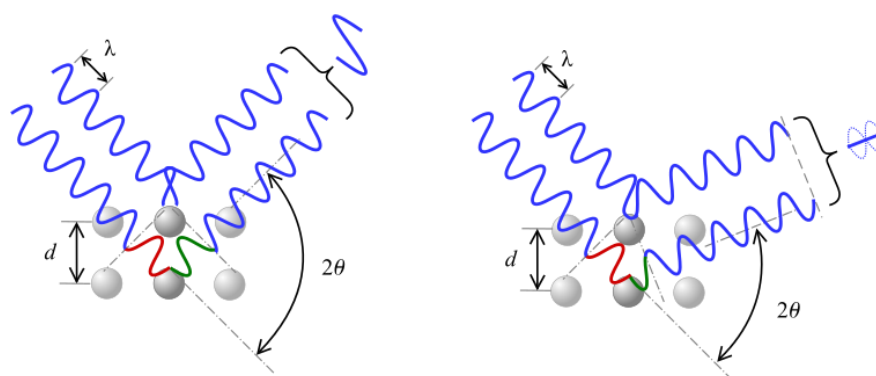


Figure 42. Illustration of the 2θ deviation, which causes a phase shift resulting in either constructive (left figure) or destructive (right figure) interferences.

By scanning the sample through a range of 2θ angles, all possible diffraction directions of the lattice should be attained due to the random orientation of the powdered material. Mathematically, XRD signal is best-known to follow Bragg's Law for constructive interference (**Fig. 43**):

$$2d \sin(\theta) = n\lambda \quad (11)$$

Where, d is the separation between the Bragg planes, θ is the Bragg angle, n is the diffraction order, and λ is the X-ray wavelength. The term Bragg planes refers to planes that are comprised of these constructively diffracting atoms. Conversion of the diffraction peaks to d -spacing allows one to chemical identity of the sample because each material has a set of unique d -spacing. Typically, this is achieved by comparing the obtained results with that of d -spacing from standard reference patterns.

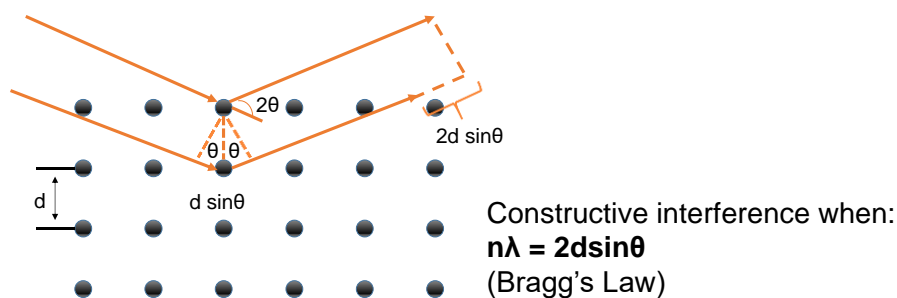


Figure 43. Illustration of constructive interference when Bragg's law is satisfied.

4.1.2 Grazing incidence X-ray diffraction

Usually the penetration depths of X-rays, i.e. the corresponding $1/\mu$ values, are found to be in the 10 - 100 μm range, respectively, where μ , is the absorption coefficient. However, in most thin-film investigations the thickness is substantially less, thus causing a large fraction of the diffraction pattern as measured via symmetric $\theta:2\theta$ configuration, to originate from the substrate rather than the deposited thin film structure itself [257]. Thus, in the cases of thin films with thicknesses in the few nanometer range or less, only negligible structural information can be gained using this measurement configuration. This is because the path traveled (which is of the order of $\sin(\theta)/\mu$) by the X-ray in the sample, is too short for typical Bragg angles to deliver X-ray reflections of sufficient peak-to-noise ratio. In such cases for the analysis of thin films, X-ray diffraction techniques have been introduced [257,258], for which the primary beam enters the sample at very *small angles* of incidence and hence named as grazing incidence X-ray diffraction (GIXRD). This small angle of entrance leads to a significant increase in the path traveled by the X-rays and the structural information contained in the diffractogram to come primarily from the thin film.

The configuration for the GIXRD analysis is asymmetric and is schematically shown in **Fig. 44(a)**. The angle between the incoming beam and the sample surface is very small. This angle will be denoted by α . The GIXRD measurement is performed such that the angle α is kept constant, while the detector is moved along the 2θ circle. This is the major difference compared to the symmetric configuration where the entrance angle θ is also changed during the measurement [257,258].

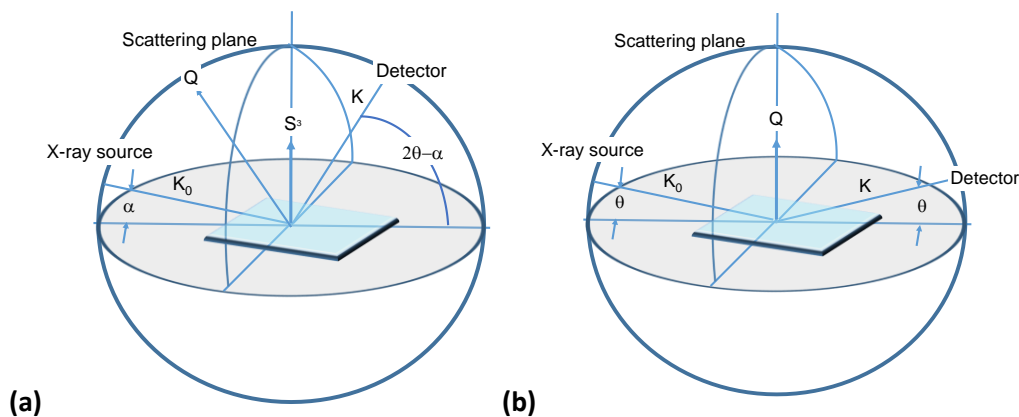


Figure 44. (a) The geometry in grazing incidence diffraction is characterized by a small angle α that is kept constant during the measurement. (b) XRR experiment from the viewpoint of the sample reference frame. From Birkholz *et al.* [257].

4.1.3 X-ray Reflectometry (XRR)

The working principle of the method involves monitoring the intensity of the X-ray beam reflected by a sample at grazing (small) angles. The diffractometer is operated in the symmetric $\theta:2\theta$ configuration, but with much smaller angles i.e. ω (in Fig. 44(b)), than those in $\theta:2\theta$ diffraction [257]. A monochromatic X-ray beam irradiates a sample at an angle ω and the reflected intensity at an angle 2θ is recorded by a detector. The figure portrays reflection where the condition is satisfied with, $\omega = 2\theta/2$. As the operation mode is symmetric $\theta:2\theta$ mode, assuring the incident angle is half of the angle of diffraction. The reflection from surface and interfaces is due to the different electron densities in the different layers, which corresponds to different reflective indexes. For the angle of incidence θ below a critical angle, a total external reflection occurs. The density of the material is determined from the critical angle (θ_c). Above θ_c , the reflection from the interfaces interfere and give rise to interference fringes. The period of the interference fringes and the drop (slope) in the intensity are related to the thickness and the roughness of the layer(s) [257]. The typical range for these measurements are between 0° and 6° in θ , but can of course be analyzed further depending on the roughness of the structure.

4.2 Atomic Force Microscopy (AFM)

Atomic force microscope (AFM) is used to explore the surface topography including the surface roughness. The AFM employed in study is a Park System, PSIA XE-100, mounted over Table Stable, TS-155 and utilizes a Light Bank LS-F100HS for live imaging. The software used to examine the topographic images is a XEP 1.8.0 Data Acquisition Program and Gwyddion (32-bit) software.

AFM is kind of technique similar to that of scanning probe microscope, which is used to map the topography and to study the properties of material on a nanoscale, based on the interactions between a tip and a sample surface. AFM was first invented at IBM Zurich in 1986 by Gerd Binnig *et al.* [259], based on the principal of scanning tunneling microscope (already invented in 1981). In AFM the probing tip is a spring like cantilever with one end fixed and the other end having tip that interacts with the sample surface [259–262]. The tip that is attached to the free end of the cantilever comes in contact or close proximity of the sample surface, attractive and/ or repulsive forces as a consequence of interactions between the tip and the surface, causing either a negative or positive bending of the cantilever [262,263], thus giving topographic information of the sample. These phenomena can be attributed to basic types of working modes in AFM and is given by Pauli Exclusion Principle [263] in Fig. 45.

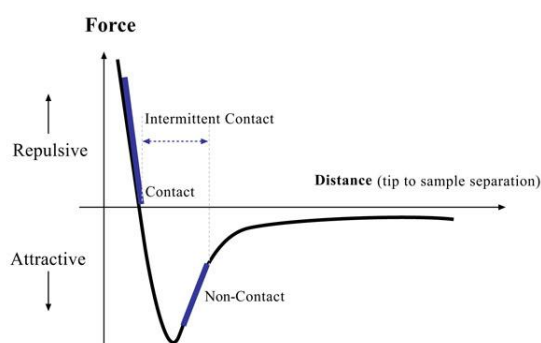


Figure 45. The relationship between force and distance. From Maghsoudy-Louyeh *et al.* [264]

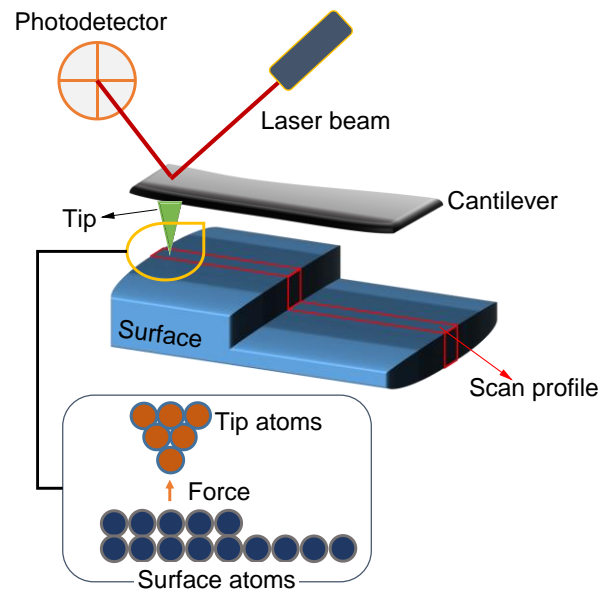


Figure 46. Schematic working principal of AFM.

As in AFM the cantilever can be thought of as a spring. In this case the force generated between the tip and the surface depends on the spring constant of the cantilever and the distance between the tip and the surface. Considering spring constant this force can be determined using Hooke's Law [262,263]:

$$F = k \cdot x \quad (12)$$

Where, F is force, k is the spring constant and x is the cantilever deflection. As the tip moves across the sample, it moves up and down relative to the sample. These fluctuations are governed by the interactions, for instance, as a result of electrostatic, magnetic, capillary, Van der Waals forces between the tip and the sample [265]. A sophisticated position detector monitors the displacement of the tip and a topographical image is obtained. **Fig. 46** shows the schematic of typical AFM working principle.

4.2.1 Working Modes

Contact mode (CM) - AFM

A Contact mode (CM) tip having a radius of < 10 nm, is employed for contact mode having a resonance frequency of 13 kHz. In CM-AFM, the probe is dragged while in contact, across the surface [262]. The tip-sample interacting forces are in the repulsive regime. In this mode the feedback loop keeps the deflection of the cantilever constantly at the set-point. This unchanged deflection can also be referred to as the equiforce mode [265]. As the tip scans across, any bend in the cantilever from surface topography, corresponds to a deflection of the probe tip in z -direction equal to z_d , relative to an un-deflected cantilever in its initial position. The motion of the z -scanner is directly proportional to the sample topography. Basic principle of CM-AFM is shown in **Fig. 47**.

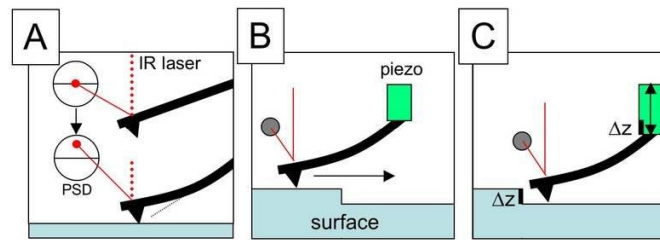


Figure 47. The working principle of AFM in contact mode, where the tip contacts the sample surface with a small cantilever deflection and the feedback loop keeps the deflection constant [266].

Tapping mode

For tapping mode Tap300Al-G tip is utilized having a resonance frequency of 300 kHz. In tapping mode, although the resolution of the image is similar to that of CM-AFM image, the applied forces between tip and sample are lower. Thus the problem of having high-lateral forces between the tip and surface can be solved by having the tip touch the surface only for a short time [262,263,265], thereby avoiding the issue of lateral forces and drag across the surface. Hence it is called tapping mode (Fig. 48). In this mode cantilever oscillates back and forth near its resonance frequency. While during oscillations, the tip makes contact with the surface for a very short duration in each oscillation cycle. A feedback loop provides the oscillation amplitude to remain constant during scan so that a constant tip-sample interaction is conserved during the scan [262].

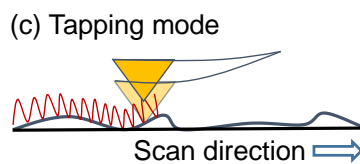


Figure 48. The Principle working mechanism of atomic force microscopy in tapping mode.

4.3 Scanning electron microscopy (SEM)

Electron microscopy

Electron microscopy is applied to get a topographic, cross-sectional and projection images of the fabricated structures, along with the elemental and structural determination. In this study Zeiss Supra 35 scanning electron microscope (SEM) and Jeol ARM 200F transmission electron microscopy (TEM) was utilized for structural and elemental analysis.

EM can be defined as a tool that uses beam of electrons to generate an image of a specimen [267]. In contrast, to optical microscope that uses visible light to illuminate sample and a series of optical lenses to magnify samples in the range approximately between 10 to 1,000 times their original sizes. EM needs to be operated in the vacuum and the electron beam is focused on to the sample and magnification of images is carried out via set of electromagnetic lenses. The EM has the advantage of using considerably much shorter wavelength of the electron (for instance, $\lambda = 0.005$ nm at a given accelerating voltage of ~ 50 kV) which for optical microscope when compared have visible light with $\lambda = 400$ nm to 700 nm [268]. In EM the resolution can be controlled by varying accelerating voltage, i.e. shorter wavelength is obtained via increasing the velocity of electrons, results in increased resolving power (accelerating voltage) [269].

The two principal types of EM techniques are:

- Scanning electron microscope (SEM)
- Transmission electron microscope (TEM)

Even though both were invented in the same decade, however, they differ fundamentally in their uses, magnification, working principal, and sample preparation techniques. In brief, SEM generates 3D image with the help of secondary electrons, while the TEM projects electrons through an ultrathin portion of the sample to produce a 2D image. A third and less used type is the scanning transmission electron microscope (STEM) which encompasses features of both SEM and TEM.

The basics of SEM

The SEM permits the observation of materials in macro and submicron ranges. The instrument is capable of generating three-dimensional images for analysis of topographic features. In the SEM, a beam of electrons is focused on a spot volume of the specimen, resulting in the transfer of energy to the spot. These bombarding electrons, also referred to as primary electrons, dislodge electrons from the specimen itself. These, dislodged electrons are known as secondary electrons (SE), are attracted and collected by a positively biased grid or detector, and then translated into a signal. To produce an SEM image, the electron beam is swept across the area being inspected, producing many such signals. These signals are then amplified, analyzed, and translated into images of the topography being inspected. Finally, the image is shown on a computer screen. The energy of the primary incident electrons determines the quantity of secondary electrons collected during inspection. The emission of SE from the specimen increases as the energy of the primary electron beam increases, until a certain limit is reached. Beyond this limit, the collected SEs diminish as the energy of the primary beam is increased. Further, this is because the primary electron beam is already activating electrons deep below the surface of the specimen. Electrons coming from such depths usually recombine before reaching the surface for emission. Aside from secondary electrons, the primary electron beam results in the emission of backscattered (or reflected) electrons (BE) from the specimen. BE possess more energy than SE, and have a definite direction. As such, they can not be collected by a secondary electron detector, unless the detector is directly in their path of travel. All electrons with energy above 50 eV are considered to be BE. Backscattered electron imaging is useful in distinguishing one material from another, since the yield of the collected backscattered electrons increases monotonically with the specimen's atomic number. Backscatter imaging can distinguish elements with atomic number differences of at least 3, i.e., materials with atomic number differences of at least 3 would appear with good contrast on the image.

Detection

For the SE detection the Everhart-Thornley detector is mainly used. The detector consist of a scintillator which is coated on the tip of the detector enclosed in a farad cage. A positive high voltage is applied to detector ($\sim 10\text{kV}$). The SE form the sample is attracted towards the high voltage and is then converted to light as they hit the scintillator. The light is then directed to a photomultiplier tube through a light guide passage. The light is then converted to electrons and are amplified as an electric signal [269,270]. To mention here the SE detector is placed at a certain angle on the side of the electron column in order to increase its efficiency. Moreover, an addition supplementary electrode is placed before the scintillator with a few hundred volts applied to it in order to help the scintillator acquire SE. A basic schematic of the detector is shown in [Fig. 50](#).

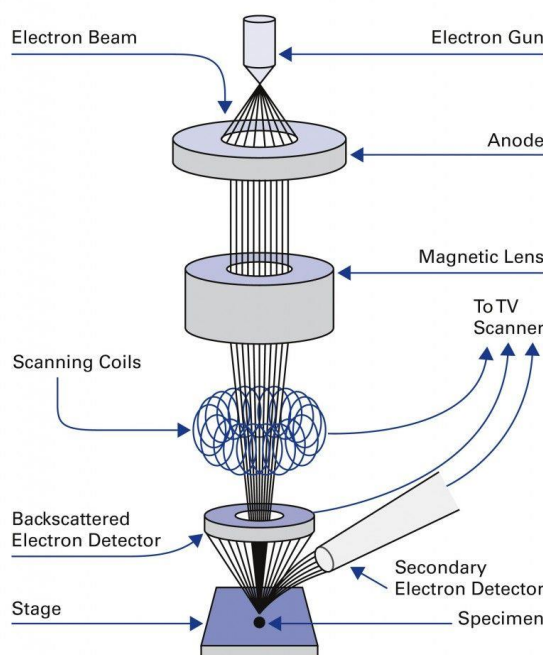


Figure 49. Basic construction of SEM.

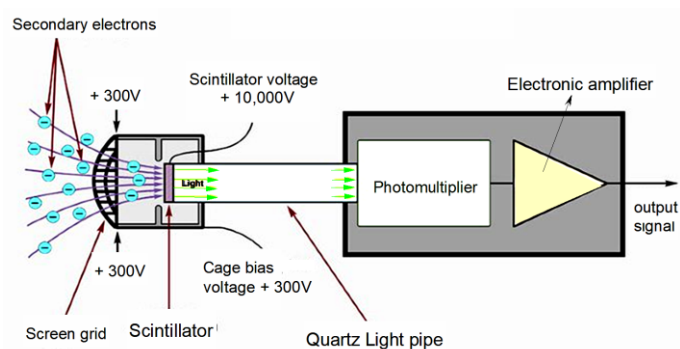


Figure 50. Construction of Everhart-Thorney (SE) detector [271].

4.4 Photocurrent (spectral) analysis

Photocurrent (PC) measurements were performed via homebuilt setup. The measurement setup consisted of Keithley 2400 source meter and Keithley 617 electrometer, Acton-SpectrPro 150 monochromator with 600–1400 nm wavelength range, cryostat with four optical windows and a QTH10 (/M) quartz tungsten-halogen lamp (50mW optical output power) as a light source and a set of quartz lenses to focus and guide the light beam.

The setup schematic description follows as: the light from the source first encounters a quartz lens, and then enters the monochromator. The monochromator is equipped with two windows, i.e. entrance and exit respectively, along with two grating slits of 600 mm/line and 1200 mm/line. The entrance window was outfitted with a custom built slot which can grip the bandpass filters OG500 or RG1000. The purpose of filters is to cancel the first and second derivative of the light. The light enters the monochromator through the lens system and filters and then it is guided through optics and gratings system before it exits from secondary window. The exit window is placed directly in contact with a custom-built black box equipped with a set of lenses, and a cryostat vacuum chamber. The cryostat chamber consist of a column quipped with a insulated sample stage, temperature controller (complemented

with a lake shore). The system can be cooled down via liquid Nitrogen down to 70 K. Photoconductivity measurements were performed in dc-regime at applied voltage between two parallel $2 \times 4 \text{ mm}^2$ coplanar Al contacts that are separated by 4 mm distance. The contacts were deposited with electron-beam evaporation. Two point contacts were than brought to contact with the Al-contacts. The points were connected with electrometer 617 and Kiethley 2400 as a gain and source meters respectively, via BNC-connectors. The monochromator, Kitehley electrometer and Lakeshore are connected with GiPIB interface to the system, which can be controlled via LabVIEW software.

The photocurrent spectra were acquired by subtracting the dark current from the spectra measured under illumination and then normalizing outcome to the spectral irradiation intensity of the light source. The setup is capable to go down to 77 K (as restricted by liquid N₂) and can apply bias up to 200 V, that is limited by Kiethly source meter 2400. Further, the step size (in nm) and the time per scan can be varied to a large degree but is restricted by the limitations of source meter as well.

Chapter 5

5 Summary of papers

Paper I: Enhanced photoconductivity of SiGe nanocrystals in SiO₂ driven by mild annealing

SiGe nanocrystals were obtained by annealing the structures (Si_p/SiO₂-buffer/SiO₂/SiGe/SiO₂) fabricated via rfMS method for short time, so as to avoid any degradation of optical properties of structure as a consequence of deterioration of structural or interface integrity. Moreover, an interesting lens-like formation of NCs was observed and was attributed to be due to competition between crystallization of the NCs and a resulting development of stress field in the structure. The structure showed an increased photoconductivity of more than an order magnitude higher compared to as-grown structures, with response threshold upto ~1200 nm.

Paper II: Enhanced photoconductivity of embedded SiGe nanoparticles by hydrogenation

In this study Si and Ge were co-deposited via dcMS and HiPIMS method respectively, in structure comprising of Si_p/SiO₂/SiGe/SiO₂. This approach of incorporating HiPIMS resulted in formation of SiGe nanocrystallites in as-grown state without the need of anneal treatment. The structures in as-grown state were exposed to hydrogen plasma for 10 min for several intervals. This resulted in an increased photoconductivity of an order magnitude higher than un-hydrogenated structures. The resultant enhancement in photoconductivity is attributed to neutralization of dangling bonds and passivation of non-radiative centers via chemical bonding of atomic hydrogen forming Si-H bonds, along with reduction in positive oxide charges and ordering of the amorphous oxide matrix along with improved interface quality.

Paper III: Efficacy of annealing and fabrication parameters on photo-response of SiGe in TiO₂ matrix

(TiO₂/SiGe/TiO₂)_n multilayer structures on a p-type Si substrate, were fabricated via dcMS method, and were annealed at 600 °C for 5 min. The aim of the study is to avoid formation of SiO₂ at the interface between TiO₂ and SiGe and/or phase separation and segregation of Ge from SiGe NCs, which is a commonly observed downside of annealing such structures, resulting in degradation of photoconductive properties. Mild annealing exposure of structures resulted in crystalline structure with SiGe NCs and anatase TiO₂ matrix. An increased photoconductivity of more than two order magnitude was attained without any formation of insulting SiO₂ layer, as evident by STEM elemental mapping and TEM analysis. Several spectral peaks obtained and were assigned to strain, interface related localized states, photoeffect from NCs and coupling effect from the Si substrate.

Paper IV: Fabrication and characterization of Si_{1-x}Ge_x nanocrystals in as-grown and annealed structures: A comparative study by hydrogenation

In this work the as-grown structures (having ~20 nm of SiGe layer thickness) from Paper II underwent rapid thermal annealing (550 – 900 °C for 1 min) in N₂ ambient atmosphere. An interesting periodically arranged columnar self-assembly of core-shell SiGe nanocrystals was observed as evident by TEM analysis. Such a columnar self-assembly of NCs was attributed to presence of nanocrystallites in as-grown structure which acts as a seed/ catalyst for heterogeneous nucleations, and that the use of HiPIMS method resulted in formation of strong wetting layer thus reducing the nucleation barrier. Further, for the periodicity, the crystallization process during annealing develops a stress field in the SiGe film plane, which is the anticipated reason for obtaining equidistant / quasiperiodic SiGe NCs arrangement. The SiGe NCs in such structures are stress-free in the normal direction on the film and have shown no internal defects. However the structure, with thicker SiGe layer of ~200 nm when annealed under similar conditions resulted in formation of planar sharing defects, stacking faults and microtwins in SiGe NCs. The photoconductivity in structures with 20 nm SiGe after increased by approximately an order magnitude higher with increased annealing temperature.

Paper V: Obtaining SiGe nano-crystallites between crystalline TiO₂ layers by HiPIMS without annealing

The work aims to fabricate anneal free crystalline TiO₂/SiGe/TiO₂ as-grown structures having SiGe NCs. For this purpose HiPIMS method was employed. A control over HiPIMS discharge parameters resulted have shown to obtain various crystalline polymorphous of TiO₂ i.e. either anatase, rutile or a mixture of both. Further, a control over the size of SiGe NCs have been demonstrated by varying repetition frequency in range of 300 to 650 Hz, and is also dependent on the oxide matrix enveloping the NCs i.e. the crystallinity of TiO₂. The as-grown structure having SiGe nanocrystallites sandwiched within either amorphous, anatase or rutile TiO₂ deposited via HiPIMS, were compared with already studied structures in paper III. The structure showed roughly 2-order magnitude increase in spectral intensity as compared to structure fabricated via dcMS method with subsequent anneal treatment.

Paper VI: SiGe nanocrystals in SiO₂ with high photosensitivity from VIS to SWIR

In this paper we study the films formed of SiGe NCs embedded in SiO₂ matrix with high photosensitivity in VIS-SWIR. For this purpose, structures with two different SiGe compositions (Si:Ge:SiO₂ of 25:25:50 – samples S1 and 5:45:50 – samples S2) were deposited by magnetron sputtering and then nanostructured by rapid thermal annealing at 700, 800 and 1000 °C for SiGe NCs formation in SiO₂ matrix. The influence of Si:Ge ratio and annealing temperature on the film morphology and structure is discussed. Also, the electrical and photoconductive properties at nanoscale are analyzed in relation with morphology and structure in order to find how they can be tuned. The structures annealed at 800 °C, resulted in an impressive photocurrent/dark current ratio of ~10 and ~10³. Moreover, the cutoff wavelengths are in SWIR: 1239 nm for sample S1 800 °C RTA measured at RT, and 1345 nm for S2 800 °C RTA also at RT extended to 1630 nm (S2, 100 K). The photoresponsivities (calculated for each photocurrent spectrum maximum) we achieved are 3.52 AW⁻¹ for sample S1 800 °C RTA, and 5.23 and 9.35 AW⁻¹ for sample S2 800 °C RTA, measured at RT and 100 K, respectively. Furthermore, interesting morphological changes in structures were observed depending on composition and RTA temperature and are discussed in detail for their origin and effect over the spectral response. These films have a great potential to be used in discrete optical sensors or integrated photodetectors including their integration with other materials in hybrid devices.

Paper VII: Structural and photoluminescence study of self-assembled Si_{1-x}Ge_x nanoislands over HiPIMS sputtered TiO₂ layer

We study the surface morphology and growth process of SiGe nanoislands under varying anneal parameters (i.e. 500 to 750 °C for 30 min to 20 hr) over the TiO₂ films (either in as-grown or annealed state) being deposited over Si (001) substrate. Atomic force and scanning electron microscopy revealed the formation of SiGe nanoislands over the TiO₂ films, along with the structural analysis investigated via grazing incidence X-ray diffraction. It is found that polycrystalline TiO₂ facilitates the formation of nanoislands preferably along the grain boundaries due to their higher interfacial energy as compared to as-grown TiO₂, that result in random distribution of nanoislands across film area. Further, it was evaluated that the size of nanoislands increases with increase in anneal time which then starts to collapse forming porous SiGe layer and later resulting in melting of SiGe film. Photoluminescence study have been performed over structures from room temperature down to 20 K to detect the light emission and further to validate origin of the obtained peaks, respectively.

Some part of the manuscript has been discussed in section 2.4, dealing with formation of nanoislands over Si(001) substrate. While the mentioned manuscript mainly deals with formation of nanoislands over oxide surface, which follows Volmer-Weber growth mode, contrary to that of Stranski–Krastanov growth mode for nanoislands over Si(001) substrate.

Chapter 6

6 Summary

In summary, the work incorporates fabrication of structure having SiGe NCs sandwiched between either SiO₂ or TiO₂ matrix. Various magnetron sputtering methods i.e. rfMS, dcMS and HiPIMS, in conjunction with subsequent anneal parameters and/or hydrogen plasma treatment were employed. A systematic evaluation and control of parameters for respective sputter plasma discharge, consequent anneal treatment, and hydrogen plasma treatment was carried out, in order to increase the photocurrent intensity with increased spectral response in NIR regime. Initially the structural analysis of the structures were characterized and discussed in light of GiXRD, XRR, TEM, SEM, EDX, STEM and AFM analysis. Later the electrical and spectral analysis over the structure were made. The photocurrent spectra was de-convoluted and the obtained peaks were assigned to be due to strain, interface related localized states, photoeffect from the NCs and to coupling effect from the Si-substrate, respectively. The highlights of the results obtained includes, how the high temperature annealing or longer annealing time can be replaced in creating anneal free crystalline structures. Initially a control over anneal parameters was made by lowering the temperature and time (minimum upto 1 min in CFA and 15 sec in RTA), resulting in increased photoconductivity of structures more than 2 order magnitude higher than that obtained via high temperature annealing, with wider range of spectra response.

Later the structure fabricated via incorporation of HiPIMS in conjunction with dcMS method, that resulted in SiGe NCs in as-grown structures and crystalline a TiO₂ matrix when sputtered via HiPIMS method. An increase in spectral intensity of few order magnitude higher was attained for such structures, as compared to those deposited via dcMS and rfMS method alone, which needs to be anneal treated.

Additionally structures fabricated via incorporation of HiPIMS method, was further exposed to hydrogen plasma treatment and/or annealed at varying temperature in order to exploit the effect of respective methods in increasing the spectral sensitivity (intensity). The exposure of structures (either in as-grown or annealed states) to hydrogen plasma treatment resulted in neutralization of dangling bonds and to passivation of nonradiative defects in the oxide matrix and at SiGe/ matrix interfaces, resulting in approximately an increased photocurrent intensity of more than an order magnitude, without altering the size of NCs. The exposure of structures to anneal treatment procedures resulted in an interesting periodically arranged columnar core-shell self-organized NCs. Such self-organization of NCs was attributed to be due to heterogeneous nucleation as a dominant process for the crystallization of already present nuclei in as-grown state which may have acted as seed crystals, rather than conventional homogenous nucleation. Furthermore, utilizing the HiPIMS method resulted in formation of a better wetting of SiGe layer, which in turn reduces the free energy of change and thus the nucleation barrier. Additionally, the SiGe NCs are ~20 nm long (oriented perpendicular to the SiGe film) and ~7 – 8 nm large. In fact, we have not classical core-shell NCs, but a Ge-rich Si_{1-x}Ge_x core surrounded by a shell of crystalline Si in amorphous SiGeO, making them more interesting. During the crystallization process (NCs formation) we have a

self-organization (self-assembling) of the SiGe nuclei due to the stress field developed in the film. This is the anticipated reason for the periodicity (quite equal distances between) of SiGe NCs. The crystallization process during annealing develops a stress field in the SiGe film plane that is the key factor for obtaining equidistant / quasiperiodic SiGe NCs arrangement. The SiGe NCs are stress-free in the normal direction on the film and show no internal defect.

Bibliography

- [1] Aqua J N, Berbezier I, Favre L, Frisch T and Ronda A 2013 Growth and self-organization of SiGe nanostructures *Phys. Rep.* **522** 59–189
- [2] Haddara Y.M., Ashburn P., Bagnall D.M. (2017) Silicon-Germanium: Properties, Growth and Applications. In: Kasap S., Capper P. (eds) Springer Handbook of Electronic and Photonic Materials. Springer Handbooks. Springer, Cham
- [3] Ye H and Yu J 2014 Germanium epitaxy on silicon *Sci. Technol. Adv. Mater.* **15** 024601
- [4] Long E S 2013 *Nanostructuring and Ge redistribution in thin films of Silicon-Germanium by thermal oxidation* (PhD thesis) University of Oslo, Norway
- [5] Berbezier I, Ronda A and Portavoce A 2002 SiGe nanostructures: new insights into growth processes *J. Phys. Condens. Matter* **14** 8283–331
- [6] Berbezier I and Ronda A 2009 SiGe nanostructures *Surf. Sci. Rep.* **64** 47-98
- [7] Zhang B, Yao Y, Patterson R, Shrestha S, Green M A and Conibeer G 2011 Electrical properties of conductive Ge nanocrystal thin films fabricated by low temperature in situ growth *Nanotechnology* **22** 125204
- [8] Tzeng S S and Li P W 2008 Enhanced 400–600 nm photoresponsivity of metal–oxide–semiconductor diodes with multi-stack germanium quantum dots *Nanotechnology* **19** 235203
- [9] Sood A K, Zeller J W, Richwine R A, Puri Y R, Efstathiadis H, Haldar P, Dhar N K and Polla D L 2015 SiGe based visible-NIR photodetector technology for optoelectronic applications, in *Advances in Optical Fiber Technology: Fundamental Optical Phenomena and Applications* ed M Yasin (InTech)
- [10] Liu P, Cosentino S, Le S T, Lee S, Paine D, Zaslavsky A, Pacifici D, Mirabella S, Miritello M, Crupi I and Terrasi A 2012 Transient photoresponse and incident power dependence of high-efficiency germanium quantum dot photodetectors *J. Appl. Phys.* **112** 083103
- [11] Church C P, Muthuswamy E, Zhai G, Kauzlarich S M and Carter S A 2013 Quantum dot Ge/TiO₂ heterojunction photoconductor fabrication and performance *Appl. Phys. Lett.* **103** 223506
- [12] Pethuraja G G, Welser R E, Sood A K, Lee C, Alexander N J, Efstathiadis H, Haldar P and Harvey J L 2012 Effect of Ge incorporation on bandgap and photosensitivity of amorphous SiGe thin films *Mater. Sci. Appl.* **03** 67–71
- [13] Tshikiyo K, Tokunaga M, Takeoka S, Fujii M and Hayashi S 2001 Electron spin resonance study of defects in Si_{1-x}Ge_x alloy nanocrystals embedded in SiO₂ matrices: Mechanism of luminescence quenching *J. Appl. Phys.* **89** 4917–20
- [14] Granitzer P and Rumpf K 2014 *Nanostructured Semiconductors: From Basic Research to Applications* Pan Stanford Publishing (Jenny Stanford Publishing, New York)
- [15] Vázquez-Valerdi D E, Luna-López J A, Carrillo-López J, García-Salgado G, Benítez-Lara A and Espinosa-Torres N D 2014 Compositional and optical properties of SiO_x films and (SiO_x/SiO_y) junctions deposited by HFCVD *Nanoscale Res. Lett.* **9** 422

- [16] Houssa M, Pourtois G, Meuris M, Heyns M M, Afanas'ev V V and Stesmans A 2011 Experimental and theoretical investigation of defects at (100) Si_{1-x}Ge_x/oxide interfaces *Microelectron. Eng.* **88** 383–7
- [17] Vieira E M F, Toudert J, Rolo A G, Parisini A, Leitão J P, Correia M R, Franco N, Alves E, Chahboun A, Martín-Sánchez J, Serna R and Gomes M J M 2017 SiGe layer thickness effect on the structural and optical properties of well-organized SiGe/SiO₂ multilayers *Nanotechnology* **28** 345701
- [18] Ye H and Yu J 2014 Germanium epitaxy on silicon *Sci. Technol. Adv. Mater.* **15** 024601
- [19] Zatyrb G, Misiewicz J, Wilson P R J, Wojcik J, Mascher P and Podhorodecki A 2014 Stress transition from compressive to tensile for silicon nanocrystals embedded in amorphous silica matrix *Thin Solid Films* **571** 18–22
- [20] Bahariqushchi R, Raciti R, Kasapoğlu A E, Gür E, Sezen M, Kalay E, Mirabella S and Aydinli A 2018 Stress evolution of Ge nanocrystals in dielectric matrices *Nanotechnology* **29** 185704
- [21] Zatyrb G, Podhorodecki A, Misiewicz J, Cardin J and Gourbilleau F 2013 Correlation between matrix structural order and compressive stress exerted on silicon nanocrystals embedded in silicon-rich silicon oxide thesis *Nanoscale Res. Lett.* **8** 40
- [22] Lepadatu A-M, Stavarache I, Stoica T F and Ciurea M L 2011 Study of Ge nanoparticles embedded in an amorphous SiO₂ matrix with photoconductive properties *Dig. J. Nanomater. Biostructures* **6** 67–73
- [23] Lepadatu A-M, Stoica T, Stavarache I, Teodorescu V S, Buca D and Ciurea M L 2013 Dense Ge nanocrystal layers embedded in oxide obtained by controlling the diffusion–crystallization process *J. Nanoparticle Res.* **15** 1981
- [24] Stavarache I, Lepadatu A-M, Stoica T and Ciurea M L 2013 Annealing temperature effect on structure and electrical properties of films formed of Ge nanoparticles in SiO₂ *Appl. Surf. Sci.* **285** 175–9
- [25] Choi W ., Kanakaraju S, Shen Z . and Li W . 1999 Characterization of Ge nanocrystals in a-SiO₂ synthesized by rapid thermal annealing *Appl. Surf. Sci.* **144–145** 697–701
- [26] Jie Y X, Wu X, Huan C H A, Wee A T S, Guo Y, Zhang T J, Pan J S, Chai J and Chua S J 1999 Synthesis and characterization of Ge nanocrystals immersed in amorphous SiO_x matrix *Surf. Interface Anal.* **28** 195–9
- [27] Dasović J, Dubček P, Pucić I, Bernstorff S, Radić N and Pivac B 2017 The interface quality of Ge nanoparticles grown in thick silica matrix *Appl. Surf. Sci.* **414** 1–7
- [28] Sultan M T, Gudmundsson J T, Manolescu A, Stoica T, Ciurea M L and Svavarsson H G 2019 Enhanced photoconductivity of embedded SiGe nanoparticles by hydrogenation *Appl. Surf. Sci.* **479** 403–9
- [29] Sultan M T, Manolescu A, Gudmundsson J T, Torfason K, Alexandru Nemnes G, Stavarache I, Logofatu C, Teodorescu V S, Ciurea M L and Svavarsson H G 2019 Enhanced photoconductivity of SiGe nanocrystals in SiO₂ driven by mild annealing *Appl. Surf. Sci.* **469** 870–8
- [30] Vieira E M F, Pinto S R C, Levichev S, Rolo A G, Chahboun A, Buljan M, Barradas N P, Alves E, Bernstorff S, Conde O and Gomes M J M 2011 Influence of the deposition parameters on the growth of SiGe nanocrystals embedded in Al₂O₃ matrix *Microelectron. Eng.* **88** 509–13

- [31] Ray S K, Das S, Singha R K, Manna S and Dhar A 2011 Structural and optical properties of germanium nanostructures on Si(100) and embedded in high-k oxides *Nanoscale Res. Lett.* **6** 224
- [32] Lepadatu A-M, Slav A, Palade C, Dascalescu I, Enculescu M, Iftimie S, Lazanu S, Teodorescu V S, Ciurea M L and Stoica T 2018 Dense Ge nanocrystals embedded in TiO₂ with exponentially increased photoconduction by field effect *Sci. Rep.* **8** 4898
- [33] Dalapati G K, Chatterjee S, Samanta S K and Maiti C K 2003 Electrical characterization of low temperature deposited TiO₂ films on strained-SiGe layers *Appl. Surf. Sci.* **210** 249–54
- [34] Khan A F, Mehmood M, Ali T and Fayaz H 2013 Structural and optical studies of nanostructured TiO₂-Ge multi-layer thin films *Thin Solid Films* **536** 220–8
- [35] Ibrahim A S, Khan A F, Binti B and Razak A 2014 Ge/TiO₂ composite thin films prepared by RF magnetron sputtering for Photovoltaic Applications 3rd IET International Conference on Clean Energy and Technology (CEAT) 2014, Kuching, 1-5.
- [36] Sultan M T, Gudmundsson J T, Manolescu A, Teodorescu V S, Ciurea M L and Svavarsson H G 2019 Efficacy of annealing and fabrication parameters on photo-response of SiGe in TiO₂ matrix *Nanotechnology* **30** 365604
- [37] Barradas N P, Alves E, Vieira E M F, Parisini A, Conde O, Martín-Sánchez J, Rolo A G, Chahboun A and Gomes M J M 2014 IBA study of SiGe/SiO₂ nanostructured multilayers *Nucl. Instruments Methods Phys. Res. Sect. B Beam Interact. with Mater. Atoms* **331** 89–92
- [38] Sarakinos K, Alami J and Wuttig M 2007 Process characteristics and film properties upon growth of TiO_x films by high power pulsed magnetron sputtering *J. Phys. D: Appl. Phys.* **40** 2108–14
- [39] Hanaor D A H and Sorrell C C 2011 Review of the anatase to rutile phase transformation *J. Mater. Sci.* **46** 855–74
- [40] Jia J, Mu L, Lin Y and Zhou X 2018 Rutile versus anatase for quantum dot sensitized solar cell *Electrochim. Acta* **266** 103–9
- [41] Schönberger W, Bartzsch H, Schippel S and Bachmann T 2016 Deposition of rutile TiO₂ films by pulsed and high power pulsed magnetron sputtering *Surf. Coatings Technol.* **293** 16–20
- [42] Löbl P, Huppertz M and Mergel D 1994 Nucleation and growth in TiO₂ films prepared by sputtering and evaporation *Thin Solid Films* **251** 72–9
- [43] Cemin F, Tsukamoto M, Keraudy J, Antunes V G, Helmersson U, Alvarez F, Minea T and Lundin D 2018 Low-energy ion irradiation in HiPIMS to enable anatase TiO₂ selective growth *J. Phys. D: Appl. Phys.* **51** 235301
- [44] Connelly K, Wahab A K and Idriss H 2012 Photoreaction of Au/TiO₂ for hydrogen production from renewables: a review on the synergistic effect between anatase and rutile phases of TiO₂ *Mater. Renew. Sustain. Energy* **1** 3
- [45] Luttrell T, Halpegamage S, Tao J, Kramer A, Sutter E and Batzill M 2015 Why is anatase a better photocatalyst than rutile? Model studies on epitaxial TiO₂ films *Sci. Rep.* **4** 4043

- [46] Yamada Y and Kanemitsu Y 2012 Determination of electron and hole lifetimes of rutile and anatase TiO₂ single crystals *Appl. Phys. Lett.* **101** 133907
- [47] Agnarsson B, Magnus F, Tryggvason T K, Ingason A S, Leosson K, Olafsson S and Gudmundsson J T 2013 Rutile TiO₂ thin films grown by reactive high power impulse magnetron sputtering *Thin Solid Films* **545** 445–50
- [48] Wiggins M D, Nelson M C and Aita C R 1996 Phase development in sputter deposited titanium dioxide *J. Vac. Sci. Technol. A Vacuum, Surfaces, Film.* **14** 772–6
- [49] Rafieian D, Ogieglo W, Savenije T and Lammertink R G H 2015 Controlled formation of anatase and rutile TiO₂ thin films by reactive magnetron sputtering *AIP Adv.* **5** 097168
- [50] Nair P B, Justinictor V B, Daniel G P, Joy K, James Raju K C, Devraj Kumar D and Thomas P V 2014 Optical parameters induced by phase transformation in RF magnetron sputtered TiO₂ nanostructured thin films *Prog. Nat. Sci. Mater. Int.* **24** 218–25
- [51] Pinto S R C, Kashtiban R J, Rolo A G, Buljan M, Chahboun A, Bangert U, Barradas N P, Alves E and Gomes M J M 2010 Structural study of Si_{1-x}Ge_x nanocrystals embedded in SiO₂ films *Thin Solid Films* **518** 2569–72
- [52] Abd Rahim A F, Hashim M R, Ali N K, Rusop M, Johan Ooi M D and Yusoff M Z M 2013 Self-assembled Ge islands and nanocrystals by RF magnetron sputtering and rapid thermal processing: The role of annealing temperature *Appl. Surf. Sci.* **275** 193–200
- [53] Ray S K and Das K 2005 Luminescence characteristics of Ge nanocrystals embedded in SiO₂ matrix *Opt. Mater. (Amst).* **27** 948–52
- [54] Mogaddam N A P, Alagoz A S, Yerci S, Turan R, Foss S and Finstad T G 2008 Phase separation in SiGe nanocrystals embedded in SiO₂ matrix during high temperature annealing *J. Appl. Phys.* **104** 124309
- [55] Zschintzsch M, Sahle C J, Borany J von, Sternemann C, Mücklich A, Nyrow A, Schwamberger A and Tolan M 2011 Ge-Si-O phase separation and Ge nanocrystal growth in Ge:SiO_(x)/SiO₍₂₎ multilayers—a new dc magnetron approach *Nanotechnology* **22** 485303
- [56] Wang X X, Zhang J G, Ding L, Cheng B W, Ge W K, Yu J Z and Wang Q M 2005 Origin and evolution of photoluminescence from Si nanocrystals embedded in a SiO₂ matrix *Phys. Rev. B* **72** 195313
- [57] Tuğay E and Turan R 2016 Investigation of Photoluminescence Mechanisms from SiO₂/Si:SiO₂/SiO₂ Structures in Weak Quantum Confined Regime by Deconvolution of Photoluminescence Spectra *J. Nanosci. Nanotechnol.* **16** 4052–64
- [58] Tuğay E, Ilday S, Turan R and Finstad T G 2014 Influence of Ge content and annealing conditions on the PL properties of nc-Si_{1-x}Ge_x embedded in SiO₂ matrix in weak quantum confined regime *J. Lumin.* **155** 170–9
- [59] Nayak D K, Kamjoo K, Park J S, Woo J C S and Wang K L 1992 Rapid isothermal processing of strained GeSi layers *IEEE Trans. Electron Devices* **39** 56–63
- [60] Ditchfield R and Seebauer E G 1998 Beyond Thermal Budget: Using D·t In Kinetic Optimization Of RTP *MRS Proc.* **525** 57-62
- [61] Hiller D, Goetze S and Zacharias M 2011 Rapid thermal annealing of size-controlled Si nanocrystals: Dependence of interface defect density on thermal budget *J. Appl. Phys.* **109** 054308

- [62] Hiller D, Gutsch S, Hartel A M, Löper P, Gebel T and Zacharias M 2014 A low thermal impact annealing process for SiO₂-embedded Si nanocrystals with optimized interface quality *J. Appl. Phys.* **115** 134311
- [63] Kepa J, Stesmans A and Afanas'ev V V 2014 Comparative analysis of thermally induced degradation of condensation-grown (1 0 0) Ge_{0.75}Si_{0.25}/SiO₂ interfaces by electron spin resonance *Appl. Surf. Sci.* **291** 20–4
- [64] Madia O, Nguyen A P D, Thoan N H, Afanas'ev V, Stesmans A, Souriau L, Slotte J and Tuomisto F 2014 Impact of strain on the passivation efficiency of Ge dangling bond interface defects in condensation grown SiO₂/Ge_xSi_{1-x}/SiO₂/(100)Si structures with nm-thin Ge_xSi_{1-x} layers *Appl. Surf. Sci.* **291** 11–5
- [65] Tsetseris L and Pantelides S T 2011 Defect formation and annihilation at interfaces *Microelectron. Eng.* **88** 395–8
- [66] Yu H, Zeng J-Q and Qiu Z-R 2011 Silicon nanocrystals *Crystalline Silicon - Properties and Uses* Ed. S Basu (InTech, Croatia)
- [67] Sood A K, Zeller J W, Richwine R A, Puri Y R, Efstathiadis H, Haldar P, Dhar N K and Polla D L 2015 SiGe based visible-NIR photodetector technology for optoelectronic applications *Advances in Optical Fiber Technology: Fundamental Optical Phenomena and Applications* ed M Yasin (InTech)
- [68] Canham L T 1990 Silicon quantum wire array fabrication by electrochemical and chemical dissolution of wafers *Appl. Phys. Lett.* **57** 1046–8
- [69] Schneider C, Höfling S and Forchel A 2012 *Growth of III–V semiconductor quantum dots* in QUANTUM DOTS: Optics, Electron Transport And Future Applications ed Tartakovskii A (Cambridge University Press, United Kingdom)
- [70] Bukowski T J and Simmons J H 2002 Quantum Dot Research: Current State and Future Prospects *Crit. Rev. Solid State Mater. Sci.* **27** 119–42
- [71] Myronov M (2019) Nano-Silicon Group Available at : <https://warwick.ac.uk/fac/sci/physics/research/condensedmatt/silicon/> (Accessed: August 2019)
- [72] Halperin W P 1986 Quantum size effects in metal particles *Rev. Mod. Phys.* **58** 533–606
- [73] Henglein A 1995 Electronics of Colloidal Nanometer Particles *Berichte der Bunsengesellschaft für Phys. Chemie* **99** 903–13
- [74] Link S and El-Sayed M A 1999 Size and Temperature Dependence of the Plasmon Absorption of Colloidal Gold Nanoparticles *J. Phys. Chem. B* **103** 4212–4217
- [75] Alivisatos A P 1996 Semiconductor Clusters, Nanocrystals, and Quantum Dots *Science* **271** 933–7
- [76] Shang X-J 2012 *Study of quantum dots on solar energy applications* (PhD thesis) Royal Institute of Technology, Stockholm, Sweden
- [77] Brazis P W 2017 Quantum dots and their potential impact on lighting and display applications (2017) Available at: <https://legacy-uploads.ul.com/wp-content/uploads/sites/40/2017/07/UL-Quantum-Dots-White-Paper.pdf> (Accessed: August 2019)

- [78] Bukowski T J 2002 *The optical and photoconductive response in germanium quantum dots and indium tin oxide composite thin film structures* (PhD thesis) University of Florida, Gainesville, Florida, US
- [79] Hojabri A Synthesis and characterization of Germanium quantum dots for thermoelectric applications (Master thesis) Royal Institute of Technology (KTH), Stockholm, Sweden
- [80] Joseph Simmons and Kelly S. Potter 2000 *Optical materials* (Academic Press, San Diego, California)
- [81] Cullis A G and Canham L T 1991 Visible light emission due to quantum size effects in highly porous crystalline silicon *Nature* **353** 335–8
- [82] Cullis A G, Canham L T and Calcott P D J 1998 The structural and luminescence properties of porous silicon *J. Appl. Phys.* **82** 909
- [83] Scardera G, Puzzer T, Perez-Wurfl I and Conibeer G 2008 The effects of annealing temperature on the photoluminescence from silicon nitride multilayer structures *J. Cryst. Growth* **310** 3680–4
- [84] Pavesi L, Dal Negro L, Mazzoleni C, Franzò G and Priolo F 2000 Optical gain in silicon nanocrystals *Nature* **408** 440–4
- [85] Orbons S M, Spooner M G and Elliman R G 2004 Effect of material structure on photoluminescence spectra from silicon nanocrystals *J. Appl. Phys.* **96** 4650–2
- [86] Abdul-Ameer N M, Abdulrida M C, Abdul-Ameer N M and Abdulrida M C 2011 Direct Optical Energy Gap in Amorphous Silicon Quantum Dots *J. Mod. Phys.* **02** 1530–7
- [87] Karbassian F, Rajabali S, Mohajerzadeh S and Talei R 2013 Room temperature multilayer luminescent silicon nanocrystals *Sci. Iran.* **20** 1063–6
- [88] Dan'ko V A, Zlobin S O, Indutnyi I Z, Lisovskyy I P, Litovchenko V G, Mikhailovskaya E V., Shepelyavyi P E and Begun E V. 2016 Properties of Si quantum dot/SiO_x porous film structures synthesized using hydrogen fluoride technology *Mod. Electron. Mater.* **1** 16-21
- [89] López-Vidrier J, Hernández S, Hiller D, Gutsch S, López-Conesa L, Estradé S, Peiró F, Zacharias M and Garrido B 2014 Annealing temperature and barrier thickness effect on the structural and optical properties of silicon nanocrystals/SiO₂ superlattices *J. Appl. Phys.* **116** 133505
- [90] Nikitin T and Khriachtchev L 2015 Optical and Structural Properties of Si Nanocrystals in SiO₂ Films *Nanomaterials* **5** 614–55
- [91] Gardelis S, Nassiopoulou A G, Manousiadis P, Milita S, Gkanatsiou A, Frangis N and Lioutas C B 2012 Structural and optical characterization of two-dimensional arrays of Si nanocrystals embedded in SiO₂ for photovoltaic applications *J. Appl. Phys.* **111** 083536
- [92] Hao X J, Podhorodecki A P, Shen Y S, Zatoryb G, Misiewicz J and Green M A 2009 Effects of Si-rich oxide layer stoichiometry on the structural and optical properties of Si-QD/ SiO₂ multilayer films thesis *Nanotechnology* **20** 485703
- [93] Riabinina D, Durand C, Margot J, Chaker M, Botton G A and Rosei F 2006 Nucleation and growth of Si nanocrystals in an amorphous SiO₂ matrix *Phys. Rev. B* **74** 075334
- [94] Ding L, Chen T P, Liu Y, Ng C Y and Fung S 2005 Optical properties of silicon

- nanocrystals embedded in SiO₂ matrix *Phys. Rev. B* **72** 125419
- [95] Liu Y, Chen T P, Ding L, Zhang S, Fu Y Q and Fung S 2006 Charging mechanism in a SiO₂ matrix embedded with Si nanocrystals *J. Appl. Phys.* **100** 096111
- [96] Sadeghi H, Zolanvar A, Ranjgar A and Norouzi R 2014 Effective permittivity and refractive index of TiO₂/Ge and SiO₂/Ge nanostructures at high frequencies *J. Electron. Mater.* **43** 4294–300
- [97] Khan M I, Bhatti K A, Qindeel R, Althobaiti H S and Alonizan N 2017 Structural, electrical and optical properties of multilayer TiO₂ thin films deposited by sol–gel spin coating *Results Phys.* **7** 1437–9
- [98] Kim S-K, Kim B-H, Cho C-H and Park S-J 2009 Size-dependent photocurrent of photodetectors with silicon nanocrystals *Appl. Phys. Lett.* **94** 183106
- [99] López-Vidrier J, Hernández S, Hiller D, Gutsch S, López-Conesa L, Estradé S, Peiró F, Zacharias M and Garrido B 2014 Annealing temperature and barrier thickness effect on the structural and optical properties of silicon nanocrystals/SiO₂ superlattices *J. Appl. Phys.* **116** 133505
- [100] Kole A and Chaudhuri P 2014 Growth of silicon quantum dots by oxidation of the silicon nanocrystals embedded within silicon carbide matrix *AIP Adv.* **4** 107106
- [101] Nayfeh M H, Rao S, Nayfeh O M, Smith A and Therrien J 2005 UV photodetectors with thin-film Si nanoparticle active medium *IEEE Trans. Nanotechnol.* **4** 660–8
- [102] Shieh J-M, Lai Y-F, Ni W-X, Kuo H-C, Fang C-Y, Huang J Y and Pan C-L 2007 Enhanced photoresponse of a metal-oxide-semiconductor photodetector with silicon nanocrystals embedded in the oxide layer *Cit. Appl. Phys. Lett.* **90** 51105
- [103] Haller E E 2006 Germanium: From its discovery to SiGe devices *Mater. Sci. Semicond. Process.* **9** 408–22
- [104] Long E, Azarov A, Kløw F, Galeckas A, Yu Kuznetsov A and Diplas S 2012 Ge redistribution in SiO₂/SiGe structures under thermal oxidation: Dynamics and predictions *J. Appl. Phys.* **111** 024308
- [105] Zhang M, Cai R, Zhang Y, Wang C, Wang Y, Ross G G and Barba D 2014 Evolution of microstructural defects with strain effects in germanium nanocrystals synthesized at different annealing temperatures *Mater. Charact.* **93** 1–9
- [106] Rebohle L, von Borany J, Yankov R A, Skorupa W, Tyschenko I E, Fröb H and Leo K 1997 Strong blue and violet photoluminescence and electroluminescence from germanium-implanted and silicon-implanted silicon-dioxide layers *Appl. Phys. Lett.* **71** 2809–11
- [107] Bregolin F L, Behar M, Sias U S and Moreira E C 2009 Photoluminescence induced from hot Ge implantation into SiO₂ *Nucl. Instruments Methods Phys. Res. Sect. B Beam Interact. with Mater. Atoms* **267** 1321–3
- [108] Maeda Y, Tsukamoto N, Yazawa Y, Kanemitsu Y and Masumoto Y 1991 Visible photoluminescence of Ge microcrystals embedded in SiO₂ glassy matrices *Appl. Phys. Lett.* **59** 3168–70
- [109] Kanemitsu Y, Uto H, Masumoto Y and Maeda Y 1992 On the origin of visible photoluminescence in nanometer-size Ge crystallites *Appl. Phys. Lett.* **61** 2187–9
- [110] Kamata Y 2008 High-k/Ge MOSFETs for future nanoelectronics *Mater. Today* **11** 30–

- [111] Liao P H, Peng K P, Lin H C, George T and Li P W 2018 Single-fabrication-step Ge nanosphere/SiO₂/SiGe heterostructures: a key enabler for realizing Ge MOS devices thesis *Nanotechnology* **29** 205601
- [112] Liu C W and Chen L J 2004 SiGe/Si Heterostructures *Encyclopedia of Nanoscience and Nanotechnology* **9** 775-792(18)
- [113] Paul D J 2017 Si/SiGe heterostructures in *nanoelectronics Oxford Handbook of Nanoscience and Technology* (Applications vol 3) ed A V Narlikar and Y Y Fu (Oxford University Press)
- [114] Matthews J W and Blakeslee A E 1974 Defects in epitaxial multilayers *J. Cryst. Growth* **27** 118–25
- [115] Matthews J W and Blakeslee A E 1976 Defects in epitaxial multilayers. III. Preparation of almost perfect multilayers *J. Cryst. Growth* **32** 265-273
- [116] People R and Bean J C 1985 Calculation of critical layer thickness versus lattice mismatch for Ge_xSi_{1-x}/Si strained-layer heterostructures *Appl. Phys. Lett.* **47** 322-324
- [117] Liu J L, Wan J, Wang K L and Yu D P 2003 Critical thickness of self-assembled Ge quantum dot superlattices *J. Cryst. Growth* **251** 666–9
- [118] Peng X-H, Alizadeh A, Bhate N, Varanasi K K, Kumar S K and Nayak S K 2007 First-principles investigation of strain effects on the energy gaps in silicon nanoclusters *J. Phys. Condens. Matter* **19** 266212
- [119] Sun Y, Thompson S E and Nishida T 2007 Physics of strain effects in semiconductors and metal-oxide-semiconductor field-effect transistors thesis *J. Appl. Phys.* **101** 104503
- [120] King W D, Boxall D L and Lukehart C M 1997 Nanoclusters of Silicon and Germanium *J. Clust. Sci.* **8** 267–292
- [121] Henglein A 1989 Small-Particle Research: Physicochemical Properties of Extremely Small Colloidal Metal and Semiconductor Particles *Chem. Rev.* **89** 1861-1873
- [122] Stavarache I, Maraloiu V A, Negriila C, Prepelita P, Gruia I and Iordache G 2017 Photo-sensitive Ge nanocrystal based films controlled by substrate deposition temperature *Semicond. Sci. Technol.* **32** 105003
- [123] Foss S, Finstad T G, Dana A and Aydinli A 2007 Growth of Ge nanoparticles on SiO₂/Si interfaces during annealing of plasma enhanced chemical vapor deposited thin films *Thin Solid Films* **515** 6381-6384
- [124] Balakumar S, Peng S, Hoe K M, Agarwal A, Lo G Q, Kumar R, Balasubramanian N, Kwong D L and Tripathy S 2007 SiGeO layer formation mechanism at the SiGe/oxide interfaces during Ge condensation *Appl. Phys. Lett.* **90** 032111
- [125] Voigtländer B 2001 Fundamental processes in Si/Si and Ge/Si epitaxy studied by scanning tunneling microscopy during growth *Surf. Sci. Rep.* **43** 127-254
- [126] Abstreiter G, Schittenhelm P, Engel C, Silveira E, Zrenner A, Meertens D and Jäger W 1999 Growth and characterization of self-assembled Ge-rich islands on Si *Semicond. Sci. Technol.* **11** 1521–8
- [127] Samavati A, Mustafa M K, Othaman Z and Ghoshal S K 2015 Ge Nanoislands Grown by Radio Frequency Magnetron Sputtering : Comprehensive Investigation of Surface

Morphology and Optical Properties J. Nanomater **16**

- [128] Eaglesham D J and Cerullo M 1990 Dislocation-free Stranski-Krastanow growth of Ge on Si(100) *Phys. Rev. Lett.* **64** 1943-1946
- [129] Medeiros-Ribeiro, Bratkovski, Kamins, Ohlberg and Williams 1998 Shape transition of germanium nanocrystals on a silicon (001) surface from pyramids to domes *Science* **279** 353-5
- [130] Wu, Chen, Zhang and Lagally 1995 Reversal of Step Roughness on Ge-Covered Vicinal Si(001) *Phys. Rev. Lett.* **74** 574-7
- [131] Zhong L, Hojo A, Matsushita Y, Aiba Y, Hayashi K, Takeda R, Shirai H, Saito H, Matsushita J and Yoshikawa J 1996 Evidence of spontaneous formation of steps on silicon (100) *Phys. Rev. B - Condens. Matter Mater. Phys.* **54** R2304-R2307
- [132] Legoues F K, Copel M and Tromp R 1989 Novel strain-induced defect in thin molecular-beam epitaxy layers *Phys. Rev. Lett.* **63** 1826-1829
- [133] Ray S K, Maikap S, Banerjee W and Das S 2013 Nanocrystals for silicon-based light-emitting and memory devices *J. Phys. D. Appl. Phys.* **46** 153001
- [134] M. L. Ciurea A L 2015 Tuning the properties of Ge and Si nanocrystals based structures by tailoring the preparation conditions *Dig. J. Nanomater. Biostructures* **10** 59-87
- [135] Fölsch S, Martínez-Blanco J, Yang J, Kanisawa K and Erwin S C 2014 Quantum dots with single-atom precision *Nat. Nanotechnol.* **9** 505-508
- [136] Pavesi L and Turan R 2010 *Silicon Nanocrystals: Fundamentals, Synthesis and Applications* (Weinheim: Wiley-VCH)
- [137] Dhara S and Giri P K 2011 Size Dependent Anisotropic Strain and Optical Properties of Strained Si Nanocrystals *J. Nanosci. Nanotechnol.* **11** 1-7
- [138] Yang X-F, Fu K, Lu W, Xu W-L and Fu Y 2009 Strain effect in determining the geometric shape of self-assembled quantum dot *J. Phys. D. Appl. Phys.* **42** 125414
- [139] Guerra R, Degoli E and Ossicini S 2009 Size, oxidation, and strain in small Si/SiO₂ nanocrystals *Phys. Rev. B* **80** 155332
- [140] Liao P H, Hsu T C, Chen K H, Cheng T H, Hsu T M, Wang C C, George T and Li P W 2014 Size-tunable strain engineering in Ge nanocrystals embedded within SiO₂ and Si₃N₄ *Appl. Phys. Lett.* **105** 172106
- [141] Guerra R, Degoli E and Ossicini S 2010 Size, oxidation, and strain in small Si/SiO₂ nanocrystals *Phys. Rev. B* **80** 155332
- [142] Palade C, Slav A, Lepadatu A-M, Stavarache I, Dascalescu I, Maraloiu V A, Negrila C C, Logofatu C, Stoica T, Teodorescu V, Ciurea M L L and Lazanu S 2019 Orthorhombic HfO₂ with embedded Ge nanoparticles in nonvolatile memories used for the detection of ionizing radiation *Nanotechnology* **30** 445501
- [143] Dimitrakis P, Normand P, Ioannou-Sougleridis V, Bonafos C, Schamm-Chardon S, Benassayag G and Iliopoulos E 2013 Quantum dots for memory applications *Phys. Status Solidi Appl. Mater. Sci.* **210** 1490-504
- [144] Priolo F, Gregorkiewicz T, Galli M and Krauss T F 2014 Silicon nanostructures for photonics and photovoltaics *Nat. Nanotechnol.* **9** 19-32

- [145] Berbezier A, Autran J L and Michelini F 2013 Photovoltaic response in a resonant tunneling wire-dot-wire junction *Appl. Phys. Lett.* **103**
- [146] Ciurea M L and Lepadatu A M Tuning the properties of Ge and Si nanocrystals based structures by tailoring the preparation conditions *Review Dig. J. Nanomater. Biostructures* **10** 59–87
- [147] Ghosh B, Sakka Y and Shirahata N 2013 Efficient green-luminescent germanium nanocrystals *J. Mater. Chem. A* **1** 3747–51
- [148] Siontas S, Liu P, Zaslavsky A and Pacifici D 2016 Noise performance of high-efficiency germanium quantum dot photodetectors *Appl. Phys. Lett.* **109**
- [149] Chien C Y, Lai W T, Chang Y J, Wang C C, Kuo M H and Li P W 2014 Size tunable Ge quantum dots for near-ultraviolet to near-infrared photosensing with high figures of merit *Nanoscale* **6** 5303–8
- [150] Zschintzsch M, von Borany J, Jeutter N M and Mücklich A 2011 Stacked Ge nanocrystals with ultrathin SiO₂ separation layers *Nanotechnology* **22** 465302
- [151] Zhu J G, White C W, Budai J D, Withrow S P and Chen Y 1995 Growth of Ge, Si, and SiGe nanocrystals in SiO₂ matrices *J. Appl. Phys.* **78** 4386–9
- [152] Takeoka S, Toshiakiyo K, Fujii M, Hayashi S and Yamamoto K 2000 Control of photoluminescence energy of Si nanocrystals by Ge doping *J. Lumin.* **87–89** 350–2
- [153] Ferraioli L, Wang M, Pucker G, Navarro-Urrios D, Daldosso N, Kompocholis C and Pavesi L 2007 Photoluminescence of Silicon Nanocrystals in Silicon Oxide *J. Nanomater.* **43491**
- [154] Lee H C, Yeom G Y, Lee Y J, Shin J K, Baik S Il and Kim Y W 2005 *Structural and Electrical Analysis of Silicon Thin Films Deposited by Transformer-Coupled-Plasma Chemical-Vapor Deposition* *JKPS* **47** 277-82
- [155] Brown W D and Khaliq M A 1990 The effects of rapid thermal annealing on the properties of plasma-enhanced chemically vapor-deposited silicon nitride *Thin Solid Films* **186** 73–85
- [156] Lepadatu A-M, Stavarache I, Stoica T F and Ciurea M L 2011 Study of Ge nanoparticles embedded in an amorphous SiO₂ matrix with photoconductive properties *Dig. J. Nanomater. Biostructures* **6** 67–73
- [157] Jettanasen J 2015 Study of silicon nanoparticles in dielectric oxides obtained by sol-gel route Study of silicon nanoparticles in dielectric oxides obtained by sol-gel route *J. Exp. Nanosci.* **10** 1319–26
- [158] Nohira H, Kuroiwa T, Nakamura M, Hirose Y, Mitsui J, Sakai W, Nakajima K, Suzuki M, Kimura K, Sawano K, Nakagawa K, Shiraki Y and Hattori T 2004 Quality of SiO₂ and of SiGe formed by oxidation of Si/Si_{0.7}Ge_{0.3} heterostructure using atomic oxygen at 400 °C *Appl. Surf. Sci.* **237** 134–8
- [159] Lauhon L J, Gudlksen M S, Wang D and Lieber C M 2002 Epitaxial core-shell and core-multishell nanowire heterostructures *Nature* **420** 57–61
- [160] Nur O, Karlsteen M, Willander M, Turan R, Aslan B, Tanner M O and Wang K L 1998 Correlation between barrier height and band offsets in metal/Si_{1-x}Ge_x/Si heterostructures *Appl. Phys. Lett.* **73**
- [161] Dismukes J P, Ekstrom L and Paff R J 1964 Lattice Parameter and Density in

Germanium-Silicon Alloys 1 *J. Phys. Chem.* **68** 3021–7

- [162] Zhang B, Shrestha S, Aliberti P, Green M A and Conibeer G 2009 Synthesis and structural properties of Ge nanocrystals in multilayer superlattice structure *Proc. SPIE Nanoscale Photonic and Cell Technologies for Photovoltaics II* **7411** 741103
- [163] Long E, Azarov A, Kløw F, Galeckas A, Kuznetsov A Y and Diplas S 2012 Ge redistribution in SiO₂/SiGe structures under thermal oxidation: Dynamics and predictions *Cit. J. Appl. Phys.* **111** 74904
- [164] Palade C, Dascalescu I, Slav A, Lepadatu A M, Lazanu S, Stoica T, Teodorescu V S, Ciurea M L, Comanescu F, Muller R, Dinescu A and Enuica A 2017 Photosensitive GeSi/TiO₂ multilayers in VIS-NIR *Proc. Int. Semiconductor Conf. CAS (Sinaia, Romania, 11–14 October 2017)* (IEEE) pp 67–70
- [165] Slav A, Palade C, Stavarache I, Teodorescu V S, Ciurea M L, Muller R, Dinescu A, Sultan M T, Manolescu A, Gudmundsson J T and Svavarsson H G 2017 Influence of preparation conditions on structure and photosensing properties of GeSi/TiO₂ multilayers *Proc. Int. Semiconductor Conf. CAS (Sinaia, Romania, 11–14 October 2017)* (IEEE) pp 63–6
- [166] Hadjisavvas G, Remediakis I N and Kelires P C 2006 Shape and faceting of Si nanocrystals embedded in a-SiO₂: A Monte Carlo study *Phys. Rev. B* **74** 165419
- [167] Capan I, Carvalho A and Coutinho J 2014 Silicon and germanium nanocrystals: properties and characterization theis *Beilstein J. Nanotechnol.* **5** 1787–94
- [168] Pavesi L and Turan R 2010 *Silicon nanocrystals: fundamentals, synthesis and applications* (Weinheim: Wiley-VCH)
- [169] Zhang B, Shrestha S, Green M A and Conibeer G 2010 Size controlled synthesis of Ge nanocrystals in SiO₂ at temperatures below 400 °C using magnetron sputtering *Appl. Phys. Lett.* **96** 261901
- [170] Volodin V A, Cherkov A G, Vdovin V I, Stoffel M, Rinnert H and Vergnat M 2016 GeSi nanocrystals formed by high temperature annealing of GeO/SiO₂ multilayers: Structure and optical properties *Proc. SPIE* **10224** 102240C
- [171] Peng X, Tang F and Logan P Band structure of Si/Ge core-shell nanowires along the [110] direction modulated by external uniaxial strain *J. Phys. Condens. Matter* **23**
- [172] Ciurea M L, Lazanu S, Stavarache I, Lepadatu A-M, Iancu V, Mitroi M R, Nigmatullin R R and Baleanu C M 2011 Stress-induced traps in multilayered structures *J. Appl. Phys.* **109** 013717
- [173] Ciurea M L 2013 Effect of stress on trapping phenomena in silicon: From single crystal to nanostructures *Romanian Rep. Phys.* **65** 841-856
- [174] Yakimov A I, Kirienko V V, Armbrister V A and Dvurechenskii A V 2014 Hydrogen passivation of self-assembled Ge/Si quantum dots *Semicond. Sci. Technol.* **29** 085011
- [175] Dashiell M W, Denker U, Müller C, Costantini G, Manzano C, Kern K and Schmidt O G 2002 Photoluminescence of ultrasmall Ge quantum dots grown by molecular-beam epitaxy at low temperatures *Appl. Phys. Lett.* **80** 1279–81
- [176] Wolkin M V., Jorne J, Fauchet P M, Allan G and Delerue C 1999 Electronic States and Luminescence in Porous Silicon Quantum Dots: The Role of Oxygen *Phys. Rev. Lett.* **82** 197–200

- [177] Szekeres A and Alexandrova S 1996 Low-temperature treatment of Si/SiO₂ structures in an RF hydrogen plasma *Vacuum* **47** 1483–6
- [178] Puzder A, Williamson A J, Grossman J C and Galli G 2002 Surface control of optical properties in silicon nanoclusters *J. Chem. Phys.* **117** 6721–9
- [179] López M, Garrido B, García C, Pellegrino P, Pérez-Rodríguez A, Morante J R, Bonafos C, Carrada M and Claverie A 2002 Elucidation of the surface passivation role on the photoluminescence emission yield of silicon nanocrystals embedded in SiO₂ *Appl. Phys. Lett.* **80** 1637–9
- [180] Nazarov A N, Lysenko V S and Nazarova T M 2008 Hydrogen plasma treatment of silicon thin-film structures and nanostructured layers *Semicond. Physics, Quantum Electron. Optoelectron.* **11** 101–23
- [181] Ortiz M I, Rodríguez A, Sangrador J, Rodríguez T, Avella M, Jiménez J and Ballesteros C 2005 Luminescent nanostructures based on Ge nanoparticles embedded in an oxide matrix *Nanotechnology* **16** S197–S201
- [182] Conibeer G, Green M, Cho E C, König D, Cho Y H, Fangsuwannarak T, Scardera G, Pink E, Huang Y, Puzzer T, Huang S, Song D, Flynn C, Park S, Hao X and Mansfield D 2008 Silicon quantum dot nanostructures for tandem photovoltaic cells *Thin Solid Films* **516** 6748–56
- [183] Zacharias M, Heitmann J, Scholz R, Kahler U, Schmidt M and Bläsing J 2002 Size-controlled highly luminescent silicon nanocrystals: A SiO/SiO₂ superlattice approach *Appl. Phys. Lett.* **80** 661–3
- [184] Gudmundsson J T 1998 Experimental studies of H₂/Ar plasma in a planar inductive discharge *Plasma Sources Sci. Technol.* **7** 330–6
- [185] Kimura T and Kasugai H 2010 Properties of inductively coupled RF Ar/H₂ plasmas: Experiment and global model *J. Appl. Phys.* **107** 083308
- [186] Cielaszyk E S, Kirmse K H R, Stewart R A and Wendt A E 1995 Mechanisms for polycrystalline silicon defect passivation by hydrogenation in an electron cyclotron resonance plasma *Appl. Phys. Lett.* **67** 3099–101
- [187] Yeh C F, Chen T J, Liu C, Gudmundsson J T and Lieberman M A 1999 Hydrogenation of polysilicon thin-film transistor in a planar inductive H₂/Ar discharge *IEEE Electron Device Lett.* **20** 223–5
- [188] Glover M and Meldrum A 2005 Effect of “buffer layers” on the optical properties of silicon nanocrystal superlattices *Opt. Mater. (Amst.)* **27** 977–82
- [189] Avella M, Prieto Á C, Jiménez J, Rodríguez A, Sangrador J, Rodríguez T, Ortiz M I and Ballesteros C 2008 Influence of the crystallization process on the luminescence of multilayers of SiGe nanocrystals embedded in SiO₂ *Mater. Sci. Eng. B* **147** 200–4
- [190] Mayandi J, Finstad T G, Heng C L, Li Y J, Thogersen. A, Foss S and Klette H 2007 A Comparison between 1.5µm Photoluminescence from Er-Doped Si-Rich SiO₂ Films and (Er,Ge) Co-Doped SiO₂ Films *Dans European Nano Systems Workshop - ENS 2006 Paris France (2006) 14-15 December 2006*
- [191] Pan S W, Zhou B, Chen S Y, Li C, Huang W and Lai H K 2011 Optical property investigation of SiGe nanocrystals formed by electrochemical anodization *Appl. Surf. Sci.* **258** 30–3

- [192] Kassabov J, Atanassova E, Dimitrov D and Vasileva J 1988 Effects of hydrogen plasma on thin-oxide Si-SiO₂ structures *Semicond. Sci. Technol.* **3** 686–90
- [193] Danielsson D M, Gudmundsson J T and Svavarsson H G 2010 Effect of hydrogenation on minority carrier lifetime in low-grade silicon *Phys. Scr.* **T141** 014005
- [194] Olafsson H ., Gudmundsson J ., Svavarsson H . and Gislason H . 1999 Hydrogen passivation of Al_xGa_{1-x}As/GaAs studied by surface photovoltage spectroscopy *Phys. B Condens. Matter* **273–274** 689–92
- [195] Mews M, Conrad E, Kirner S, Mingirulli N and Korte L 2014 Hydrogen plasma treatments of amorphous/crystalline silicon heterojunctions *Energy Procedia* **55** 827–33
- [196] Lepadatu A M, Stavarache I, Maraloiu A, Palade C, Serban T V and Magdalena C L 2012 Electrical behaviour related to structure of nanostructured GeSi films annealed at 700 °C *Proc. Int. Semiconductor Conf. CAS (Sinaia, Romania, 15–17 October 2012)* (IEEE) pp 109-12
- [197] Mazzucato S, Nardin D, Polimeni A, Capizzi M, Granados D and García J M 2005 Hydrogenation of Stacked Self-Assembled InAs/GaAs Quantum Dots *AIP Conf Proc.* **772** 621–2
- [198] Ru E C Le, Siverns P D and Murray R 2000 Luminescence enhancement from hydrogen-passivated self-assembled quantum dots *Appl. Phys. Lett.* **77** 2446–8
- [199] Yamada S, Kurokawa Y, Miyajima S and Konagai M 2014 Investigation of hydrogen plasma treatment for reducing defects in silicon quantum dot superlattice structure with amorphous silicon carbide matrix *Nanoscale Res. Lett.* **9** 72
- [200] Jacob A P, Zhao Q X, Willander M, Ferdos F, Sadeghi M and Wang S M 2002 Hydrogen passivation of self assembled InAs quantum dots *J. Appl. Phys.* **92** 6794–8
- [201] Indutnyy I Z, Lysenko V S, Maidanchuk I Y, Min’ko V I, Nazarov A N, Tkachenko A S, Shepeliavyi P E and Dan’ko V A 2006 Effect of chemical and radiofrequency plasma treatment on photoluminescence of SiO_x films thesis *Semicond. Physics, Quantum Electron. Optoelectron.* **9** 9–13
- [202] Arima K, Shigetoshi T, Kakiuchi H and Morita M 2006 Surface photovoltage measurements of intrinsic hydrogenated amorphous Si films on Si wafers on the nanometer scale *Phys. B Condens. Matter* **376–377** 893–6
- [203] Zhou H P, Xu M, Xu S, Liu L L, Liu C X, Kwek L C and Xu L X 2016 Hydrogen-plasma-induced Rapid, Low-Temperature Crystallization of μm-thick a-Si:H Films *Sci. Rep.* **6** 32716
- [204] Reynolds S, Brinza M, Benkhedir M L and Adriaenssens G J 2017 Photoconductivity in materials research in *Springer Handbook of Electronic and Photonic Materials* ed S Kasap and P Capper (Springer International Publishing, Switzerland)
- [205] Łukasiak L and Jakubowski A 2010 History of Semiconductors *JTIT* **1** 3-9
- [206] Mort J and Pai D M 1976 *Photoconductivity and related phenomena* (New York: Elsevier Scientific Pub. Co.)
- [207] Bube R 1960 *Photoconductivity of solids* (New York: Wiley)
- [208] Gudmundsson J. T. and Lundin D., in High Power Impulse Magnetron Sputtering: Fundamentals, Technologies, Challenges and Applications, edited by D. Lundin, T. Minea, and J. T. Gudmundsson (Elsevier, Amsterdam, The Netherlands, 2020), pp. 1–

48.

- [209] Almtoft K P 2006 *Structural Characterization of Nanocrystalline Thin Films Grown by Magnetron Sputtering* (PhD thesis) University of Aarhus, Denmark
- [210] Swann S 1988 Magnetron sputtering *Phys. Technol.* **19** 67–75
- [211] Depla D, Heirwegh S, Mahieu S, Haemers J, Gryse R De, Depla D, Heirwegh S, Mahieu S, Haemers J and Gryse R De 2012 Understanding the discharge voltage behavior during reactive sputtering of oxides *J. Appl. Phys.* **101** 013301
- [212] Gudmundsson J T, Brenning N, Lundin D and Helmersson U 2012 High power impulse magnetron sputtering discharge *J. Vac. Sci. Technol. A Vacuum, Surfaces, Film* **30** 030801–34
- [213] Ngaruiya J M 2004 *Fundamental processes in growth of reactive DC magnetron sputtered thin films* (PhD thesis) RWTH Aachen University, Germany
- [214] Depla D, Mahieu S and Greene J E 2010 Sputter deposition processes *Handbook of Deposition Technologies for Films and Coatings Science, Applications and Technology* (3rd edition) ed P M Martin (Elsevier Inc.) 253-296
- [215] Trinh D H 2006 *Synthesis and Characterisation of Magnetron Sputtered Alumina-Zirconia Thin Films* (PhD thesis) Linköping University, Sweden
- [216] Georgiana CONSTANTIN D, Apreutesei M, Arvinte R, Marin A, Cella ANDREI O and Munteanu D 2011 *Magnetron sputtering technique used for coatings deposition; technologies and applications 7th International Conference on Materials Science and Engineering – BRAMAT 2011 Braşov 24 – 26 February*
- [217] Kelly P J and Arnell R D 2000 Magnetron sputtering: A review of recent developments and applications *Vacuum* **56** 159-172
- [218] Gudmundsson J T 2010 The high power impulse magnetron sputtering discharge as an ionized physical vapor deposition tool *Vacuum* **84** 1360-1364
- [219] Bräuer G, Szyszka B, Vergöhl M and Bandorf R 2010 Magnetron sputtering - Milestones of 30 years *Vacuum* **84** 1354-1359
- [220] Micro Magnetics 2019 Magnetron Sputtering Technology Available at: <http://www.directvacuum.com/sputter.asp> (Accessed: August 2019)
- [221] Sigmund P 1969 Theory of sputtering. I. Sputtering yield of amorphous and polycrystalline targets *Phys. Rev.* **184** 383
- [222] Fruth H F 1932 Cathode sputtering, A commercial application *Physics* **2** 280–6
- [223] Gudmundsson J T and Hecimovic A 2017 Foundations of DC plasma sources *Plasma Sources Sci. Technol.* **26**
- [224] Penning V F 1936 Die glimmentladung bei niedrigem druck zwischen koaxialen zylindern in einem axialen magnetfeld *Physica* **3** 873-94
- [225] Vossen J L and Kern W 1978 *Thin Film Processes* (New York: Academic Press)
- [226] Martin P M 2009 *Handbook of Deposition Technologies for Films and Coatings : Science, Applications and Technology* (Elsevier Science: William Andrew)
- [227] Ohring M 2002 *Materials Science of Thin Films* (San Diego: Academic Press)

- [228] Lieberman M A and Lichtenberg A J 2005 Principles of Plasma Discharges and Materials Processing: Second Edition (John Wiley and Sons)
- [229] Berg S, Blom H, Larsson T and Nender C 1987 Modeling of reactive sputtering of compound materials *J. Vac. Sci. Technol. A Vacuum, Surfaces, Film.* **5** 202
- [230] Berg S, Blom H -O., Moradi M, Nender C and Larsson T 1989 Process modeling of reactive sputtering *J. Vac. Sci. Technol. A Vacuum, Surfaces, Film.* **7** 1225–9
- [231] Berg S, Blom H -O., Moradi M, Nender C and Larsson T 2002 Process modeling of reactive sputtering *J. Vac. Sci. Technol. A Vacuum, Surfaces, Film* **7** 1225
- [232] Berg S and Nyberg T 2005 Fundamental understanding and modeling of reactive sputtering processes *Thin Solid Films* **476** 215-230
- [233] Gudmundsson J T, Brenning N, Lundin D and Helmersson U 2012 High power impulse magnetron sputtering discharge *J. Vac. Sci. Technol. A. Vacuum, Surfaces, Film.* **30** 030801
- [234] Helmersson U, Lattemann M, Bohlmark J, Ehiasarian A P and Gudmundsson J T 2006 Ionized physical vapor deposition (IPVD): A review of technology and applications *Thin Solid Films* **513** 1–24
- [235] Liu C Y, He F, Zhang Y F, Zang S G, Zuo Y and Ma J R 2015 Effect of oxygen partial pressure on properties of ZnO/Al thin films prepared by pulsed dc reactive magnetron sputtering with SpeedFlo controller *Mater. Technol.* **30** 249–56
- [236] Kouznetsov V, MacÁk K, Schneider J M, Helmersson U and Petrov I 1999 A novel pulsed magnetron sputter technique utilizing very high target power densities *Surf. Coatings Technol.* **122** 290–3
- [237] Macák K, Kouznetsov V, Schneider J, Helmersson U and Petrov I 2000 Ionized sputter deposition using an extremely high plasma density pulsed magnetron discharge *J. Vac. Sci. Technol. A Vacuum, Surfaces, Film.* **18** 1533–7
- [238] Gudmundsson J T 2010 The high power impulse magnetron sputtering discharge as an ionized physical vapor deposition tool *Vacuum* **84** 1360–4
- [239] Sarakinos K, Alami J and Konstantinidis S 2010 High power pulsed magnetron sputtering: A review on scientific and engineering state of the art *Surf. Coatings Technol.* **204** 1661–84
- [240] Anders A 2011 Discharge physics of high power impulse magnetron sputtering *Surf. Coatings Technol.* **205** S1-S9
- [241] Lin J, Sproul W D, Moore J J, Wu Z, Lee S, Chistyakov R and Abraham B 2011 Recent advances in modulated pulsed power magnetron sputtering for surface engineering *JOM* **63** 48–58
- [242] Lundin D and Sarakinos K 2012 An introduction to thin film processing using high-power impulse magnetron sputtering *J. Mater. Res.* **27** 780–92
- [243] Alami J, Persson P O Å, Music D, Gudmundsson J T, Bohlmark J and Helmersson U 2005 Ion-assisted physical vapor deposition for enhanced film properties on nonflat surfaces *J. Vac. Sci. Technol. A Vacuum, Surfaces, Film.* **23** 278–80
- [244] Alami J, Bolz S and Sarakinos K 2009 High power pulsed magnetron sputtering: Fundamentals and applications *J. Alloys Compd.* **483** 530–4

- [245] Gudmundsson J T 2016 On reactive high power impulse magnetron sputtering *Plasma Phys. Control. Fusion* **58** 014002
- [246] Hajihoseini H, Čada M, Hubička Z, Ünalđi S, Raadu M A, Brenning N, Gudmundsson J T, Lundin D, Hajihoseini H, Čada M, Hubička Z, Ünalđi S, Raadu M A, Brenning N, Gudmundsson J T and Lundin D 2019 The Effect of Magnetic Field Strength and Geometry on the Deposition Rate and Ionized Flux Fraction in the HiPIMS Discharge *Plasma* **2** 201–21
- [247] Yu H, Meng L, Szott M M, Mclain J T, Cho T S and Ruzic D N 2013 Investigation and optimization of the magnetic field configuration in high-power impulse magnetron sputtering *Plasma Sources Sci. Technol* **22** 45012–22
- [248] Čapek J, Hála M, Zabeida O, Klemberg-Sapieha J E and Martinu L 2012 Steady state discharge optimization in high-power impulse magnetron sputtering through the control of the magnetic field *J. Appl. Phys.* **111** 023301
- [249] Gudmundsson J T 2008 Ionized physical vapor deposition (IPVD): Magnetron sputtering discharges *J. Phys. Conf. Ser.* **100** 082002
- [250] Horwat D and Anders A 2010 Compression and strong rarefaction in high power impulse magnetron sputtering discharges *J. Appl. Phys.* **108** 123306
- [251] Magnus F, Tryggvason T K, Olafsson S and Gudmundsson J T 2012 Current–voltage–time characteristics of the reactive Ar/O₂ high power impulse magnetron sputtering discharge *J. Vac. Sci. Technol. A Vacuum, Surfaces, Film.* **30** 050601
- [252] Straňák V, Quaas M, Wulff H, Hubička Z, Wrehde S, Tichý M and Hippler R 2008 Formation of TiO_x films produced by high-power pulsed magnetron sputtering *J. Phys. D. Appl. Phys.* **41** 055202
- [253] Benzeggouta D, Hugon M C, Bretagne J and Ganciu M 2009 Study of a HPPMS discharge in Ar/O₂ mixture: I. Discharge characteristics with Ru cathode *Plasma Sources Sci. Technol.* **18** 045025
- [254] Magnus F, Sveinsson O B, Olafsson S and Gudmundsson J T 2011 Current-voltage-time characteristics of the reactive Ar/N₂ high power impulse magnetron sputtering discharge *J. Appl. Phys.* **110** 083306
- [255] Moreira M A, Törndahl T, Katardjiev I and Kubart T 2015 Deposition of highly textured AlN thin films by reactive high power impulse magnetron sputtering *J. Vac. Sci. Technol. A Vacuum, Surfaces, Film.* **33** 021518
- [256] Gudmundsson J T, Lundin D, Brenning N, Raadu M A, Huo C and Minea T M 2016 An ionization region model of the reactive Ar/O₂ high power impulse magnetron sputtering discharge *Plasma Sources Sci. Technol.* **25** 065004
- [257] Birkholz M 2006 *Thin Film Analysis by X-Ray Scattering* (Winheim: WILEY-VCH)
- [258] Widjonarko N 2016 Introduction to Advanced X-ray Diffraction Techniques for Polymeric Thin Films *Coatings* **6** 54
- [259] G. Binnig G, Quate C F and Gerber Ch. 1986 Atomic Force Microscope *Phys. Rev. Lett.* **56** 930
- [260] Binnig G, Gerber C, Stoll E, Albrecht T R and Quate C F 1987 Atomic resolution with atomic force microscope *EPL* **3**
- [261] Binnig G K 1987 Atomic-Force Microscopy *Phys. Scr.* **T19A** 53–4

- [262] Jagtap R N and Ambre A H 2006 Overview literature on atomic force microscopy (AFM): Basics and its important applications for polymer characterization *IJEMS* **13** 368-84
- [263] Kyeyune B (2017) Atomic Force Microscopy Available at: https://www.researchgate.net/publication/322294428_Atomic_Force_Microscopy (Accessed: August 2019)
- [264] Maghsoudy-Louyeh S, Kropf M and Tittmann B R 2019 Review of Progress in Atomic Force Microscopy *Open Neuroimag. J.* **12** 86–104
- [265] Meyer E 1992 Atomic force microscopy *Prog. Surf. Sci.* **41** 3–49
- [266] Max-Planck-Gesellschaft, München (2003) AFM - Atomic Force Microscope Available at: <https://www.mpie.de/3098949/AFM> (Accessed: August 2019)
- [267] Bozzola J J and Russell L D 1992 *Electron microscopy : principles and techniques for biologists* (Boston: Jones and Bartlett Publishers)
- [268] Stadtländer T K –H 2007 Scanning Electron Microscopy and Transmission Electron Microscopy of Mollicutes: Challenges and Opportunities *Modern Research and Educational Topics in Microscopy* (vol. 2) ed M Vilas and J Díaz (Formatex) p 122-31
- [269] Flegler S L, Heckman J W and Klomparens K L 1993 Scanning and Transmission Electron Microscopy: An Introduction (New York : W.H. Freeman)
- [270] JOEL () *Scanning Electron Microscope A To Z* Available at: https://www.jeol.co.jp/en/applications/pdf/sm/sem_atoz_all.pdf (Accessed: September 2019)
- [271] Scharf D (1998) Detectors Available at: <http://www.scharfphoto.com/articles/detectors> (Accessed: Semptember 2019)

Appendix

Paper I

Enhanced photoconductivity of SiGe nanocrystals in SiO₂ driven by mild annealing

*Sultan M T¹, Manolescu A¹, Gudmundsson J T^{2,3}, Torfason K¹, Alexandru Nemnes G⁴, Stavarache I⁵, Logofatu C⁵, Teodorescu V S⁵, Ciurea M L⁵ and *Svavarsson H G¹

¹School of Science and Engineering, Reykjavik University, IS-101 Reykjavik, Iceland

²Department of Space and Plasma Physics, School of Electrical Engineering and Computer Science, KTH-Royal Institute of Technology, SE-100 44, Stockholm, Sweden

³Science Institute, University of Iceland, IS-101 Reykjavik, Iceland

⁴University of Bucharest, Faculty of Physics, MDEO Research Center, 077125 Magurele, Romania

⁵National Institute of Materials Physics, 077125 Magurele, Romania

⁶Academy of Romanian Scientists, 050094 Bucharest, Romania

Published: Applied Surface Science, vol. 469, pp. 870-8, 2019.

DOI: <https://doi.org/10.1016/j.apsusc.2018.07.006>



Full Length Article

Enhanced photoconductivity of SiGe nanocrystals in SiO₂ driven by mild annealing

Muhammad Taha Sultan^{a,*}, Andrei Manolescu^b, Jon Tomas Gudmundsson^{b,c}, Kristinn Torfason^a, George Alexandru Nemnes^d, Ionel Stavarache^e, Constantin Logofatu^e, Valentin Serban Teodorescu^e, Magdalena Lidia Ciurea^{e,f}, Halldor Gudfinnur Svavarsson^{a,*}

^a School of Science and Engineering, Reykjavik University, IS-101 Reykjavik, Iceland

^b Department of Space and Plasma Physics, School of Electrical Engineering and Computer Science, KTH-Royal Institute of Technology, SE-100 44 Stockholm, Sweden

^c Science Institute, University of Iceland, IS-101 Reykjavik, Iceland

^d University of Bucharest, Faculty of Physics, MDEO Research Center, 077125 Magurele, Romania

^e National Institute of Materials Physics, 077125 Magurele, Romania

^f Academy of Romanian Scientists, 050094 Bucharest, Romania

ARTICLE INFO

Keywords:

SiO₂
Si_{1-x}Ge_x nanocrystals
Strain
Radio frequency magnetron sputtering
Thermal annealing
Photoconductivity

ABSTRACT

Photosensitive films based on finely dispersed semiconductor nanocrystals (NCs) in dielectric films have great potential for sensor applications. Here we report on preparation and characterization of photosensitive Si_{1-x}Ge_x NCs sandwiched between SiO₂ matrix. A radio-frequency magnetron sputtering was applied to obtain a multi-layer-structures (MLs) by depositing SiO₂/SiGe/SiO₂ films on Si (0 0 1) substrate. The Si_{1-x}Ge_x NCs were formed by a post-deposition annealing at 100–700 °C for 1–5 min. The effect of annealing temperature and time on MLs morphology and NCs size and density was studied using grazing incidence X-ray diffraction, transmission electron microscopy, X-ray photoelectron spectroscopy, energy-dispersive X-ray spectroscopy and measurements of spectral distribution of photocurrent. It is demonstrated how the photoconductive properties of the MLs can be enhanced and tailored by controlling the NCs formation conditions and the presence of stress field in MLs and defects acting as traps and recombination centers. All these features can be adjusted/controlled by altering the annealing conditions (temperature and time). The MLs photosensitivity was increased of more than an order of magnitude by the annealing process. A mechanism, where a competition between crystallization process (NCs formation and evolution i.e. size and shapes) and stress field appearance determines the peak position in the photocurrent spectra, was identified.



Enhanced photoconductivity of SiGe nanocrystals in SiO₂ driven by mild annealing

*Muhammad Taha Sultan¹, Andrei Manolescu¹, Jón Tómas Guðmundsson^{2,3}, Kristinn Torfason¹, George Alexandru Nemnes⁴, Ionel. Stavarache⁵, Constantin Logofatu⁵, Valentin Serban Teodorescu⁵, Magdalena Lidia Ciurea^{5,6}, *Halldór Guðfínnur Svavarsson¹

¹School of Science and Engineering, Reykjavik University, IS-101 Reykjavik, Iceland

²Department of Space and Plasma Physics, School of Electrical Engineering and Computer Science, KTH-Royal Institute of Technology, SE-100 44, Stockholm, Sweden

³Science Institute, University of Iceland, IS-101 Reykjavik, Iceland

⁴University of Bucharest, Faculty of Physics, MDEO Research Center, 077125 Magurele, Romania

⁵National Institute of Materials Physics, 077125 Magurele, Romania

⁶Academy of Romanian Scientists, 050094 Bucharest, Romania

Abstract

Photosensitive films based on finely dispersed semiconductor nanocrystals (NCs) in dielectric films have great potential for sensor applications. Here we report on preparation and characterization of photosensitive Si_{1-x}Ge_x NCs sandwiched between SiO₂ matrix. A radio-frequency magnetron sputtering was applied to obtain a multilayer-structures (MLs) by depositing SiO₂/SiGe/SiO₂ films on Si (001) substrate. The Si_{1-x}Ge_x NCs were formed by a post-deposition annealing at 100 - 700 °C for 1-5 minutes. The effect of annealing temperature and time on MLs morphology and NCs size and density was studied using grazing incidence X-ray diffraction, transmission electron microscopy, X-ray photoelectron spectroscopy, energy-dispersive X-ray spectroscopy and measurements of spectral distribution of photocurrent. It is demonstrated how the photoconductive properties of the MLs can be enhanced and tailored by controlling the NCs formation conditions and the presence of stress field in MLs and defects acting as traps and recombination centers. All these features can be adjusted/controlled by altering the annealing conditions (temperature and time). The MLs photosensitivity was increased of more than an order of magnitude by the annealing process. A mechanism, where a competition between crystallization process (NCs formation and evolution *i.e.* size and shapes) and stress field appearance determines the peak position in the photocurrent spectra, was identified.

Keywords: SiO₂, Si_{1-x}Ge_x nanocrystals, strain, radio frequency magnetron sputtering, thermal annealing, photoconductivity.

1. Introduction

One of the challenges faced by modern day technology is the fabrication of high quality films incorporating nanoparticles with improved optoelectronic properties for sensitive functional devices. For this purpose, silicon-germanium (SiGe) quantum dots (QDs) have attracted the interest of numerous researchers [1, 2, 3, 4, 5] due to the compatibility of Ge with Si and their self-assembled structures. One of the objectives is to increase the efficiency of photoconductive devices by widening the spectral sensitivity interval from visible to near infrared with the aim towards applications in photovoltaics [6], optoelectronics [7, 8], photodetectors [9], and optical-telecommunications [8]. The misfit between

the Si and Ge lattices (4.2% lattice mismatch) was considered an obstacle in the fabrication of such structures. However, more recently, SiGe systems turned out to be quite useful for electronic and optoelectronic devices due to the possibility of optimizing the band gap of the device [4, 10]. Being an indirect bandgap semiconductor, Si has relatively poor light absorption. Mixing it with Ge results in reduced bandgap and increased absorption coefficient at longer wavelengths. The bandgap can be further reduced by introducing strain in the $\text{Si}_{1-x}\text{Ge}_x$ system [4]. Ge is also an indirect bandgap material but with much smaller energy difference between the indirect and direct bandgaps than in the case of Si (136 meV for Ge vs 2.4 eV for Si) [11]. Introducing a tensile strain in the crystal lattice additionally reduces the energy difference between the direct and indirect bandgaps because the direct bandgap shrinks faster than the indirect one. Thus, the bandgap of the SiGe nanocrystals (NCs) can be adjusted to enhance energy conversion efficiency and optical properties by utilizing strain engineering [12, 13].

In previous studies, a considerable interest has been paid to Si and Ge nanocrystals embedded in oxide matrices such as SiO_2 [1, 14, 15, 16], high-dielectric Al_2O_3 [17, 18], and HfO_2 [18]. Of these materials, SiO_2 has been shown to be one of the most interesting since it remains amorphous up to high annealing temperatures while providing lateral confinement to the nanoparticles [19, 20], and also due to compatibility with the well-established Si technology [21]. Among methods used to fabricate SiGe NCs embedded in a SiO_2 matrix are sol-gel [22], molecular beam epitaxy [23, 18], ion implantation [24], and radio frequency (rf) magnetron sputtering [1, 16, 22, 25], the last one being the most common. It is well understood that the NCs size determines the bandgap energy, and hence the electronic and optical properties of the device that are governed by quantum confinement effects [16, 26].

The present work addresses the effect of mild annealing in furnace (i.e. from temperature as low as 100 to 600 °C for a minuscule period of 1 min) on the morphology of multilayer-structure (MLs) with SiGe nanocrystals sandwiched between in SiO_2 matrix and its photoconductive properties. The sample is exposed to heat treatment for short period after the furnace reaches desired annealing temperature. The aim here is to attain high photosensitivity with their application in silicon based devices which requires low processing temperature to preserve the functionality of devices.

2. Experiment

Multilayers of SiO_2 and SiGe were deposited on $12 \times 12 \text{ mm}^2$ Si (001) substrates by rf magnetron sputtering using CESAR[®] 136 rf power generator (13.56 MHz). Prior to deposition, the substrates were etched with 2M HF for 120 s to remove native oxide. Firstly, the deposition chamber was throttled to 5×10^{-6} Pa and then Argon (Ar) of 99.999% (5N) purity was used as a working gas. For the SiO_2 deposition, the working gas was mixed with 5N O_2 in order to prevent oxygen deficiency of SiO_2 films. The flow rates for Ar ($q_{\text{Ar}} = 20$ sccm) and O_2 ($q_{\text{O}_2} = 1.5$ sccm) were controlled by mass flow controller (~ 93% Ar and 7 % vol. O_2), and throttle valves were adjusted to stabilize growth pressure of 0.4 Pa during deposition.

For the SiGe deposition, we used a custom build target, consisting of flat Si (6N) and Ge (6N) pieces being attached with a thermal paste on Si-wafer. A negative substrate bias of 10 V was maintained during the SiGe deposition whereas zero bias was applied for the SiO_2 deposition. Sputtering powers of 150 W and 60 W rf were used for depositing SiO_2 and SiGe, respectively. The stacking order of the deposited multilayer structure (MLs) is Si wafer/ buffer SiO_2 (200 nm)/ SiO_2 (50 nm) / SiGe (200 nm) / top SiO_2 (25 nm) (see Fig. 1). The sample holder was placed on a rotating assembly, which could be positioned directly above the required target for a uniform deposition with 120 mm distance between

target and sample holder. After deposition, the samples were annealed in a furnace in N₂ (5N) ambient at temperature ranging from 100 to 600 °C for a duration of 1 to 5 min.

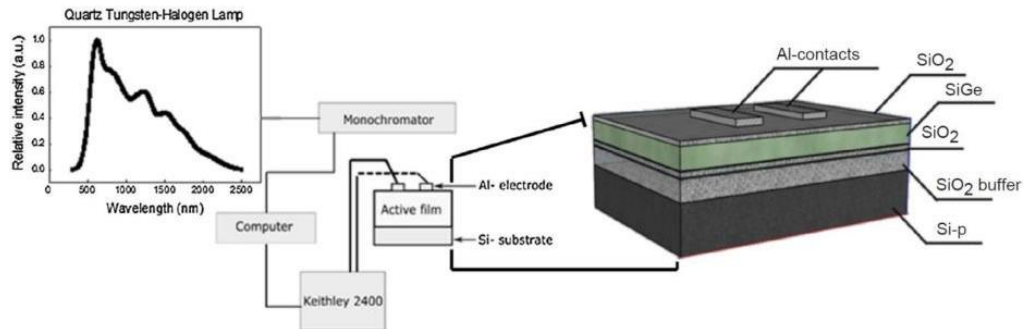


Figure 1. MLs scheme consisting of Si-wafer/ buffer-SiO₂ (200 nm)/ SiO₂ (50 nm) / SiGe (200 nm) / top-SiO₂ (25 nm); Al contacts are illustrated on the top side of MLs.

The crystalline structure of the annealed samples was studied using Jeol ARM 200F transmission electron microscopy (TEM) and Philips X'pert diffractometer (CuK α , 0.15406 nm) with hybrid monochromator on incident stage and collimator slit of 0.27° to get X-ray diffractograms.

The XPS recorded spectra were obtained using SPECS XPS spectrometer based on Phoibos analyzer with monochromatic X-rays emitted by an anti-cathode of Al (1486.7 eV).

Photoconductivity measurements were performed in DC regime at applied voltage of 1 V between two parallel 2×4 mm² coplanar Al contacts that are separated by 4 mm distance. The contacts were deposited with electron-beam evaporation. The measurement setup consisted of Keithley 2400 electrometer, Acton-SpectrPro 150 monochromator with 600 – 1400 nm wavelength range, cryostat with four optical windows and a QTH10 (/M) quartz tungsten-halogen lamp (50 mW optical output power) as light source and quartz lens to focus light.

The photocurrent spectra were acquired by subtracting the dark current from measured data under illumination and were normalized to the spectral irradiation intensity of the light source provided by the manufacturer...

3. Result and Discussion

Two sample series were fabricated, one in which the annealing temperature was kept constant at 600 °C and annealing time was varied (1, 3 and 5 min) and other one in which the annealing time was kept constant (1 min) and the annealing temperature was varied from 100 to 600 °C. A list of the samples is shown in Table 1.

Table 1. Process parameters of fabricated MLs.

Annealing time (min)	Annealing temperature (°C)							
	100	300	400	500	550	600	650	700
1	×	×	×	×	×	×	×	×
3						×		
5						×		

The diffractograms of as-deposited (asd) and 600 °C annealed samples for 1 min, (Si-wafer/ buffer SiO₂/ SiO₂/ SiGe/ top SiO₂), are presented in Fig. 2. For the asd sample, only broad diffraction peaks are seen, indicating amorphous nanoparticles or clusters. In contrast, sharp peaks are seen for the annealed sample, demonstrating the presence of crystalline SiGe with approximately 30-70 composition (as calculated from XRD peak positions). These peaks correspond to (111), (220) and (311) crystallographic planes positioned between cubic Si and Ge shown by vertical dotted lines in Fig. 2 [27].

The transition from amorphous to crystalline structure for samples annealed at 100-700 °C for 1 min is shown by the GiXRD graph in Fig. 3. For samples annealed at 100 – 400 °C, only broad humps are seen, whereas annealing at temperatures of 500 °C and higher results in sharp distinct peaks, indicating crystalline SiGe. In the case of MLs annealed from 500 to 700 °C, the crystallinity is associated with the formation of SiGe NCs, while for both the asd and MLs annealed in the 100 - 400 °C range, the broad humps point out that SiGe is mainly amorphous.

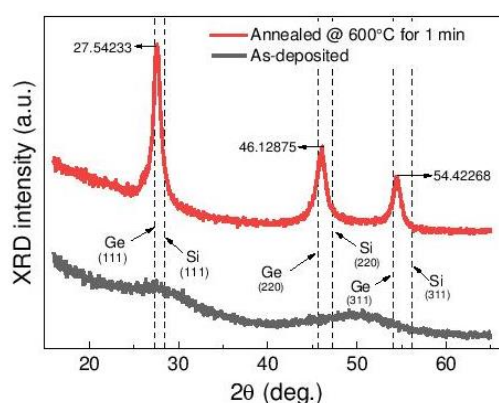


Figure 2. XRD graph for Si wafer/ buffer SiO₂/ SiO₂/ SiGe/ top SiO₂ in asd (lower line) and annealed at 600 °C for 1 min (upper line); arrows indicate peak positions and vertical dashed lines correspond to standard tabulated positions for cubic Ge ($2\theta = 27.45^\circ; 45.59^\circ; 54.04^\circ$ - ASTM 01-079-0001) and cubic Si ($28.45^\circ; 47.31^\circ; 56.13^\circ$ - ASTM 01-070-5680).

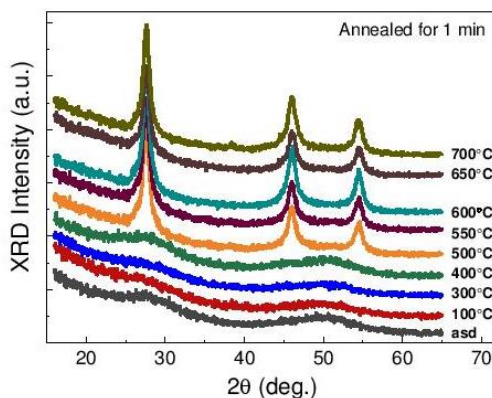


Figure 3. GiXRD graphs for asd MLs and MLs annealed at various temperature for 1 min.

Fig. 4 shows how the lattice strain and crystallites size changes with annealing temperature (a) and (c) and annealing time (b) and (d). The size of the SiGe crystallites and measured lattice strain of the MLs were calculated on the bases of the (111) crystallographic peaks in Fig. 3 using Scherrer equation [28]. The mentioned approach is an inexplicit approximation to analyze the change in strain, since the effect of change in 'x' for $\text{Si}_{1-x}\text{Ge}_x$ after annealing, strain broadening, lattice imperfections and instrumental error cannot be ruled out.

It was assumed that some clusters would form in the amorphous samples annealed at temperatures lower than 400 °C (Fig. 3), and therefore the NCs sizes were calculated only for annealing temperature higher than 400 °C. In general, the lattice strain increases and the crystal size decreases with increasing annealing temperature (Fig. 4(a, c)). However, for 550 °C annealing temperature the lattice strain is highest and the NCs are smallest. The above uncommon reduction in size of crystallite and the effect of strain is discussed below together with TEM analysis. To mention here, we tried rapid annealing in conventional furnace by carrying exposures for such short durations and it can expected that the temperature over MLs under exposure does not reach the desired temperature fully. Rather the temperature mentioned is the temperature of the furnace tube which was held there for 30 min (excluding ramping time) before the samples were inserted. In this regard, we expect to have small-scale and cogent changes in the size of nanocrystals.

With reference to the lattice strain, a similar trend at higher temperature has also been discussed in details by others [29]. The significance of Fig. 4 will be discussed later in following section with reference to effect of strain and size on photocurrent intensity and shift in peak position caused by annealing temperature and time.

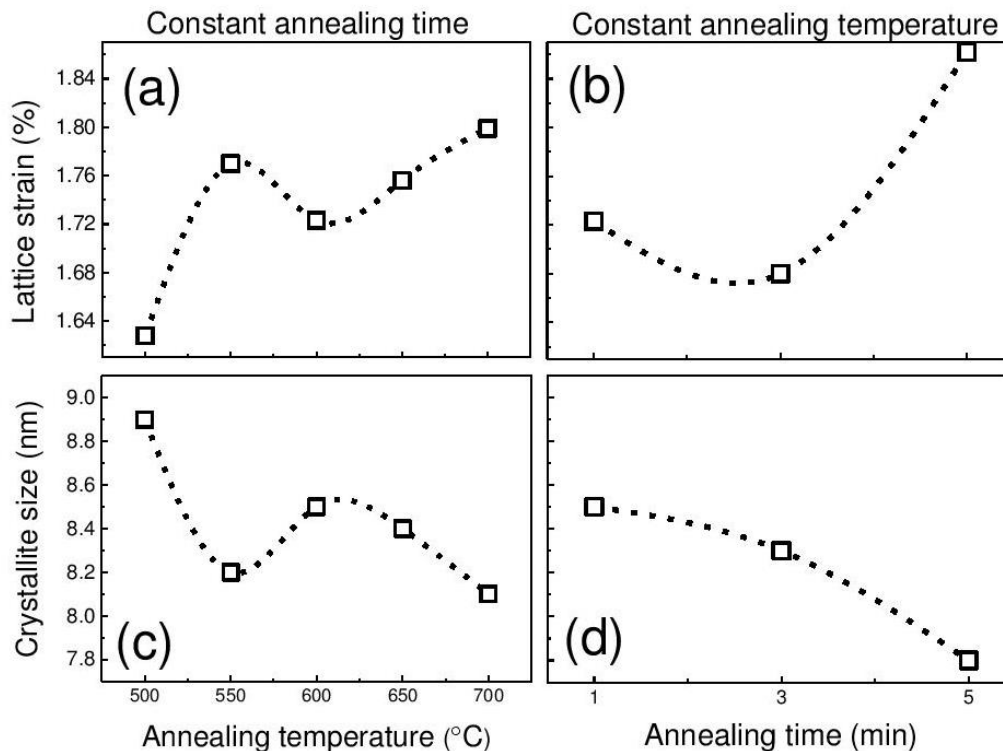


Figure 4. Effect of annealing temperature (a, c) and annealing time (b, d) on MLs lattice strain, and SiGe crystallites size.

Fig. 5(a) presents a cross-section TEM (XTEM) image at low magnification of a sample annealed at 600 °C for 1 min together with the sizes of each layer in the structure. Fig. 5(b) shows the EDX spectrum measured in the middle of the SiGe layer (area encircled in Fig 5(a)). One can see that the total thickness of the SiO₂ buffer layer together with the first deposited SiO₂ layer is about 230 nm, while the SiGe layer is 195 nm thick and a top SiO₂ layer of 35 nm. The SiGe layer composition is shown in Fig. 5(b) from which it results that Si:Ge ratio in the SiGe layer is 40:60, compared to 30:70 ratio obtained from the XRD graph in Fig. 2.

In Fig. 6, we present the electron diffraction measurements. The area used for electron diffraction (shown in Fig. 6(a)) was selected in order to have the Si substrate spots together with the ring spots of the SiGe polycrystalline layer. The Si diffraction spots are used as an inside reference for measuring SiGe layer ring spots as shown in the SAED pattern in Fig. 6(b, c). These measurements indicate a lattice parameter value of 0.557 ± 0.003 nm for the cubic SiGe structure, which corresponds to SiGe with 35:65 composition [30], which is in the middle of the two values obtained above. In addition, the value of lattice parameter obtained from GiXRD plot by peak (220) positioned at 46.043° (2θ) for MLs annealed at 600 °C for 1 min (Fig. 3) is consistent with the value obtained by EDX i.e. 0.5571 nm.

The inconsistency in the Si:Ge ratios derived from EDX, XRD and electron diffractions is due to silicon oxide formed in the SiGe layer that contain an appreciable amount of oxygen, i.e. 16 % oxygen and some Ar (Fig 5(b)). Thus, EDX gives the total amount of atoms in SiGe layer while the diffraction data are only related to the crystalline phase.

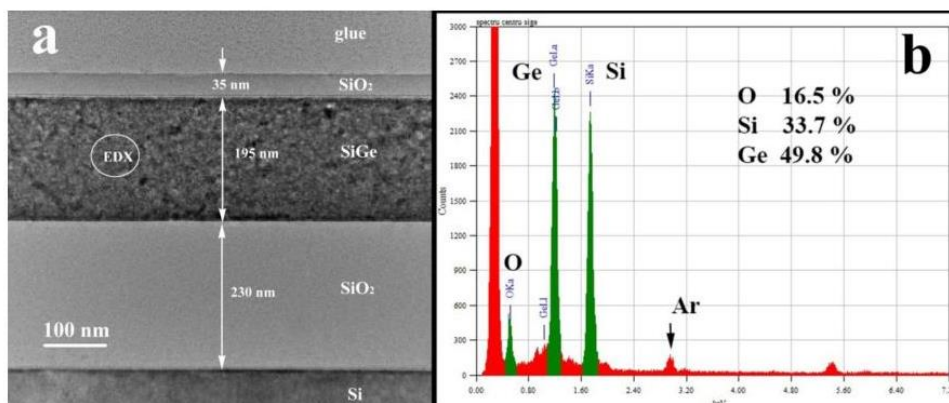


Figure 5. (a) Low magnification XTEM image taken on sample annealed at 600 °C for 1 min; (b) EDX spectrum measured in the middle of the SiGe layer.

Fig. 7 shows TEM images of defects in SiGe NCs (Fig. 7(a)) and the corresponding HRTEM detail (Fig. 7 (b)) of a sample annealed at 600 °C for 1 min. The HRTEM image emphasizes that SiGe NCs have a lens-like morphology that is formed by a sequence of shearing lattice defects inside a SiGe nanocrystal, due to a partial relaxation of the stress field. These planar sharing defects are more complex than stacking faults and micro-twins, that also appear in SiGe layer images (not shown). Figure 7(c) shows a defocused TEM image of the SiGe layer in the very thin area of the specimen, showing the presence of a high density of spherical nanopores. These nanopores have an average diameter of about 7 nm and are probably filled with Ar-gas, as indicated by the EDX spectrum in Fig. 5.

The observed decrease of the SiGe NC size with increasing annealing temperature and time (seen in Fig. 4(c, d)) is an uncommon result, but it can be explained on basis of the competition between the

stress field developed inside the SiGe structure during the crystal growth process and the relaxation mechanism by the defect formation. The 600 °C annealing involves a rapid crystal growth. In this process, the amorphous oxide species present inside the asd SiGe layer can be incorporated inside the growing SiGe NC, forming the defects shown in Fig 7(b). The rest of the amorphous oxide (mainly Si oxide) remains in between the SiGe NCs. Consequently, XRD will indicates smaller size for the coherent crystallite size in samples annealed at higher temperature. At lower annealing temperature, the oxides atomic species did not get incorporated by the crystal growth process. The stress field is partially released by producing planar shearing defects inside the SiGe NCs.

The rapid deposition of the amorphous SiGe layer leads to Ar and O gas incorporation in the deposited layer. The Ar diffusion and segregation during SiGe film crystallization leads to nanovoids formation. The oxygen, on the other hand, remains inside the SiGe layer and decorates the interfaces between the SiGe crystallites. Our estimation indicates that about 5 % of the SiGe layer volume represents nanovoids and about 10 % of the SiGe layer volume is amorphous oxide. Therefore, the SiGe crystallization in the presence of nano-voids formation and oxide phase can explain the uncommon evolution of the SiGe NCs size with annealing temperature.

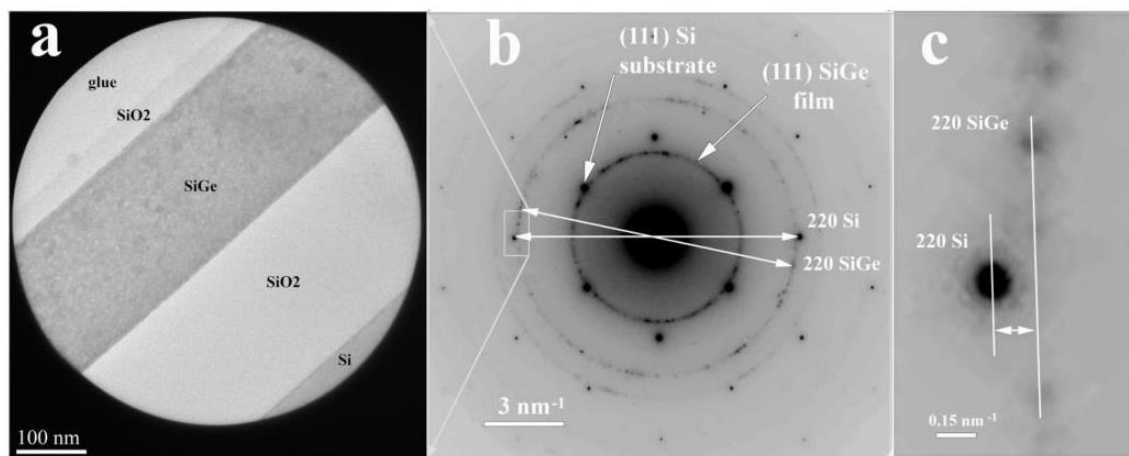


Figure 6. Selected area electron diffraction measurements: a) selected area used for electron diffraction, in order to obtain comparable intensities for the Si substrate spots and the SiGe ring spots; b) SAED pattern and the enlarged detail (image c) of the measurements between the Si (220) spot and the (220) SiGe ring spots. The estimated error of the measurements is 0.5%.

Fig. 8 presents XPS spectra taken on the free surface on the top SiO₂ layer, together with deconvoluted curves and fit. One can see that the curve presents a peak corresponding to the top SiO₂ layer, another one to metalloid Si and a small peak corresponding to SiO_x [31]. For Ge no peak was detected. As there might be a possibility that the Ge may have had diffused into top SiO₂ layer after annealing [32, 33].

Dark current-voltage characteristics of all samples were symmetric shape and a low rectifying behaviour. The results obtained on MLs annealed at 600 °C for 1 min are presented in Fig. 9. The relatively high value of the currents measured in dark and under illumination (in the coplanar configuration of the electrodes) is due to the presence of metallic Si inside the SiO₂ top layer as revealed by XPS spectra in Fig. 8. The current measured under illumination evidences the high photosensitivity

of the sample (for example, the photocurrent at applied voltage of 1.5 V is more than an order of magnitude higher than the dark current).

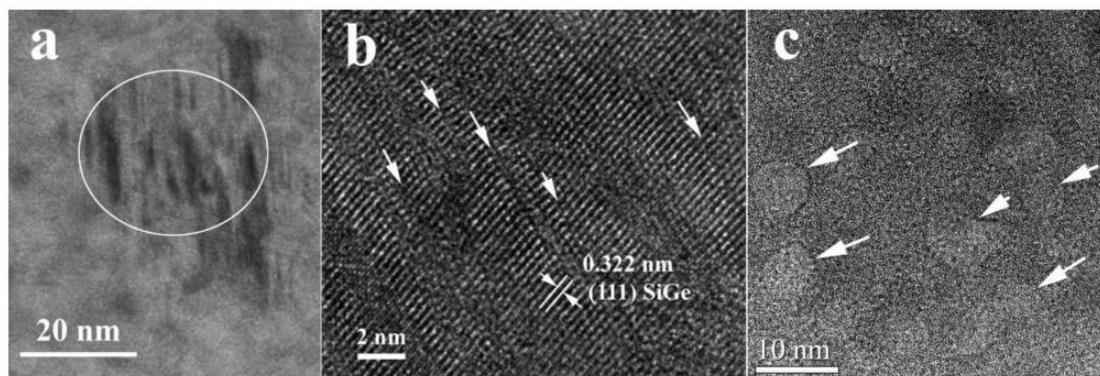


Figure 7. TEM images of the SiGe layer obtained from the cross section specimen: a) Bragg contrast of the lens-like morphology of the SiGe crystallites; b) HRTEM detail of the area shown in Fig. 7(a); c) Defocused TEM image showing high density of spherical nanopores (arrowed).

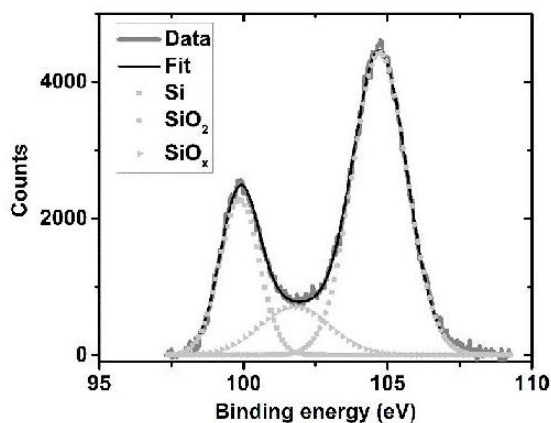


Figure 8. XPS spectra Si 2p line – 10nm depth ($Al_{K\alpha 1}$, monochromatic RX, 1486.7 eV) measured on the free surface of the top SiO_2 layer: ■ metallic Si; ► SiO_x ; ● SiO_2 [31].

Figs. 10(a, b) shows the photocurrent spectra for samples annealed at different temperatures for 1 min. For the sake of clarity, the spectra for asd MLs and annealed at 100 to 600 °C on one hand, and MLs annealed at 600 to 700 °C on the other hand, are plotted separately. The spectra in both Figs. 10(a, b) may be divided into two regions, A and B. Region B extends from 840-1030 nm and is due to NCs contribution in annealed MLs. Then there is region A (674-840 nm), which we assign to the presence of stress that can produce defects (trapping and/or recombination centers) inside the structure and at NCs interfaces [34, 35]. A prominent peak (*N*) located in region B and a shoulder (*D*) which evolves to become the second peak in Region A at higher annealing temperature, is seen.

The dependence of photocurrent spectra on annealing temperatures is further investigated by deconvolution using Gaussian fitting (Fig. 11). The deconvolution is done over three individual components at 756, 951 and 1030 nm; the two first components (756 and 951 nm) are the center position

of regions A and B in Fig. 10, given the labels C_A and C_B (which represents the shoulder D and peak N), respectively. Component C_A is assigned to presence of defects due to strain and C_B to photo-response from NCs as ascribed earlier for the two regions, whereas peak C_C can be assigned to surface photo-voltage and gating effect in MLs as described by Lepadatu *et al.* [36].

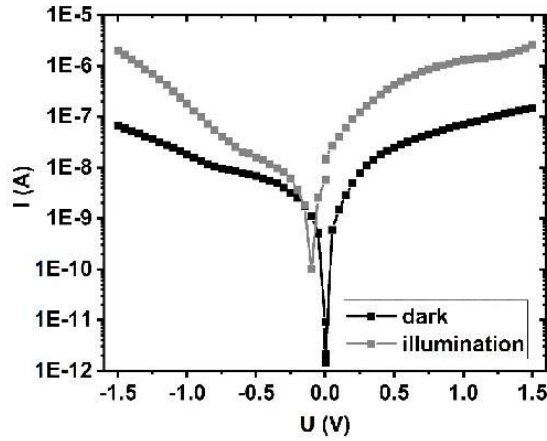


Figure 9. I-V characteristics in dark and under illumination with a 20W incandescence lamp measured on MLs annealed at 600 °C for 1 min.

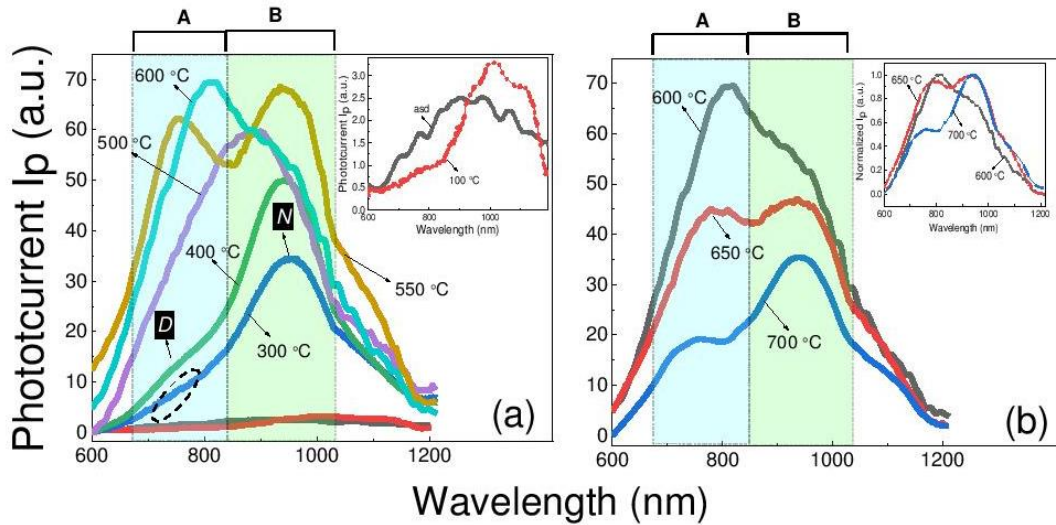


Figure 10. Photocurrent spectra measured at room temperature for: (a) MLs asd and annealed at 100 to 600 °C for 1 min. Inset shows a zoomed-in spectra of the asd MLs and MLs annealed at 100 °C; (b) MLs annealed at 600 to 700 °C with the normalized curves to unity, in inset.

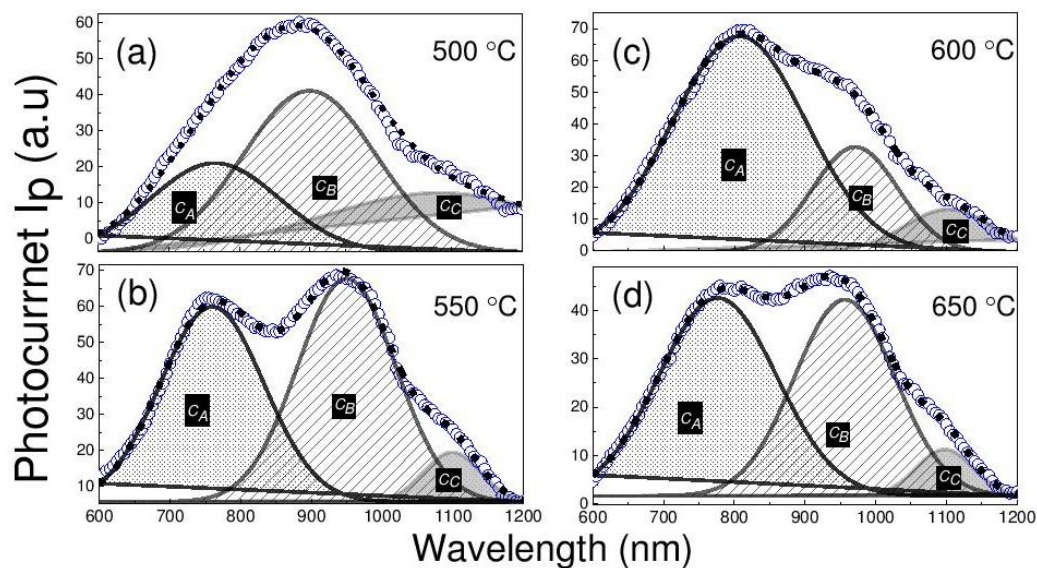


Figure 11. Deconvolution of spectrum for MLs annealed at 500, 550, 600 and 650 °C for 1 min. The open circles are measured spectra and the black dotted lines shows the sum of the three Gaussian curves (C_A , C_B and C_C).

The average intensity $[(C_A + C_B)/2]$ of photocurrent spectra versus annealing temperature are shown in Fig. 12.

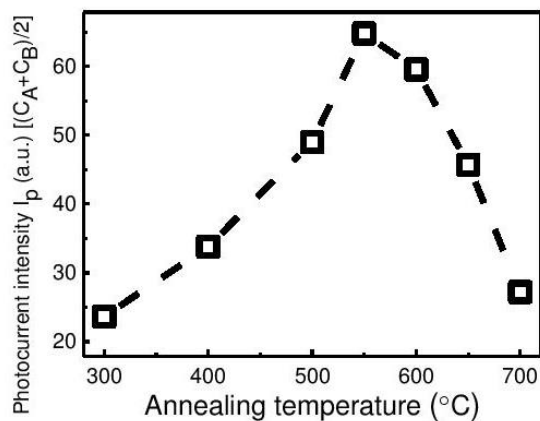


Figure 12. Average intensity of peaks C_A and C_B for MLs annealed at various temperatures for 1 min in Fig. 10.

The shift in peak position with increasing annealing temperature (Fig. 10) is accompanied by a considerable increase in the photocurrent intensity up to 600 °C (Fig. 12), after which it drops. The decrease in intensity for MLs annealed from 600 to 700 °C is in good agreement with HRTEM results. This change in intensity may be further clarified by Fig (4), where the decrease and increase of strain is indicative of increase and decrease of spectral intensity, respectively, and can be explained by the increase of planar defects density produced inside the SiGe NCs, acting as recombination centers and/or

traps. It is well-known that, besides the NCs size and density, the alteration in defects density and/or change in interface quality can influence the aspect of photocurrent spectra [37, 38, 39].

We can conclude on the effect of strain over photocurrent spectra of MLs annealed from 550 to 700 °C, that: (1) the strain determines the increase or decrease of spectral intensity. (2) The strain exerted by degree of matrix ordering causes the NCs to reduce in size together with SiGe NCs distortion forming a lens like morphology and defect inside NCs resulting in appearance of peak C_A . The behavior of strain and its effect on size and shape on NCs is discussed later in this section.

The shift of the C_A and C_B peak positions and the relative change in height/ intensity observed by increasing annealing temperature (Fig. 10 and 11) is due to the weight change of the two contributions of SiGe NCs (in region B) and of defects and strain (region A). The impact of NCs resulted from the cut of the coherence length by complex shearing planar defects formation is not evidenced in the photocurrent curves, as the potential barrier introduced by these defects is too small.

Fig. 13 shows photocurrent spectra for MLs annealed at fixed temperature of 600 °C, for different time intervals of 1, 3, and 5 min. The regions A^* and B^* can be considered analog to regions A and B in Fig. 10. Here, the bimodal feature is also clearly visible, similar to that seen in Fig. 10. For the shortest annealing time (1 min), the photocurrent spectrum has one maximum at ~ 800 nm and a shoulder on the red side, while for the longest annealing time (5 min) the maximum intensity is located at ~ 950 nm (the shoulder position in 1 min annealed sample) and a shoulder at ~ 800 nm. As seen, both maxima coexist after the intermediate annealing time (3 min) as also emphasized with the inset showing intensity normalized to unity. A similar behavior is observed for the case of annealing temperature at constant time from 600 to 700 °C (inset Fig. 10(b)). The changes in the photocurrent curves for samples annealed at 600 °C for 1, 3 and 5 min can be explained in light of the observation shown in Fig. 7 and 4(b), where the spectral intensity changes in accordance with the strain *i.e.* decrease in strain results in an increase of spectral intensity. The alteration in spectral intensity (C_{A^*}) and a shift in peak position (C_{B^*}) from 971, 960 to 908 nm, is assigned to two different mechanism *i.e.* C_{B^*} exhibit blue shift as the NCs size reduces, whereas changes of relative intensity (and height) of C_{A^*} with respect C_{B^*} is attributed to strain exerted over NCs by the surrounding dielectric matrix.

The peak N in region B and B^* , located at about 950 nm wavelength (seen in Figs. 10 and 14, respectively) can be correlated with SiGe NCs of about 8 nm diameter. For pure Ge NCs of 8 nm size a bandgap of about 1 +/- 0.1 eV, was measured by tunneling spectroscopy [40] in agreement with earlier calculations based on tight-binding or $k\cdot p$ approximations [41]. For pure Si NCs of 8 nm size, the tunneling spectroscopy measurements gave about 1.4 +/- 0.1 eV [42], in agreement with earlier photoluminescence data [43]. It is therefore reasonable to assume that the energy gap of a SiGe nanocrystal, with similar size (8 nm) would be in between these two values. To test this hypothesis we performed DFT based atomistic simulations using the software SIESTA [44]. However, NCs of 8 nm diameter, correspond to about 10000-12000 Si or Ge atoms, which is too large for a realistic computational power. Instead, we considered spherical clusters of about 3 nm diameter, with 516 Si or Ge atoms, passivated at the surface with H. For pure Ge and Si cases we obtained $E_g = 1.53$ eV and 1.98 eV, respectively. For several Si_xGe_{1-x} mixtures with random spatial configurations we obtained, after the relaxation, $E_g = 1.90$ eV for $x = 0.55$, 1.87 eV for $x = 0.50$, and 1.85 eV for $x = 0.45$. The standard deviation of these energy gaps are below 1%. Note that the results are above the mean value of the gaps for pure Ge and pure Si. Therefore we conclude that an estimated gap of 1.3 eV for our 8 nm GeSi NCs, *i.e.* slightly above the mean value of 1.2 eV of the mentioned experimental data, matching the 950 nm, explains the peak in region B and B^* .

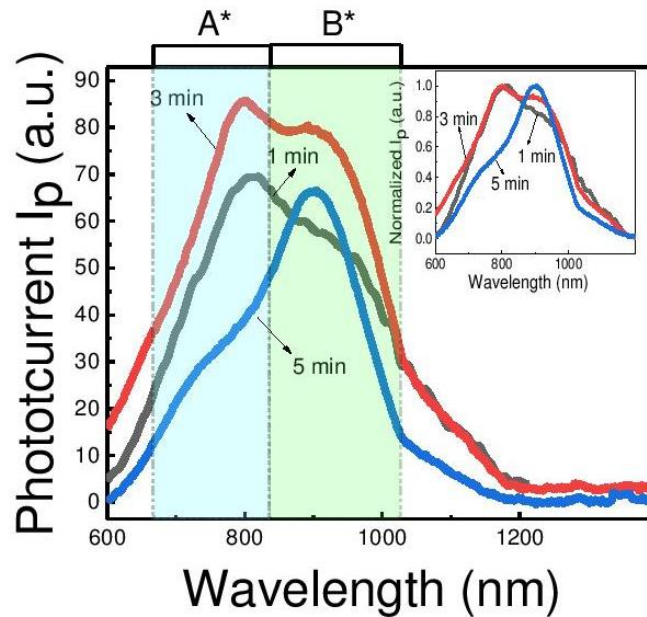


Figure 13. The effect of annealing time on photocurrent spectra taken on MLs annealed at 600°C for 1, 3 and 5 min. The inset shows a zoomed-in view of spectra normalized to unity.

The peak observed in regions A and A* can be explained by the presence of stress field in the structure or strain in the structure. One of the issues with embedding NCs in amorphous or dielectric matrix is the formation of residual stresses [45]. This is due to lattice mismatch between Si and Ge (in our case), different thermal expansion coefficient and density gradient between NCs and SiO₂. It is believed that strain is present in MLs and after annealing when the two structures are merged at the interface, one of the two components will deform in order to accommodate the transition/restructuring in ordering of network [46]. Thus we can expect that the interface between SiGe NCs to be discontinuous *i.e.* incoherent, in according to TEM investigations.

It has been shown that the NCs crystallinity and shape is affected by degree of matrix ordering and that it can produce strain in the structure especially at nanocrystals/ matrix interface [47, 48]. These strains causes the NCs to deform which also in turn alters the band gap. It is well documented that NCs are under large stress when embedded in an oxide matrix [45, 47, 49, 50] and that the magnitude of either compressive or tensile stress varies with NCs size. According to Zatoryb *et al* [50] small nanocrystals are under compressive stress, the magnitude of which depends upon the matrix ordering. That is, ordering of matrix network determines the accommodation of expanding NCs. Consequently, large compressive stress will be exerted over NCs if the matrix forms an ordered structure, resisting them to expand freely [47]. Thus, we assume that the increase in height of peak A (and A*) is due to deformation of NCs which are under compressive stress state, and does collapse after a given strain energy barrier is exceeded. Thus forming a lens like structure and creating defect inside NCs, as evident

in the HRTEM image for MLs annealed at 600 °C for 1 min (Fig. 7) and Fig. 10 and 11(c) where peak C_A is higher than the C_B , portraying large compressive stress present over the NCs.

In summary it is demonstrated how short exposure (1 min) of conventional furnace annealing for temperature range 100 – 700 °C can exhibit enhanced photocurrent intensity of SiGe nanocrystals in SiO₂ matrix. A 29-fold increment in photocurrent intensity was obtained, in contrast to structure containing Ge NCs embedded in TiO₂ matrix [36] where an increment of up to 3 fold is observed for structure annealed via rapid thermal processor at 550 °C relative to as-deposited ones. In addition, temperature as low as 300 °C for 1 min markedly exhibits the light sensitivity of the film. This suggests that even amorphous (or just slightly crystalline at best) nanoparticles/clusters does significantly contribute to the improved photosensitivity. In this relation, it may be noticed that amorphous materials have been demonstrated to show strong quantum confinement at the same time as crystalline material only exhibited medium confinement, regardless of the system confinement dimensions [51].

Conclusion

Si wafer/ buffer SiO₂ (230 nm) / SiGe (195 nm)/ top SiO₂ (35 nm) ML with SiGe NCs were prepared by using rf magnetron sputtering followed by short annealing in furnace with the aim to enhance its photoconductive properties in the infrared region. By using short thermal annealing time (1 min), we hamper deterioration of the structure and consequent degradation of the photosensitivity. An average NCs size of roughly 8 nm was formed by the annealing process. An increased sensitivity in the infrared region (~ 950 nm) of more than an order of magnitude higher was established compared to as-deposited MLs. The top SiO₂ contains metallic Si, which lower the resistivity of the film. Consequently, dc currents in dark and under illumination could easily be measured. The dark current-voltage characteristics are symmetric and have low rectifying behaviour.

Further, we have shown that SiGe layer has a complex morphology due to uncommon feature of the rf sputtering that leads to the incorporation of argon and oxygen inside SiGe layer. This leads to the formation of an amorphous oxide layer at NCs interfaces. Some of oxide species are embedded in the growing NCs due to the rapid crystallization process (at high temperatures). This leads to the formation of uncommon morphology of SiGe layer and of smaller NC size at high temperature in respect to low temperature.

At intermediate annealing conditions, a bimodal spectral-curve with two maximums is observed. The relative ratio between the two peaks, and their intensity, can be controlled by the annealing time and temperature in certain range. We hypothesis that this bimodal behavior is caused by the presence of NCs (spherical and lens-shaped) and a strain field as a result of annealing. A competition between the growth/ crystallization of the NCs and a resulting structural stress, determines the prevailing shape of spectral curve. The possibility of modulating the spectral sensitivity makes this structure a possible candidate for various optical sensors applications.

AUTHOR INFORMATION

Corresponding Author

Halldór Guðfinnur Svavarsson

*E-mail: halldorsv@ru.is

Muhammad. Taha Sultan

*E-mail: muhammad16@ru.is

Acknowledgements

This work is funded through M-ERA.NET project PhotoNanoP UEFISCDI Contract no. 33/2016, PCE project UEFISCDI Contract no. 122/2017 and by Romanian Ministry of Research and Innovation through NIMP Core Program PN16-480102 and by the Technology Development Fund of the Icelandic Centre for Research, grant no. 159006-0611. The atomistic simulation were performed via high performance computer cluster, garpur.ihpc.hi.is, which is operated by the University of Iceland and Reykjavik University.

References

- [1] S.R.C. Pinto, R.J. Kashtiban, A.G. Rolo, M. Buljan, A. Chahboun, U. Bangert, N.P. Barradas, E. Alves, M.J.M. Gomes, Structural study of $\text{Si}_{1-x}\text{Ge}_x$ nanocrystals embedded in SiO_2 films, *Thin Solid Films*. 518 (2009) 2569–2572. doi:10.1016/j.tsf.2009.09.148.
- [2] D.N. Lobanov, A.V. Novikov, K.E. Kudryavtsev, A.N. Yablonskiy, A.V. Antonov, Y.N. Drozdov, D.V. Shengurov, V.B. Shmagin, Z.F. Krasilnik, N.D. Zakharov, P. Werner, Electroluminescence and photoconductivity of GeSi heterostructures with self-assembled islands in the wavelength range 1.3–1.55 μm , *Phys. E Low-Dimensional Syst. Nanostructures*. 41 (2009) 935–938. doi:10.1016/J.PHYSE.2008.08.003.
- [3] N.A.P. Mogaddam, A.S. Alagoz, S. Yerci, R. Turan, S. Foss, T.G. Finstad, Phase separation in SiGe nanocrystals embedded in SiO_2 matrix during high temperature annealing, *J. Appl. Phys.* 104 (2008) 124309. doi:10.1063/1.3048543.
- [4] J.-N. Aqua, I. Berbezier, L. Favre, T. Frisch, A. Ronda, G.E.W. Bauer, Growth and self-organization of SiGe nanostructures, *Phys. Rep.* 522 (2013) 59–189. doi:10.1016/j.physrep.2012.09.006.
- [5] A. Lepadatu, M. Ciurea, Tuning the properties of Ge and Si nanocrystals based structures by tailoring the preparation conditions, *Dig. J. Nanomater. Biostructures*. 10 (2015) 59–87. <http://www.infim.ro/papers/tuning-properties-ge-and-si-nanocrystals-based-structures-tailoring-preparation-conditions> (accessed August 11, 2018).
- [6] B. Zhang, Y. Yao, R. Patterson, S. Shrestha, M.A. Green, G. Conibeer, Electrical properties of conductive Ge nanocrystal thin films fabricated by low temperature *in situ* growth, *Nanotechnology*. 22 (2011) 125204. doi:10.1088/0957-4484/22/12/125204.
- [7] S.S. Tzeng, P.W. Li, Enhanced 400–600 nm photoresponsivity of metal–oxide–semiconductor diodes with multi-stack germanium quantum dots, *Nanotechnology*. 19 (2008) 235203. doi:10.1088/0957-4484/19/23/235203.
- [8] A.K. Sood, J.W. Zeller, R.A. Richwine, Y.R. Puri, H. Efstathiadis, P. Haldar, N.K. Dhar, D.L. Polla, SiGe Based Visible-NIR Photodetector Technology for Optoelectronic Applications, in: *Adv. Opt. Fiber Technol. Fundam. Opt. Phenom. Appl., InTech*, 2015. doi:10.5772/59065.
- [9] P. Liu, S. Cosentino, S.T. Le, S. Lee, D. Paine, A. Zaslavsky, D. Pacifici, S. Mirabella, M. Miritello, I. Crupi, A. Terrasi, Transient photoresponse and incident power dependence of high-efficiency germanium quantum dot photodetectors, *J. Appl. Phys.* 112 (2012) 083103. doi:10.1063/1.4759252.

- [10] P.H. Liao, K.P. Peng, H.C. Lin, T. George, P.W. Li, Single-fabrication-step Ge nanosphere/SiO₂/SiGe heterostructures: a key enabler for realizing Ge MOS devices, *Nanotechnology*. 29 (2018) 205601. doi:10.1088/1361-6528/aab17b.
- [11] H. Ye, J. Yu, Germanium epitaxy on silicon, *Sci. Technol. Adv. Mater.* 15 (2014) 024601. doi:10.1088/1468-6996/15/2/024601.
- [12] C.P. Church, E. Muthuswamy, G. Zhai, S.M. Kauzlarich, S.A. Carter, Quantum dot Ge/TiO₂ heterojunction photoconductor fabrication and performance, *Appl. Phys. Lett.* 103 (2013) 223506. doi:10.1063/1.4826916.
- [13] G.G. Pethuraja, R.E. Welsler, A.K. Sood, C. Lee, N.J. Alexander, H. Efstathiadis, P. Haldar, J.L. Harvey, Effect of Ge Incorporation on Bandgap and Photosensitivity of Amorphous SiGe Thin Films, *Mater. Sci. Appl.* 03 (2012) 67–71. doi:10.4236/msa.2012.32010.
- [14] I. Stavarache, A.-M. Lepadatu, T. Stoica, M.L. Ciurea, Annealing temperature effect on structure and electrical properties of films formed of Ge nanoparticles in SiO₂, *Appl. Surf. Sci.* 285 (2013) 175–179. doi:10.1016/J.APSUSC.2013.08.031.
- [15] W. Choi, S. Kanakaraju, Z. Shen, W. Li, Characterization of Ge nanocrystals in a-SiO₂ synthesized by rapid thermal annealing, *Appl. Surf. Sci.* 144–145 (1999) 697–701. doi:10.1016/S0169-4332(98)00908-8.
- [16] Y.X. Jie, X. Wu, C.H.A. Huan, A.T.S. Wee, Y. Guo, T.J. Zhang, J.S. Pan, J. Chai, S.J. Chua, Synthesis and characterization of Ge nanocrystals immersed in amorphous SiO_x matrix, *Surf. Interface Anal.* 28 (1999) 195–199. doi:10.1002/(SICI)1096-9918(199908)28:1<195::AID-SIA606>3.0.CO;2-L.
- [17] E.M.F. Vieira, S.R.C. Pinto, S. Levichev, A.G. Rolo, A. Chahboun, M. Buljan, N.P. Barradas, E. Alves, S. Bernstorff, O. Conde, M.J.M. Gomes, Influence of the deposition parameters on the growth of SiGe nanocrystals embedded in Al₂O₃ matrix, *Microelectron. Eng.* 88 (2011) 509–513. doi:10.1016/J.MEE.2010.10.016.
- [18] S.K. Ray, S. Das, R.K. Singha, S. Manna, A. Dhar, Structural and optical properties of germanium nanostructures on Si(100) and embedded in high-k oxides., *Nanoscale Res. Lett.* 6 (2011) 224. doi:10.1186/1556-276X-6-224.
- [19] H.G. Chew, W.K. Choi, Y.L. Foo, F. Zheng, W.K. Chim, Z.J. Voon, K.C. Seow, E.A. Fitzgerald, D.M.Y. Lai, Effect of germanium concentration and oxide diffusion barrier on the formation and distribution of germanium nanocrystals in silicon oxide matrix, *Nanotechnology*. 17 (2006) 1964–1968. doi:10.1088/0957-4484/17/8/028.
- [20] M. Zschintzsch, J. von Borany, N.M. Jeutter, A. Mücklich, Stacked Ge nanocrystals with ultrathin SiO₂ separation layers, *Nanotechnology*. 22 (2011) 465302. doi:10.1088/0957-4484/22/46/465302.
- [21] N.P. Barradas, E. Alves, E.M.F. Vieira, A. Parisini, O. Conde, J. Martín-Sánchez, A.G. Rolo, A. Chahboun, M.J.M. Gomes, IBA study of SiGe/SiO₂ nanostructured multilayers, *Nucl. Instruments Methods Phys. Res. Sect. B Beam Interact. with Mater. Atoms.* 331 (2014) 89–92. doi:10.1016/J.NIMB.2013.11.025.
- [22] A.-M. Lepadatu, I. Stavarache, T. F. Stoica, M. L. Ciurea STUDY of Ge nanoparticles embedded in an amorphous SiO₂ matrix with photoconductive properties, *Dig. J. Nanomater. Biostructures.* 6 (2011) 67–73. <http://www.infim.ro/content/study-ge-nanoparticles-embedded-amorphous-sio2-matrix-photoconductive-properties> (accessed August 11, 2018).
- [23] H. Nohira, T. Kuroiwa, M. Nakamura, Y. Hirose, J. Mitsui, W. Sakai, K. Nakajima, M. Suzuki, K. Kimura, K. Sawano, K. Nakagawa, Y. Shiraki, T. Hattori, Quality of SiO₂ and of SiGe formed by oxidation of Si/Si_{0.7}Ge_{0.3} heterostructure using atomic oxygen at 400 °C, *Appl. Surf. Sci.* 237 (2004) 134–138. doi:10.1016/J.APSUSC.2004.06.042.
- [24] J.G. Zhu, C.W. White, J.D. Budai, S.P. Withrow, Y. Chen, Growth of Ge, Si, and SiGe nanocrystals in SiO₂ matrices, *J. Appl. Phys.* 78 (1995) 4386–4389. doi:10.1063/1.359843.
- [25] S.K. Ray, K. Das, Luminescence characteristics of Ge nanocrystals embedded in SiO₂ matrix, *Opt. Mater. (Amst).* 27 (2005) 948–952. doi:10.1016/J.OPTMAT.2004.08.041.
- [26] M.L. Ciurea, M. Draghici, V. Iancu, M. Reshotko, I. Balberg, Coupled confinement effect on the photoluminescence and electrical transport in porous silicon, *J. Lumin.* 102–103 (2003) 492–497. doi:10.1016/S0022-2313(02)00589-6.
- [27] M.L. Ciurea, I. Stavarache, A.-M. Lepadatu, I. Pasuk, V.S. Teodorescu, Electrical properties related to the structure of GeSi nanostructured films, *Phys. Status Solidi.* 251 (2014) 1340–1346. doi:10.1002/pssb.201350112.
- [28] A.L. Patterson, The Scherrer Formula for X-Ray Particle Size Determination, *Phys. Rev.* 56 (1939) 978–982.

doi:10.1103/PhysRev.56.978.

- [29] F. Zheng, W.K. Choi, F. Lin, S. Tripathy, J.X. Zhang, Stress Tuning of Ge Nanocrystals Embedded in Dielectrics, *J. Phys. Chem. C*. 112 (2008) 9223–9228. doi:10.1021/jp801529j.
- [30] J.P. Dismukes, L. Ekstrom, R.J. Paff, Lattice Parameter and Density in Germanium-Silicon Alloys¹, *J. Phys. Chem.* 68 (1964) 3021–3027. doi:10.1021/j100792a049.
- [31] R. Ghita, C. Logofatu, C.-C. Negrila, F. Ungureanu, C. Cotirlan, A.-S. Manea, M.-F. Lazarescu, C. Ghic, Study of SiO₂/Si Interface by Surface Techniques, in: *Cryst. Silicon - Prop. Uses, InTech*, 2011. doi:10.5772/23174.
- [32] S. Balakumar, S. Peng, K.M. Hoe, A. Agarwal, G.Q. Lo, R. Kumar, N. Balasubramanian, D.L. Kwong, S. Tripathy, SiGeO layer formation mechanism at the SiGe/oxide interfaces during Ge condensation, *Appl. Phys. Lett.* 90 (2007) 032111. doi:10.1063/1.2432252.
- [33] S. Foss, T.G. Finstad, A. Dana, A. Aydinli, Growth of Ge nanoparticles on SiO₂/Si interfaces during annealing of plasma enhanced chemical vapor deposited thin films, (2007). doi:10.1016/j.tsf.2006.11.094.
- [34] J. Dasović, P. Dubček, I. Pucić, S. Bernstorff, N. Radić, B. Pivac, The interface quality of Ge nanoparticles grown in thick silica matrix, *Appl. Surf. Sci.* 414 (2017) 1–7. doi:10.1016/J.APSUSC.2017.03.264.
- [35] M.L. Ciurea, S. Lazanu, I. Stavarache, A.-M. Lepadatu, V. Iancu, M.R. Mitroi, R.R. Nigmatullin, C.M. Baleanu, Stress-induced traps in multilayered structures, (2011). doi:10.1063/1.3525582.
- [36] A.-M. Lepadatu, A. Slav, C. Palade, I. Dascalescu, M. Enculescu, S. Iftimie, S. Lazanu, V.S. Teodorescu, M.L. Ciurea, T. Stoica, Dense Ge nanocrystals embedded in TiO₂ with exponentially increased photoconduction by field effect, *Sci. Rep.* 8 (2018) 4898. doi:10.1038/s41598-018-23316-3.
- [37] X.X. Wang, J.G. Zhang, L. Ding, B.W. Cheng, W.K. Ge, J.Z. Yu, Q.M. Wang, Origin and evolution of photoluminescence from Si nanocrystals embedded in a SiO₂ matrix, (n.d.). doi:10.1103/PhysRevB.72.195313.
- [38] F. Gourbilleau, C. Ternon, C. Dufour, X. Portier, R. Rizk, Formation of Si-nc by Reactive Magnetron Sputtering, in: *Silicon Nanocrystals*, Wiley-VCH Verlag GmbH & Co. KGaA, Weinheim, Germany, 2010: pp. 275–295. doi:10.1002/9783527629954.ch11.
- [39] S.W. Pan, B. Zhou, S.Y. Chen, C. Li, W. Huang, H.K. Lai, Optical property investigation of SiGe nanocrystals formed by electrochemical anodization, *Appl. Surf. Sci.* 258 (2011) 30–33. doi:10.1016/J.APSUSC.2011.07.141.
- [40] O. Millo, I. Balberg, D. Azulay, T.K. Purkait, A.K. Swarnakar, E. Rivard, J.G.C. Veinot, Direct Evaluation of the Quantum Confinement Effect in Single Isolated Ge Nanocrystals, *J. Phys. Chem. Lett.* 6 (2015) 3396–3402. doi:10.1021/acs.jpcllett.5b01541.
- [41] Y.M. Niquet, G. Allan, C. Delerue, M. Lannoo, Quantum confinement in germanium nanocrystals, *Appl. Phys. Lett.* 77 (2000) 1182. doi:10.1063/1.1289659.
- [42] O. Wolf, M. Dasog, Z. Yang, I. Balberg, J.G.C. Veinot, O. Millo, Doping and Quantum Confinement Effects in Single Si Nanocrystals Observed by Scanning Tunneling Spectroscopy, *Nano Lett.* 13 (2013) 2516–2521. doi:10.1021/nl400570p.
- [43] M.I. Alonso, I.C. Marcus, M. Garriga, A.R. Goñi, J. Jedrzejewski, I. Balberg, Evidence of quantum confinement effects on interband optical transitions in Si nanocrystals, *Phys. Rev. B.* 82 (2010) 045302. doi:10.1103/PhysRevB.82.045302.
- [44] J.M. Soler, E. Artacho, J.D. Gale, A. García, J. Junquera, P. Ordejón, D. Sánchez-Portal, The SIESTA method for *ab initio* order-*N* materials simulation, *J. Phys. Condens. Matter.* 14 (2002) 2745–2779. doi:10.1088/0953-8984/14/11/302.
- [45] R. Bahariqushchi, R. Raciti, A.E. Kasapoğlu, E. Gür, M. Sezen, E. Kalay, S. Mirabella, A. Aydinli, Stress evolution of Ge nanocrystals in dielectric matrices, *Nanotechnology.* 29 (2018) 185704. doi:10.1088/1361-6528/aaaffa.
- [46] G. Hadjisavvas, P.C. Kelires, Structure and Energetics of Si Nanocrystals Embedded in a-SiO₂, *Phys. Rev. Lett.* 93 (2004) 226104. doi:10.1103/PhysRevLett.93.226104.
- [47] G. Zatyrb, A. Podhorodecki, J. Misiewicz, J. Cardin, F. Gourbilleau, Correlation between matrix structural order and compressive stress exerted on silicon nanocrystals embedded in silicon-rich silicon oxide, *Nanoscale Res. Lett.* 8 (2013) 40. doi:10.1186/1556-276X-8-40.

- [48] G. Hadjisavvas, I.N. Remediakis, P.C. Kelires, Shape and faceting of Si nanocrystals embedded in a-SiO₂: A Monte Carlo study, (n.d.). doi:10.1103/PhysRevB.74.165419.
- [49] P.H. Liao, T.C. Hsu, K.H. Chen, T.H. Cheng, T.M. Hsu, C.C. Wang, T. George, P.W. Li, Size-tunable strain engineering in Ge nanocrystals embedded within SiO₂ and Si₃N₄, Appl. Phys. Lett. 105 (2014) 172106. doi:10.1063/1.4900942.
- [50] G. Zatoryb, J. Misiewicz, P.R.J. Wilson, J. Wojcik, P. Mascher, A. Podhorodecki, Stress transition from compressive to tensile for silicon nanocrystals embedded in amorphous silica matrix, Thin Solid Films. 571 (2014) 18–22. doi:10.1016/j.tsf.2014.09.046.
- [51] E.G. Barbagiovanni, D.J. Lockwood, P.J. Simpson, L. V. Goncharova, Quantum confinement in Si and Ge nanostructures, J. Appl. Phys. 111 (2012) 034307. doi:10.1063/1.3680884.

Paper II

Enhanced photoconductivity of embedded SiGe nanoparticles by hydrogenation

*Sultan M T¹, Gudmundsson J T^{2,3}, Manolescu A¹, Stoica T⁴, Ciurea M L^{4,5} and
*Svavarsson H G¹

¹School of Science and Engineering, Reykjavik University, IS-101 Reykjavik, Iceland

²Department of Space and Plasma Physics, School of Electrical Engineering and Computer Science, KTH-Royal Institute of Technology, SE-100 44, Stockholm, Sweden

³Science Institute, University of Iceland, IS-101 Reykjavik, Iceland

⁴National Institute of Materials Physics, 077125 Magurele, Romania

⁵Academy of Romanian Scientists, 050094 Bucharest, Romania

Published: Applied Surface Science, vol. 479, pp. 403-9, 2019.

DOI: <https://doi.org/10.1016/j.apsusc.2019.02.096>

Applied Surface Science 479 (2019) 403–409



Contents lists available at ScienceDirect

Applied Surface Science

journal homepage: www.elsevier.com/locate/apsusc



Full length article

Enhanced photoconductivity of embedded SiGe nanoparticles by hydrogenation



M.T. Sultan^{a,*}, J.T. Gudmundsson^{b,c}, A. Manolescu^a, T. Stoica^d, M.L. Ciurea^{d,e}, H.G. Svavarsson^{a,*}

^a Reykjavik University, School of Science and Engineering, IS-101 Reykjavik, Iceland

^b Department of Space and Plasma Physics, School of Electrical Engineering and Computer Science, KTH-Royal Institute of Technology, SE-100 44 Stockholm, Sweden

^c Science Institute, University of Iceland, Dunhaga 3, IS-107 Reykjavik, Iceland

^d National Institute of Materials Physics, 077125 Magurele, Romania

^e Academy of Romanian Scientists, 050094 Bucharest, Romania

ARTICLE INFO

Keywords:

SiGe
SiO₂
Nanoparticles
Photocurrent
Hydrogen plasma
Passivation

ABSTRACT

We investigate the effect of room-temperature hydrogen-plasma treatment on the photoconductivity of SiGe nanoparticles sandwiched within SiO₂ layers. An increase in photocurrent intensity of more than an order magnitude is observed after the hydrogen plasma treatment. The enhancement is attributed to neutralization of dangling bonds at the nanoparticles and to passivation of nonradiative defects in the oxide matrix and at SiGe/matrix interfaces. We find that increasing the partial pressure of hydrogen to pressures where H₃⁺ and H₂⁺ were the dominant ions results in increased photocurrent.



Enhanced photoconductivity of embedded SiGe nanoparticles by hydrogenation

M. T. Sultan¹, J. T. Gudmundsson^{2,3}, A. Manolescu¹, T. Stoica⁴, M. L. Ciurea^{4,5}, H. G. Svavarsson¹

¹Reykjavik University, School of Science and Engineering, IS-101 Reykjavik, Iceland

²Department of Space and Plasma Physics, School of Electrical Engineering and Computer Science, KTH-Royal Institute of Technology, SE-100 44, Stockholm, Sweden

³Science Institute, University of Iceland, Dunhaga 3, IS-107 Reykjavik, Iceland

⁴National Institute of Materials Physics, 077125 Magurele, Romania

⁵Academy of Romanian Scientists, 050094 Bucharest, Romania

Abstract

We investigate the effect of room-temperature hydrogen-plasma treatment on the photoconduction of SiGe nanoparticles sandwiched within SiO₂ layers. An increase in photocurrent intensity of more than an order magnitude is observed after the hydrogen plasma treatment. The enhancement is attributed to neutralization of dangling bonds at the nanoparticles and to passivation of nonradioactive defects in the oxide matrix and at SiGe/matrix interfaces. We find that increasing the partial pressure of hydrogen to pressures where H₃⁺ and H₂⁺ were the dominant ions results in increased photocurrent.

Keywords: SiGe; SiO₂; nanoparticles; photocurrent; hydrogen plasma; passivation

1. Introduction

Functional devices with advanced electrical and optical properties, based on oxide and dielectric films with incorporated nanoparticles, have gained interest for the last few decades [1, 2, 3]. In particular, attempts have been made to broaden the spectral sensitivity from the visible-to-infrared regime and to improve charge transport by suppressing defect concentration, neutralizing radiation defect and dangling bonds, with aim towards applications in photovoltaics [4], optoelectronics [5, 6], and photodetectors [7]. For that purpose, substantial studies have been made on SiGe nanoparticles embedded in oxide matrices such as SiO₂ [8, 9, 10], and high-dielectric constant

materials such as Al_2O_3 [11, 12] and HfO_2 [12]. Of these matrices, SiO_2 has gained the most interest since it remains amorphous while providing lateral confinement to the nanoparticles [13, 14] up to high annealing temperatures and due to its compatibility with the well-established Si technology [15]. Several methods exist to fabricate SiGe nanoparticles in a SiO_2 matrix, such as sol-gel [16], molecular beam epitaxy [12], ion implantation [17] and magnetron sputtering [8, 9, 10, 16, 18, 19, 24], the last one being the most common. It is well established that the size and distribution of the nanoparticles affects the optoelectronic properties of the devices in question, partly by tailoring the bandgap energy [10, 20], while the charge transport mechanism is governed by electrical behavior of the films [21]. With enhanced optical and electrical properties of Si(Ge) nanoparticles in mind, several different approaches to control the size and size distribution of the nanoparticles have been proposed; such as incorporating barrier or buffer layer [22, 23, 24], exploiting growth or post annealing temperatures [25, 21, 26, 27], doping [28, 29], super-lattice structure [26, 30, 31] and varying the Si/Ge ratios [32, 33]. Still another common approach is to apply hydrogenation during the fabrication process in which the device is exposed to hydrogen plasma for a certain time.

It is well established that exposure to hydrogen plasma can passivate shallow and deep-level traps and defects in many semiconductors [34, 35, 36, 37, 38, 39, 40]. Hydrogenation also works efficiently on structures containing nanoparticles in amorphous matrix [19] and increase in photoluminescence (PL) intensity has been achieved for InAs/GaAs [41, 42] quantum dots (QDs), Si, SiGe QDs [43, 40] and InAs QDs [44] due to hydrogenation. Hydrogenation tends to passivate non-radiative centers (P_b) located at or in close proximity of QDs. Defects in the form of dangling bonds act as active recombination centers which tends to degrade optical properties of the structures. It has been demonstrated by several researchers [45, 37, 40] that introducing atomic hydrogen in semiconductor structures results in reduction of Si dangling bonds and increase the durability of devices incorporating such materials [38]. In addition, it is discussed by Nazarov et al. [38], that hydrogenation is good for amorphous structures containing crystalline inclusions.

In a very recent study, we investigated the effect of mild annealing on the photoconductivity of a comparable system (SiO_2 film containing SiGe nanoparticles) [8]. The novelty of the present study is that we examine the effect of hydrogenation on such system (but with thinner SiGe film, 20 vs 200 nm). Although the effect of hydrogenation on photoluminescence of similar structures

has been studied, its effect on photoconductivity remains to be explored. We apply short (10 min) interval exposure time and low temperature (roughly room temperature) hydrogenation treatment to avoid degradation of optical properties of the structure.

2. Experimental apparatus and method

Multilayer (ML) sandwiched structure of SiO₂ and SiGe were deposited on 12×12 mm² Si (001) substrates. Prior to deposition, the substrates were etched with 2M hydrofluoric acid (HF) for 120 s to remove native oxide.

The SiO₂ deposition was carried out with reactive direct current magnetron sputtering (dcMS) from a Si (99.9999 wt.% pure; 6N) target in constant-power mode at 150 W using Advanced Energy MDX500 power supply. The chamber was throttled to 5×10⁻⁷ Pa before deposition. Argon (Ar) of 6N purity was used as a working gas. The working gas was mixed with 5N O₂. The flow rates for Ar (q_{Ar} = 100 sccm) and O₂ (q_{O_2} = 2 sccm) were controlled by mass flow controller and throttle valves were adjusted to stabilize growth pressure of 0.7 Pa during deposition.

The SiGe deposition was carried out by co-sputtering 6N Si and Ge targets, using dcMS and HiPIMS respectively. The dcMS deposition was done in constant-power mode at 230 W using Advanced Energy MDX500 power supply. For the HiPIMS setup, the power was supplied by SPIK1000A pulse unit (Melec GmbH) operating in unipolar negative mode at a constant voltage, which in turn was charged by a DC power supply (ADL GS30). The HiPIMS deposition was done using square current-voltage waveform with pulse length of 200 μs and repetition frequency of 100 - 300 Hz was maintained during the deposition. An average current density and peak power density was 230 ± 10 mA/cm² and 106 ± 6 W/cm², respectively, at 470 V averaged over the full target area. The discharge current and voltage were monitored using a combined current transformer and a voltage divider unit (Melec GmbH) and the data were recorded with a digital storage oscilloscope (Agilent 54624A). The deposition rates were adjusted to obtain 50:50 Si-Ge ratio.

The stacking order of the deposited MLs is a SiO₂ (buffer)/SiGe/SiO₂ (top) films with thicknesses of 250/20/40 nm respectively, on a p-type Si substrate. The top SiO₂ acts as a capping layer to control the size of nanoparticles [46, 13]. Its purpose is to prevent a formation of large SiGe nanoislands [47] and possible diffusion of atmospheric oxygen into SiGe. The targets are positioned at 45° from flat sample holder at a distance of 200 mm. The substrate was rotated continuously while sputtering to maintain uniform deposition over the substrate.

A custom build inductively couple discharge in cylindrical geometry was applied for the H₂/Ar plasma treatment. The sample was placed inside a 290 mm long cylindrical quartz tube with inside diameter of 34 mm, with one end connected to a sputter chamber and the other end closed. The quartz tube was placed in a circular inductive coil (4½ turns) with inside diameter of 54 mm, prepared from 85 cm long and 10 mm thick copper tube. The gas consist of ~ 70/30 % / H₂/Ar gas mixture. The flow rates ($q_{\text{Ar}} = 4$ sccm, $q_{\text{H}_2} = 14$ sccm) were controlled via mass flow controllers and the throttle valves were adjusted to the required pressure using butterfly valve in sputter chamber. During the hydrogenation, the gas pressure was in the range of 0.6 - 20 mTorr. Radio frequency CESAR[®] 136 radio frequency (rf) power generator (13.56 MHz) source coupled with impedance matching unit was used to generate the plasma. A schematic of the setup is shown in Fig. 1. The MLs in its final stage, i.e. after depositing Al-contacts, were hydrogenated without any external heating. To determine the temperature during hydrogenation, color-changing temperature stripes were placed inside the hydrogenation chamber.

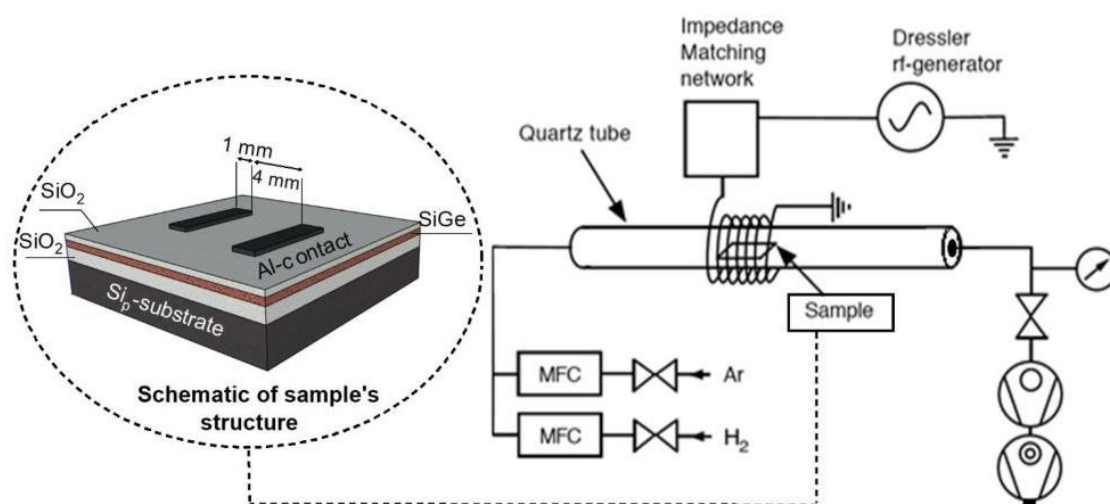


Figure 1. Schematic of the cylindrical inductively coupled discharge H₂/Ar used for hydrogenation. The inset shows a schematic of intended structure *i.e.* Si_p/SiO₂/SiGe/SiO₂.

The structural analysis of the multilayered structures was carried out by the grazing incidence X-ray diffraction (GIXRD) via Philips X'pert diffractometer (CuK_α, 0.15406 nm and having precision of 0.00001°), using 2×Ge (220) asymmetrical hybrid monochromator utilizing

line focus, a divergence slit ($1/4^\circ$) and a parallel plate collimator (0.27°). The measurement run was made with step size of 0.005° and time per step of 1 sec.

Photoconductivity measurements were performed by measuring the current passing between two parallel $1 \times 4 \text{ mm}^2$ coplanar Al-contacts separated with 4 mm gap at applied voltage of 1 V under illumination from a tungsten-halogen lamp. The photocurrent spectra were obtained by extracting the dark current from the originally measured photocurrent and then normalizing the outcome to the light source spectrum. The instrumental setup consisted of Keithley 2400 electrometer, Acton-SpectrPro 150 monochromator with 600 – 1400 nm wavelength range, cryostat with four optical windows and a QTH10 (/M) tungsten-halogen lamp (50 mV optical output power) with two quartz lenses. A schematic of the photo current setup can be found elsewhere [8].

3. Results and Discussion

Results from a morphology study of the un-hydrogenated films and photocurrent measurements prior to and post hydrogenation are presented and discussed here.

3.1. Morphology of the deposited films

It is well established that HiPIMS deposition results in high electron density (plasma density) and higher ionization fraction of the sputtered material than obtained by dcMS [48, 49]. This increase in ionization via HiPIMS has been demonstrated to give a better control over the energy and direction of the sputtered species, thus resulting in improve quality of films with increased density and low surface roughness. To explore the influence of HiPIMS, pure Ge-films were deposited with various repetition frequencies (100- 300 Hz) at fixed voltage and pulse length (470 V and 200 μs , respectively) and compared with Ge films obtained with conventional dcMS at 30 - 100 W. The thickness in all the cases was kept constant ($\sim 30 \text{ nm}$). For HiPIMS, the power varies from 41 to 121 W when frequencies changes from 100 to 300 Hz, respectively, with an average current density of $230 \pm 10 \text{ mA/cm}^2$ and power density of $104 \pm 6 \text{ W/cm}^2$. Fig. 2(a) shows the GiXRD diffractograms of the corresponding as-grown multilayers (for dcMS, only Ge sputtered at 100 W is shown). A completely amorphous structure is revealed for the dcMS sputtered structure. This is different from the HiPIMS deposited structure where a broad band appear already

at the lowest frequency (100 Hz) and gradually rise with increasing frequency up to the highest applied frequency (300 Hz). The two broad humps seen corresponds to plane (111) and planes (220) and (311) together, indicating the presence of nanoparticles within the as-deposited amorphous Ge layer. A very similar diffractogram (analogous to our result at 300 Hz) was observed by Bertan et al. [50] for Si nano-crystallites in amorphous Si matrix obtained by plasma enhanced chemical vapor deposition (PECVD). In a work by Lee et al. [51], the percent crystallinity of Si in amorphous Si matrix was also shown to increase with increased rf power, complementing the case of our Ge films with increasing frequency. GiXRD diffractograms of SiGe MLs are shown in Fig. 2(b). Broad diffraction peaks are seen, indicating presence of small SiGe nano-crystallites in amorphous SiGe layer sandwiched between SiO₂ layers. The (111) peak of the MLs (red colored line) is slightly right-shifted in respect to that of pure Ge (black colored line). To support our results, a comparison to similar structure obtained with dcMS is shown. The GiXRD pattern for such structure (blue colored line in Fig. 2(b)) exhibit completely amorphous feature. The dotted lines shows standard tabulated maximum for cubic Ge and Si respectively. For the case of MLs, the peak (111) is positioned between the Si and Ge tabulated ones. Thus, HiPIMS with increased repetition frequency results in increased formation of SiGe nano-crystallites within the amorphous SiGe layer.

In Fig. 2(c), a deconvolution of the as-deposited MLs diffractogram in Fig. 2(b) is shown. It was processed by subtracting the background using Origin software (10.0) (counter checked using X'Pert HighScore Plus software from PANalytical (ver. 2.2)). The instrumental error, i.e. beam broadening, was taken as 0.12. From the parameters obtained, the atomic ratio of Si-Ge was found to be close to the stoichiometric ratio 1:1. The size of the crystallites were calculated from (111) crystallographic plane using Scherrer equation with shape (k)-factor being 0.9. The size was found to be 8.7 ± 0.8 nm. It should be noted, however, that this is a rather ambiguous approximation of determining crystallite size, since the effect from micro strain broadening, lattice imperfections and instrumental error cannot be ruled out.

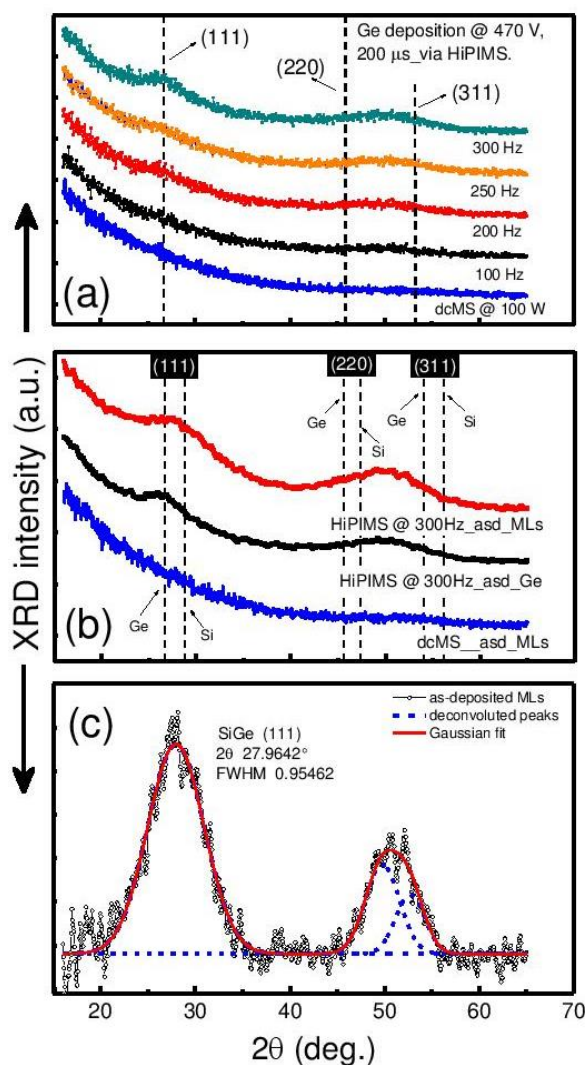


Figure 2. (a) GiXRD diffractogram of: (a) as-deposited Ge (20 nm) deposited via HiPIMS at varying repetition frequency (100-300 Hz) for fixed applied voltage (470 V) and pulse width (200 μ s). A comparison to structure obtained by dcMS at 40 W is given with the blue line. (b) as-deposited Ge (HiPIMS) along with as-deposited MLs sputtered via HiPIMS and dcMS, where vertical dashed lines correspond to standard tabulated positions for cubic Ge ($2\theta = 27.45^\circ$; 45.59° ; 54.04° - ASTM 01-079-0001) and cubic Si (28.45° ; 47.31° ; 56.13° - ASTM 01-070-5680). Labeling under each plot denotes its distinctive fabrication parameter. (c) Deconvoluted GiXRD pattern of as-deposited MLs obtained after subtracting background from the diffractogram in Fig. 2(b). The deconvoluted peak (111) positioned between the standard Si and Ge tabulated one, giving value of x in $\text{Si}_x\text{Ge}_{1-x}$ to be ~ 0.5 .

3.2. Photocurrent measurements

The current-voltage (I - V) curves of all the structures explored for both polarities deviated slightly from perfect ohmic behavior and a small rectifying character, due to interface junction, was observed. Results obtained on MLs prior to hydrogenation are shown in Fig. 3. The current measured under illumination evidences the high photosensitivity of the MLs. At 1 V, the photocurrent under illumination is two orders of magnitude higher than the dark current. The conductivity of the film is however much higher than one would expect from a SiO_2 film. An XPS spectrum, measured on the surface of the top SiO_2 -layer revealed that, it partially consist of elementary Si [8]. This elementary Si has much higher conductivity than SiO_2 so the photocurrent could be measured directly with a Keithley electrometer without the need of lock-in amplifier in a dc mode.

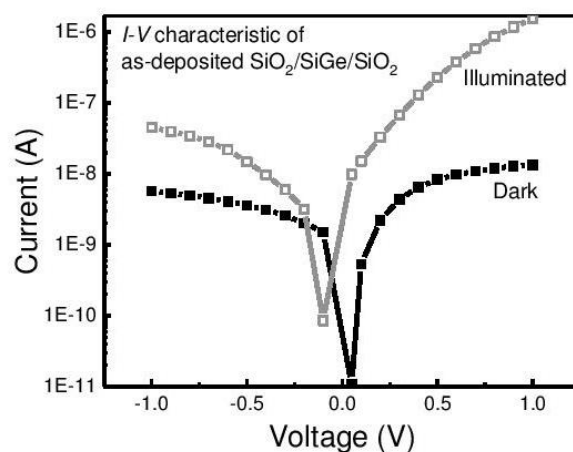


Figure 3. I - V characteristics of as-deposited MLs prior to hydrogenation in dark (filled boxes) and under illumination (open boxes) from a white light source (50 mW optical output power).

A photocurrent spectrum of as-deposited MLs is shown in Fig. 4. In which a presence of three peaks are evident., The peaks are attributed to interface (SiGe/SiO_2 and $\text{SiGe}/\text{SiGeO}_{(\text{amorphous})}$) related localized states (peak A), photo-effect from SiGe nanoparticles (peak B), and to surface photo-voltage (SPV) and gating effect (peak C) as explained elsewhere [8, 52, 53]. The peaks labeled A, B and C are positioned at 782, 990 and 1089 nm (position determined by deconvolution of the spectrum).

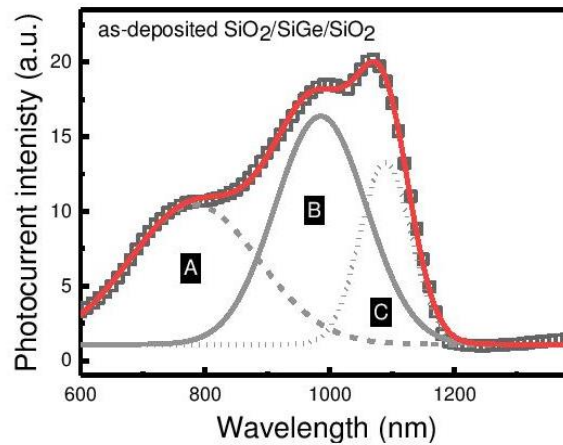


Figure 4. Photocurrent spectra (measured at 1 V) of as-deposited MLs prior to hydrogenation. Open boxes denote the measured spectrum and the red solid line shows the sum of the three deconvoluted curves, A, B and C.

The origin of peak C can be explained based on the study of Lepadatu et al. [52]. There it is ascribed to surface photo voltage and gating effect from the Si substrate; the intensity of which decreases and saturates by increasing applied bias. A similar behavior was observed in a complementary experiment (not published here) where the intensity of peak C was found to saturate at ~ 13 V.

In order to evaluate the origins of peaks A and B, a previous study of photoluminescence spectra from a Si:SiO₂ structure [33] can be utilized for explanation. The photocurrent spectra of the SiO₂/SiGe/SiO₂ MLs, measured at varying temperatures (300, 250, 200 and 150 K), is shown in Fig. 5. The spectra was measured at constant bias of 7 V in order to suppress the effect from peak C. To clearly demonstrate the variations in spectral features, the maximum of the photo current intensity (peak B) is normalized to unity for all the spectral curves. A red-shift (932 to 987 nm) in peak B is observed with decreased T. An expected contribution to this peak shift is the bandgap increase in nanocrystals with the temperature increase although other causes such as NCs size distribution cannot be ruled out. This red-shift of 55 nm (obtained by deconvolution of the spectra) suggests an important contribution from the bandgap variation with T. Concurrently, there is a negligible shift in peak A, whereas the intensity decreases with the temperature decrease. For low temperature (\sim below or at 200 K) hopping of charge carriers to interface related localized states are weak (where thermally activated processes dominate), thus excitons created by illumination are

more localized in the NCs. This result in large contribution (intensity) from peak *B* and lower contribution from peak *A* as is evident in Fig. 5. For temperature above ~ 200 K the non-radiative processes become activated, resulting in an increased intensity of peak *A*. Thus, it can be deduced that, if the peak *A* is due to photo-effect from NCs, it should follow a band gap dependence over temperature showing a shift in peak position.

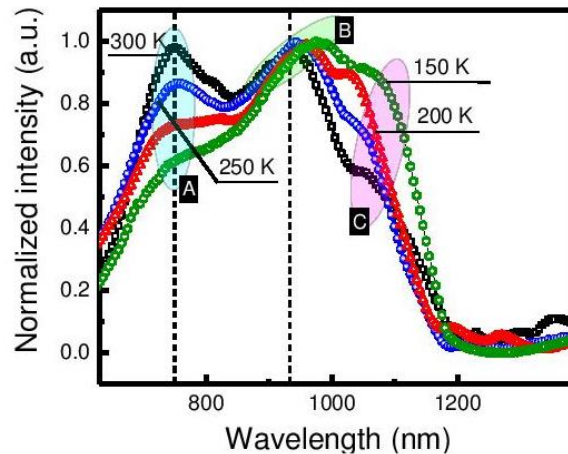


Figure 5. The photocurrent spectra from the SiO₂/SiGe/SiO₂ MLs at constant bias of 7 V for several different temperatures.

3.3. Effect of hydrogenation time on photocurrent intensity

Hydrogenation was carried out in the cylindrical inductively coupled discharge without any external heating. The highest temperature reached during operation was approximately 48 °C (measured by thermal stripes placed inside the hydrogenation chamber) which was obtained at the highest hydrogen pressure of 20 mTorr. Thus, we can assume the obtained photocurrent intensity to be solely due to H₂ plasma treatment without any deliberate or marked thermal effects.

As suggested in the discussion by Nazaroz et al. [38], hydrogenation was carried out over totally fabricated system i.e. with metal contacts on top of the fabricated structure. Fig. 6(a) shows the photocurrent spectra for MLs before and after H₂ plasma treatment. The sample in as-deposited condition underwent hydrogenation for several cycles of 10 min. There is a clear increase in intensity with each hydrogenation cycle. Fig. 6(b) shows intensity of peak-B with respect to the accumulative hydrogenation time. The photocurrent intensity increases rather linearly up to an order of magnitude higher intensity, until a fair saturation in the intensity sets in. To verify the

stability of the hydrogenation, the as-deposited MLs after the last hydrogenation cycle was re-measured after being stored at room temperature at daylight for 5 weeks. Only a small change in the photocurrent intensity (reduction of $\sim 0.97\%$) was observed, thus indicating the stability of the hydrogenation effect. The large increase in photosensitivity, suggest that there is practically little if any surface damage caused by the hydrogenation process when carried out at mild temperature (slightly above room temperature) and in short time intervals. In the work of Jacob et al. [44] and Honda et al. [54], the photoluminescence intensity of InAs quantum dots (capped with $\text{In}_x\text{Ga}_{1-x}\text{As}$ and GaAs) and polycrystalline-Si films respectively, originally at-first increased upon hydrogenation but later showed a reduction when carried out for 120 min and 60 min, respectively. This reduced intensity was assigned to surface damage caused by the hydrogenation process. The increase in photocurrent intensity, obtained with hydrogenation, can be associated with the reasoning that hydrogen in the form of H and H^+ (either directly from plasma or from dissociation of H_2^+ , H_3^+ into H and H^+ at the sample surface) from the plasma diffuses into the SiO_2 matrix. The ions are then collected at the SiGe nanoparticle/ SiO_2 -amorphous matrix interface and at defects in the matrix associated with SiO_2 non-stoichiometry [38].

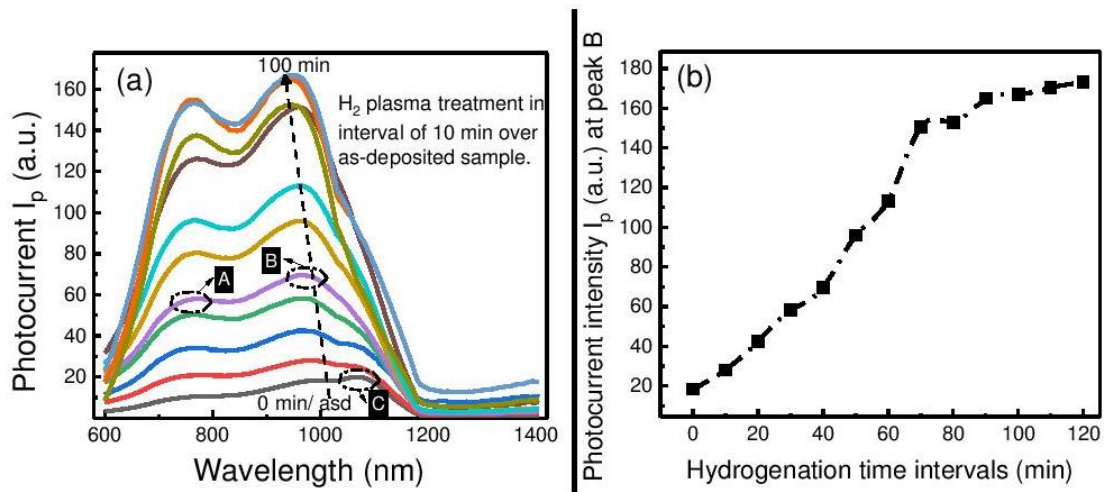


Figure 6. (a) Photocurrent spectra (measured at 1 V) from $\text{SiO}_2/\text{SiGe}/\text{SiO}_2$ MLs in as-deposited condition and after hydrogenation in intervals of 10 min. The dotted line shows the time interval from 0 (asd) to 100 min. (b) The relative intensity of peak B vs. hydrogenation time.

Atomic hydrogen plays a vital role in the hydrogenation of the SiO₂/SiGe interface, resulting in the reduction of positive fixed charges in the dielectric, i.e. SiO₂ in our study [55, 39]. In addition, there is a considerable decrease in electron trapping within the SiO₂ matrix after H₂/Ar plasma treatment due to reduction of structural defects in the oxide matrix resulting in ordering of the SiO₂ amorphous network [38]. This might be the reason for the decrease in peak C intensity and an increase in photocurrent intensity of peak A. Thus, as a consequence of enhanced interface quality due to hydrogenation, electron mobility increases resulting in an increased intensity of peak A and the spectrum as a whole (Fig. 6(a)). In addition, hydrogenation supports the formation of relaxed amorphous oxide matrix with less defect concentration and better (maximal) binding energy, therefore improving the quality of interface (*i.e.* increase in the intensity of peak A). Hydrogenation at room temperature results in reduction of structural defect concentration inside oxide matrixes, subsurface semiconducting layers and surface states concentration on the interfaces [56]. Insignificant or none alteration in size of nanoparticles was observed as evidenced by a negligible shift in position of peak B in Fig. 6(a). A similar observation has been reported by others [39].

Furthermore, an increase in photocurrent intensity for MLs after hydrogenation (Fig. 6) is related to the passivation of non-radiative centers, which might be located in the oxide matrix or at the interface between nanoparticles and the surrounding oxide matrix. Several researchers have studied the critical role of non-radiative centers caused by Si-dangling bond [40, 44, 39]. These dangling bonds can be passivated by hydrogenation, directly by exposure of sample to plasma and introduction of atomic hydrogen in structure, which causes reduction in dangling bond at the boundaries and at the surface via formation of Si-H bonds and annealing of defects [57, 58, 40, 38]. The passivation during hydrogenation can be of two types: one in which hydrogen chemically bonds with defects at interfaces of nanoparticles and a dielectric matrix or with dangling bonds present. In the other type, the hydrogen acts as a radical stimulus, which promotes relaxation of mechanical stress or defect transformation after which it leaves the structure. These configurational change results in relaxation of oxide network with minimal potential energy [38, 59]. It is most likely that the former type of hydrogen activity dominates in our case, i.e. chemical binding. The passivation is carried out by neutralization of defects, dangling bond and by breaking of strained Si-Si bonds and/or bonds of Si-O-Si in SiO₂ where charged carrier can be trapped. The excess atomic hydrogen enters these strained bonds and break them into Si-H and Si-OH. Moreover,

hydrogenation prevents formation of the Si-O bond and can passivate $\text{O}_3\equiv\text{Si}\cdot$ and $\text{O}_3\equiv\text{Si}\cdot\text{O}\cdot$ dangling bonds. Thus, hydrogenation results in decrease of the charge carrier trapping by passivating and restructuring of the dangling and strained Si-bonds.

3.4. Effect of hydrogenation partial pressure

The effectiveness of hydrogen activity associated with the ion energy distribution at varying partial pressures has been studied extensively through the years. Cielaszyk et al. [45] found that $[\text{H}^+]/[\text{H}_2^+]$ ion density ratio is dependent on neutral gas pressure ranging from 0.254 – 2.25 mTorr in hydrogen electron cyclotron resonance discharge. They hypothesized that H and H^+ were responsible for the effective hydrogenation. In other studies [60, 61], the main effectiveness was attributed to the presence of H_3^+ and H_2^+ ions. It was further established that the electron density increased with increasing fractional Ar pressure and that the $[\text{H}_3^+]/[\text{H}_2^+]$ ratio did not change when argon was added. Moreover, the hydrogenation time is reduced by operating at higher plasma density. In all aforementioned studies, it was concluded that the density of H^+ ions grew with decreasing pressure and that the density of H_3^+ and H_2^+ grew with increasing pressure.

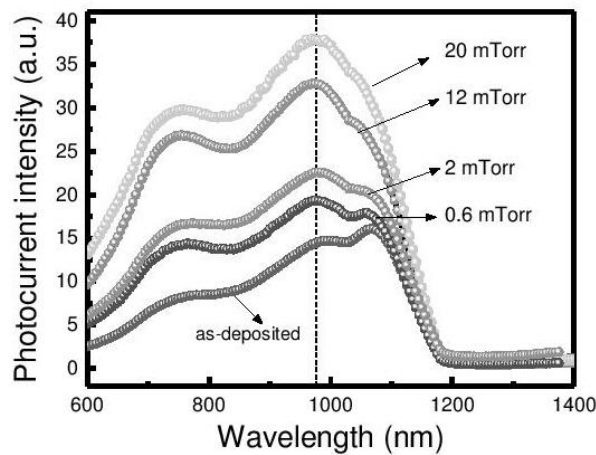


Figure 7. Effect of H_2 :Ar (70:30 ratio) pressure on photocurrent spectra (measured at 1 V) of $\text{SiO}_2/\text{SiGe}/\text{SiO}_2$ MLs in as-deposited condition. The hydrogenation exposure time was constant at 10 min.

The effect of hydrogenation on photoconductivity at varying total pressure in the H_2 /Ar discharge (10 min exposure) is shown in Fig. 7. The pressure values are the sum of the H_2 and Ar partial pressures but the H_2 :Ar ratio was kept constant at 70:30. All the MLs fabricated belong to same batch. A gradual ~160% increase in the photocurrent intensity for peaks A and B, compared

to untreated as-deposited MLs, was observed as the H₂:Ar pressure increased to 20 mTorr. The relative contribution of peak C becomes smaller as the pressure gets higher. This is due to supplementary hydrogen ions increasing carrier mobility and reducing formation of positive fixed charges at the interface of SiO₂, causing reduced electron trapping. No change in the peaks position is observed, indicating that the size of the NCs remain unaffected.

The increase in photocurrent intensity with increased gas pressure can be attributed to dominant H₂⁺ and H₃⁺ ions available at higher pressures. It has been hypothesized [61, 60] that in pure H₂ plasma, the efficiency to create H₂⁺ is inadequate due to small ionization cross-section of H₂. Addition of Ar in plasma tend to enhance the ionization of H₂ [61]. This would result in increased creation of H₂⁺, out of which some portion of it will chemically react to form H₃⁺. Therefore, increased partial pressure of either H₂ or Ar increases the [H₃⁺]/[H₂⁺] ratio as well as the electron density [60]. Increased concentration of H₃⁺ and H₂⁺ implies that higher number of these ions will reach the surface where it dissociates into H and H⁺ that diffuse into the surface, resulting in more effective hydrogenation [45].

4. Conclusion

We report a study of photoconductivity of Si_p/SiO₂/SiGe/SiO₂ structure subjected to hydrogenation in H₂/Ar plasma. The structure underwent hydrogenation in cycles of small time intervals (10 min) and the maximum temperature observed during the process was less than 48 °C. More than an order of magnitude increase in photoconductivity was observed upon the hydrogenation.

The functionality of the hydrogenation is attributed to passivation of non-radiative centers via chemical bonding of atomic hydrogen forming Si-H bonds and ordering of the amorphous oxide matrix along with improved interface quality. A reduction in electron trapping is assigned to reduction in peak due to surface photo-voltage and gating effect.

AUTHOR INFORMATION

Corresponding Author

Halldór Guðfínnur Svavarsson

*E-mail: halldorsv@ru.is

Muhammad. Taha Sultan

*E-mail: muhammad16@ru.is

Acknowledgements

This work is funded through M-ERA.NET project PhotoNanoP UEFISCDI Contract no. 33/2016, PCE project UEFISCDI Contract no. 122/2017 and by Romanian Ministry of Research and Innovation through NIMP Core Program PN16-480102 and by the Technology Development Fund of the Icelandic Centre for Research, grant no. 159006-0611.

References

- [1] D. Lehninger, J. Beyer, J. Heitmann, A Review on Ge Nanocrystals Embedded in SiO₂ and High-k Dielectrics, *Phys. Status Solidia*. 215 (2018) 1701028. doi:10.1002/pssa.201701028.
- [2] I. Capan, A. Carvalho, J. Coutinho, Silicon and germanium nanocrystals: properties and characterization, *Beilstein J. Nanotechnol.* 5 (2014) 1787–1794. doi:10.3762/bjnano.5.189.
- [3] E.-C. Cho, M.A. Green, G. Conibeer, D. Song, Y.-H. Cho, G. Scardera, S. Huang, S. Park, X.J. Hao, Y. Huang, L. Van Dao, Silicon Quantum Dots in a Dielectric Matrix for All-Silicon Tandem Solar Cells, *Adv. Optoelectron.* (2007) 69578. doi:10.1155/2007/69578.
- [4] B. Zhang, Y. Yao, R. Patterson, S. Shrestha, M.A. Green, G. Conibeer, Electrical properties of conductive Ge nanocrystal thin films fabricated by low temperature *in situ* growth, *Nanotechnology*. 22 (2011) 125204. doi:10.1088/0957-4484/22/12/125204.
- [5] S.S. Tzeng, P.W. Li, Enhanced 400–600 nm photoresponsivity of metal–oxide–semiconductor diodes with multi-stack germanium quantum dots, *Nanotechnology*. 19 (2008) 235203. doi:10.1088/0957-4484/19/23/235203.
- [6] A.K. Sood, J.W. Zeller, R.A. Richwine, Y.R. Puri, H. Efstathiadis, P. Haldar, N.K. Dhar, D.L. Polla, SiGe Based Visible -NIR Photodetector Technology for Optoelectronic Applications, in Moh. Yasin and Hamzah Arof and Sulaiman Wadi Harun (eds.), *Advances in Optical Fiber Technology: Fundamental Optical Phenomena and Applications*, pp. 315-361, London, InTech, 2015. doi:10.5772/59065.
- [7] P. Liu, S. Cosentino, S.T. Le, S. Lee, D. Paine, A. Zaslavsky, D. Pacifici, S. Mirabella, M. Miritello, I. Crupi, A. Terrasi, Transient photoresponse and incident power dependence of high-efficiency germanium quantum dot photodetectors, *J. Appl. Phys.* 112 (2012) 083103. doi:10.1063/1.4759252.
- [8] M.T. Sultan, A. Manolescu, J.T. Gudmundsson, K. Torfason, G.A. Nemnes, I. Stavarache, C. Logofatu, V.S. Teodorescu, M.L. Ciurea, H.G. Svavarsson, Enhanced photoconductivity of SiGe nanocrystals in SiO₂ driven by mild annealing, *Appl. Surf. Sci.* 469 (2018) 870-878. doi:10.1016/J.APSUSC.2018.11.061.
- [9] S.R.C. Pinto, R.J. Kashtiban, A.G. Rolo, M. Buljan, A. Chahboun, U. Bangert, N.P. Barradas, E. Alves, M.J.M. Gomes, Structural study of Si 1 – x Ge x nanocrystals embedded in SiO₂ films, *Thin Solid Films*. 518 (2009) 2569–2572. doi:10.1016/j.tsf.2009.09.148.
- [10] Y.X. Jie, X. Wu, C.H.A. Huan, A.T.S. Wee, Y. Guo, T.J. Zhang, J.S. Pan, J. Chai, S.J. Chua, Synthesis and

- characterization of Ge nanocrystals immersed in amorphous SiO_x matrix, *Surf. Interface Anal.* 28 (1999) 195–199. doi:10.1002/(SICI)1096-9918(199908)28:1<195::AID-SIA606>3.0.CO;2-L.
- [11] E.M.F. Vieira, S.R.C. Pinto, S. Levichev, A.G. Rolo, A. Chahboun, M. Buljan, N.P. Barradas, E. Alves, S. Bernstorff, O. Conde, M.J.M. Gomes, Influence of the deposition parameters on the growth of SiGe nanocrystals embedded in Al₂O₃ matrix, *Microelectron. Eng.* 88 (2011) 509–513. doi:10.1016/J.MEE.2010.10.016.
- [12] S.K. Ray, S. Das, R.K. Singha, S. Manna, A. Dhar, Structural and optical properties of germanium nanostructures on Si(100) and embedded in high-k oxides., *Nanoscale Res. Lett.* 6 (2011) 224. doi:10.1186/1556-276X-6-224.
- [13] H.G. Chew, W.K. Choi, Y.L. Foo, F. Zheng, W.K. Chim, Z.J. Voon, K.C. Seow, E.A. Fitzgerald, D.M.Y. Lai, Effect of germanium concentration and oxide diffusion barrier on the formation and distribution of germanium nanocrystals in silicon oxide matrix, *Nanotechnology.* 17 (2006) 1964–1968. doi:10.1088/0957-4484/17/8/028.
- [14] M. Zschintzsch, J. von Borany, N.M. Jeutter, A. Mücklich, Stacked Ge nanocrystals with ultrathin SiO₂ separation layers, *Nanotechnology.* 22 (2011) 465302. doi:10.1088/0957-4484/22/46/465302.
- [15] N.P. Barradas, E. Alves, E.M.F. Vieira, A. Parisini, O. Conde, J. Martín-Sánchez, A.G. Rolo, A. Chahboun, M.J.M. Gomes, IBA study of SiGe/SiO₂ nanostructured multilayers, *Nucl. Instruments Methods Phys. Res. Sect. B Beam Interact. with Mater. Atoms.* 331 (2014) 89–92. doi:10.1016/J.NIMB.2013.11.025.
- [16] A.-M. Lepadatu, I. Stavarache, T.F. Stoica, M.L. Ciurea, Study of Ge nanoparticles embedded in an amorphous SiO₂ matrix with photoconductive properties, *Dig. J. Nanomater. Biostructures.* 6 (2011) 67–73. http://www.chalcogen.ro/67_Ciurea.pdf (accessed November 14, 2018).
- [17] J.G. Zhu, C.W. White, J.D. Budai, S.P. Withrow, Y. Chen, Growth of Ge, Si, and SiGe nanocrystals in SiO₂ matrices, *J. Appl. Phys.* 78 (1995) 4386–4389. doi:10.1063/1.359843.
- [18] S.K. Ray, K. Das, Luminescence characteristics of Ge nanocrystals embedded in SiO₂ matrix, *Opt. Mater. (Amst).* 27 (2005) 948–952. doi:10.1016/J.OPTMAT.2004.08.041.
- [19] A.M. Lepadatu, I. Stavarache, A. Maraloiu, C. Palade, T.V. Serban, M.L. Ciurea, Electrical behaviour related to structure of nanostructured GeSi films annealed at 700 °C, *Proc. Int. Semicond. Conf. CAS.* 1 (2012) 109–112. doi:10.1109/SMICND.2012.6400683.
- [20] M.L. Ciurea, M. Draghici, V. Iancu, M. Reshotko, I. Balberg, Coupled confinement effect on the photoluminescence and electrical transport in porous silicon, *J. Lumin.* 102–103 (2003) 492–497. doi:10.1016/S0022-2313(02)00589-6.
- [21] I. Stavarache, A.-M. Lepadatu, T. Stoica, M.L. Ciurea, Annealing temperature effect on structure and electrical properties of films formed of Ge nanoparticles in SiO₂, *Appl. Surf. Sci.* 285 (2013) 175–179. doi:10.1016/J.APSUSC.2013.08.031.
- [22] M. Glover, A. Meldrum, Effect of “buffer layers” on the optical properties of silicon nanocrystal superlattices, *Opt. Mater. (Amst).* 27 (2005) 977–982. doi:10.1016/j.optmat.2004.08.047.
- [23] J. López-Vidrier, S. Hernández, D. Hiller, S. Gutsch, L. López-Conesa, S. Estradé, F. Peiró, M. Zacharias, B. Garrido, Annealing temperature and barrier thickness effect on the structural and optical properties of silicon nanocrystals/SiO₂ superlattices, *J. Appl. Phys.* 116 (2014) 133505. doi:10.1063/1.4896878.
- [24] W.-H. Chang, W.-Y. Chen, A.-T. Chou, T.-M. Hsu, P.-S. Chen, Z. Pei, L.-S. Lai, Effects of spacer thickness on optical properties of stacked Ge/Si quantum dots grown by chemical vapor deposition, *J. Appl. Phys.* 93 (2003) 4999–5002. doi:10.1063/1.1564883.
- [25] I. Stavarache, V.A. Maraloiu, C. Negrița, P. Prepelita, I. Gruia, G. Iordache, Photo-sensitive Ge nanocrystal based films controlled by substrate deposition temperature, *Semicond. Sci. Technol.* 32 (2017) 105003. doi:10.1088/1361-6641/aa8154.

- [26] M. Avella, Á.C. Prieto, J. Jiménez, A. Rodríguez, J. Sangrador, T. Rodríguez, M.I. Ortiz, C. Ballesteros, Influence of the crystallization process on the luminescence of multilayers of SiGe nanocrystals embedded in SiO₂, *Mater. Sci. Eng. B.* 147 (2008) 200–204. doi:10.1016/J.MSEB.2007.08.016.
- [27] W. Choi, S. Kanakaraju, Z. Shen, W. Li, Characterization of Ge nanocrystals in a-SiO₂ synthesized by rapid thermal annealing, *Appl. Surf. Sci.* 144–145 (1999) 697–701. doi:10.1016/S0169-4332(98)00908-8.
- [28] J. Mayandi, T.G. Finstad, C.L. Heng, Y.J. Li, A. Thøgersen., S. Foss and H. Klette, A Comparison between 1.5 μm Photoluminescence from Er-Doped Si-Rich SiO₂ Films and (Er,Ge) Co-Doped SiO₂ Films, Proceedings of European Nano Systems (ENS 2006), Paris, France, 14–15 December 2006, TIMA Editions, Grenoble, France, pp. 1 – 4. <http://arxiv.org/abs/0708.1426> (accessed November 14, 2018).
- [29] S. Takeoka, K. Tshikiyo, M. Fujii, S. Hayashi, K. Yamamoto, Control of photoluminescence energy of Si nanocrystals by Ge doping, *J. Lumin.* 87–89 (2000) 350–352. doi:10.1016/S0022-2313(99)00378-6.
- [30] E.M.F. Vieira, J. Toudert, A.G. Rolo, A. Parisini, J.P. Leitão, M.R. Correia, N. Franco, E. Alves, A. Chahboun, J. Martín-Sánchez, R. Serna, M.J.M. Gomes, SiGe layer thickness effect on the structural and optical properties of well-organized SiGe/SiO₂ multilayers, *Nanotechnology.* 28 (2017) 345701. doi:10.1088/1361-6528/aa7a50.
- [31] J.L. Liu, J. Wan, K.L. Wang, D.P. Yu, Critical thickness of self-assembled Ge quantum dot superlattices, *J. Cryst. Growth.* 251 (2003) 666–669. doi:10.1016/S0022-0248(02)02509-5.
- [32] S.W. Pan, B. Zhou, S.Y. Chen, C. Li, W. Huang, H.K. Lai, Optical property investigation of SiGe nanocrystals formed by electrochemical anodization, *Appl. Surf. Sci.* 258 (2011) 30–33. doi:10.1016/J.APSUSC.2011.07.141.
- [33] X.X. Wang, J.G. Zhang, L. Ding, B.W. Cheng, W.K. Ge, J.Z. Yu, Q.M. Wang, Origin and evolution of photoluminescence from Si nanocrystals embedded in a SiO₂ matrix, *Phys. Rev. B.* 72 (2005) 195313. doi:10.1103/PhysRevB.72.195313.
- [34] J. Kassabov, E. Atanassova, D. Dimitrov, J. Vasileva, Effects of hydrogen plasma on thin-oxide Si-SiO₂ structures, *Semicond. Sci. Technol.* 3 (1988) 686–690. doi:10.1088/0268-1242/3/7/009.
- [35] D.M. Danielsson, J.T. Gudmundsson, H.G. Svavarsson, Effect of hydrogenation on minority carrier lifetime in low-grade silicon, *Phys. Scr. T141* (2010) 014005. doi:10.1088/0031-8949/2010/T141/014005.
- [36] H. Olafsson, J.T. Gudmundsson, H.G. Svavarsson, H. Gislason, Hydrogen passivation of Al_xGa_{1-x}As/GaAs studied by surface photovoltage spectroscopy, *Phys. B Condens. Matter.* 273–274 (1999) 689–692. doi:10.1016/S0921-4526(99)00611-0.
- [37] M. Mews, E. Conrad, S. Kirner, N. Mingirulli, L. Korte, Hydrogen Plasma Treatments of Amorphous/Crystalline Silicon Heterojunctions, *Energy Procedia.* 55 (2014) 827–833. doi:10.1016/J.EGYPRO.2014.08.066.
- [38] A.N. Nazarov, V.S. Lysenko, T.M. Nazarova, Hydrogen plasma treatment of silicon thin-film structures and nanostructured layers, *Semicond. Physics, Quantum Electron. Optoelectron.* 11 (2008) 101–123. <https://www.semanticscholar.org/paper/Hydrogen-plasma-treatment-of-silicon-thin-film-and-Nazarov-Lysenko/098f8c5347cc6950c9a9c4cc5f8d714c048d7f51> (accessed November 5, 2018).
- [39] I.Z. Indutnyy, V.S. Lysenko, I.Y. Maidanchuk, V.I. Min'ko, A.N. Nazarov, A.S. Tkachenko, P.E. Shepeliavyyi, V.A. Dan'ko, Effect of chemical and radiofrequency plasma treatment on photoluminescence of SiO_x films, *Semicond. Physics, Quantum Electron. Optoelectron.* 9 (2006) 9–13. http://journal-spqeo.org.ua/n1_2006/v9n1-p009-013.pdf (accessed November 14, 2018).
- [40] A.I. Yakimov, V. V Kirienko, V.A. Armbrister, A. V Dvurechenskii, Hydrogen passivation of self-assembled Ge/Si quantum dots, *Semicond. Sci. Technol.* 29 (2014) 085011. doi:10.1088/0268-1242/29/8/085011.
- [41] S. Mazzucato, D. Nardin, A. Polimeni, M. Capizzi, D. Granados, J.M. García, Hydrogenation of Stacked Self-Assembled InAs/GaAs Quantum Dots, in: *AIP Conf. Proc.*, AIP, 2005: pp. 621–622. doi:10.1063/1.1994260.
- [42] E.C. Le Ru, P.D. Siverns, R. Murray, Luminescence enhancement from hydrogen-passivated self-assembled

- quantum dots, *Appl. Phys. Lett.* 77 (2000) 2446–2448. doi:10.1063/1.1318931.
- [43] S. Yamada, Y. Kurokawa, S. Miyajima, M. Konagai, Investigation of hydrogen plasma treatment for reducing defects in silicon quantum dot superlattice structure with amorphous silicon carbide matrix, *Nanoscale Res. Lett.* 9 (2014) 72. doi:10.1186/1556-276X-9-72.
- [44] A.P. Jacob, Q.X. Zhao, M. Willander, F. Ferdos, M. Sadeghi, S.M. Wang, Hydrogen passivation of self assembled InAs quantum dots, *J. Appl. Phys.* 92 (2002) 6794–6798. doi:10.1063/1.1515379.
- [45] E.S. Cielaszyk, K.H.R. Kirmse, R.A. Stewart, A.E. Wendt, Mechanisms for polycrystalline silicon defect passivation by hydrogenation in an electron cyclotron resonance plasma, *Appl. Phys. Lett.* 67 (1995) 3099–3101. doi:10.1063/1.114877.
- [46] R. Bahariqushchi, R. Raciti, A.E. Kasapoğlu, E. Gür, M. Sezen, E. Kalay, S. Mirabella, A. Aydinli, Stress evolution of Ge nanocrystals in dielectric matrices, *Nanotechnology.* 29 (2018) 185704. doi:10.1088/1361-6528/aaaffa.
- [47] A. Slav, C. Palade, I. Stavarache, V.S. Teodorescu, M.L. Ciurea, R. Muller, A. Dinescu, M.T. Sultan, A. Manolescu, J.T. Gudmundsson, H.G. Svavarsson, Influence of preparation conditions on structure and photosensing properties of GeSi/TiO₂ multilayers, in: 2017 Int. Semicond. Conf., IEEE, 2017: pp. 63–66. doi:10.1109/SMICND.2017.8101154.
- [48] J.T. Gudmundsson, D. Lundin, N. Brenning, M.A. Raadu, C. Huo, T.M. Minea, An ionization region model of the reactive Ar/O₂ high power impulse magnetron sputtering discharge, *Plasma Sources Sci. Technol.* 25 (2016) 065004. doi:10.1088/0963-0252/25/6/065004.
- [49] J.T. Gudmundsson, The high power impulse magnetron sputtering discharge as an ionized physical vapor deposition tool, *Vacuum.* 84 (2010) 1360–1364. doi:10.1016/j.vacuum.2009.12.022.
- [50] E. Bertran, S.N. Sharma, G. Viera, J. Costa, P. St'ahel, P.R. i Cabarocas, Effect of the Nanoparticles on the Structure and Crystallization of Amorphous Silicon Thin Films Produced by rf Glow Discharge, *J. Mater. Res.* 13 (1998) 2476–2479. doi:10.1557/JMR.1998.0347.
- [51] H.C. Lee, G.Y. Yeom, Y.J. Lee, J.K. Shin, S. Il Baik, Y.W. Kim, Structural and Electrical Analysis of Silicon Thin Films Deposited by Transformer-Coupled-Plasma Chemical-Vapor Deposition, *J. Korean Phys. Soc.* 47 (2005) 277–282. https://spl.skku.ac.kr/_res/pnpl/etc/2005-19.pdf (accessed November 14, 2018).
- [52] A.-M. Lepadatu, A. Slav, C. Palade, I. Dascalescu, M. Enculescu, S. Iftimie, S. Lazanu, V.S. Teodorescu, M.L. Ciurea, T. Stoica, Dense Ge nanocrystals embedded in TiO₂ with exponentially increased photoconduction by field effect, *Sci. Rep.* 8 (2018) 4898. doi:10.1038/s41598-018-23316-3.
- [53] C. Palade, I. Dascalescu, A. Slav, A.M. Lepadatu, S. Lazanu, T. Stoica, V.S. Teodorescu, M.L. Ciurea, F. Comanescu, R. Muller, A. Dinescu, A. Enuica, Photosensitive GeSi/TiO₂ multilayers in VIS-NIR, in: 2017 Int. Semicond. Conf., IEEE, 2017: pp. 67–70. doi:10.1109/SMICND.2017.8101155.
- [54] S. Honda, T. Mates, M. Ledinsky, J. Oswald, A. Fejfar, J. Kočka, T. Yamazaki, Y. Uraoka, T. Fuyuki, Effect of hydrogen passivation on polycrystalline silicon thin films, *Thin Solid Films.* 487 (2005) 152–156. doi:10.1016/j.tsf.2005.01.056.
- [55] A. Szekeres, S. Alexandrova, Low-temperature treatment of Si/SiO₂ structures in an RF hydrogen plasma, *Vacuum.* 47 (1996) 1483–1486. doi:10.1016/S0042-207X(96)00175-3.
- [56] K. Arima, T. Shigetoshi, H. Kakiuchi, M. Morita, Surface photovoltage measurements of intrinsic hydrogenated amorphous Si films on Si wafers on the nanometer scale, *Phys. B Condens. Matter.* 376–377 (2006) 893–896. doi:10.1016/J.PHYSB.2005.12.223.
- [57] E. Cartier, J.H. Stathis, D.A. Buchanan, Passivation and depassivation of silicon dangling bonds at the Si/SiO₂ interface by atomic hydrogen, *Appl. Phys. Lett.* 63 (1993) 1510–1512. doi:10.1063/1.110758.
- [58] L.-P. Scheller, M. Weizman, P. Simon, M. Fehr, N.H. Nickel, Hydrogen passivation of polycrystalline silicon thin films, *J. Appl. Phys.* 112 (2012) 063711. doi:10.1063/1.4752268.

- [59] H.P. Zhou, M. Xu, S. Xu, L.L. Liu, C.X. Liu, L.C. Kwek, L.X. Xu, Hydrogen-plasma-induced Rapid, Low-Temperature Crystallization of μm -thick a-Si:H Films, *Sci. Rep.* 6 (2016) 32716. doi:10.1038/srep32716.
- [60] J.T. Gudmundsson, Experimental studies of H_2/Ar plasma in a planar inductive discharge, *Plasma Sources Sci. Technol.* 7 (1998) 330–336. doi:10.1088/0963-0252/7/3/011.
- [61] C.F. Yeh, T.J. Chen, C. Liu, J.T. Gudmundsson, M.A. Lieberman, Hydrogenation of polysilicon thin-film transistor in a planar inductive H_2/Ar discharge, *IEEE Electron Device Lett.* 20 (1999) 223–225. doi:10.1109/55.761021.

Paper III

Efficacy of annealing and fabrication parameters on photo-response of SiGe in TiO₂ matrix

*Sultan M T¹, Gudmundsson J T^{2,3}, Manolescu A¹, Teodorescu V S⁴, Ciurea M L^{4,5} and *Svavarsson H G¹

¹School of Science and Engineering, Reykjavik University, IS-101 Reykjavik, Iceland

²Department of Space and Plasma Physics, School of Electrical Engineering and Computer Science, KTH-Royal Institute of Technology, SE-100 44, Stockholm, Sweden

³Science Institute, University of Iceland, IS-101 Reykjavik, Iceland

⁴National Institute of Materials Physics, 077125 Magurele, Romania

⁵Academy of Romanian Scientists, 050094 Bucharest, Romania

Published: Nanotechnology, vol. 30, pp. 365604, 2019.

DOI: <https://doi.org/10.1088/1361-6528/ab260e>

IOP Publishing

Nanotechnology

Nanotechnology 30 (2019) 365604 (12pp)

<https://doi.org/10.1088/1361-6528/ab260e>

Efficacy of annealing and fabrication parameters on photo-response of SiGe in TiO₂ matrix

M T Sultan^{1,6}, J T Gudmundsson^{2,3}, A Manolescu¹, V S Teodorescu⁴, M L Ciurea^{4,5} and H G Svavarsson^{1,6}

¹Reykjavik University, School of Science and Engineering, IS-101 Reykjavik, Iceland

²Department of Space and Plasma Physics, School of Electrical Engineering and Computer Science, KTH Royal Institute of Technology, SE-100 44, Stockholm, Sweden

³Science Institute, University of Iceland, Dunhaga 3, IS-107 Reykjavik, Iceland

⁴National Institute of Materials Physics, 077125 Magurele, Romania

⁵Academy of Romanian Scientists, 050094 Bucharest, Romania

E-mail: muhammad16@ru.is and halldorsv@ru.is

Received 9 February 2019, revised 3 May 2019

Accepted for publication 31 May 2019

Published 24 June 2019



Efficacy of annealing and fabrication parameters on photo-response of SiGe in TiO₂ matrix

M.T. Sultan¹, J. T. Gudmundsson^{2,3}, A. Manolescu¹, V. S. Teodorescu⁴, M. L. Ciurea^{4,5}, H. G. Svavarsson¹

¹ Reykjavik University, School of Science and Engineering, IS-101 Reykjavik, Iceland

² Department of Space and Plasma Physics, School of Electrical Engineering and Computer Science, KTH-Royal Institute of Technology, SE-100 44, Stockholm, Sweden

³ Science Institute, University of Iceland, Dunhaga 3, IS-107 Reykjavik, Iceland

⁴ National Institute of Materials Physics, 077125 Magurele, Romania

⁵ Academy of Romanian Scientists, 050094 Bucharest, Romania

E-mail: muhammad16@ru.is

Abstract

SiGe nanoparticles dispersed in a dielectric matrix exhibit properties different from those of bulk and have shown great potential in devices for application in advanced optoelectronics. Annealing is a common step used to increase crystallinity and to form nanoparticles in such a system. A frequent downside of such annealing treatment is the formation of insulating SiO₂ at the matrix/SiGe interface, degrading the optical properties of the structure. Annealing process that could bypass this downside would therefore be of great interest. In this work, a short-time furnace annealing of a SiGe/TiO₂ system is applied to obtain SiGe nanoparticles without formation of the undesired SiO₂ layer between the dielectric matrix (TiO₂) and SiGe. The structures were prepared by depositing alternate layers of TiO₂ and SiGe films, using direct-current magnetron sputtering technique. A wide range spectral response with a response-threshold up to ~1300 nm was obtained, accompanied with an increase in photo-response of more than 2-orders of magnitude. Scanning electron microscopy, transmission electron microscopy, energy-dispersive X-ray spectroscopy and grazing incidence X-ray diffraction were used to analyze the morphological changes in respective structures. Photoconductive properties were studied by measuring photocurrent spectra using applied dc-voltages at various temperatures.

Keywords: SiGe nanocrystals, SiO₂, TiO₂, photocurrent, TEM, thermal annealing

1. Introduction

To present, the compatibility of silicon (Si) with germanium (Ge) and their transition from two-dimensional structure to nano-crystallites (NCs) or nanoparticles has grasped the interest of numerous researchers. A considerable effort has been devoted to the clarification of their self-assembly, and whether nanoparticles with dense arrays can be achieved with better control and reliability of their properties. These structures have drawn interest especially because of their potential bandgap-tuning by quantization to the optimal power and energies for conversion efficiency and enhancement of optical properties[1,2]. SiGe nanostructures embedded in dielectric/ oxide matrices are potential elements for application in optoelectronic devices. Examples of methods adopted to fabricate SiGe NCs embedded in an oxide matrix include molecular beam epitaxy, ion

implantation, sol-gel and magnetron sputtering, the last one being the most common [3–5]. The properties of such structures can be tuned by altering the stoichiometric parameter x in $\text{Si}_{1-x}\text{Ge}_x$ (i.e. the Ge fraction) and by controlling the size of NCs [3,4,6,7]. In addition, strain engineering can be utilized to determine the bandgap of the SiGe nanocrystals (NCs) for the purpose of enhancing energy conversion efficiency and optical properties [1,2,8]. Moreover, it is well documented in several studies that the effect of surrounding matrix and the resulting strain formation determines the optical properties of such structures [9,10]. Among the various possible oxide matrices such as SiO_2 , HfO_2 and Al_2O_3 [3,4], titanium dioxide (TiO_2) showed potential candidacy due to its high dielectric constant, thermodynamic stability and dense structure [11–13]. In this relation, TiO_2 films are being intensively studied for applications in sensors, solar cells, and photoconductivity. In optics, TiO_2 find a wide range of use due to its high refractive index and transparency in the visible and infra-red (IR) spectral range. In bulk form, TiO_2 exists commonly in three morphological phases: two tetragonal (anatase and rutile) and one orthorhombic (brookite) [14]. In contrast to bulk form, only anatase and rutile phases are observed in thin films [15]. The bandgap energy of TiO_2 roughly equal's to 3 eV (3.0 for rutile and 3.2 for anatase), thus making TiO_2 active in the ultra-violet (UV) range [16].

Composites of TiO_2 and Si(/Ge) have been found to increase the spectral range and a TiO_2/Ge multilayer system, which exhibits quantum confinement effects with a tuneable bandgap, have been prepared by controlled annealing [17,18]. Aiming at increased photocurrent, Church et al. [1] fabricated Ge/ TiO_2 photodetectors that exhibited five orders of magnitude increment in photocurrent relative to a previously fabricated system containing Ge quantum dots (QDs). Li et al. [19], grew TiO_2 films with embedded Ge (QDs), resulting in an increased optical response from UV to the infrared regime.

Many other studies have been conducted on Si(/Ge) NCs embedded in oxide matrices, to determine the effect of strain [3,9,10,20,21] and post-annealing [4,22–26] on the NCs' size, shape and degree of crystallinity. The effect of the type of strain (compressive or tensile) and diffusivity of Si, Ge and oxygen (O) in such systems has also been studied in respect to its optical and electrical properties [4,23,27–29].

A commonly observed downside of annealing such a structure is the inter-diffusion of oxygen from the (oxide) matrix towards the NCs' interface. This results in blunting and degradation of the interfaces, deteriorating the structure and/or forming insulating SiO_2 at the matrix/NCs interfaces [27,30–33]. Thus, to preserve the functionality of incorporated Si-based electronics, a low processing temperature is required [27,32].

The aim of this study is to demonstrate that short-time (5 min) furnace annealing of $\text{Si}_{\text{sub}}/\text{SiO}_2$ -buffer/ $(\text{TiO}_2/\text{SiGe}/\text{TiO}_2)_n$ system at moderate temperature (600 °C) is applicable to create embedded SiGe NCs in a TiO_2 matrix without the formation of SiO_2 insulating layer (in contrast to what occurs in similar system composed of SiO_2 matrix instead of TiO_2 [30,31]). Thus increasing the spectral intensity of the structure in the spectral range from the visible to the near infrared regime. The temperature value of 600 °C was selected, as it is documented that this temperature is suitable to obtain both crystalline meta-stable anatase TiO_2 phase [34] and crystalline SiGe NCs. Such structure can be adapted to fabricate photosensitive or integrated devices on Si or a flexible substrate where low processing temperature is required.

2. Experiment

2.1 Materials and methods

Multilayer structures, consisting of SiGe-layer sandwiched between dielectric TiO_2 films, were prepared. All the structures were deposited on polished $10 \times 10 \text{ mm}^2$ p-type Si (100) substrates. The TiO_2 layers were grown by reactive direct-

current magnetron sputtering (dcMS) 99.999% (5N) pure Ti target of 3-inch diameter in argon (Ar) and oxygen (O_2) plasma. The SiGe layers (30 nm thick) were obtained by co-sputtering 6N 3-inch diameter Si and Ge targets with dcMS in an argon plasma. The deposition was carried out in constant-power mode at 25 and 80 W power for the Ge and Si targets, respectively, at 0.7 Pa Ar working gas pressure, using Advanced Energy MDX500 power supply. The flow rate for Ar ($q_{Ar} = 37$ sccm) and O_2 ($q_{O_2} = 1.2$ sccm) were controlled by the mass-flow controller, and throttle valves were adjusted to stabilize growth pressure of 0.7 Pa during the TiO_2 deposition. No intentional heating was applied to the substrate and the substrate was electrically floating during deposition.

In order to explore the mechanism of the NCs growth, one sample was fabricated in two discontinuous stages (TS) and underwent two annealing steps in respective stages. The first stage was deposition of TiO_2 layer followed by co-sputtering of Si and Ge and subsequent annealing at 600 °C for 30 min (referred to as TS₁-30), resulting in the formation of crystalline TiO_2 and the break-up of SiGe layer into spherical nano-islands. In the second stage, the structure (TS₁-30) was then sputtered again with a cap/top layer of TiO_2 . After deposition of the TiO_2 top-layer, the sample underwent second annealing step, at 600 °C for 30 min (referred to as TS₂-30), in order to obtain crystalline TiO_2 top layer.

All other samples were fabricated in a single stage (SS) continuous process with a variable number of GeSi/ TiO_2 stacks in a Si-sub/ SiO_2 -buffer/ TiO_2 /(GeSi/ TiO_2)_n structure ($n = 1, 3$ and 5). After deposition, the structures were annealed for a minuscule period of 5 min at 600°C (after that referred to as SS1-5, SS3-5 and SS5-5, for $n = 1, 2$ and 5, respectively). Fig. 1 schematically shows the fabrication schemes for both double and single step procedures. The name of the sample denotes its fabrication scheme (TS or SS) along with the stacking number (n) and the annealing time separated by a hyphen. Table 1 lists the MLs names and processing characteristics.

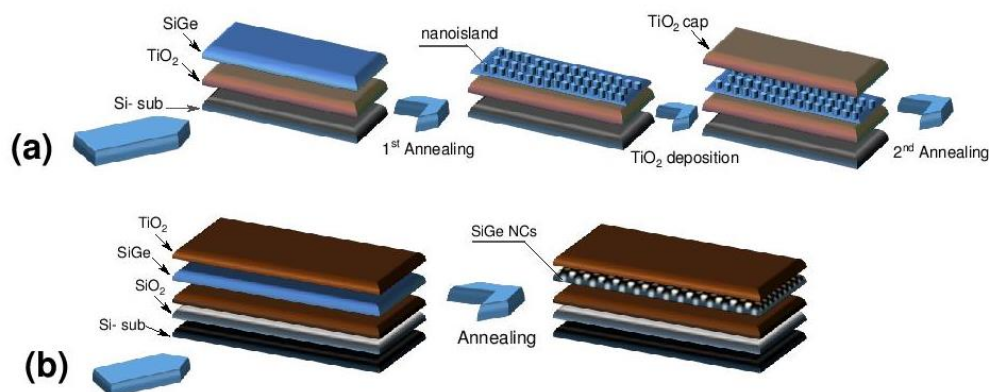


Figure 1. Schematic of (a) double step fabrication and (b) single step fabrication schemes followed by respective annealing steps.

Table 1. Multilayer structures and corresponding fabrication steps.

Samples name	MLs Structure	Annealing (°C, min)
TS ₁ -30	TiO ₂ /SiGe	600, 30
TS ₂ -30	TS ₁ -30/ TiO₂(cap)	600, 30
SS1-5	SiO ₂ /TiO ₂ / (SiGe/TiO₂)₁	600, 5
SS1-5*	SiO ₂ /TiO ₂ / (Si/SiGe/Si/TiO₂)₁	600, 5
SS3-5	SiO ₂ /TiO ₂ / (SiGe/TiO₂)₃	600, 5
SS5-5	SiO ₂ /TiO ₂ / (SiGe/TiO₂)₅	600, 5

The annealing was executed in a conventional furnace in N₂ ambient of 6N purity. Prior to annealing, the furnace was held for approximately 30 min at the desired temperature in order to assure stable condition. After annealing, the sample was allowed to cool to room temperature in atmospheric air.

For photoelectrical measurements, coplanar aluminum contacts, separated by 4 mm distance, were thermally evaporated on top of the annealed structures. A direct current passing through the contacts at constant 1V bias, while being illuminated with monochromatic light, was measured. The setup consists of Keithley 2400 electrometer, Acton-SpectrPro 150 monochromator with 600 – 1400 nm wavelength range, cryostat with four optical windows and a QTH10 (/M) quartz-tungsten-halogen lamp light source (50 mW optical output power) and quartz lens to focus the light. The photocurrent curves were obtained by subtracting the dark current from the spectra measured under illumination and then normalizing the outcome to the spectral irradiation intensity of the light source.

2. Results and Discussion

3.1. Structural analysis

GiXRD measurements were carried out on all the MLs. Figs. 2 (a) and (b) presents the recorded diffractogram for TS₂-30 and SS3-5, respectively. Tabulated positions of the (111), (200) and (311) crystallographic planes for Si and Ge are shown with dotted lines[35]. As seen, we observe peaks located between the position of the Si and Ge-planes, evidencing the presence of crystalline SiGe-nanoparticles (the NCs can be seen in TEM later in this section). In Fig. 2(a), the (111) peak for TS₂-30 is positioned close to Ge standard (~ 27.55°) and that for MLs SS3-5 in Fig. 2(b) around 27.852°. The main peak at 25.3° in both figures corresponds to anatase TiO₂. From the respective GiXRD diffractograms and microscopic analysis presented later in this section, it is apparent that short term (5 min) furnace annealing results in the formation of crystalline Si_{1-x}Ge_x NCs (with x ≈ 0.55 for SS fabricated MLs, as calculated from GiXRD diffractogram), and TiO₂ anatase phase.

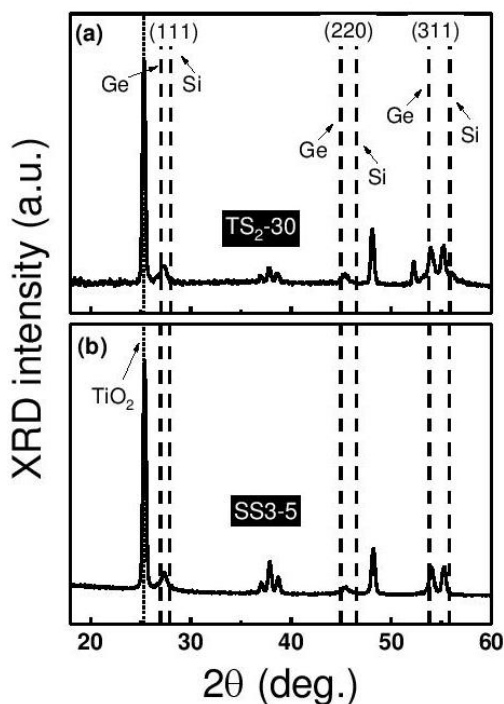


Figure 2. GiXRD diffractogram of sample (a) TS₂-30 and (b) SS3-5, where vertical dashed and dotted lines correspond to standard tabulated positions for cubic Ge ($2\theta = 27.45^\circ$; 45.59° ; 54.04° - ASTM 01-079-0001), cubic Si (28.45° ; 47.31° ; 56.13° - ASTM 01-070-5680) and to TiO₂ anatase (JCPDS 21-1272).

For TS-30, the SiGe layer dissociates into nanoislands (Fig. 3) as described by the classical Stranski-Krastanov (SK) mode[36]. These nanoislands form due to relaxation of elastic strain after formation of wetting-layer by SK growth mode where the formation of nano-dots is governed by the competition between thermodynamics and kinetics[36]. The SK mode describes the case when two-dimensional growth starts (layer by layer), and later continues as a three-dimensional (island) growth. The classical stages of nano-island formation involve nucleation and subsequent growth of islands by coarsening (including Ostwald ripening and diffusion mechanism). A SEM image of the surface (Fig. 3) evidences the presence of spherically shaped nanoislands with size ranging from 100 to 200 nm in diameter and 5-12 nm in height (determined by AFM) as a result of annealing at 600 °C for 30 min. Later on, sample TS₁-30 was capped with TiO₂ and annealed again in a similar fashion (TS₂-30). As discussed elsewhere[10,37,38], deposition of capping layer alters and controls the size of the nanoislands. A similar system was discussed by Aqua et al. [36] where transformation of spherical shaped nanoislands along with decreasing size, was attributed to the propensity of nanoislands to form a stable surface by banishing higher angle and energy facets (also discussed by Hadjisavvas et al. [21], via Monte Carlo study over Si-NCs embedded in SiO₂ matrix). A concurrent intermixing and segregation of Ge was attributed to a strain-driven process. Thus, a significant size reduction of the SiGe nanoislands is observed upon the second annealing and polycrystalline NCs of 20-30 nm in diameter are seen in the TEM images in Fig. 4. This is accompanied with separation and segregation of Ge and oxidation of SiGe films forming an insulating layer, mainly consisting of amorphous SiO₂, as visualized in Fig. 4(a). The formation of SiO₂ from SiGe is more exothermic than that of

GeO₂ from Ge, thus making GeO₂ less stable and ensuing Ge segregation[39]. The most probable source of oxygen is the adjacent TiO₂ films being below and above the Si-Ge layer, but a contribution from atmospheric oxygen cannot be ruled out.

The EDX spectra obtained from the focused beam on the Ge(Si) nanocrystals indicate Si/Ge atomic ratio of 1/3 (Fig. 5(a)), in rough agreement with the GiXRD diffractogram (Fig. 2(a)) where the (111) peak lies closer to Ge than the Si position. The (111) lattice distance was measured by the HRTEM image in Fig. 5(b) as 0.324 +/- 0.001 nm (an average value of 10 fringes), compared to the known value of 0.326 nm for Ge lattice. This indicates Si fraction of about 15-17%, less than the EDX measurements (which may have picked up some of the Si signals from the surrounding amorphous matrix, thus overestimating its amount in the NCs). Furthermore, the TiO₂ (anatase) bottom layer tends to form regions of monocrystalline plates (~ 420 nm wide) which contains a high density of faceted voids of about 10 nm in size (see Fig. 6(a), (b)).

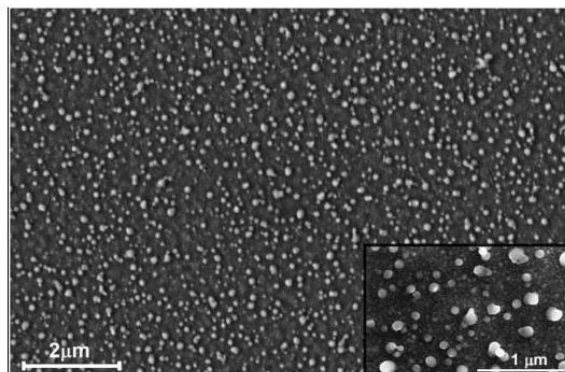


Figure 3. SEM micrograph (at 10.00 K x magnification) of TS₁₋₃₀ after the former annealing step (i.e. without the TiO₂ capping layer). The bright spots are the Si_{1-x}Ge_x nanocrystals with diameters ranging from 80 - 200 nm and height of 5 - 12 nm. The inset shows the surface in higher magnification (50.00 K x).

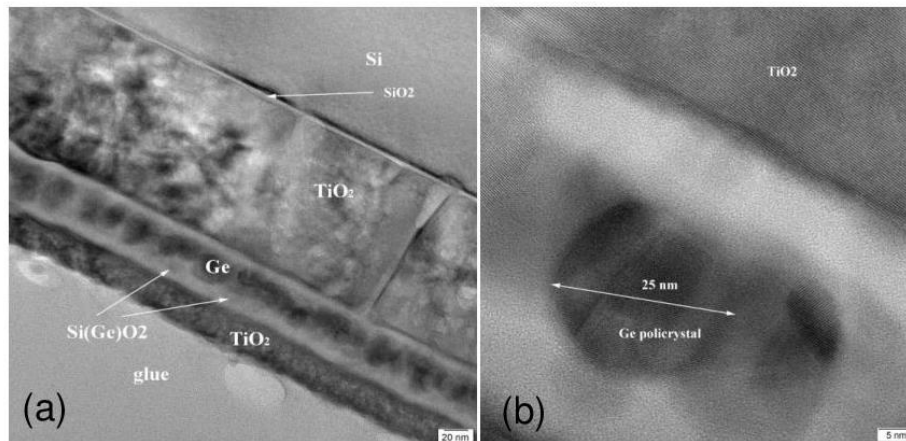


Figure 4. HRTEM images of TS₂₋₃₀ (a) after deposition of TiO₂ cap-layer on top of TS₁₋₃₀ and annealing. (b) Showing segregation of Ge nanocrystal within oxidized intermediate layer (Si(Ge)O₂) sandwich between TiO₂ layers.

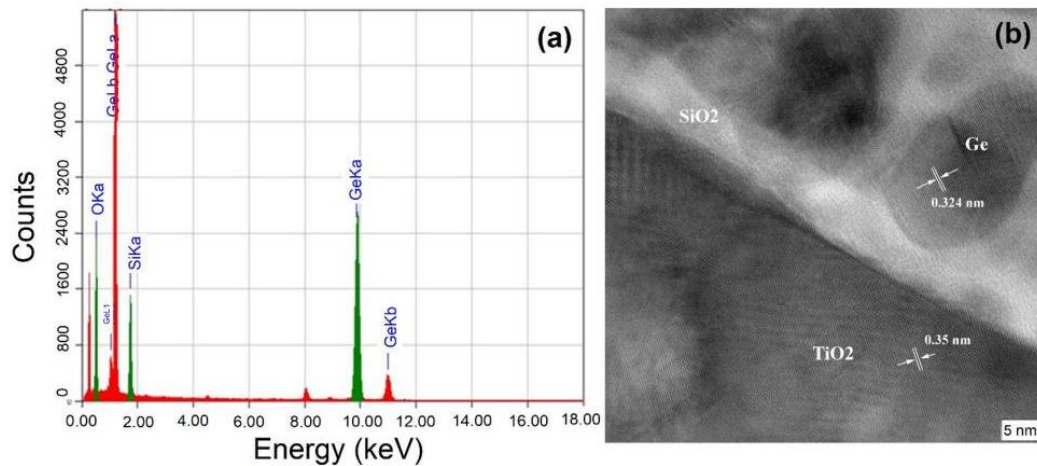


Figure 5. (a) EDX spectrum from TS₂₋₃₀ of a Ge(Si) crystallite embedded in the intermediate layer: O-53.56%; Si- 11.69%; Ge 34.52%; Ti-0.23%. Oxygen signals appear from the surrounding matrix. (b) HRTEM image of Ge(Si) crystallites in the intermediate SiGeO layer.

The realization to avoid the formation of SiO₂ insulating layer involves fabrication of a multilayer in a single step with subsequent annealing of the structure. An effect of retrenching annealing parameters (600 °C, 5 min) is considered in order to obtain photoconductive response from the structures without any formation of insulating SiO₂ layer at the interface of the TiO₂-matrix and the-SiGe-layer (containing nanocrystals) as observed in sample TS₂₋₃₀ (Fig. 4) and elsewhere[30,31]. For the single stage approach, SiO₂/TiO₂/(SiGe/TiO₂)_n MLs with n = 1, 3 and 5 were fabricated (samples SS1-5, SS3-5 and SS5-5, respectively). TEM analysis conducted over SS3-5 structure (Fig. 7) shows a general cross-sectional overview and elemental mapping. Three SiGe layers are evident with no sign of Ti within the SiGe layers but a slight population of oxygen can be seen.

TEM images of the middle and bottom SiGe-layers for sample SS3-5 are shown in Figs. 8(a) and (b), respectively. Roughly, 30 nm thick SiGe layers and non-planar SiGe/TiO₂ interface are seen. For both layers, SiGe NCs of 5 – 10 nm are present in amorphous SiGe layer. In the bottom SiGe-layer, interesting self-assembly of nanocrystals was observed where they form parallel columns, perpendicular to the SiGe layer. Interestingly, the columns being formed are periodically arranged, where the width of NCs is ~ 10 – 15 nm, with a gap of roughly 5 - 6 nm amorphous SiGeO. This presence of the SiGe columnar self-assembly can be due to dominant strain relaxation process as discussed by Yang et al.[40], where strain coupling of dots in adjacent layers may cause them to align in growth direction in order to minimize the strain energy. To mention here in accordance with aim of the investigation, no abrupt and apparent formation of SiO₂ layer at SiGe/TiO₂ interface was visible.

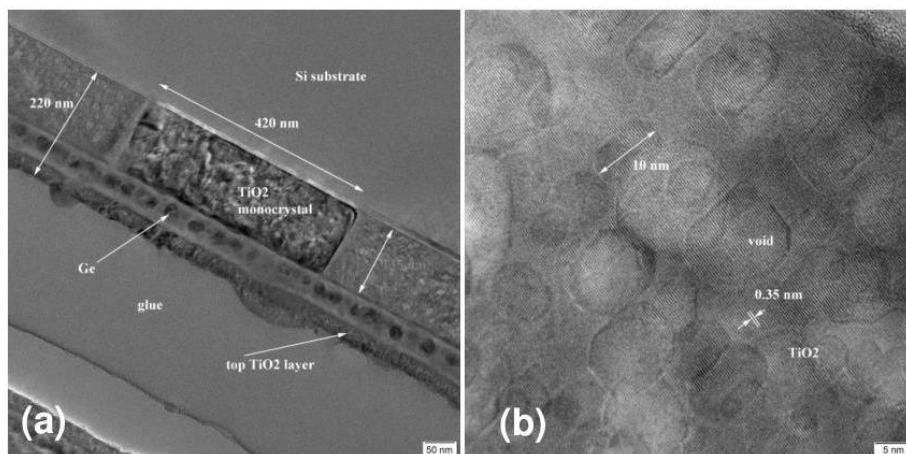


Figure 6. HRTEM image of sample TS₂-30, showing presence of (a) monocrystalline plates of bottom TiO₂ (anatase) and (b) faceted voids in monocrystals regions.

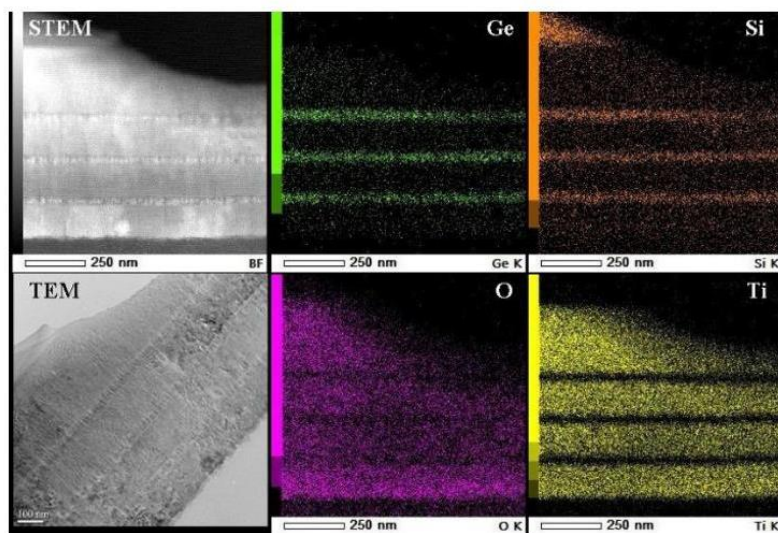


Figure 7. Cross-sectional STEM and TEM images of MLs SS3-5 (left column) along with elemental mapping of Si, Ge, O and Ti (middle and right column).

2.2. Photo response/spectral analysis

Current-voltage (*I-V*) measurements of MLs TS₂-30 in dark and under illumination of 350 and 400 nm light are shown in Fig. 9(a). Roughly, a two orders of magnitude increase in current was observed upon the illumination. However, the structure failed to show any photo-response above 480 nm and in the infrared regime (not shown). This lack of response can be attributed to the formation of an insulating matrix (Si(Ge)O) containing Ge segregated nanoparticles. Such structures contain bonding-related defects at Ge-NCs/Si(Ge)O₂ interfaces plus shearing defects and micro twins inside the nanoparticles, acting as traps or recombination centers, degrading the structure's optical response. Moreover, a double stage fabrication process as in this case

results in the formation of voids in the TiO_2 layers (Fig. 6(b)), which further plays a vital role in degrading the photoconductivity of the structure. Fig. 9(b) shows the photoconductivity versus time under 2V bias during exposure to white light for 40 min and in dark. A very slow optical response is observed. This can be due to localized states in the TiO_2 matrix alone (i.e. limited by the 3.2 eV bandgap of anatase TiO_2) and not due to the nanocrystals formed in the insulating SiO_2 layer, which have created a large amount of recombination centers, trap-levels and defect states in the bandgap.

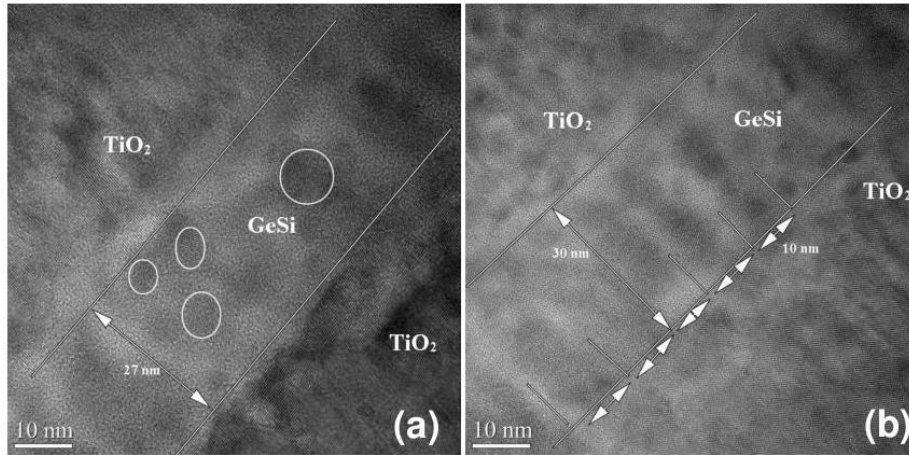


Figure 8. TEM images of sample SS3-5: (a) middle SiGe layer with spherical nanoparticles and (b) bottom SiGe layer showing presence of columnar formation of SiGe nanoparticles (~ 10 nm) having a gap between them of $\sim 5 - 6$ nm.

For the single stage approach (continuous fabrication), the MLs showed a wide range in the photo-response (for the wavelength range from 560-1400 nm) as displayed in Fig. 10. It is well established that increasing the stacking number results in an increase of photocurrent intensity[37]. With this in mind, MLs with 3 and 5 stacks (labeled as SS3-5 and SS5-5, respectively) were prepared and annealed in a similar fashion as MLs SS1-5 i.e. 600°C for 5 min (Fig. 10). An increase in the intensity of over 1 and 2-orders was attained for SS3-5 and SS5-5, respectively, compared to that of SS1-5. In order to evaluate the peaks nature, all the measured spectra were de-convoluted using Origin 10.0 software via multiple peak fit (Gaussian fitting) feature. Several (de-convoluted) peaks were identified (Fig. 11) and are attributed briefly to:

1. Localized states (radiative defects) inside polycrystalline matrix i.e. TiO_2 (peak-1)
2. Strain in structure (peak-2)
3. Interface related localized states (peak-3)
4. Photo-response from $\text{Si}_{1-x}\text{Ge}_x$ NCs (peak-4)
5. Coupling effect (i.e. SPV and gating effect from Si substrate) (peak-5).

The deconvolution (Fig. 11) is carried out in order to investigate the presence and variation in peak position and intensities. In following section, the afore-mentioned peaks will be discussed in respect to their origin or ascribed phenomena.

It is also worth mentioning that with increased stacking order, peaks 3 and 4 show red and blue shifts respectively (Fig. 12). The peak positions are determined using deconvolution of obtained spectra in Fig. 11.

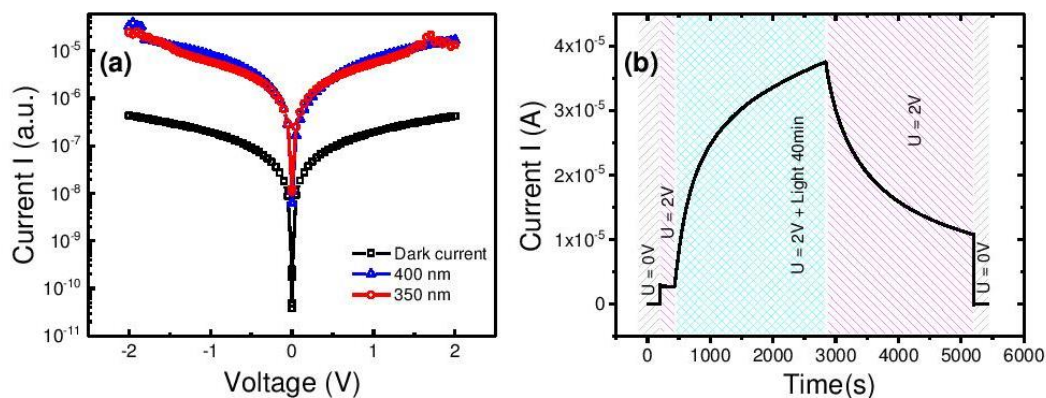


Figure 9. (a) I-V characteristic and (b) charging and discharging behavior of TS₂-30 after the second step annealing (thus, at final fabrication stage).

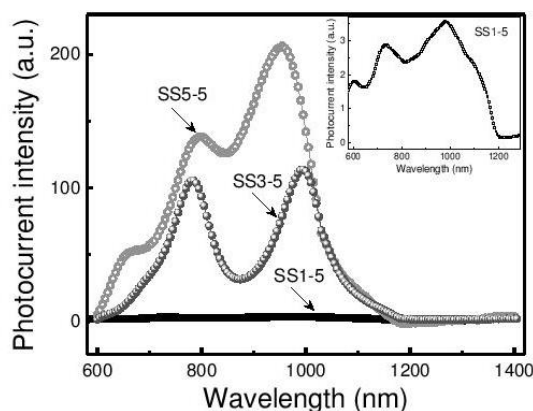


Figure 10. Room temperature photocurrent spectra of MLs fabricated in single stage (SS) with $n = 1, 3$ and 5 , annealed at 600 °C for 5 min. The inset shows zoomed-in view of SS1-5 MLs.

In Fig. 11, a pronounced appearance of the stress-related peak-2 is observed with increased stacking number (i.e. $n = 1$ to 5). The intensity of peak-1 modulates due to reconstruction and ordering of TiO_2 matrix[9,41], which in turn also induces and governs the strain in the NCs and affects their crystallinity. It has been demonstrated that the NCs' crystallinity and shape are affected by the degree of matrix ordering and that it can produce strain in the structure, especially at nanocrystals/matrix interface[3,9,21]. It is also documented that NCs are under large stress when embedded in an oxide matrix[9,10,20,42] and that the magnitude of either compressive or tensile stress varies with the NCs size. Small NCs are under compressive stress, which magnitude depends upon the matrix ordering[42] and the accommodation of expanding NCs is determined by the ordering of the matrix network. Consequently, large compressive stress will be exerted on the NCs if the matrix forms an ordered structure, resisting them to expand freely[9]. In addition, thermal expansion and lattice mismatch (4.2% for Si/Ge[36,43]) between Si, Ge and TiO_2 matrix, does assist in the development of structural strain[10]. This strain causes the NCs to deform which in turn

alters the bandgap. Various groups have studied the effect of strain in relation to energy gap (EG) of systems (often Si-NCs embedded in SiO₂ matrix), where the magnitude and the type of strain can alter the valence and/or conduction states, energy gap and the carrier dynamics. In a work by Guerra et al.[44] it was shown that strain over the NCs depends on the degree of oxidation, which in turn determines the shift in highest occupied molecular orbitals (HOMO) and lowest unoccupied molecular orbitals (LUMO) gaps thus resulting in variation of EG (where the EG is defined as the difference in energy between HOMO, i.e. valence band and the LUMO, i.e. conduction band). The variation in EG as a function of hydrostatic and non-hydrostatic strain was also studied in another work by Peng et al. [45]. There the non-hydrostatic strain was shown to have impact in altering the EG by splitting of degenerated orbitals due to breaking of tetrahedral bond symmetry. This study is complemented by the work of Sun et al.[46], where shear strain was shown to distort the crystal symmetry, leading to degeneracy lifting. Further, an enhancement in quantum confinement along with variation in bandgap is also effected by the degree of strain over the NCs exerted by the surrounding oxide matrix[8]. Considering the above criteria, it is to expect that increased stacking will determine the ordering/reconstruction of the matrix itself (i.e. peak-1 intensity changes) which in turn induces strain in structure (peak-2, of which relative intensity increases) and therefore changes the interface morphology/quality. Further, for the interface quality, it has been theoretically shown[47] that a nanoparticle of Si will form Si-O-Si bond at its surface when oxidized[48]. Such Si-O-Si and Si-Si bonds are relatively weak and likely to break due to stress at NCs/oxide matrix interfaces. These distorted bonds will either result in dangling bonds or eventually forms Si=O bridge since it does not require a large amount of energy or deformation to form[49,50]. These dangling bonds contribute to oxide positive charges (depending on the location of the bond) and interface states, which are electrically active recombination centers for charge carriers and may deteriorate the optical properties of the structure[51]. One solution is passivating the structure via hydrogen plasma treatment[52].

The spectra shown in Figs. 13 and 14 are normalized to unity to clearly demonstrate the shift in peak positions and alteration in intensity. A red shift in peak-4 from 994 to 1045 nm in Fig. 13 (due to SiGe NCs) was observed. The shift is most easily explained on the basis of the well-known phenomena of bandgap dependence on temperature, in nanocrystals. Concurrently, the intensity of peak-3 decreases with decreased temperature from 300 to 100 K and becomes just a small shoulder. At the same time, only a negligible shift in the peak-3 position is observed. It can be deduced that if the peak-3 is due to photo-effect from NCs, it should follow the behavior of temperature dependence of the bandgap. However, its position's insensitivity to temperature and voltage implies that the origin of this peak is not attributed to NCs itself but rather to interface (between NCs and amorphous SiGe and TiO₂ matrix) defects due to radiative recombination from localized states. A similar hypothesis has also been proposed to explain the behavior of photoluminescence spectra from a Si:SiO₂ based structure[53].

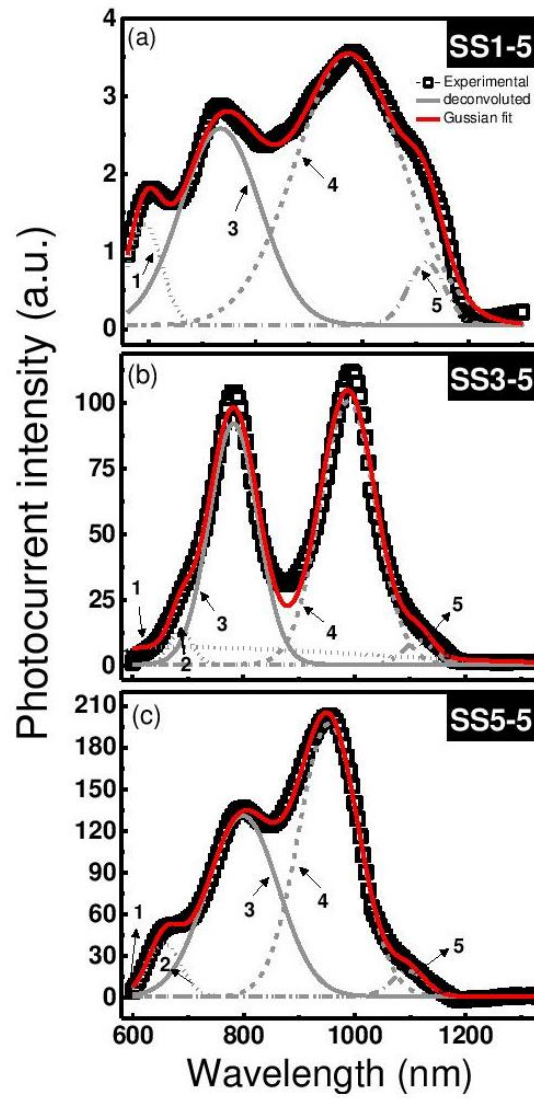


Figure 11. De-convoluted spectra for MLs fabricated in single stage (SS) with $n = 1, 3$ and 5 , annealed at $600\text{ }^{\circ}\text{C}$ for 5 min . The open square is the experimental data, red line represents Gaussian fitting and gray lines are the de-convoluted peaks. The deconvolution is carried out via Origin 10.0 software using multi-peak fitting feature.

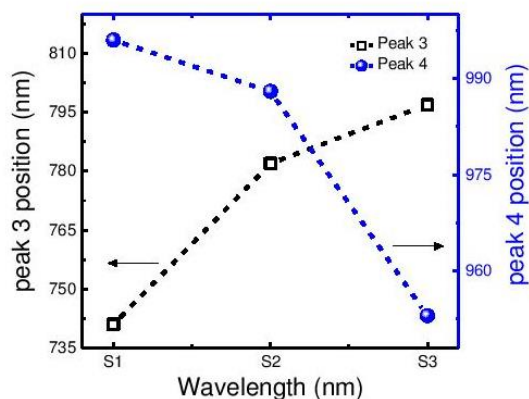


Figure 12. Double y-axis showing shift in peak position for peak-3 (left) and 4 (right) with increase in stacking number (i.e. $n = 1, 3$ and 5). Deconvolution of the spectra was utilized to obtain the peak positions.

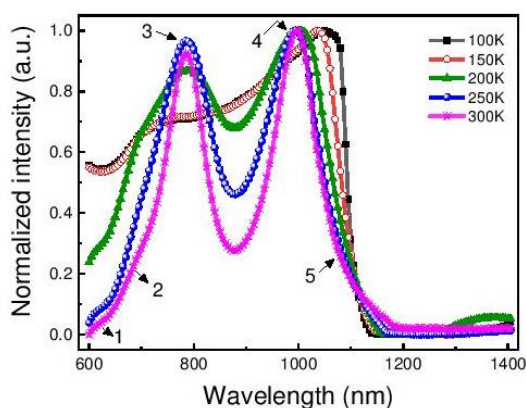


Figure 13. Photocurrent spectra of MLs SS3-5 at varying temperature (300 -100 K) for a fixed bias of 11 V.

To elaborate further on this, the mechanism of energy transfer from one nanocrystal to another is crucial in explaining the photo-spectra of the structure. The energy transfer is the process in which energy is transferred between any two different electronic states. It is explained elsewhere[41] that at low temperature (\sim below 200 K) when the hopping of charge carriers to the interface related localized states are weak and that the thermally activated processes dominate, the excitons due to illumination are more localized in NCs, thus resulting in large contribution from peak-4 and lower than for that of peak-3 as is evident in Fig. 13. Later, when the temperature is increased to 200 K or above the non-radiative channels become activated resulting in an increased intensity of peak-3. That is by increasing the temperature; the NC to NC transfer along with the migration of charge carrier effect becomes more important. Thus, indicating the need to understand and consider the effect of interface related recombination along with the NC-NC energy transfer mechanism to explain the photo spectra of oxide enveloping NCs based structures.

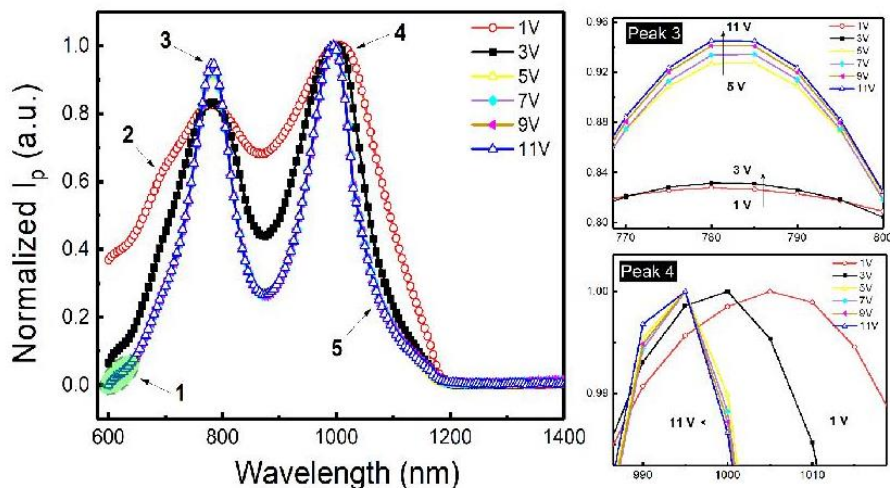


Figure 14. Room temperature photocurrent spectra of MLs SS3-5 at different bias (1- 11 V). The figures on the right show a zoomed-in view of peak 3(top) and 4(bottom) with x and y axes being normalized I_p (a.u.) and wavelength in nm, respectively.

For de-convoluted peak-5 (Fig. 11), a detailed analysis has been carried out elsewhere[54]. The origin of the peak was attributed to the coupling effect from surface photo-voltage (SPV) and gating effect the intensity of which can be modulated by altering the (buffer layer) thickness. Thus, one can see that the shoulder of peak-5 decreases with increased stacking number (Fig. 11(a-c)). Furthermore, increased bias-voltage tends to decrease the intensity of peak-5 (Fig. 14), which then starts to saturate at approximately 7 V. A similar behavior has been observed for Ge NCs embedded in TiO_2 matrix[54], where the intensity of peak due to coupling effect starts to saturate at ~ 12 V. As mentioned by Lepadatu et al.[54], this difference in saturation value is possibly due to difference in thickness of the buffer oxide. In addition, to explain the effect of increase in applied bias over the relative change in intensity and position of peak-3 and 4 respectively (Fig. 14), a similar study could be utilized. The applied bias induces internal electric field due to the formation of charged regions between the Al/TiO_2 (top) and at the TiO_2/SiGe , $\alpha\text{-SiGe/SiGe-NCs}$ and TiO_2 (buffer)/Si-substrate interfaces. These charge regions result in increased photocurrent due to field effect and its associated components *i.e.* SPV and gating effect. This field effect, in turn, alters the Fermi-level causing increased photoconduction by changing the conduction properties and recombination of carriers by the creation of hole-depleted zone with less concentration of dark carrier and increased photosensitivity.

At last, in order to signify the presence of peak-2 as being due to strain, a single stack- MLs was prepared similarly to SS1-5 except that it contains a buffer and capping layer of Si (~ 10 nm) below and above the intermediate laying SiGe layer (denoted as SS1-5*). The room temperature photo spectra is shown in Fig. 15. One can see explicitly the presence of peak-2 as compared to MLs SS1-5 where there is no visible peak accounted for the strain. Moreover, peak-1 shows a blue shift from 596 to 581 nm for MLs SS1-5 and SS1-5* respectively, due to the reconstruction of the matrix accordingly. As explained above regarding interface integrity and a consequential generation of strain due to different thermal expansion coefficient and dielectric constants, the supplemental thin Si film will provide an addition interface and a source for dangling bonds acting as electrically active trapping centers tending to degrade the optical properties. It has been asserted in [4] that the presence of strain in structure can influence the properties of structure either impeding or improving them. Thus, as stated here earlier and elsewhere [55,56], the presence of strain creates defects and/or local deformation in structure and/or NCs. These defects/

distorted regions (especially at interface) acts as traps reducing the charge carrier concentration, and is eventually compensated by a reduction in recombination rates. Therefore, in case for MLs SS1-5* the photocurrent intensity is reduced down to 1/3 compared to that of MLs SS1-5.

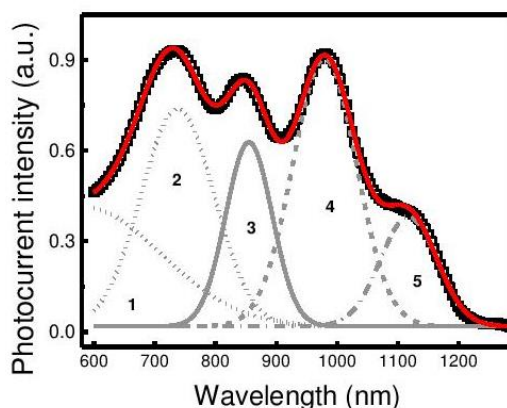


Figure 15. Deconvoluted room temperature photocurrent spectra of MLs SS1-5*.

To conclude, in all the temperature dependent photo spectra the peak/ shoulder due to SPV and gating effect decays and saturates with a decrease in measurement temperature. An investigation to reduce the post-annealing temperature down to 300 °C or even lower is under-consideration, where the effect of stress governing the crystallinity is utilized, as already being discussed elsewhere[10]. For the purpose of inducing strain field, higher deposition rates and/or introduction of an intermediate buffer/capping layer is being utilized. Such retrenching of annealing parameters will make the structure available for the development of Si-based optoelectronic devices where low processing temperature is a requisite.

3. Conclusion

$\text{Si}_p\text{-sub/SiO}_2\text{-buffer/TiO}_2\text{/(SiGe/TiO}_2)_n$ structures were fabricated using direct current magnetron sputtering and furnace annealed at 600°C for either 5 or 30 minutes with aims towards increased photoconductivity and broader spectral range. It was shown that a conventional furnace annealing with low-temperature short exposure can facilitate the formation of SiGe NCs and without formation of detrimental SiO_2 barrier layer in a TiO_2 matrix based system. Upon such mild annealing, the photoconductivity of the structure was increased by more than two orders of magnitude, for stacking number n above one. The photocurrent spectra obtained were de-convoluted to respective peaks accounted from different origins/phenomena. A competition between crystallinity, the degree of matrix ordering, strain field and interface defects, was shown to determine the spectral feature and sensitivity of the obtained spectra.

AUTHOR INFORMATION

Corresponding Author

Halldór Guðfínnur Svavarsson

*E-mail: halldorsv@ru.is

Muhammad. Taha Sultan

*E-mail: muhammad16@ru.is

Acknowledgements

This work is funded through M-ERA.NET project PhotoNanoP UEFISCDI Contract no. 33/2016, PCE project UEFISCDI Contract no. 122/2017 and by Romanian Ministry of Research and Innovation through NIMP Core Program PN19-03 (Contract no. 21N/08.02.2019)” and by the Technology Development Fund of the Icelandic Centre for Research, grant no. 159006-0611.

References

- [1] Church C P, Muthuswamy E, Zhai G, Kauzlarich S M and Carter S A 2013 Quantum dot Ge/TiO₂ heterojunction photoconductor fabrication and performance *Appl. Phys. Lett.* **103** 223506
- [2] Pethuraja G G, Welser R E, Sood A K, Lee C, Alexander N J, Efstathiadis H, Haldar P and Harvey J L 2012 Effect of Ge Incorporation on Bandgap and Photosensitivity of Amorphous SiGe Thin Films *Mater. Sci. Appl.* **03** 67–71
- [3] Sultan M T, Manolescu A, Gudmundsson J T, Torfason K, Alexandru Nemnes G, Stavarache I, Logofatu C, Teodorescu V S, Ciurea M L and Svavarsson H G 2019 Enhanced photoconductivity of SiGe nanocrystals in SiO₂ driven by mild annealing *Appl. Surf. Sci.* **469** 870–8
- [4] Ciurea M L, Lepadatu A-M 2015 Tuning the properties of Ge and Si nanocrystals based structures by tailoring the preparation conditions *Dig. J. Nanomater. Biostructures* **10** 59–87
- [5] Volodin V A, Cherkov A G, Vdovin V I, Stoffel M, Rinnert H and Vergnat M 2016 GeSi nanocrystals formed by high temperature annealing of GeO/SiO₂ multilayers: structure and optical properties, ed V F Lukichev and K V. Rudenko (Proceedings of the SPIE, International Society for Optics and Photonics) **10224** 102240C
- [6] Pan S W, Zhou B, Chen S Y, Li C, Huang W and Lai H K 2011 Optical property investigation of SiGe nanocrystals formed by electrochemical anodization *Appl. Surf. Sci.* **258** 30–3
- [7] Tuğay E, Ilday S, Turan R and Finstad T G 2014 Influence of Ge content and annealing conditions on the PL properties of nc-Si_{1-x}Ge_x embedded in SiO₂ matrix in weak quantum confined regime *J. Lumin.* **155** 170–9
- [8] Dhara S and Giri P K 2011 Size Dependent Anisotropic Strain and Optical Properties of Strained Si Nanocrystals *J. Nanosci. Nanotechnol.* **11** 1–7
- [9] Zatyrb G, Podhorodecki A, Misiewicz J, Cardin J and Gourbilleau F 2013 Correlation between matrix structural order and compressive stress exerted on silicon nanocrystals embedded in silicon-rich silicon oxide *Nanoscale Res. Lett.* **8** 40
- [10] Bahariqushchi R, Raciti R, Kasapoğlu A E, Gür E, Sezen M, Kalay E, Mirabella S and Aydinli A 2018 Stress evolution of Ge nanocrystals in dielectric matrices *Nanotechnology* **29** 185704
- [11] Dalapati G K, Chatterjee S, Samanta S K and Maiti C K 2003 Electrical characterization of low temperature deposited TiO₂ films on strained-SiGe layers *Appl. Surf. Sci.* **210** 249–54
- [12] Yamada Y and Kanemitsu Y 2012 Determination of electron and hole lifetimes of rutile and anatase TiO₂ single crystals *Appl. Phys. Lett.* **101** 133907
- [13] Sarakinos K, Alami J and Wuttig M 2007 Process characteristics and film properties upon growth of TiO₂ films by high power pulsed magnetron sputtering *J. Phys. D: Appl. Phys.* **40** 2108–14
- [14] Schönberger W, Bartzsch H, Schippel S and Bachmann T 2016 Deposition of rutile TiO₂ films by pulsed and high power pulsed magnetron sputtering *Surf. Coatings Technol.* **293** 16–20
- [15] Agnarsson B, Magnus F, Tryggvason T K, Ingason a. S, Leosson K, Olafsson S and Gudmundsson J T 2013 Rutile TiO₂ thin films grown by reactive high power impulse magnetron sputtering *Thin Solid Films* **545** 445–50
- [16] Luttrell T, Halpegamage S, Tao J, Kramer A, Sutter E and Batzill M 2015 Why is anatase a better photocatalyst than rutile? -

- Model studies on epitaxial TiO₂ films *Sci. Rep.* **4** 4043
- [17] Khan A F, Mehmood M, Ali T and Fayaz H 2013 Structural and optical studies of nanostructured TiO₂-Ge multi-layer thin films *Thin Solid Films* **536** 220–8
- [18] Khan A F, Mehmood M, Aslam M and Shah S I 2010 Nanostructured multilayer TiO₂-Ge films with quantum confinement effects for photovoltaic applications *J. Colloid Interface Sci.* **343** 271–80
- [19] Li X, He F, Liu G, Huang Y, Pan C and Guo C 2012 Fabrication of Ge quantum dots doped TiO₂ films with high optical absorption properties via layer-by-layer ion-beam sputtering *Mater. Lett.* **67** 369–72
- [20] Liao P H, Hsu T C, Chen K H, Cheng T H, Hsu T M, Wang C C, George T and Li P W 2014 Size-tunable strain engineering in Ge nanocrystals embedded within SiO₂ and Si₃N₄ *Appl. Phys. Lett.* **105** 172106
- [21] Hadjisavvas G, Remediakis I N and Kelires P C 2006 Shape and faceting of Si nanocrystals embedded in a-SiO₂: A Monte Carlo study *Phys. Rev. B* **74** 165419
- [22] Pinto S R C, Kashitiban R J, Rolo A G, Buljan M, Chahboun A, Bangert U, Barradas N P, Alves E and Gomes M J M 2010 Structural study of Si_{1-x}Ge_x nanocrystals embedded in SiO₂ films *Thin Solid Films* **518** 2569–72
- [23] Stavarache I, Lepadatu A-M, Stoica T and Ciurea M L 2013 Annealing temperature effect on structure and electrical properties of films formed of Ge nanoparticles in SiO₂ *Appl. Surf. Sci.* **285** 175–9
- [24] Zhang B, Shrestha S, Green M A and Conibeer G 2010 Size controlled synthesis of Ge nanocrystals in SiO₂ at temperatures below 400 °C using magnetron sputtering *Appl. Phys. Lett.* **96** 261901
- [25] Lepadatu A-M, Stavarache I, Stoica T F, Ciurea M L 2011 Study of Ge nanoparticles embedded in an amorphous SiO₂ matrix with photoconductive properties *Dig. J. Nanomater. Biostructures* **6** 67–73
- [26] Vieira E M F, Pinto S R C, Levichev S, Rolo A G, Chahboun A, Buljan M, Barradas N P, Alves E, Bernstorff S, Conde O and Gomes M J M 2011 Influence of the deposition parameters on the growth of SiGe nanocrystals embedded in Al₂O₃ matrix *Microelectron. Eng.* **88** 509–13
- [27] Zhang B, Shrestha S, Aliberti P, Green M A and Conibeer G 2009 Synthesis and structural properties of Ge nanocrystals in multilayer superlattice structure ed L Tsakalakos Proc. SPIE 7411 p 741103
- [28] Long E, Azarov A, Kløw F, Galeckas A, Yu Kuznetsov A and Diplas S 2012 Ge redistribution in SiO₂/SiGe structures under thermal oxidation: Dynamics and predictions *J. Appl. Phys.* **111** 024308
- [29] Lepadatu A-M, Stoica T, Stavarache I, Teodorescu V S, Buca D and Ciurea M L 2013 Dense Ge nanocrystal layers embedded in oxide obtained by controlling the diffusion-crystallization process *J. Nanoparticle Res.* **15** 1981
- [30] Palade C, Dascalescu I, Slav A, Lepadatu AM, Lazanu S, Stoica T, Teodorescu V S, Ciurea M L, Comanescu F, Muller R, Dinescu A and Enuica A 2017 Photosensitive GeSi/TiO₂ multilayers in VIS-NIR In Proceeding of the International Semiconductor Conference CAS (IEEE), Sinaia, Romania, October 11 - 14, 2017; pp 67-70.
- [31] Slav A, Palade C, Stavarache I, Teodorescu V S, Ciurea M L, Muller R, Dinescu A, Sultan M T, Manolescu A, Gudmundsson J T and Svavarsson H G 2017 Influence of preparation conditions on structure and photosensing properties of GeSi/TiO₂ multilayers In Proceeding of the International Semiconductor Conference CAS (IEEE), Sinaia, Romania, October 11 - 14, 2017; pp 63-66.
- [32] Hiller D, Gutsch S, Hartel A M, Löper P, Gebel T and Zacharias M 2014 A low thermal impact annealing process for SiO₂-embedded Si nanocrystals with optimized interface quality *J. Appl. Phys.* **115** 134311
- [33] Kepa J, Stesmans A and Afanas'ev V V 2014 Comparative analysis of thermally induced degradation of condensation-grown (100) Ge_{0.75}Si_{0.25}/SiO₂ interfaces by electron spin resonance *Appl. Surf. Sci.* **291** 20–4
- [34] Cemin F, Tsukamoto M, Keraudy J, Antunes V G, Helmersson U, Alvarez F, Minea T and Lundin D 2018 Low-energy ion irradiation in HiPIMS to enable anatase TiO₂ selective growth *J. Phys. D: Appl. Phys.* **51** 235301
- [35] Ciurea M L, Stavarache I, Lepadatu A-M, Pasuk I and Teodorescu V S 2014 Electrical properties related to the structure of GeSi nanostructured films *Phys. Status Solidi B* **251** 1340–6
- [36] Aqua J N, Berbezier I, Favre L, Frisch T and Ronda A 2013 Growth and self-organization of SiGe nanostructures *Phys. Rep.* **522** 59–189
- [37] Vieira E M F, Toudert J, Rolo A G, Parisini A, Leitão J P, Correia M R, Franco N, Alves E, Chahboun A, Martín-Sánchez J, Serna R and Gomes M J M 2017 SiGe layer thickness effect on the structural and optical properties of well-organized SiGe/SiO₂ multilayers *Nanotechnology* **28** 345701
- [38] Chew H G, Choi W K, Foo Y L, Zheng F, Chim W K, Voon Z J, Seow K C, Fitzgerald E A and Lai D M Y 2006 Effect of germanium concentration and oxide diffusion barrier on the formation and distribution of germanium nanocrystals in silicon oxide matrix *Nanotechnology* **17** 1964–8
- [39] Yu D and Hwang G S 2008 Structure and Dynamics of Ge in the Si-SiO₂ System: Implications for Oxide-Embedded Ge Nanoparticle Formation *Electrochem. Solid-State Lett.* **11** 17–9
- [40] Yang X-F, Fu K, Lu W, Xu W-L and Fu Y 2009 Strain effect in determining the geometric shape of self-assembled quantum dot *J. Phys. D: Appl. Phys.* **42** 125414
- [41] Tuğay E and Turan R 2016 Investigation of Photoluminescence Mechanisms from SiO₂/Si:SiO₂/SiO₂ Structures in Weak Quantum Confined Regime by Deconvolution of Photoluminescence Spectra *J. Nanosci. Nanotechnol.* **16** 4052–64
- [42] Zatyrb G, Misiewicz J, Wilson P R J, Wojcik J, Mascher P and Podhorodecki A 2014 Stress transition from compressive to tensile for silicon nanocrystals embedded in amorphous silica matrix *Thin Solid Films* **571** 18–22
- [43] Ye H and Yu J 2014 Germanium epitaxy on silicon *Sci. Technol. Adv. Mater.* **15** 024601
- [44] Guerra R, Degoli E and Ossicini S 2009 Size, oxidation, and strain in small Si/SiO₂ nanocrystals *Phys. Rev. B* **80** 155332
- [45] Peng X-H, Alizadeh A, Bhate N, Varanasi K K, Kumar S K and Nayak S K 2007 First-principles investigation of strain effects on the energy gaps in silicon nanoclusters *J. Phys. Condens. Matter* **19** 266212
- [46] Sun Y, Thompson S E and Nishida T 2007 Physics of strain effects in semiconductors and metal-oxide-semiconductor field-effect transistors *J. Appl. Phys.* **101** 104503

- [47] Wolkin M V., Jorne J, Fauchet P M, Allan G and Delerue C 1999 Electronic States and Luminescence in Porous Silicon Quantum Dots: The Role of Oxygen *Phys. Rev. Lett.* **82** 197–200
- [48] Szekeres A and Alexandrova S 1996 Low-temperature treatment of Si/SiO₂ structures in an RF hydrogen plasma *Vacuum* **47** 1483–6
- [49] Puzder A, Williamson A J, Grossman J C and Galli G 2002 Surface control of optical properties in silicon nanoclusters *J. Chem. Phys.* **117** 6721–9
- [50] López M, Garrido B, García C, Pellegrino P, Pérez-Rodríguez A, Morante J R, Bonafos C, Carrada M and Claverie A 2002 Elucidation of the surface passivation role on the photoluminescence emission yield of silicon nanocrystals embedded in SiO₂ *Appl. Phys. Lett.* **80** 1637–9
- [51] Yakimov A I, Kirienko V V, Armbrister V A and Dvurechenskii A V 2014 Hydrogen passivation of self-assembled Ge/Si quantum dots *Semicond. Sci. Technol.* **29** 085011
- [52] Sultan M T, Gudmundsson J T, Manolescu A, Stoica T, Ciurea M L and Svavarsson H G 2019 Enhanced photoconductivity of embedded SiGe nanoparticles by hydrogenation *Appl. Surf. Sci.* **479** 403–9
- [53] Wang X X, Zhang J G, Ding L, Cheng B W, Ge W K, Yu J Z and Wang Q M 2005 Origin and evolution of photoluminescence from Si nanocrystals embedded in a SiO₂ matrix *Phys. Rev. B* **72** 195313
- [54] Lepadatu A-M, Slav A, Palade C, Dascalescu I, Enculescu M, Iftimie S, Lazanu S, Teodorescu V S, Ciurea M L and Stoica T 2018 Dense Ge nanocrystals embedded in TiO₂ with exponentially increased photoconduction by field effect *Sci. Rep.* **8** 4898
- [55] Ciurea M L, Lazanu S, Stavarache I, Lepadatu A-M, Iancu V, Mitroi M R, Nigmatullin R R and Baleanu C M 2011 Stress-induced traps in multilayered structures *J. Appl. Phys.* **109** 013717
- [56] Ciurea M L 2013 Effect of stress on trapping phenomena in silicon: from single crystal to nanostructures *Rom. Rep. Phys.* **65** 841-856

Paper IV

Fabrication and characterization of Si_{1-x}Ge_x nanocrystals in as-grown and annealed structures: A comparative study by hydrogenation

*Sultan M T¹, Maraloiu A V², Stavarache I², Gudmundsson J T^{3,4}, Manolescu A¹, Teodorescu V S^{2,5}, Ciurea M L^{2,5}, *Svavarsson H G¹

¹School of Science and Engineering, Reykjavik University, IS-101 Reykjavik, Iceland

²National Institute of Materials Physics, 077125 Magurele, Romania

³Department of Space and Plasma Physics, School of Electrical Engineering and Computer Science, KTH-Royal Institute of Technology, SE-100 44, Stockholm, Sweden

⁴Science Institute, University of Iceland, IS-101 Reykjavik, Iceland

⁵Academy of Romanian Scientists, 050094 Bucharest, Romania

Published: Beilstein Journal of Nanotechnology, vol. 10, pp. 1873-1882, 2019.

DOI: <https://doi.org/10.3762/bxiv.2019.16.v1>



BEILSTEIN JOURNAL OF NANOTECHNOLOGY

Fabrication and characterization of Si_{1-x}Ge_x nanocrystals in as-grown and annealed structures: a comparative study

Muhammad Taha Sultan¹, Adrian Valentin Maraloiu², Ionel Stavarache², Jón Tómas Gudmundsson^{3,4}, Andrei Manolescu¹, Valentin Serban Teodorescu^{2,5}, Magdalena Lidia Ciurea^{2,5} and Halldór Guðfínnur Svavarsson¹

Full Research Paper		Open Access
<p>Address: ¹Reykjavik University, School of Science and Engineering, IS-101 Reykjavik, Iceland, ²National Institute of Materials Physics, 077125 Magurele, Romania, ³Science Institute, University of Iceland, Dunhaga 3, IS-107 Reykjavik, Iceland, ⁴Department of Space and Plasma Physics, School of Electrical Engineering and Computer Science, KTH Royal Institute of Technology, SE-100 44, Stockholm, Sweden and ⁵Academy of Romanian Scientists, 050094 Bucharest, Romania</p>		
<p>Email: Muhammad Taha Sultan[*] - muhammad16@ru.is; Halldór Guðfínnur Svavarsson[*] - halldorsv@ru.is</p>		
<p>* Corresponding author</p>		
<p>Keywords: grazing incidence XRD (GIXRD); high-power impulse magnetron sputtering (HIPIMS); HRTEM; magnetron sputtering; photocurrent spectra; SiGe nanocrystals in SiO₂/SiGe/SiO₂ multilayers; STEM-HAADF; TEM</p>		
<p>Beilstein J. Nanotechnol. 2019, 10, 1873–1882. doi:10.3762/bjnano.10.182</p>		<p>Received: 26 April 2019 Accepted: 28 August 2019 Published: 17 September 2019</p>
<p>Associate Editor: C. T. Yavuz</p>		<p>© 2019 Sultan et al.; licensee Beilstein-Institut. License and terms: see end of document.</p>



Fabrication and characterization of Si_{1-x}Ge_x nanocrystals in as-grown and annealed structures: A comparative study

Muhammad Taha Sultan^{1*}, Adrian Valentin Maraloiu², Ionel Stavarache², Jon Tomas Gudmundsson^{3, 4}, Andrei Manolescu¹, Valentin Serban Teodorescu^{2, 5}, Magdalena Lidia Ciurea^{2, 5}, Halldor Gudfinnur Svavarsson^{1*}

¹Reykjavik University, School of Science and Engineering, IS-101 Reykjavik, Iceland

²National Institute of Materials Physics, 077125 Magurele, Romania

³Science Institute, University of Iceland, Dunhaga 3, IS-107 Reykjavik, Iceland

⁴Department of Space and Plasma Physics, School of Electrical Engineering and Computer Science, KTH Royal Institute of Technology, SE-100 44, Stockholm, Sweden

⁵Academy of Romanian Scientists, 050094 Bucharest, Romania

Abstract

Multilayer structure comprising of SiO₂/SiGe/SiO₂ were obtained by depositing SiO₂ layers using reactive direct current magnetron sputtering (dcMS), whereas, Si and Ge were co-sputtered using dcMS and high impulse power magnetron sputtering (HiPIMS), respectively. The as-grown structures subsequently underwent rapid thermal annealing (550 – 900 °C for 1 min) in N₂ ambient atmosphere. The structures were investigated using X-ray diffraction, high-resolution transmission electron microscopy together with spectral photocurrent measurements, to explore structural changes and corresponding properties. It is observed that the employment of HiPIMS facilitates the formation of SiGe nano-particles (~ 2.1 ± 0.8 nm) in the as-grown structure, and that presence of such nano-particles acts as a seed for heterogeneous nucleation, which upon annealing results in formation of periodically arranged columnar self-assembly of core-shell like SiGe nanocrystals. Consequently, an increase in photocurrent intensity by more than an order of magnitude was achieved by the annealing. Furthermore, a detailed discussion is provided on strain development within the structures, the consequent interface characteristics and its effect on the photocurrent spectra.

Keywords

GiXRD; magnetron sputtering, HiPIMS; photocurrent spectra; SiGe nanocrystals in SiO₂/SiGe/SiO₂ multilayers; TEM, HRTEM, STEM-HAADF

Introduction

Currently, a considerable interest has been devoted to the growth of self-assembled quantum dots due to its quantum confinement effect and its numerous application in optoelectronics and nano-based structures. Semiconducting Si, Ge and SiGe nanocrystals (NCs/NPs), embedded in a dielectric oxide matrix have for instance been found to exhibit strong quantum confinement. These NCs present unique and interesting size-dependent physical properties for a wide range of application including lighting, in non-volatile memories, electronic and photovoltaic applications[1–3]. SiGe nano-based structures provide stronger quantum confinement effect than Si NCs[4] and have the advantage of a band gap fine tuning by varying the Ge atomic fraction[5,6]. Such properties are useful for optoelectronic devices employed for the visible to far-infrared regime [4,7].

Issues commonly observed with fabrication of such structures include inhomogeneity at the matrix/nanoparticle (NCs/NPs) interfaces. Several studies have been devoted to the morphology of the interface between oxide matrices and NCs[8–10]. The interface of such structure has been a matter of concern in studying optical response as it may give rise to dangling bonds acting as electrically active interface traps (known as P_b-type defects). These interface traps produce scattering centers, which can affect the mobility of charge carriers, thus altering the transport properties[11]. Moreover, sharp interfaces with an abrupt change in the dielectric constant or thermal expansion coefficients, gives rise to surface polarization effect due to the local field built up (which assumes a crucial role for systems characterized by strong charge inhomogeneity). Further the strain development in the structure influences the size and shape of the NCs, thus resulting in alteration of the bandgap energy.

A common method to obtain NCs embedded in an oxide matrix is by thermal anneal treatment of multilayer structures. Several oxide matrices have been studied already[12–18], of which SiO₂ is the most studied as it remains amorphous up to high temperatures and due to its compatibility with Si-based technology [19–21]. Various fabrication methods have been utilized to fabricate structures with embedded SiGe NCs in an oxide matrix[13,17,22,23]. Magnetron sputtering is one of the most versatile method and it allows a good control over the NCs formation[24] by a complementary addition of rapid thermal annealing. A rather recent variation of the magnetron sputtering technique, so-called high power impulse magnetron sputtering (HiPIMS), provides an alternative approach. It is an ionized physical vapor deposition method and has shown great promise in thin film processing[25,26]. HiPIMS operates by pulsing the target with short unipolar voltage pulses at low frequency and short duty cycle, achieving high discharge current densities leading to a high ionization fraction of the sputtered material[27,28]. This

approach gives denser films[29] and of higher crystallinity[30] than conventional direct current magnetron sputtering (dcMS) deposition technique.

Thermal treatment, being one of the most common method to obtain NCs embedded in an oxide matrix, improves the efficiency and stability of the devices by altering the size of the embedded NCs[31,32]. In the present study, a short (1 min) exposure to rapid thermal annealing is carried out over earlier investigated structures[22], where the use of HiPIMS to obtain $\text{Si}_{1-x}\text{Ge}_x$ NCs in as-grown samples is demonstrated. Upon rapid thermal annealing, periodically arranged columnar self-assembled SiGe NCs are obtained. The NCs are characterized using grazing incidence X-ray diffraction (GiXRD) and high resolution transmission electron microscopy (HRTEM). The role of different character of strain relaxation and its consequent effect over NCs formation and resulting interface integrity was studied and compared with structures having thicker (~200 nm) SiGe layer[23], deposited by radio-frequency magnetron sputtering (rfMS). In another previous study[22] we demonstrated NCs in as-grown structures with broader spectral response and improved efficiency after exposure to hydrogen plasma. The effect of annealing of such structures is yet to be explored, so as to make such structures available for devices which require controlled thermal treatments to preserve the functionality of devices[32]. A comparison is made to present the effect of SiGe thickness over strain accumulation in NCs (which have a deliberate effect over the size and formation of NCs, and eventually influences the photocurrent spectra), and demonstrate the effectiveness of mild thermal exposure, applicable to structures prone to decomposition at elevated temperature.

Results and Discussion

The multilayer structures (MLs) deposited in present study are similar to structures studied in our recent work[22] as regard the stacking order (i.e. $\text{SiO}_2/\text{SiGe}/\text{SiO}_2$) and the individual layer thicknesses. The difference in the fabrication is that for co-sputtering of SiGe layer, here we apply lower cathode voltage for the Ge deposition, i.e. 445 V instead of 470 V, at repetition frequency of 300 Hz, with an average power of 103 W. For Si (co-deposited via dcMS) the power is kept constant at 180 W.

Structural analysis

Earlier we demonstrated that for structures with pure Ge-film sandwiched between SiO_2 layers, the Ge film were crystalline when sputtered by the HiPIMS method due to its high electron density in the plasma (high power density). The higher electron density increases the ionization of Ge sputtered off the target, leading to better quality of film through ion bombardment. As described later in the experimental section and also in our earlier study[22], the $\text{Si}_{1-x}\text{Ge}_x$ layer was co-deposited via combined dcMS and HiPIMS

from Si and Ge targets, respectively. Fig. 1(a) shows the GiXRD diffractograms for the as-grown and annealed MLs (550 - 900 °C). Two broad bands are evident for the as-grown structure. The first one corresponds to crystallographic plane (111) and the second one to the (220) and (311) planes overlapping indicating the presence of (nano) crystallites[22]. In Fig. 1(b), a deconvolution of diffractogram for the as-grown MLs was achieved by subtracting the background using Origin software (10.0) (counter checked using X'Pert HighScore Plus software from PANalytical, ver. 2.2). The size of the crystallites was calculated from the peak representing (111) crystallographic plane using Scherrer equation[33,34] with shape (k)-factor being 0.9 and instrumental error i.e. beam broadening of 0.12. Although this is an indecisive approach[22,23], the parameters used to calculate the crystallites size are mentioned in Fig. 1(b) and it was found to be 2.1 ± 0.8 nm. This reduction in crystallite size, compared to previously investigated structures is due to variation in deposition parameters such as cathode voltage.

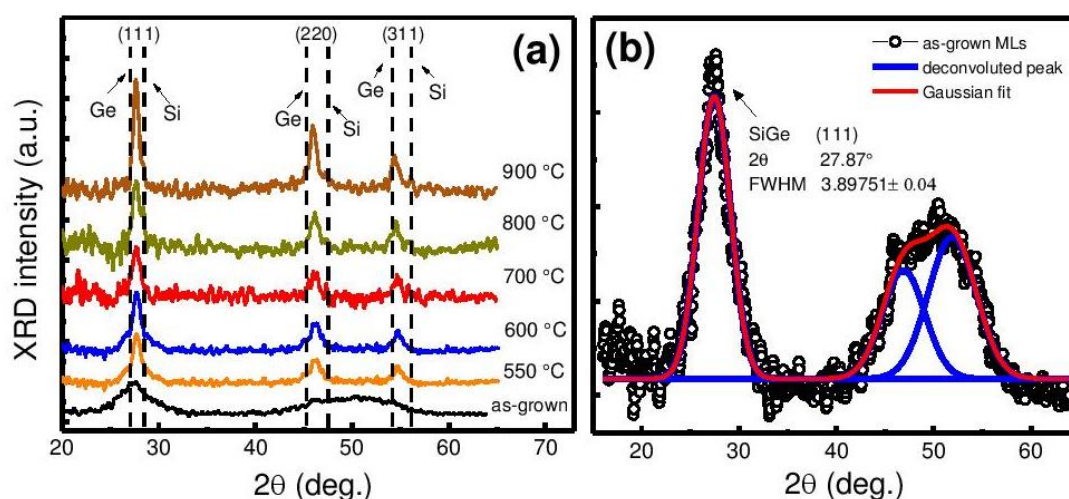


Figure 1. (a) GiXRD diffractogram of MLs annealed from 550 – 900 °C along with the as-grown MLs. The SiGe crystallographic peaks (111), (220) and (311) are positioned between Si and Ge tabulated ones presented by the dotted lines (for cubic Ge ($2\theta = 27.45^\circ; 45.59^\circ; 54.04^\circ$ - ASTM 01-079-0001) and cubic Si ($28.45^\circ; 47.31^\circ; 56.13^\circ$ - ASTM 01-070-5680)). (b) Deconvoluted GiXRD diffractogram for SiO₂/SiGe/SiO₂ MLs, as-deposited (black circles) where, the Gaussian fit is shown by red line while deconvoluted peaks are shown in blue.

After annealing, three separate and distinctive peak are evident (Fig. 1(a)). An increase in the XRD peak intensity was observed along with a decrease in full width half maxima (FWHM), indicating an increased crystallinity obtained via increasing anneal temperature. The size of the NCs was determined, using the crystallographic peak (111)

via Scherrer equation, to vary from 7.32 to 13.4 ± 0.8 nm, for annealing temperature ranging from 550 to 900 °C. For this purpose, a more precise run was made with smaller step size and larger time per step, which then was processed by Origin 10.0 software using multiple peak feature (not shown here). To summarize, the NCs size, is roughly 2 nm in the as-grown structure and increases to 7.3 – 13.4 nm upon annealing.

Another feature to be observed here is that, for samples annealed at 550 and 600 °C (Fig. 1(a)), a sharp peak over a broad hump (extending from 25 to 31 degrees) is seen, indicating that the SiGe layer is mainly amorphous but with crystalline regions (nanoparticles) (as seen in TEM images later in Fig. 5(a) and (c)). With increased annealing temperature, peaks corresponding to the (111), (220) and (311) planes get sharper and narrower as a sign of increased crystallinity of the SiGe layer. Moreover, a small peak positioned at Si standard tabulated positions (28.45°) is observed at annealing temperatures above 600 °C (Fig. 2, selected zoomed view of peak (111) for MLs annealed at 800 °C), along with a shoulder positioned at Ge standard position (27.45°). Based on these observations, it can be concluded that the structure consists of core-shell like NCs/NPs with the core being Ge-rich $\text{Si}_{1-x}\text{Ge}_x$ NCs (crystallographic peak (111) position, shifts from 27.87° to 27.754° for MLs in as-grown and annealed at 800 °C states, respectively) surrounded by a shell of crystalline Si in amorphous SiGeO. This behavior can be explained by phase separation in the SiGe nanoparticles due to Ge segregation[34,35] at higher temperature (i.e. Ge rich SiGe core) leaving a crystalline Si shell. A similar GiXRD diffractogram was observed by Tuğay et al.[6], for a comparable structure composed of SiGe NCs embedded in SiO_2 matrix fabricated via magnetron sputtering and thermally annealed. A TEM analysis, discussed later in this section, will further elaborate on the observed nanostructure.

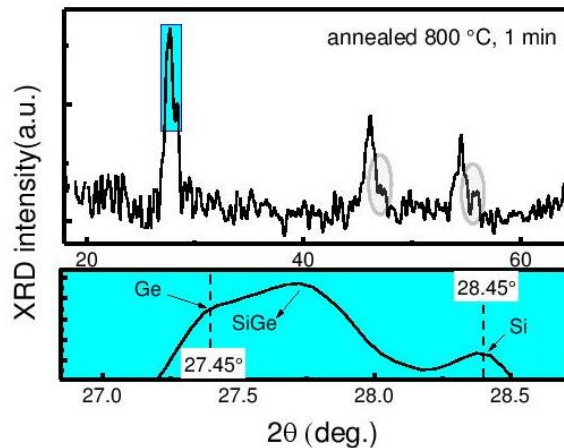


Figure 2. GiXRD diffractogram (upper part) with zoomed-in view (lower part) of crystallographic plane (111) of MLs annealed at 800 °C for 1 min.

Fig. 3 shows the X-ray reflectometry (XRR) plot for as-deposited and annealed MLs. An increase in the mass density of SiGe (3.55 to 4.17 gm/cm³) with increased annealing temperature was perceived, represented by the vertical dashed lines. In addition, a decrease in the SiGe thickness (19.57 to 17.8 nm (± 3 % error)) and the interface roughness (3.56 to 3.28 nm) was observed with increased annealing temperature from room temperature (as-grown) to 900 °C. All the parameters were determined by fitting the data using the X'Pert Reflectivity software. A clear evolution of fringes can be seen (shown in an enclosed area by dashed line in Fig. 3) for annealing temperature up to 700 °C, which then starts to coalesce at 800 °C and later showed appearance of Kiessing fringes (green arrows) due to scattering from the film surface and internal interfaces, thus demonstrating the alteration in the internal interface morphology. This can be further explained by the observed reduction in thickness when annealed at 800 - 900 °C and might be due to out-diffusion of Si forming Si-shell (as also explained earlier, where the crystallographic peak (111) shifts towards standard Ge position) or SiO_x (will be discussed later in this section). Hence, with increased anneal temperature; formation of additional interfaces is likely to occur.

In Fig. 4(a), cross-sectional transmission electron microscopy (XTEM) image of a sample annealed at 600 °C for 1 min is presented. The thicknesses of the SiO₂ bottom (buffer) and top layers are about 250 nm and 40 nm, respectively while the SiGe layer is 20 nm thick. Fig. 4(b) present selected area electron diffraction (SAED) pattern. The area used for electron diffraction was selected in order to have the Si substrate spots together with the ring spots of the SiGe polycrystalline layer. A description of such analysis is given in our previous work [23]. The bright spots are due to Si substrate and the smaller and less bright spots are due to SiGe NCs. The white hollow circular cloud corresponds to amorphous SiO₂. Our measurements have an estimated error of 0.5% and the results are in good agreement with the XDR measurements which corresponds to 30:70 composition for Si:Ge[36] (i.e. 0.599 nm is the lattice constant measured by XRD calculated via (220) crystallographic plane).

The white contrast seen in high-angle annular dark-field scanning transmission electron microscopy (HAADF-STEM) image (Fig. 5(b)) emphasizes the Ge atoms density, revealing the morphology of the SiGe crystallites. The SiGe NCs have columnar/ellipsoidal morphology oriented with the large axis parallel with the film's normal (Figs. 5(a and c)). The crystallization process during annealing develops a stress field in the SiGe film plane that is the key factor for obtaining equidistant / quasiperiodic SiGe NCs arrangement. The SiGe NCs are stress-free in the normal direction on the film and show no internal defect. The formation or modification of the planar morphology of the 20 nm SiGe layer is expected to be due to accumulation of strain field exerted by the SiO₂ matrix, which has been relaxed by forming corrugated edges of the SiGe film (Fig. 4(a) and 5). In contrast, for the thicker SiGe films, the strain is (partially) relaxed by forming planar defects

as we demonstrated elsewhere[23] and discuss further below. Periodic SiGe crystallites with a ~ 12.5 nm period covered with amorphous SiGeO oxide (Si-rich) are visible in Fig. 5. The size of 12.5 nm correspond in fact to the diameter of the SiGe ellipsoid plus the thickness of the SiGeO oxide cover-layer *i.e.* each SiGe crystallite is covered by a 2 -3 nm of SiGeO oxide, looking like a core-shell particle. An elemental mapping over a structure $(\text{TiO}_2/\text{SiGe}/\text{TiO}_2)_3$ annealed at 600 °C in our previous study [37], showed similar formation of columnar self-assembly of NCs. The analysis showed a well-defined mapping of Si, Ge and Ti ($/\text{TiO}_2$) with a slight population of oxygen observed with in SiGe layer. The NCs columns being formed were arranged periodically, having the width of NCs of ~ 10 – 15 nm, with a gap constituting of ~ 5 – 6 nm amorphous SiGeO.

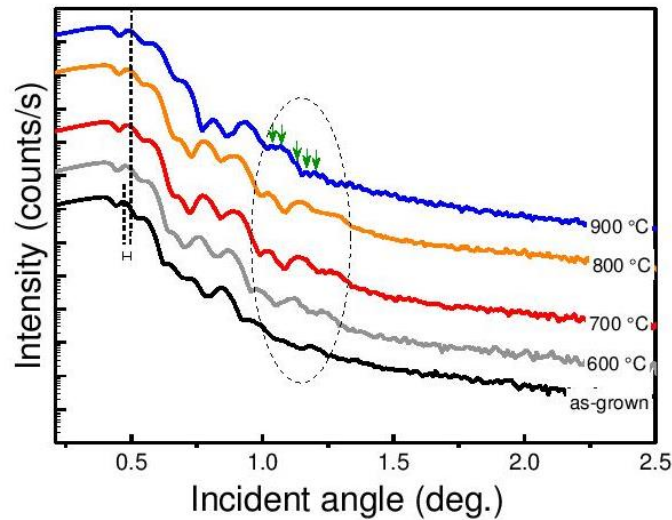


Figure 3. XRR plot for as-deposited and annealed (for 1 min) structures. The vertical dashed lines shows the difference in incident angle, whereas, the labeling next to each curve represents the annealing temperature.

We note that the small SiGe nano-crystallites present in as-deposited MLs may have acted as a seed/nuclei for the directional crystallization of the nanoparticles as has also been suggested by Bertan et al.[38]. It is postulated there, that the nano-sized ordered domains of Si have acted as seed crystals, resulting in a swift growth of crystals upon annealing as compared to structures without having nuclei initially present. This indicates that a similar behavior may have caused such a columnar self-organization of NCs in our structures, as depicted in Figs. 4 and 5. Thus, we can anticipate heterogeneous nucleation to be a dominant process during such crystallization rather than conventional homogenous nucleation. This can be due to a better wetting of SiGe layer, which in turn reduces the free energy of change and reduces the nucleation barrier. It can also be argued that since heterogeneous nucleation occurs at preferential sites (as in our case),

small NCs in as-grown MLs or even the crystallites which are under strain[39–42], will further reduce the surface energy and facilitate nucleation.

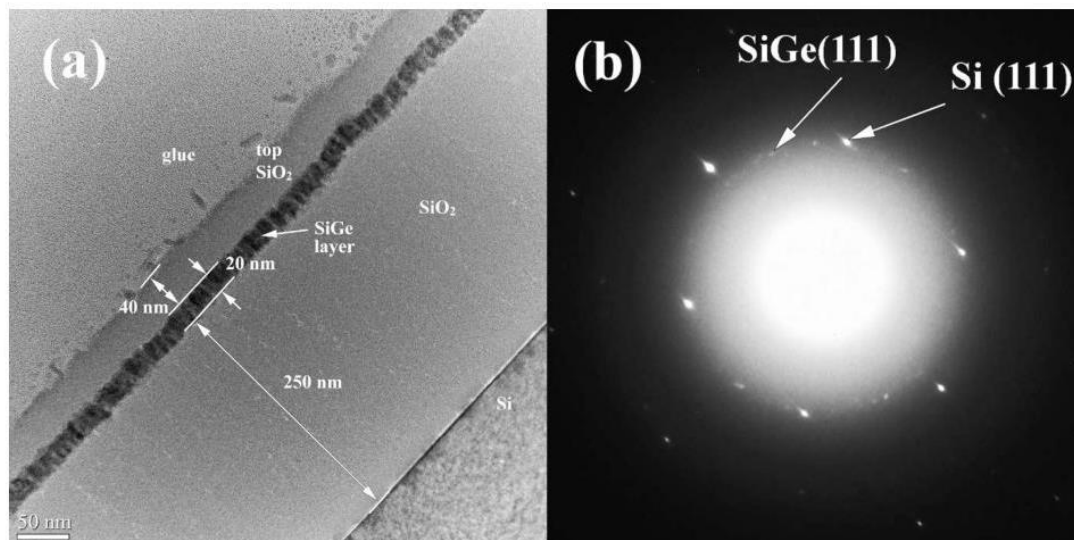


Figure 4. XTEM images of (a) MLs with 20 nm SiGe layer after 600 °C annealing for 1 min, (b) SAED pattern taken on annealed MLs (600 °C, 1 min).

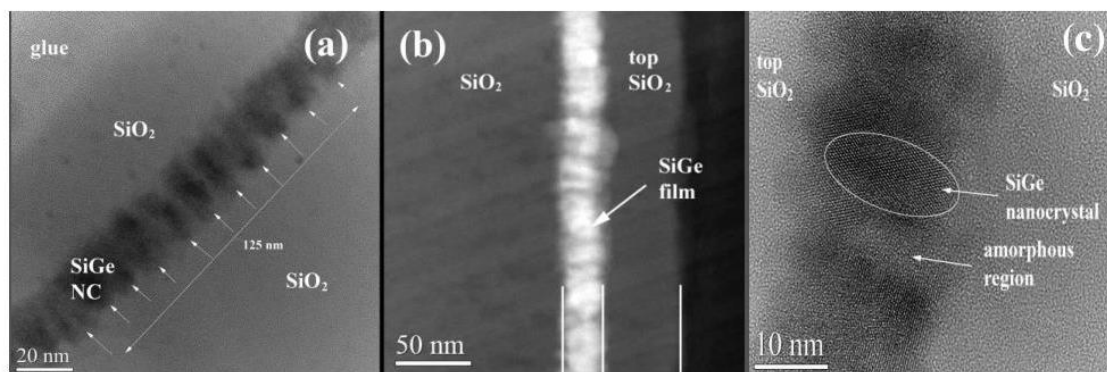


Figure 5. (a) XTEM image of MLs annealed at 600 °C (1 min) showing columnar morphology of SiGe NCs in film. The crystallites have a periodicity of ~12.5 nm. (b) STEM-HAADF image. (c) HRTEM image with SiGe NCs separated by amorphous regions (with SiGeO).

In order to demonstrate the effect of the SiGe layer thickness on the relaxation processes Fig. 6, depicts micrographs of the previously studied structures[23], where the thickness of the SiGe films was approximately 200 nm. The NCs in the thicker films takes the form of lens-like morphology (Fig. 6(a)), due to the creation of shearing lattice defects (Fig. 6(b)) inside the NCs, which then partially relax the stress field. These planar sharing

defects are more complex than the stacking faults and the micro-twins observed[43] in a very thin area of the structure (Fig. 6(c)). In the rest of the specimen area, the shearing defects are superposed and more complicated, as detailed in our previous study[23]. These defects appear only in relatively thick SiGe films in MLs as the only relaxation process-taking place. In the thin SiGe films explored here (~ 20 nm, comparable with the SiGe NCs size); these defects do not appear because other relaxation processes takes place as shown earlier. Since these shearing defects are near or in the (111) packing planes of the SiGe structure, the NC-size along the direction that is parallel to the defect plane remains large and the two others (related also to the $\{111\}$ family of planes) are reduced in size, as emphasized in the TEM images in Fig. 6. A detailed microstructural TEM analysis over a relatively similar structure has been made by Zhang et al.[43]. Their analysis revealed that the defects in NCs and twinning in structures is mainly related to coalescence of small nanoparticles when the structure underwent annealing whose prevalence increases with increased annealing temperature along with an increase in NCs size. A part of the stress in the structure relieves by the formation of dislocations and the remaining stress is accommodated as local stress at the NC/matrix interface.

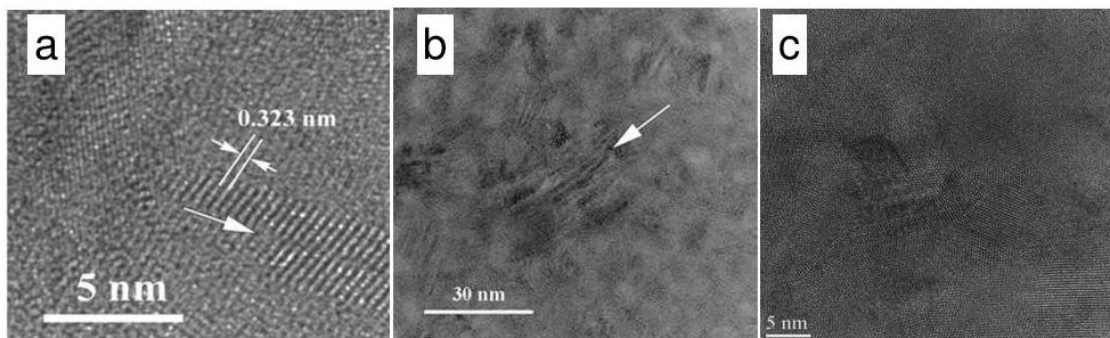


Figure 6.(a) TEM low-magnification image showing the contrast due to the shearing defects appearing in the SiGe crystallites, of a sample annealed at 600 °C for 1 min. (b) High resolution transmission electron microscope (HRTEM) image showing the lens-like shape of SiGe crystallites as a result of shearing defects. The arrows indicate the shearing planes. (c) Sequence of microtwin bands, observed in a very thin area of the XTEM specimen (MLs with 200 nm thick SiGe[23]), where the SiGe NCs are not superposed in the specimen thickness. The micrographs in this figure corresponds to structure in study[23].

Photocurrent measurements

The photocurrent spectra of as-grown structure (SiGe via dcMS and HiPIMS) is shown in Fig. 7(a). Deconvolution was carried out to obtain the individual peaks. The observed peaks were assigned to be due to: interface related localized states (peak I), photo effect from NCs (peak N) and to capacitive coupling from Si substrate i.e. surface

photo-voltage (SPV) and gating effect (peak S). Fig. 7(b) shows the photocurrent for structures of the same batch that underwent annealing procedure for a short period of 1 min at different temperatures. A large increase in intensity was observed by increased annealing temperature; over ~ 1.2 -orders of magnitude higher intensity was obtained upon annealing at 900 °C (Fig. 7(c), right y-axis), compared to as-grown structure. In this context, it is worth mentioning that samples with SiGe deposited via dcMS alone resulted in amorphous structure[22], which did not show any measureable photoresponse.

To demonstrate clearly the shift in peak positions and the variation in the relative peak intensities, all the spectra Fig. 7(b) were normalized to unity. One can see that with increased annealing temperature, the relative intensity of peak I increases with respect to peak N (also shown in Fig. 7(c) (left y-axis) where the ratio of the peak intensities I/N is plotted). This modification in spectral feature can be explained based on previous work by Qin and Li[44] who studied interface morphology and related dangling bond affects due to annealing. In light of their results, it has been postulated that there is a critical NCs size above which the interface effect prevails and below which the photoresponse is associated with quantum confinement. That is, size and surface chemistry of the NCs and oxygen-related bonds are the factors determining the photocurrent spectra. It is well understood that annealing results in the formation of dangling bonds in the structures either at the interface of the NCs or in the surrounding matrix results in alteration of interface quality[45–47]. Additionally, it is well established, that in the case of increased annealing temperature, a formation of Si = O bonds, along with an increase in number of dangling bonds may be possible. Increased number of dangling bonds increases the number of localized states in the band-structure along with an increase in non-radiative centers (P_b)[48,49]. This result in energy-width broadening of localized states with annealing temperature, resulting in bandgap alteration (Fig. 7(d) shows that both peak I and peak N blue shifts with increasing annealing temperature). These dangling bonds also acts as electrically active recombination centers, which results in increased photo-response from peak I, hence an increased relative intensity with respect to peak N, as graphically expressed in Fig. 7(c).

For interface quality, it has been theoretically shown[50] that Si-O-Si bond are formed at the surface when a Si-NCs is oxidized[51]. It is likely that these relatively weak Si-O-Si and Si-Si bonds will break due to stress at the NCs/oxide-matrix interface. Thus, distorted bonds will either result in dangling bonds or eventually form a Si = O bridge since it does not require large additional amount of energy or deformation to form[52,53]. These dangling bonds which act as electrically active recombination centers for charge carriers and can alter the optical properties of the structure, by contributing to oxide positive charges (depending on the location of the bond) and interface states[45]. One solution to passivate such dangling bonds and/or electrically active recombination center is the exposure of structure to hydrogen plasma treatment, as already carried out in our previous

study [22] or by annealing of structures in H_2/N_2 ambient. This result in passivation of P_b -type defects, dangling bonds and oxide fixed charges, thus increasing the overall sensitivity of the structure. However, the passivation of structures via plasma treatment showed much better response than that obtained by annealing in H_2/N_2 ambient, in terms of increasing spectral sensitivity. Additionally, the annealing in H_2/N_2 ambient results in blue shift of peak N and is limited by anneal parameters as H_2 tends to leave the structure when annealed above 400 °C[. Further to elucidate the origin of peaks I and N, the previous studies [22,37] were carried out in light of spectral analysis at varying measurement temperatures (80 - 300K) and at varying applied bias (1 – 11 V).

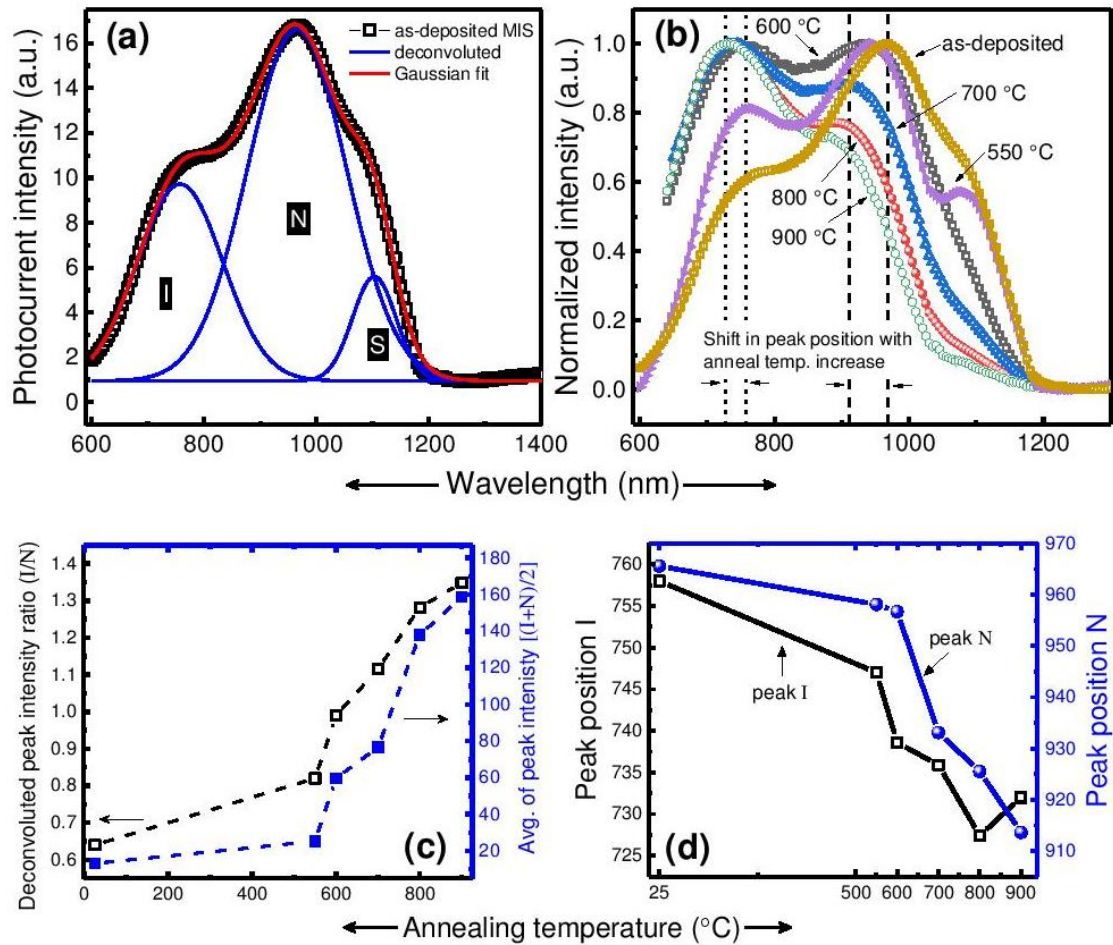


Figure 7. (a) Deconvoluted (Gaussian fit) room temperature photocurrent spectra of as-grown MLs. (b) Normalized photocurrent spectra of annealed (550 – 900 °C) and as-grown MLs (dotted line in the plot represents a blue-shift in peak position with increased annealing temperature). (c) Double y-axis plot, with left y-axis for alteration in intensity of

peak I with respect to peak N (i.e. peak I/N) and right y-axis showing an increase in spectral intensity as an average of peaks $[(I+N)/2]$, as a function of annealing temperature. (d) Peak positions of curves I and N versus temperature for fixed annealing time of 1 min (values obtained by deconvoluting the spectra).

In addition, the annealing of the structure results in reconstruction/ordering of the matrix structure[54], which consequently govern the strain induced over the NCs, and can affect the NCs crystallinity[40,41]. The degree of matrix ordering determines the accommodation of the growing crystallites i.e. the matrix will resist the NCs to expand freely. Thus, as a result of growing crystallites, strain is introduced at the interface between the matrix and NCs[39,40,55], which in turn alters the bandgap (Fig. 7(d)). Additionally, the role of thermal expansion coefficient of SiGe/ SiO₂ and lattice mismatch between Si and Ge (4.2 % [31,56]), that assists in the development of strain in structure, should be taken into account[39]. From the above discussion, it can be summarized that the annealing temperature does affect the structuring of the oxide matrix, which in turn induces strain in the structure and therefore alters the interface morphology, hence inducing a change in the intensity ratio of peak I/N (Fig. 7(d)).

Conclusion

SiGe NCs sandwiched between SiO₂ layers were fabricated by co-sputtering using HiPIMS and dcMS followed by rapid thermal annealing (1 min) at various temperatures. It is shown that application of HiPIMS deposition facilitates the formation of small nanoparticles/clusters in the as-grown structures. A suitable selection of annealing temperature and time results in the formation of columnar (core-shell like structure) self-assembly of SiGe NCs, as comprehensively studied by GiXRD and TEM analysis. Such columnar self-assembly is attributed to stated dominant strain relaxation process, further assisted by already present small nanoparticles in the as-grown structures, acting as seed crystals for heterogeneous nucleation. The photocurrent study reveals that the presence of structural strain and resulting NCs/matrix interface morphology plays a vital role in determining the spectral feature and sensitivity.

Experimental apparatus and method

Multilayer structure with stacking order of SiO₂/SiGe/SiO₂ was prepared by magnetron sputtering over a 12×12 mm² Si (001) substrates. Prior to deposition, the substrate was etched with 2M hydrofluoric acid (HF) for 120 s to remove native oxide. For the SiGe films, co-sputtering was carried out from individual targets of (6N purity) Si and Ge, respectively. Deposition of Si was carried out via dcMS at 180 W, whereas Ge was sputtered via HiPIMS operating at 445 V cathode voltage at a repetition frequency of 300 Hz. An average power of 103 W, with an average current density and peak power density

of 233 mA/cm² and 107 W/cm², respectively was maintained over the full target area. 3.0" MAK Planar Magnetron Sputter Source, MeiVac, with Nd/FeB magnets was employed. Each individual target (Si and Ge) experience different magnetic field strength |B|, stronger for the Ge target and weaker for Si (opposite to our previous study[22] i.e. stronger for Si and weaker for Ge). Since the deposition rate of Ge is usually higher than that of Si, the |B| is selected accordingly. It has been acknowledged for both dcMS and HiPIMS that the increase in |B| results in decreased deposition rate (DR)[57–59], and for HiPIMS it often increased ionized flux fraction. This explanation justifies the need to reconsider the differences in sputter parameters and deposition rates and the resulting change in crystalline size as mentioned in result and discussion section. Additionally, a constant ratio between Si and Ge was maintained in the present study, as confirmed by GiXRD analysis.

For the SiO₂ layers, deposition was carried out via reactive dcMS sputtering. A detailed description of the sputter technique and equipment used, along with a schematic of as-grown structure is given elsewhere[22]. After deposition, the structure underwent annealing for 1 min in a rapid thermal processor (RTA, Jipelec JetFirst 200) at temperatures ranging from 550 to 900 °C, in an N₂ ambient atmosphere.

The structural investigation of the fabricated MLs was carried out by grazing incidence XRD (GIXRD) and X-ray reflectometry (XRR) via Philips X'pert diffractometer (CuK_α, 0.15406 nm, precision of 0.00001°) and Jeol ARM 200F transmission electron microscopy (TEM). For the X-ray diffraction scans, 2×Ge (220) asymmetrical hybrid monochromator utilizing line focus, with a 1/4° divergence slit and a 0.27° parallel plate collimator was used. The measurement run was made over 0.005 %s. scan speed.

For photoconductive measurement, Al-contacts (1×4 mm²) in co-planar geometry with a gap of 4 mm between them were deposited by evaporation. A schematic of the photocurrent setup and the procedure to acquire photo-spectra can be found elsewhere[23].

AUTHOR INFORMATION

***Corresponding Author**

Halldór Guðfínnur Svavarsson

*E-mail: halldorsv@ru.is

Muhammad. Taha Sultan

*E-mail: muhammad16@ru.is

Acknowledgements

This work is funded through M-ERA.NET project PhotoNanoP UEFISCDI Contract no. 33/2016, PCE project UEFISCDI Contract no. 122/2017 and by Romanian Ministry of Research and Innovation through NIMP Core Program PN19-03, contract no. 21 N/08.02.2019 and by the Technology Development Fund of the Icelandic Centre for Research, grant no. 159006-0611.

References

- (1) Tevaarwerk, E.; Rugheimer, P.; Castellini, O. M.; Keppel, D. G.; Utley, S. T.; Savage, D. E.; Lagally, M. G.; Eriksson, M. A. *Appl. Phys. Lett.* **2002**, *80*, 4626–4628.
- (2) Buljan, M.; Pinto, S. R. C.; Kashtiban, R. J.; Rolo, A. G.; Chahboun, A.; Bangert, U.; Levichev, S.; Holý, V.; Gomes, M. J. M. *J. Appl. Phys.* **2009**, *106*, 084319.
- (3) Mihalache, D. *J. Optoelectron. Adv. Mater* **2011**, *13*, 1055–1066.
- (4) Lepadatu, A. M.; Stavarache, I.; Maraloiu, A.; Palade, C.; Serban, T. V.; Magdalena, C. L. In CAS 2012 (International Semiconductor Conference), Sinaia, Romania, October 15 - 17, 2012; IEEE: New York, 2012; Vol. 1, pp 109–112.
- (5) Pan, S. W.; Zhou, B.; Chen, S. Y.; Li, C.; Huang, W.; Lai, H. K. *Appl. Surf. Sci.* **2011**, *258*, 30–33.
- (6) Tuğay, E.; Ilday, S.; Turan, R.; Finstad, T. G. *J. Lumin.* **2014**, *155*, 170–179.
- (7) Vieira, E. M. F.; Toudert, J.; Rolo, A. G.; Parisini, A.; Leitão, J. P.; Correia, M. R.; Franco, N.; Alves, E.; Chahboun, A.; Martín-Sánchez, J.; Serna, R.; Gomes, M. J. M. *Nanotechnology* **2017**, *28* (34), 345701.
- (8) Kepa, J.; Stesmans, A.; Afanas'ev, V. V. *Appl. Surf. Sci.* **2014**, *291*, 20–24.
- (9) Houssa, M.; Pourtois, G.; Meuris, M.; Heyns, M. M.; Afanas'ev, V. V.; Stesmans, A. *Microelectron. Eng.* **2011**, *88*, 383–387.
- (10) Madia, O.; Nguyen, A. P. D.; Thoan, N. H.; Afanas'ev, V.; Stesmans, A.; Souriau, L.; Slotte, J.; Tuomisto, F. *Appl. Surf. Sci.* **2014**, *291*, 11–15.
- (11) Tsetseris, L.; Pantelides, S. T. *Microelectron. Eng.* **2011**, *88*, 395–398.
- (12) Lepadatu, A.-M.; Slav, A.; Palade, C.; Dascalescu, I.; Enculescu, M.; Iftimie, S.; Lazanu, S.; Teodorescu, V. S.; Ciurea, M. L.; Stoica, T. *Sci. Rep.* **2018**, *8*, 4898.
- (13) Pinto, S. R. C.; Kashtiban, R. J.; Rolo, A. G.; Buljan, M.; Chahboun, A.; Bangert, U.;

- Barradas, N. P.; Alves, E.; Gomes, M. J. M. *Thin Solid Films* **2010**, *518*, 2569–2572.
- (14) Stavarache, I.; Lepadatu, A.-M.; Stoica, T.; Ciurea, M. L. *Appl. Surf. Sci.* **2013**, *285*, 175–179.
- (15) Choi, W. .; Kanakaraju, S.; Shen, Z. .; Li, W. *Appl. Surf. Sci.* **1999**, *144–145*, 697–701.
- (16) Jie, Y. X.; Wu, X.; Huan, C. H. A.; Wee, A. T. S.; Guo, Y.; Zhang, T. J.; Pan, J. S.; Chai, J.; Chua, S. J. *Surf. Interface Anal.* **1999**, *28*, 195–199.
- (17) Vieira, E. M. F.; Pinto, S. R. C.; Levichev, S.; Rolo, A. G.; Chahboun, A.; Buljan, M.; Barradas, N. P.; Alves, E.; Bernstorff, S.; Conde, O.; Gomes, M. J. M. *Microelectron. Eng.* **2011**, *88*, 509–513.
- (18) Ray, S. K.; Das, S.; Singha, R. K.; Manna, S.; Dhar, A. *Nanoscale Res. Lett.* **2011**, *6* (1), 224.
- (19) Chew, H. G.; Choi, W. K.; Foo, Y. L.; Zheng, F.; Chim, W. K.; Voon, Z. J.; Seow, K. C.; Fitzgerald, E. A.; Lai, D. M. Y. *Nanotechnology* **2006**, *17*, 1964–1968.
- (20) Zschintzsch, M.; von Borany, J.; Jeutter, N. M.; Mücklich, A. *Nanotechnology* **2011**, *22* (46), 465302.
- (21) Barradas, N. P.; Alves, E.; Vieira, E. M. F.; Parisini, A.; Conde, O.; Martín-Sánchez, J.; Rolo, A. G.; Chahboun, A.; Gomes, M. J. M. *Nucl. Instruments Methods Phys. Res. Sect. B Beam Interact. with Mater. Atoms* **2014**, *331*, 89–92.
- (22) Sultan, M. T.; Gudmundsson, J. T.; Manolescu, A.; Stoica, T.; Ciurea, M. L.; Svavarsson, H. G. *Appl. Surf. Sci.* **2019**, *479*, 403–409.
- (23) Sultan, M. T.; Manolescu, A.; Gudmundsson, J. T.; Torfason, K.; Nemnes, G. A.; Stavarache, I.; Logofatu, C.; Teodorescu, V. S.; Ciurea, M. L.; Svavarsson, H. G. *Appl. Surf. Sci.* **2019**, *469*, 870–878.
- (24) Palade, C.; Slav, A.; Lepadatu, A. M.; Maraloiu, A. V.; Dascalescu, I.; Iftimie, S.; Lazanu, S.; Ciurea, M. L.; Stoica, T. *Appl. Phys. Lett.* **2018**, *113*, 213106.
- (25) Helmersson, U.; Lattemann, M.; Bohlmark, J.; Ehiasarian, A. P.; Gudmundsson, J. T. *Thin Solid Films* **2006**, *513*, 1–24.
- (26) Lundin, D.; Sarakinos, K. *J. Mater. Res.* **2012**, *27*, 780–792.
- (27) Gudmundsson, J. T. *Vacuum* **2010**, *84*, 1360–1364.
- (28) Gudmundsson, J. T.; Brenning, N.; Lundin, D.; Helmersson, U. *A Vacuum, Surfaces, Film.* **2012**, *30*, 030801.

- (29) Samuelsson, M.; Lundin, D.; Jensen, J.; Raadu, M. A.; Gudmundsson, J. T.; Helmersson, U. *Surf. Coatings Technol.* **2010**, *205*, 591–596.
- (30) Alami, J.; Persson, P. O. Å.; Music, D.; Gudmundsson, J. T.; Bohlmark, J.; Helmersson, U. *J. Vac. Sci. Technol. A Vacuum, Surfaces, Film.* **2005**, *23*, 278–280.
- (31) Aqua, J. N.; Berbezier, I.; Favre, L.; Frisch, T.; Ronda, A. *Phys. Rep.* **2013**, *522*, 59–189.
- (32) Stavarache, I.; Maraloiu, V. A.; Negrila, C.; Prepelita, P.; Gruia, I.; Iordache, G. *Semicond. Sci. Technol.* **2017**, *32*, 105003.
- (33) Patterson, A. L. *Phys. Rev.* **1939**, *56*, 978–982.
- (34) Mogaddam, N. A. P.; Alagoz, A. S.; Yerci, S.; Turan, R.; Foss, S.; Finstad, T. G. *J. Appl. Phys.* **2008**, *104*, 124309.
- (35) Ciurea, M. L.; Lepadatu, A. M. *Dig. J. Nanomater. Bios* **2015**, *10*, 59–87.
- (36) Dismukes, J. P.; Ekstrom, L.; Paff, R. J. *J. Phys. Chem.* **1964**, *68*, 3021–3027.
- (37) Sultan, M. T.; Gudmundsson, J. T.; Manolescu, A.; Teodorescu, V. S.; Ciurea, M. L.; Svavarsson, H. G. *Nanotechnology* **2019**, *30*, 365604.
- (38) Bertran, E.; Sharma, S. N.; Viera, G.; Costa, J.; St'ahel, P.; Cabarrocas, P. R. i. *J. Mater. Res.* **1998**, *13*, 2476–2479.
- (39) Bahariqushchi, R.; Raciti, R.; Kasapoğlu, A. E.; Gür, E.; Sezen, M.; Kalay, E.; Mirabella, S.; Aydinli, A. *Nanotechnology* **2018**, *29*, 185704.
- (40) Zatoryb, G.; Podhorodecki, A.; Misiewicz, J.; Cardin, J.; Gourbilleau, F. *Nanoscale Res. Lett.* **2013**, *8* (1), 40.
- (41) Liao, P. H.; Hsu, T. C.; Chen, K. H.; Cheng, T. H.; Hsu, T. M.; Wang, C. C.; George, T.; Li, P. W. *Appl. Phys. Lett.* **2014**, *105*, 172106.
- (42) Zatoryb, G.; Misiewicz, J.; Wilson, P. R. J.; Wojcik, J.; Mascher, P.; Podhorodecki, A. *Thin Solid Films* **2014**, *571*, 18–22.
- (43) Zhang, M.; Cai, R.; Zhang, Y.; Wang, C.; Wang, Y.; Ross, G. G.; Barba, D. *Mater. Charact.* **2014**, *93*, 1–9.
- (44) Qin, G. G.; Li, Y. J. *Phys. Rev. B* **2003**, *68*, 085309.
- (45) Yakimov, A. I.; Kirienko, V. V.; Armbrister, V. A.; Dvurechenskii, A. V. *Semicond. Sci. Technol.* **2014**, *29*, 085011.

- (46) Brown, W. D.; Khaliq, M. A. *Thin Solid Films* **1990**, *186*, 73–85.
- (47) Dashiell, M. W.; Denker, U.; Müller, C.; Costantini, G.; Manzano, C.; Kern, K.; Schmidt, O. G. *Appl. Phys. Lett.* **2002**, *80*, 1279–1281.
- (48) Nazarov, A. N.; Lysenko, V. S.; Nazarova, T. M. *Semicond. Physics, Quantum Electron. Optoelectron.* **2008**, *11*, 101–123.
- (49) Nikitin, T.; Khriachtchev, L. *Nanomaterials* **2015**, *5*, 614–655.
- (50) Wolkin, M. V.; Jorne, J.; Fauchet, P. M.; Allan, G.; Delerue, C. *Phys. Rev. Lett.* **1999**, *82*, 197–200.
- (51) Szekeres, A.; Alexandrova, S. *Vacuum* **1996**, *47*, 1483–1486.
- (52) Puzder, A.; Williamson, A. J.; Grossman, J. C.; Galli, G. *J. Chem. Phys.* **2002**, *117*, 6721–6729.
- (53) López, M.; Garrido, B.; García, C.; Pellegrino, P.; Pérez-Rodríguez, A.; Morante, J. R.; Bonafos, C.; Carrada, M.; Claverie, A. *Appl. Phys. Lett.* **2002**, *80*, 1637–1639.
- (54) Hadjisavvas, G.; Kelires, P. C. *Phys. Rev. Lett.* **2004**, *93*, 226104.
- (55) Hadjisavvas, G.; Remediakis, I. N.; Kelires, P. C. *Phys. Rev. B* **2006**, *74*, 165419.
- (56) Ye, H.; Yu, J. *Sci. Technol. Adv. Mater.* **2014**, *15*, 024601.
- (57) Ekpe, S. D.; Jimenez, F. J.; Field, D. J.; Davis, M. J.; Dew, S. K. *J. Vac. Sci. Technol. A Vacuum, Surfaces, Film.* **2009**, *27*, 1275–1280.
- (58) Papa, F.; Gerdes, H.; Bendorf, R.; Ehiasarian, A. P.; Kolev, I.; Braeuer, G.; Tietema, R.; Krug, T. *Thin Solid Films* **2011**, *520*, 1559–1563.
- (59) Čapek, J.; Hála, M.; Zabeida, O.; Klemberg-Sapieha, J. E.; Martinu, L. *J. Phys. D. Appl. Phys.* **2013**, *46*, 205205.

Paper V

Obtaining SiGe nano-crystallites between crystalline TiO₂ layers by HiPIMS without annealing

***Sultan M T¹, Gudmundsson J T^{2,3}, Manolescu A¹, V S Teodorescu⁴, M L Ciurea^{4,5},
*Svavarsson H G¹**

¹School of Science and Engineering, Reykjavik University, IS-101 Reykjavik, Iceland

²Department of Space and Plasma Physics, School of Electrical Engineering and Computer Science, KTH-Royal Institute of Technology, SE-100 44, Stockholm, Sweden

³Science Institute, University of Iceland, IS-101 Reykjavik, Iceland

³Science Institute, University of Iceland, Dunhaga 3, IS-107 Reykjavik, Iceland

⁴National Institute of Materials Physics, 077125 Magurele, Romania

⁵Academy of Romanian Scientists, 050094 Bucharest, Romania

Submitted for publication (under revision)



En-route to annealing-free crystallization of Si_{1-x}Ge_x nanocrystals enclosed between TiO₂ layers: role of HiPIMS sputtering method

M.T. Sultan¹, J. T. Gudmundsson^{2, 3}, A. Manolescu¹, V S Teodorescu⁴, M L Ciurea^{4,5}, H. G. Svavarsson¹

¹Reykjavik University, School of Science and Engineering, IS-101 Reykjavik, Iceland

²Department of Space and Plasma Physics, School of Electrical Engineering and Computer Science, KTH Royal Institute of Technology, SE-100 44, Stockholm, Sweden

³Science Institute, University of Iceland, Dunhaga 3, IS-107 Reykjavik, Iceland

⁴National Institute of Materials Physics, 077125 Magurele, Romania

⁵Academy of Romanian Scientists, 050094 Bucharest, Romania

Abstract

Formation of SiGe nanocrystals in an oxide matrix via deposition and subsequent annealing is a widely applied approach as it gives good control over optical properties by varying the Ge atomic fraction, the size, shape and crystallinity of the nanocrystals. A common drawback of annealing is a strain relaxation in the structure (resulting in dislocation nucleation or intermixing at the interfaces), creating dislocations, point defects, dangling bonds, Ge clustering and altered interface morphology. All these phenomena are well known to degrade the optoelectronic and electrical properties of the structure. As a proof of concept, in this study we have utilized a modern technique of high impulse power magnetron sputtering to obtain a crystalline TiO₂/SiGe/TiO₂ structure without any pre-/post-annealing. It is furthermore demonstrated how a control of the nanocrystallite size is obtained by altering the HiPIMS discharge power alone. Grazing incidence X-ray diffraction analysis was carried out for the structural characterization, while photocurrent measurements were utilized to access the role of TiO₂ structural morphology over interface integrity in determining spectral feature and sensitivity. Over 1.7-order of magnitude higher spectral intensity was achieved for as-grown structures fabricated via HiPIMS in comparison to annealed structure, sputtered with conventional direct current magnetron sputtering.

Keywords: TiO₂, SiGe, nanoparticles, HiPIMS, GiXRD, interface, photo-spectra

1. Introduction

Employment of SiGe nanocrystals hetero-structures have heightened the applications of monolithic Si-based devices because of their high light emission efficiency. The lattice mismatch of 4.2 % between Si and Ge¹, formerly a stumbling block, turn-out to materialize the advantage of such system in quantum electronic and optoelectronic devices, by tailoring the band gap of the system via quantum confinement and/or varying Ge ratio². Among the most studied Si(/Ge) nanocrystal systems are those embedded in dielectric matrices, such as TiO₂, SiO₂, Al₂O₃ and HfO₂³⁻⁵, supplemented with pre- or post-thermal annealing procedures. Out of these, TiO₂ films have gained reputation for being cost effective alternative for applications in optical sensors, solar cells, as dielectric materials, photo-catalysis, gas detectors and antireflection coatings⁶⁻⁸.

Due to its high refractive index and transparency in the ultra-violet (UV), visible and infra-red (IR) spectral range, TiO₂ find a wide range of use for optical applications. In bulk form, TiO₂ exists commonly in three morphological phases: two tetragonal (anatase and rutile) and one orthorhombic (brookite)^{8,9}. In contrast to bulk form, only anatase and rutile phases are observed in thin films form⁷⁻⁹. The rutile phase is thermodynamically more stable than the anatase phase^{10,11,12}. The bandgap energy for the rutile phase is lower than that for the anatase phase, 3.0 eV vs 3.2 eV, so the anatase structure can only be excited by UV light whereas the rutile phase exhibits response slightly extended into the visible light regime¹⁰. Furthermore, the electron-holes (e⁻ - h⁺) recombination rates are affected by the direct (rutile) and indirect (anatase) bandgaps of the structures^{10,11,13}. The rutile phase has higher recombination rates and have shown exponential decay profiles for electrons and holes, whereas the anatase phase has longer charge-carrier lifetime and non-exponential decay^{10,11}. The crystal structure of TiO₂ films exhibits a variety of properties for wide range of applications. Rutile, the densest of the three structures (4.25 g/cm³)^{11,8} is transparent in the high end of visible spectral range¹³ and has high refractive index¹² (up to 2.75 at 550 nm). Hence, rutile is broadly utilized for optical coatings¹⁴, optoelectronic and semiconductor electronics¹⁵. Its high dielectric constant also makes it a desirable candidate in microelectronic devices⁶⁻⁸. The anatase phase however, is known to exhibit photocatalytic activity superior to that of the rutile phase^{6,13}.

Several approaches have been successfully utilized to synthesize TiO₂ films, such as sol-gel, ion implantation, electron-beam evaporation, ion beam technique, chemical vapor deposition (CVD), wet chemical deposition methods, pulsed laser deposition (PLD) and magnetron sputtering (MS)^{9,15,16}. The MS technique has been considered by many as being the most versatile one. It is industrially viable and allows good control over the selective phase formation for TiO₂ polymorphs at low (even at room) temperature^{9,17}.

Synthesis of TiO₂ thin films by conventional sputtering methods usually results in amorphous films, and the phase composition of the films is mainly determined by the growth parameters, annealing temperatures and substrate biasing^{7,9,18}. Rather recently, a modified version of the magnetron sputtering method, so-called high power impulse magnetron sputtering (HiPIMS), has been demonstrated to give crystalline structures of TiO₂ already in the as-grown state without any need of external heating^{8,17,19,20}. HiPIMS operates at short unipolar pulses of voltage at low frequency and duty cycles, providing denser films with smoother surface²¹ and of higher crystallinity²², in comparison to conventional MS methods. It has been shown to give superior control over the properties of grown films by yielding discharge having sufficiently large amount of energetic ions^{23,24}. Higher ionization fraction of the sputtered material with better control over the energy and direction of the sputtered species along with higher discharge current densities are achieved via HiPIMS deposition^{25,26}. Alessandro *et al.*¹⁷ reported the formation of dense polycrystalline rutile phase at room temperature using HiPIMS with peak power density and frequency as low as 680 W/cm² at 500 Hz. Cemin *et al.*⁷ described the synthesization of anatase phase by utilizing the moderate ion irradiation available in the HiPIMS discharge. Konstantinidis *et al.*¹⁸ applied HiPIMS to signify the formation of rutile structure on glass and steel substrate without external heating and the effect of biasing the substrate over the phase structuring. Wang *et al.*²⁰ reported the use of HiPIMS technique to synthesize phase

controlled anatase, anatase-rutile mixture or rutile dominant film with high dielectric constant, by varying process parameters, substrate bias and gas pressure. Straňák *et al.*^{27,28} have presented advantage of tailoring the structure and properties of TiO₂ films, by operating at as low as 250 Hz for a cathode voltage of -620 V, with a peak discharge current of up to ~ 50 A.

Several structures with Ge(/Si) nanocrystals embedded in TiO₂ matrix have exhibited strong quantum confinements effects, increased photoconductivity and optical response^{29,30,31,32,33}. The structures properties have however degraded when fabricated in a production line as compared to that demonstrated for research devices. This is attributed to thermal budget employed in the production line, having detrimental effect on the interface quality creating strain accumulation in the structure, dislocation and dangling bonds³⁴, and clustering of Ge^{5,35}. All these phenomena are well known to degrade the optoelectronic and electrical properties of the device³⁶. Although several attempts have been made to lower the crystallization temperature, for example by controlling deposition parameters, decreased post-annealing temperatures and deposition over heated substrate³⁷, the detrimental effect of heating is still a matter of concern.

The aim of this current study is to demonstrate crystalline TiO₂/SiGe/TiO₂-based structure in as-grown state by employing HiPIMS and to optimize its spectral sensitivity by adjusting the HiPIMS discharge power. The structures are compared with direct current magnetron sputtered (dcMS) fabricated structures that have been described elsewhere³⁸. Although the effect of the strain exerted by the matrix ordering needs to be taken into consideration, a possibility to obtain a control over the size of SiGe nano-crystallites (NCs) is procured by utilizing HiPIMS discharge parameters. The effect of interface integrity in light of the study by photocurrent spectra is also discussed.

2. Experiment

In this study, three structurally similar schemes (labelled DDD, DHD and HHD) of samples were fabricated using combination of two different magnetron sputter methods, dcMS and HiPIMS. Table 1 summarizes the three schemes employed, the three digit label denotes the sputter technique employed for the corresponding film (D for dcMS and H for HiPIMS). The multilayered structures (MLs), consisting of SiGe layer sandwiched between TiO₂ layers, were deposited on 12×12 mm² p-type Si (001) substrates. Prior to deposition, native oxide was etched-off the substrate with 2M hydrofluoric acid (HF) for 120 s. The substrates were then mounted on sample holders and brought into chamber through load-lock on to a sample holder assembly (SHA) equipped with a heater, a thermocouple and 3-axis manipulator for focal point adjustment. To attain uniform film thickness, the SHA was rotated clock- and counter clock-wise using a LabVIEW program. All the sputter targets were aligned facing up at 45° to the SHA. All the magnetron assemblies (MA) were equipped with a water cooling system and pressurized air to control shutters. Fig. 1(a) shows a drawing of the sputter chamber. The stacking order of the deposited MLs is a SiO₂(buffer)/TiO₂/SiGe/TiO₂ films, as shown schematically in Fig. 1(b). The respective thicknesses of the layers are 200/40/20/40 nm.

Table 1. Sputter methods employed to individual targets for respective schemes.

Sputtering method for:			Scheme
TiO ₂	Ge	Si	label
dcMS	dcMS	dcMS	DDD
dcMS	HiPIMS	dcMS	DHD
HiPIMS	HiPIMS	dcMS	HHD

For dcMS deposition, Advanced Energy MDX500 power supply was utilized. For HiPIMS deposition, the power was supplied by SPIK1000A pulse unit (Melec GmbH) operating in unipolar negative mode at a constant voltage, which in turn was charged by a DC power supply (ADL GS30). The discharge current and voltage were monitored using a combined current transformer and a voltage divider unit (Melec GmbH) and the data were recorded with a digital storage oscilloscope (Agilent 54624A). The targets were positioned at 45° with respect to a flat sample holder at a distance of 200 mm. The substrate was rotated continuously while sputtering to maintain uniform deposition over the substrate. The annealing of the structures was carried out in a conventional resistive heating furnace. The furnace, along with sample holder tube, was preheated at the desired temperature until stabilized, after which the sample was inserted and treated for desired time, after which the sample tube was retracted and allowed to cool down to room temperature.

The deposition of SiGe intermediate layer was carried out by co-sputtering from individual targets of 99.9999% (6N) Si and Ge, using dcMS and HiPIMS respectively, for MLs DHD and HHD, as also explained in our earlier study^{39,40}. The reason for co-depositing via two different techniques is that Si has lower deposition rate than Ge, and that the magnetron assembly employed for respective targets have different magnetic field strengths⁴⁰. Thus, the co-sputtering via individual sources was made as to have a control over deposition rates (nm/s) which, if sputtered through HiPIMS alone, would result in higher Ge fraction than Si. The dcMS deposition for Si was done in constant-power mode from 180 - 350 W. The HiPIMS deposition for Ge was made using square voltage waveform with a pulse length of 200 μs at varying repetition frequency (from 250 - 650 Hz). An average current density and peak power density varies from 258 to 163 ± 10 mA/cm² and 115 to 92 ± 6 W/cm², respectively, at a constant cathode voltage of 445 V giving power averaged over the target area, of 89 to 154 W. For DDD structural scheme, the co-sputtering of Si and Ge were carried out via dcMS at 80 and 25 W respectively. The Si-Ge ratio deposition rates were ~ 47:53 (± 2) for all the three schemes.

The TiO₂ deposition was carried out via reactive sputtering using either dcMS or HiPIMS method, from a 6N Ti target. Prior to deposition, the chamber pressure was throttled to 5×10⁻⁷ Pa. Argon (Ar) gas of 6N purity was used as a working gas along with 5N oxygen gas (O₂). The flow rates for Ar (q_{Ar} = 100 sccm) and O₂ (q_{O_2} = 2.5 sccm) were controlled by mass flow controller and throttle valves were adjusted to stabilize growth pressure of 0.7 Pa during deposition. For dcMS deposition, the power was maintained at 180 W, whereas for HiPIMS deposition, the pulse length

was 200 μ s with varying repetition frequency and/or cathode voltage such as to obtain a selected constant power averaged over the target area. Due to high intensities of energetic species the temperature measured over the sample holder reaches ~ 65 °C. To ease the approach towards parametric map, Table 2 summarizes the corresponding sputter techniques and parameters for the respective structures. A detailed analysis of stand-alone TiO₂ films deposited with HiPIMS, the discharge parameters utilized and its evolution from amorphous to crystalline structure is given in section 3. The asterisk in superscript denotes annealed condition.

Table 2. Process parameters for the corresponding samples.

Sample label	dcMS power [W]			HiPIMS parameters						Annealing T and t
	TiO ₂	Si	Ge	Cat. voltage [V]			Rep. freq. [Hz]			[°C, min]
DDD	180	80	25	-	-	-	-	-	-	
DDD*	180	80	25	-	-	-	-	-	-	600, 5
DHD-1	180	180	-	-	-	445	-	-	250	
DHD-2	180	235	-	-	-	445	-	-	300	
DHD-3	180	270	-	-	-	445	-	-	400	
DHD-4	180	322	-	-	-	445	-	-	500	
DHD-5	180	370	-	-	-	445	-	-	650	
HHD-A	-	370	-	755	-	445	300	-	650	
HHD-A*	-	370	-	755	-	445	300	-	650	600, 5
HHD-R	-	370	-	813	-	445	340	-	650	

The pulse length and the working gas pressure was kept constant at 200 μ s and ~ 0.7 Pa during deposition. The ‘*’ superscript denotes that the samples is in annealed condition. The numbers after hyphen, denotes the sample’s ID for the respective scheme, and the letters after hyphen for SHH, A and R, denotes anatase and rutile TiO₂ phases, respectively.

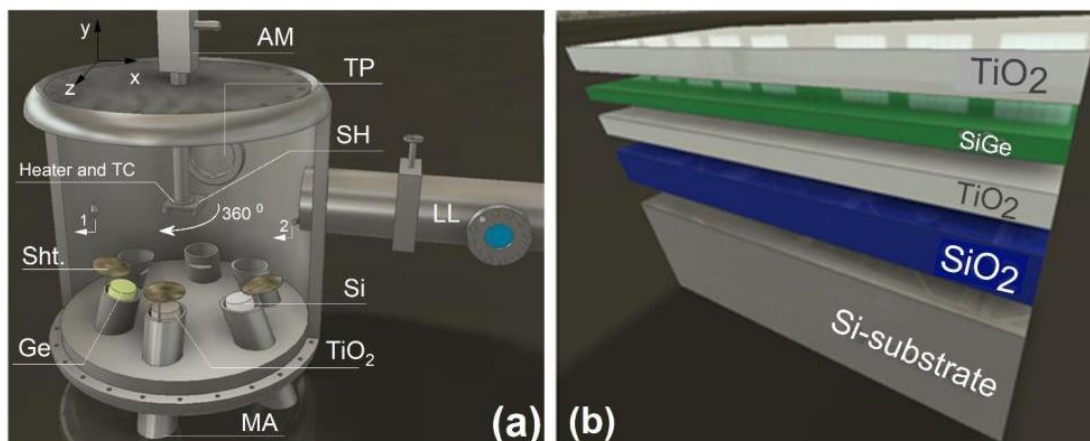


Figure 1. (a) Schematic of the sputter chamber used: (sample holder (SH); load lock (LL); temperature controller (TC); Ar and oxygen inlet (1 and 2); turbo pump (TP); target shutter (Sht.) and axis manipulator (AM). (b) Schematic of the SiO₂/TiO₂/Si_{1-x}Ge_x/TiO₂ structure (with thickness of 200/40/20/40 nm, respectively) deposited over p-type Si-substrate.

Structural and elemental analysis was conducted using X-ray reflectometry (XRR) and small angle grazing incidence X-ray diffraction (GIXRD) by Philips X'pert diffractometer (CuK α , 0.15406 nm with a precision of 0.00001 $^\circ$), Jeol ARM 200F high resolution transmission electron microscopy (HRTEM) and energy-dispersive X-ray spectroscopy (EDX). For GIXRD scans, 2 \times Ge (220) asymmetrical hybrid monochromator utilizing line focus, a divergence slit (1/4 $^\circ$) and a parallel plate collimator (0.27 $^\circ$) was used as detailed elsewhere³⁹. Two 1 \times 4 mm² co-planar Al-contacts, with a gap of 4 mm between them, were deposited on top of the structure with e-beam evaporation. The photo-spectral measurements setup and consequent processing of data can be seen elsewhere³.

3. Results and discussion

3.1. XRR analysis

XRR study was carried out over individual layers of Ge, Si and over as-grown structures (Fig. 2), to demonstrate the acclaimed effect of the HiPIMS deposition method^{19,25,26}. For Ge deposited films, a constant average power of 38 W was maintained. The discharge parameter for HiPIMS in this case was 445 V cathode voltage at pulse length of 200 μ s and repetition frequency of 100 Hz with peak current and power density of 281 mA/cm² and 124 W/cm². These values were selected in order to have power akin to when sputtered with dcMS (37 \pm 2 W). An obvious increase in the film quality including mass density (\sim 5.23 g/cm³) and smoothness (0.462 nm) for Ge sputtered with HiPIMS was obtained compared to film deposited by dcMS (\sim 4.86 g/cm³ and 1.628 nm, respectively) (Fig. 2(a)). The parameters selected for Ge is solely for XRR analysis, and are not utilized for structure fabrication, as Ge deposited via HiPIMS at 100 Hz resulted in amorphous structure, as confirmed with GIXRD analysis (not shown here) and our earlier study⁴⁰. Si deposited

via dcMS (80 W) showed high surface roughness as evident by the slope of the curve and disappearance of fringes at lower angle seen in Fig. 2(a). Reflectometry plots for both DHD and HHD schemes are shown in Fig. 2(b). A better interface quality and increased smoothness was attained in the case of HiPIMS deposition, as evident by the more distinct interference fringes.

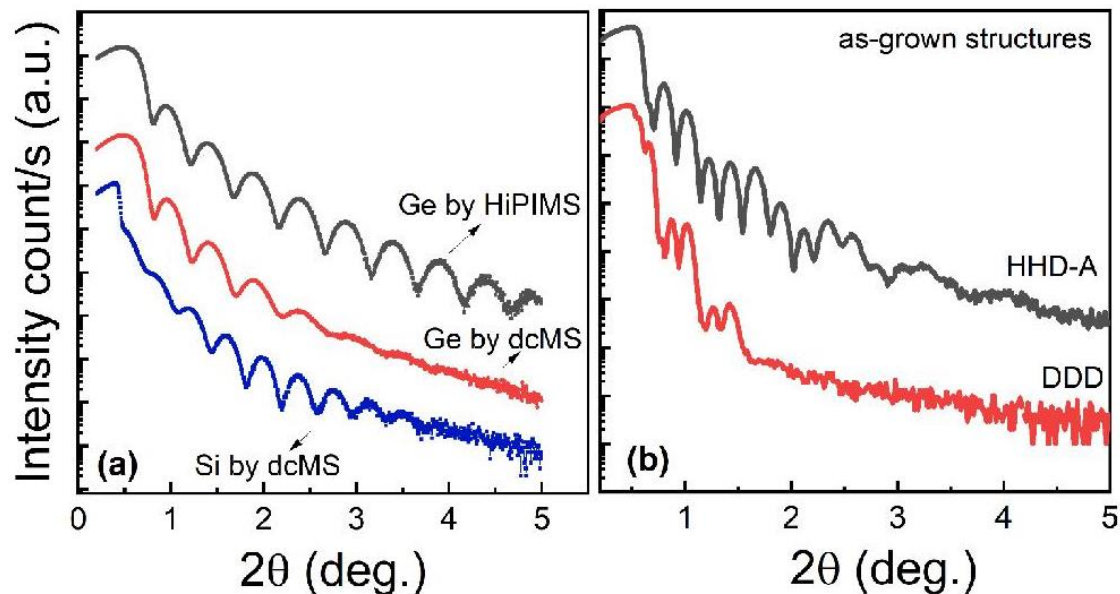


Figure 2. XRR plots for: (a) individual layers of Ge (deposited via HiPIMS and dcMS) and Si (deposited by dcMS); (b) as-grown structures i.e. TiO₂/SiGe/TiO₂ over p-type Si-substrate, for films grown with dcMS and HiPIMS (i.e. sample DDD and HHD-A, respectively).

3.2. GiXRD analysis

Scheme DHD

In this section, the effect of HiPIMS grown SiGe films, deposited between dcMS-sputtered-TiO₂ layers (i.e. scheme DHD) is further explored. The HiPIMS deposition was carried out for Ge at repetition frequencies of 250 - 650 Hz, whereas Si was deposited by dcMS. In order to obtain similar stoichiometric ratio of Si:Ge in all films, the cathode voltage over Si target during the dcMS deposition was adjusted to give sputter power of 180 - 350 W. GiXRD diffractograms of the samples are shown in Fig. 3(a). For the MLs where Ge is sputtered at repetition frequencies in range of 300 - 400 Hz (co-sputtered with Si), two broad bands are evident (Fig. 3(a)), with the first one corresponding to the crystallographic plane (111) and the other to (220) and (311) together, as already investigated in earlier study³⁹. Upon, further increase in repetition frequency to 500 and 650 Hz, three small distinguishable peaks over corresponding broad bands are visible positioned between Si and Ge tabulated ones presented by dashed lines. Similar diffraction features akin to our as-grown structures have been analyzed via X-ray diffraction, TEM and grazing-incidence small-angle scattering in several studies. Bertan *et al.*⁴¹ have shown presence of Si nano-crystallites

within amorphous silicon film fabricated with plasma enhanced chemical vapor deposition (PECVD). Additionally, Dasovic *et al.*⁴² have attributed the presence of clustered small Ge-particles in as-grown structures prepared by co-deposition using magnetron sputtering from individual Ge and SiO₂ targets. In another work by Lee *et al.*⁴³, it was demonstrated that the crystallinity was increased in an amorphous Si matrix with increasing rf sputtering power. This is in line with our results via GiXRD analysis for the co-sputtered Ge, where the average power increased with increased repetition frequency (i.e. from 89 to 154 W for repetition frequency ranging from 250 to 650 Hz). Furthermore, in a study performed by Kole *et al.*⁴⁴, presence of ~10 nm Si nanocrystals within SiC matrix were observed in as-grown structure deposited with PECVD over a heated (200 °C) substrate.

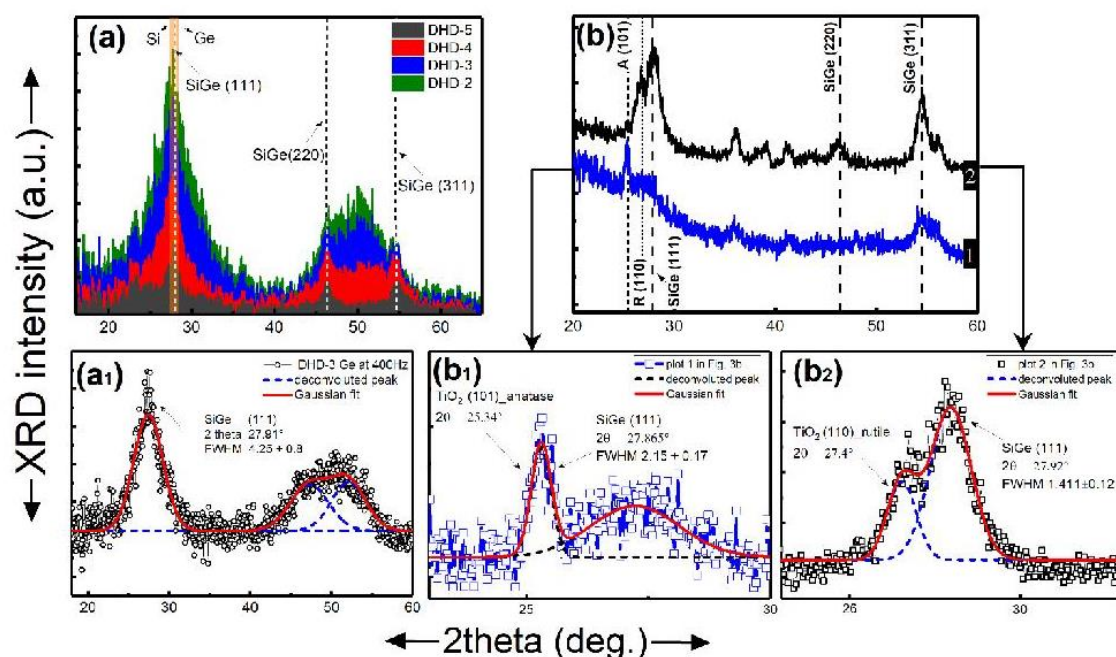


Figure 3. (a) GiXRD diffractograms of as-grown structures (DHD scheme) with dcMS sputtered TiO₂ and Si, with HiPIMS sputtered Ge at varying repetition frequencies of 300, 400, 500 and 650 Hz. The vertical dashed lines correspond to standard tabulated positions for cubic Ge ($2\theta = 27.45^\circ; 45.59^\circ; 54.04^\circ$ - ASTM 01-079-0001) and cubic Si ($28.45^\circ; 47.31^\circ; 56.13^\circ$ - ASTM 01-070-5680), respectively. (a₁) De-convoluted curve of structure having Ge sputtered at 400 Hz repetition frequency. (b) GiXRD diffractogram of two TiO₂/SiGe/TiO₂ structures, the former TiO₂ film (lower line) is sputtered with HiPIMS at 300 Hz repetition frequency and cathode voltage of 755 V with average power of 468 W forming anatase phase (HHD-A) and the second TiO₂ film (upper line) was sputtered at 340 Hz at 813 V with average power of 545 W resulting in rutile phase (i.e. HHD-R). The vertical short-dashed and dotted lines corresponds to standard TiO₂ anatase (JCPDS card no. 21-1272) and rutile (JCPDS card no. 21-1276) phases, respectively. (b₁ and b₂) Deconvolution of plots 1 and 2 in Fig. 2(b) using Gaussian fitting (for selected 2θ range), showing crystallographic peak positions for TiO₂ (anatase/ rutile) and SiGe.

Taking above studies into consideration, it can be postulated that increased average power results in increased crystallinity (together with increased size of nano-crystallites within amorphous

SiGe layer. The resulting diffractogram of as-grown structures were de-convoluted by using Origin 10.0 software to obtain peak parameters for crystallite-size determination. An example of deconvolution is shown in Fig. 3(a1). The size of the crystallites were calculated from crystallographic plane (111) employing Scherrer equation⁴⁵ with shape-factor(k) being 0.9 and instrumental error of 0.00001°. Although the aforementioned approach to determine crystallite size is indefinite³⁹, as the consequence of micro strain broadening, lattice imperfections and other instrumental error cannot be disregarded. The size of SiGe nano-crystallites were found to vary from 1.0 to 6.4 (± 0.8) nm, increasing with increasing repetition frequency in the range of 250 to 650 Hz. Note that the diffractogram showed no feature corresponding to TiO₂ phase, implying an amorphous matrix. It also implies that the use of TiO₂ as an oxide matrix instead of SiO₂ is what account for difference in degree of matrix ordering and variation in size of the SiGe NCs as compared to our earlier works^{39,40}, and will be discussed later in this section. Further, the Si:Ge ratio obtained using crystallographic peak (111) was determined to be $\sim 49.9:50.1$. Out of the mentioned structures from scheme DHD, the structure labelled as DHD-5 will be utilized further in this section and for photo spectral analysis.

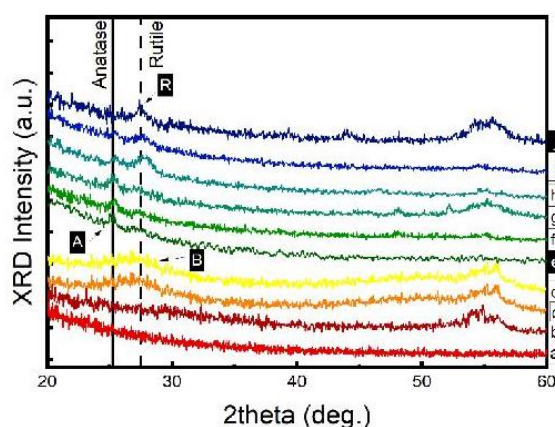


Figure 4. Structural evolution analysis by GiXRD diffractogram for TiO₂ deposited via HiPIMS. The discharge parameters are listed in Table 3. The labels R, A and B denote rutile, anatase and X-ray amorphous nature of TiO₂ thin films (~ 80 nm), with legend corresponding to sample label mentioned in Table 3. Samples ‘e’ and ‘j’, shows presence of pure anatase and rutile phase respectively, while all other samples shows presence of both anatase and rutile phases simultaneously.

Scheme HHD

Usually, TiO₂ films sputtered by conventional magnetron sputtering (i.e. dcMS) are amorphous in nature or anatase when deposited at low substrate temperatures^{7,18}. To promote crystallization of the film, additional energy is supplied to it either in form of in-situ substrate heating, substrate biasing or via high-energy particle bombardment⁷⁻⁹. The energy of the impinging particles on the growing-substrate determine whether the nucleation is preferable for anatase or rutile form or whether only amorphous structure will prevail^{9,18}. From the

studies^{7,9,17,18,20}, it is seen that films containing rutile and anatase phase can be prepared by supplying high enough energy to particles impinging on the substrate at room temperature via magnetron sputtering, HiPIMS in particular. In addition, it was graphically presented by Löbl *et al.*⁹ and also complemented in several studies^{46,47} that the parameter determining the occurrence of rutile or anatase phase is the energy of the sputter species rather than the oxygen partial pressure. In addition, the nucleation of the film is strongly influenced by the process condition during deposition including the growth pressure^{7,9} temperature^{7,19}, and substrate biasing¹⁸, which determines the formation of either phase. For the present study, our inceptive focus is on the effect of HiPIMS discharge parameters at fixed growth pressure and pulse length to provide large amount of energetic ions to the discharge, without any in-situ substrate heating or biasing.

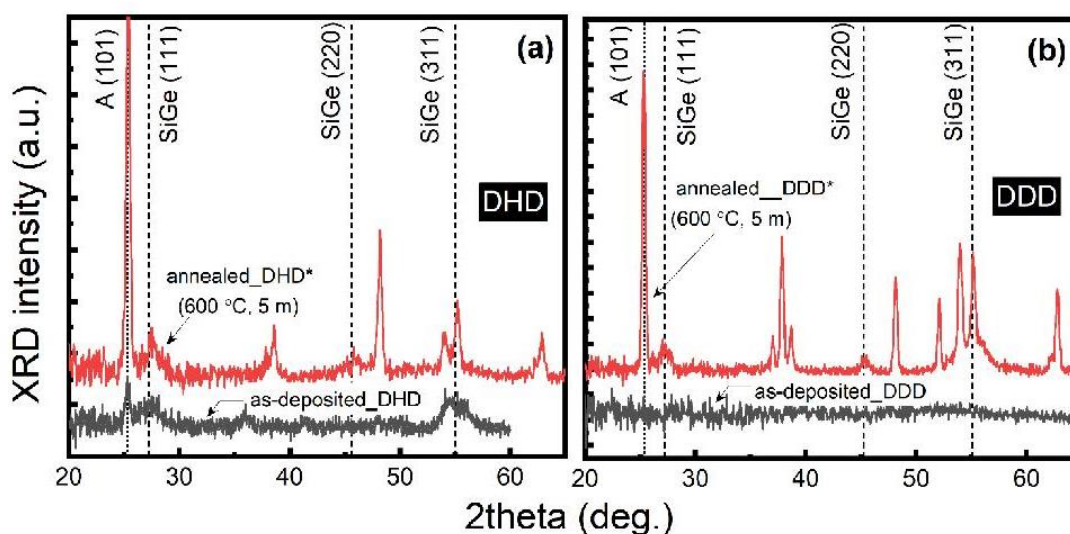


Figure 5. Diffractogram of structures (a) marked as 1 in Fig. 3b in as-grown (i.e. S-HH-A) and annealed (HHD-A* 600 °C, 5 min) states, (b) scheme DDD in as-grown and annealed (DDD* annealed at 600 °C, 5 min) states.

In order to establish a structure having a reasonable degree of crystallinity, a single TiO₂ layer alone was deposited via reactive HiPIMS deposition over Si-substrate (in contrast to dcMS, which results in amorphous oxide layer). Fig. 4 shows the GiXRD evolution of TiO₂ from amorphous to rutile phase by varying repetition frequencies and cathode voltage in order to maintain required constant average power to obtain crystalline films. The structure showed an amorphous and X-ray amorphous features when deposited at lower power ($\sim 220 \pm 5$ to 417 ± 2 W) which upon further increase in the time averaged power ($\sim 470 \pm 7$ W) showed initially a presence of anatase phase and later presence of both phases and still with further increase in power leads to rutile phase formation. Subsequently the discharge average power was increased to 543 ± 2 W. The above procedure was done to avoid erosion of the race track over Ti target⁴⁸ as it was difficult to maintain the plasma, especially after opening the shutter which results in drop of power and consequently poisoning of the target surface. The highest averaged power applied resulted in

formation of completely rutile phase. Table 3 summarizes the discharge parameters, where the pulse length and growth pressure is constant of 200 μ s. It is to be noted that the thickness of the TiO₂ layers were in all cases constant, \sim 80 nm.

Table 3. Discharge operational parameters for TiO₂ deposited via HiPIMS.

Sample label	Cathode voltage [V]	Rep. frequency [Hz]	Avg. Power (\pm 6 W)
a	500	300	212
b	550	300	225
c	730	300	417
d	700	344	418
e	755	300	468
f	700	380	471
g	740	350	473
h	720	373	477
i	800	340	543
j	813	340	545

Sample's IDs corresponds to respective plots in Fig. 4.

Taking above parametric analysis into consideration, the as-grown structures i.e. SiO₂/TiO₂/SiGe/TiO₂ (scheme HHD) were fabricated using HiPIMS with repetition frequency of 650 Hz for Ge and dcMS at 370 W for Si, akin to sample DHD-5. For TiO₂ deposition, the parameters listed in Table 3 for samples 'e' and 'j' were utilized for anatase and rutile, respectively. Fig. 3(b) shows the GiXRD diffractogram of as-grown structures for HiPIMS sputtered TiO₂ enveloping SiGe layer. Two distinct peaks seen over a broad hump (2θ ranging from \sim 24 to 30 $^\circ$) corresponding to TiO₂ anatase phase (101) and SiGe (111) crystallites for plot numbered as 1 and to rutile TiO₂ (110) and crystalline SiGe (111) nanoparticles for plot numbered as 2. For the sake of accessibility, both diffractogram, i.e. 1 and 2, were processed via deconvolution of peaks (Figs. 3b₁ and 3b₂), showing presence of anatase and rutile TiO₂ peaks (101) and (110), positioned at standard anatase and rutile tabulated ones (JCPDS card no. 21-1272 and JCPDS card no. 21-1276, respectively) along with SiGe peak (111) positioned between standard Si and Ge cubic tabulated ones^{39,49}. For further confirmation of our results, the structure having anatase characteristics (HHD-A) was annealed at 600 $^\circ$ C for 5 min (HHD-A*). The GiXRD diffractogram (Fig. 5(a)) exhibited peaks positioned at similar 2θ values as un-annealed (as-grown) MLs. The annealing temperature was selected to manifest anatase phase⁷, while the shorter exposure time (5 min) relative to long ones (i.e. for several min or hour), is maintained to preserve the integrity of the interface quality³⁸. Similar GiXRD evaluation of TiO₂ structures deposited via various magnetron sputtering methods and the effect of sputter parameters are reported in studies mentioned in section 1. It is to be noted here that the Si:Ge ratio determined via GiXRD plots (in good agreement with EDX analysis, see supplementary information) for both HHD-A and HHD-R were \sim 49.9:50.1 (\pm 0.05). Both these

structures are included in the photocurrent analysis in section 3.3. Additionally, HRTEM analysis was carried out over HHD-A structure to validate the formation of nano-crystallites and to determine their sizes (see, supplementary information). The average size of crystallites determined by TEM analysis is ~ 6.6 nm, which is relatively close to the value approximated by GiXRD diffractogram i.e. 4.3 ± 0.8 nm (see Table 4).

A typical cathode voltage and discharge current waveforms recorded during HiPIMS deposition of Ge and TiO₂-anatase are shown in Figs. 6 (a, b), respectively. For the non-reactive Ge deposition the discharge current increases to a plateau. In the reactive case Ti target in Ar/O₂ discharge we see an initial peak at about 70 μ s and then a slight drop (due to gas rarefaction) followed by a second rise (because of self-sustained sputtering)^{19,26,50}.

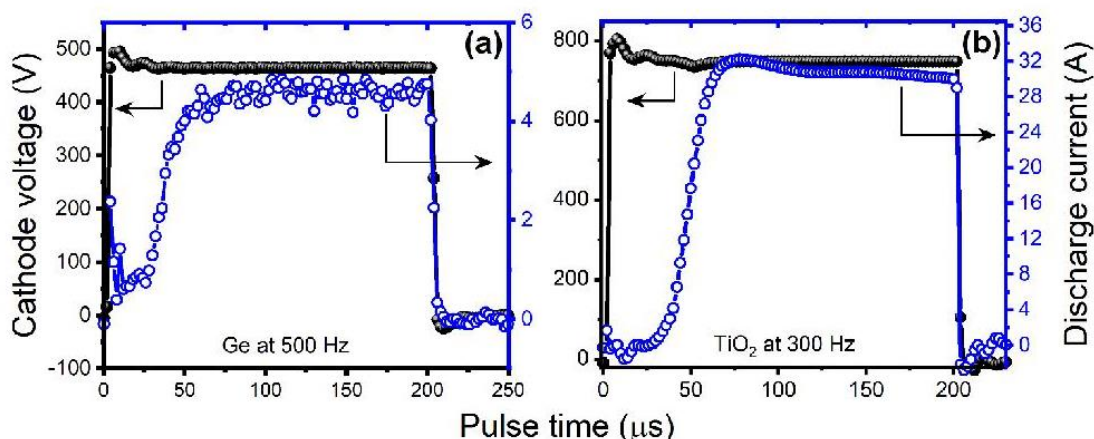


Figure 6. Cathode current and voltage waveforms during HiPIMS deposition for (a) Ge and (b) TiO₂ anatase phase, respectively.

Scheme DDD

For the third and last scheme i.e. DDD, sputtering of the TiO₂, Si and Ge was carried out via dcMS for all the three layers. The structure showed an amorphous feature in as-grown state (**Fig. 5(b)**), which when annealed at 600 °C for 5 min (DDD*) resulted in crystalline appearance of peaks for both TiO₂ (anatase) and SiGe crystallites. The reasoning of annealing at such low anneal parameters and carrying the anneal procedure (as described in section 2) is to mimic rapid thermal processing with lower ramping rate that reduces development of stress field within the structure and further to avoid degradation of structures interface morphology by formation of SiO₂ at the interfaces^{3,4,38,39}, as have been discussed elsewhere³⁸. The annealed structure (DDD*) will turn to account for photo spectral analysis in section 3.3.

In brief, three schemes with stacking sequence of SiO₂/TiO₂/SiGe/TiO₂ over p-type Si substrate, were prepared by varying combinations of dcMS and HiPIMS. The SiO₂ (buffer) layer was deposited in order to suppress the effect of capacitive coupling from substrate²⁹.

- For the DDD scheme, amorphous features are obtained for the as-grown structure while annealing resulted in the formation of crystalline structure with anatase phase for TiO₂.
- For the DHD scheme, none of the structures showed crystalline feature for the TiO₂ matrix whereas, for SiGe, the average size of the crystallites (crystallinity) increased with increased average power⁴³.
- For the HHD scheme, a crystalline structure of TiO₂ in either anatase or rutile phase was observed. A variation in size of SiGe nano-crystallites is observed and can be associated with the ordering/reconstruction of oxide matrix which determines the size of expanding nanocrystals^{38,51}, and will further be discussed later in section 3.3 in light of the spectral analysis.

We would like to further stress here that the structure labeled as DHD and HHD (deposited via HiPIMS sputter method) are un-annealed and have SiGe crystallites in as grown state. While structure labelled as DDD (deposited via dcMS sputter method) underwent anneal treatment to obtain a crystalline structure which was amorphous in as-grown state. For DHD and HHD structure, even though annealing of these structure will result in reduction of interface traps and non-radiative defects; in this study we are more concerned with preserving interface integrity and fabrication of anneal free crystalline structure, having improved photo-response. However, in our previous studies^{38,39,40}, comparable structures were treated at low anneal parameters and/or exposed to hydrogen plasma in as-grown state, resulting in an increased photocurrent intensity, as a consequence of reduction in stress field, defects and passivation of dangling bonds.

Table 4 summarizes the structural analysis results, along with determined SiGe NCs sizes.

Table 4. Results obtained by GiXRD diffractogram of samples from schemes DDD, DHD and HHD

Sample label	Structure in as-grown state		Structure in annealed state	Size of SiGe (± 0.8 nm)
	TiO ₂	Si _{1-x} Ge _x		
DDD scheme				
DDD	Amorph.	Amorph.	-	-
DDD*	-	-	Cryst.	10.3
DHD scheme				
DHD-1	Amorph.	Cryst.	-	1.0
DHD-2	Amorph.	Cryst.	-	1.3
DHD-3	Amorph.	Cryst.	-	2.5
DHD-4	Amorph.	Cryst.	-	3.7
DHD-5	Amorph.	Cryst.	-	6.4
HHD scheme				
HHD-A	Cryst.	Cryst.	-	4.3
HHD-R	Cryst.	Cryst.	-	5.5

3.3. Spectral analysis

In this section, the photocurrent spectra of MLs DDD*, DHD-5 and HH-A and HHD-R are compared and analyzed in terms of their photocurrent intensity with respect to TiO₂ crystallinity. **Fig. 7(a-d)** shows de-convoluted spectra of the corresponding structures at room temperature. The peaks obtained were ascribed^{29,39} to interface related localized states (peak I), photo-effect from nano-crystallites (peak N) and to capacitive coupling from the substrate i.e. surface photo-voltage (SPV) and gating effect²⁹. An evident increase in spectral intensity was approximately 11 and 28 folds for DHD-5 and HHD-A, respectively and more than 1.7 order of magnitude for HHD-R, as compared to structures deposited by dcMS alone which was annealed at 600 °C for 5 min (DDD*) to obtain crystalline structure. Note the scale change in the photocurrent intensity between the figures.

A notable shift in peak N position is observed and is related to the variation in the size of nano-crystallites. For samples HHD-A, HHD-R and DHD-5, the peaks are positioned at 952, 961 and 977 nm respectively, whereas for DDD* it is 996 nm (position determined by deconvolution). For sample DDD* the position is red-shifted due to annealing, which resulted in an increased size of SiGe nanocrystals to ~ 10.3 nm, as compared to ~ 4.3, 5.52 and 6.4 nm for HHD-(A and R) and DHD-5. An additional (far left) de-convoluted peak for structure DDD* is associated with localized states in TiO₂ as detailed in our previous study³⁸. A blue-shift of peak N (**Fig. 7(f)**) and increased photocurrent intensity for HHD, relative to DHD-5, can be attributed to structural transformation and respective interface morphology from amorphous to crystalline^{16,52} (i.e. anatase and to rutile^{53,54}). That is, the bandgap of TiO₂ shifts towards longer wavelengths (red shift in peak I) for transformation from amorphous to crystalline structure^{16,52-55}.

It is well established that ordering of the surrounding matrix exerts strain on the nano-crystallites, especially at the interface vicinity, and can alter the size and crystallinity of the NCs^{56,51,57}. Thus, in respect to amorphous (disordered) matrix where the crystallites can expand freely (NCs size ~6.4 nm), the crystalline TiO₂ possess a rigid interface which will hinder the growth of NCs due to larger volume of the matrix⁵⁶, thus exerting strain within the structure (at interface and on the NCs). Therefore, rutile, having larger grain size^{58,59} and higher density⁵⁸ than anatase, exhibits different matrix environment. This will induce different degree of strain in the structure^{56,51}, where the character of strain depends on the film stoichiometry (i.e. anatase and rutile constituting dissimilar stoichiometry with general formula of TiO_x⁶⁰, along with varying atoms per unit cell and shared edges in TiO₆ octahedral arrangement⁵⁸). Hence, peak N is positioned at longer wavelength for amorphous matrix due to higher degree of freedom for nano-crystallites to expand in comparison to crystalline structure, which causes reduction in NCs size due to denser and more rigid matrix (**Fig. 7(f)** depicts the variation in peak position).

It is widely known that defects and vacancies associated with semiconductors and dielectrics can lead to formation of localized states near the conduction band edge. Anatase is a metastable phase and has volatile matter, whereas rutile is the most stable phase of titania. In this

relation, the two polymorphs presents different non-stoichiometric defects per unit volume related to bandgap energy. This difference in dislocation density (highest for amorphous and decreases with increased crystallinity to rutile⁶) plays a vital role in altering the bandgap, in line with our results as seen in Fig. 7(e), where the peak I red-shifts with increased TiO₂ crystallinity. Another factor that can be taken into consideration, is the crystal parameters of anatase and rutile polymorphs, which possess different thermal expansion coefficients^{61–63}. This can set the lattice vibration to different extents⁶⁴, resulting in different band structure and variation in photo response. In addition, the rutile phase possess direct band-gap having slightly lower conduction band energy^{10,13,65} than anatase, resulting in large increase of spectral intensity. Also, anatase phase exhibits higher density of localized states⁵⁸ and larger amount of oxygen vacancies than the rutile phase⁶⁰, which results in increase of dangling bonds acting as electrically active recombination centers. The dangling bonds are present in the form of oxygen-vacancies and Ti-interstitials defects (i.e. O⁻, O₃⁻, OH group and Ti³⁺), where the oxygen vacancies are energetically favorable to form^{66,67}. These dangling bonds create energy sates near the conduction band edge of TiO₂⁶⁸. Moreover, due to its larger grain size, rutile accompanies higher recombination rate⁵⁸ and a resultant lower capacity to adsorb species (such as anatase TiO₂ utilized for water splitting) giving higher probability for photo-generated carrier to recombine. Consequently, a pronounced increase in spectral intensity and a red shift in peak I (Fig. 7(e)) is observed.

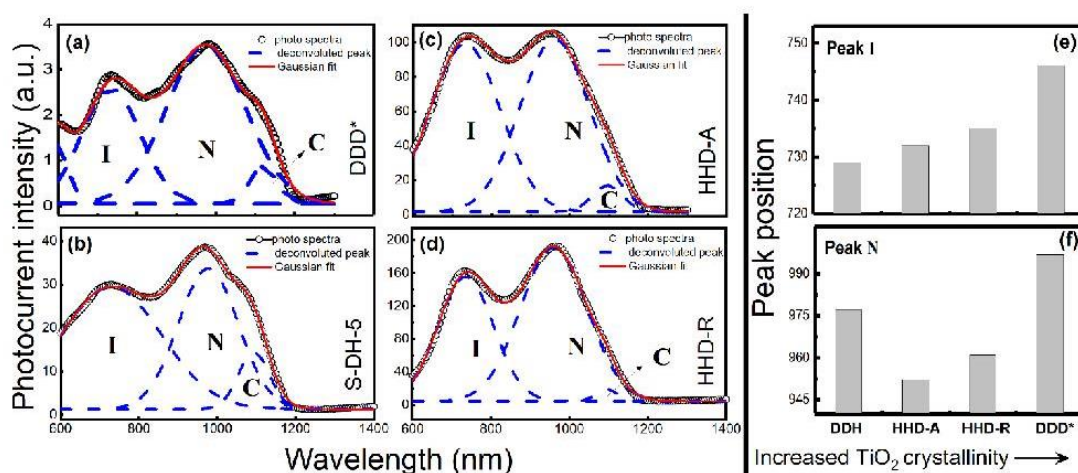


Figure 7. (a)-(d) Photocurrent room temperature spectra of samples (a) DDD*, (b) DHD-5, (c) HHD-A and (d) HHD-R, where black hollow circles are the obtained photocurrent spectra, red and dotted-blue lines represents the Gaussian fit and the de-convoluted peaks. Position of peak I (e) and N (f) are obtained via deconvolution shown with the blue dotted lines in (a)-(d).

3.4. Interface integrity in light of spectral analysis

To examine the effect of interface morphology and its effect over spectral response, several structure with varying TiO₂ thicknesses (10, 20, 40 and 60 nm) were fabricated using the HiPIMS approach with parameters leading to rutile phases i.e. HHD-R. All the spectra obtained (Fig. 8(a-

d)) were deconvoluted to clearly demonstrate the shift in peak position and spectral intensities of associated peaks. Following changes, in the photocurrent spectra were observed:

- an increase in spectral intensity with increased oxide thickness^{57,69}.
- a considerable increase in relative intensity of peak I with respect to peak N, as can be seen in Fig. 8, where the shaded area under peak I increases while that of peak N (unshaded represented by solid gray line) decreases. Thus, pointing out the role of interface-related localized states due to structural inhomogeneity and resulting incoherent interface between the matrix and SiGe layer, increasing with increased oxide thickness.
- red and blue shift of peaks I and N, respectively (Fig. 8 (e, f)). The shift in peak N is attributed to reduced size of nano-crystallites caused by increased oxide thickness. This reduction in size occur because of modification in interface morphology (red-shift in peak I) on grounds of matrix ordering and strain accumulation arriving from increased oxide thickness. Several works can be found, devoted to the matrices role on nanocrystal formation and the accompanying strain in structure^{5,51,57,69–71}.

A key observation in this work is the correlation exists between the structural ordering of the matrix, interface morphology (source for interface related localized states) and the size of NCs, which in turn determines the spectral features.

In systems with nanoparticles embedded in an oxide matrix, a common issue encountered, is the effect of surrounding matrix over the crystallites and strain formation in the structure^{51,72}. This is due to different thermal expansion coefficients of the matrix and the SiGe NCs along with the density gradient of the matrix^{51,56,61,62,73,74}. Moreover, the lattice mismatch of 4.2% between Si and Ge plays a vital role^{1,2} in inducing strain. Considering the above criteria, it is obvious that when two differently ordered structures with different dielectric constants are merged at the interface, one of them will deform to accommodate the reconstruction of other⁵¹, resulting in strain accumulation. In a study by Zatoryb *et al.*⁵¹ it was shown that the nanoparticles shape and crystallinity is affected by the degree of matrix ordering, i.e. the ordering of oxide matrix determines the size of expanding NCs. In another study by Ciurea *et al.*⁵ it was shown that the size of crystallites can be controlled by the oxide thickness. For our as-grown structures, we can expect the interface to be incoherent/non-planar. An increase in TiO₂ thickness will exert different magnitude of strain due to varying degree of matrix ordering/reconstruction, which in turn determines the size of the NCs⁷². Hence, a shift in peak I and N positions is observed as shown in Fig. 8. Furthermore, we would like to outline here that the broad peaks (i.e. full width half maxima of peak N) in Fig. 7 and 8 is due to wider size and shape distribution of SiGe nano-crystallites as evident from HRTEM image (see supplementary information), also discussed in our previous study³⁸ and in work by Evrin *et al.*⁷⁵ and Wang *et al.*⁷⁶.

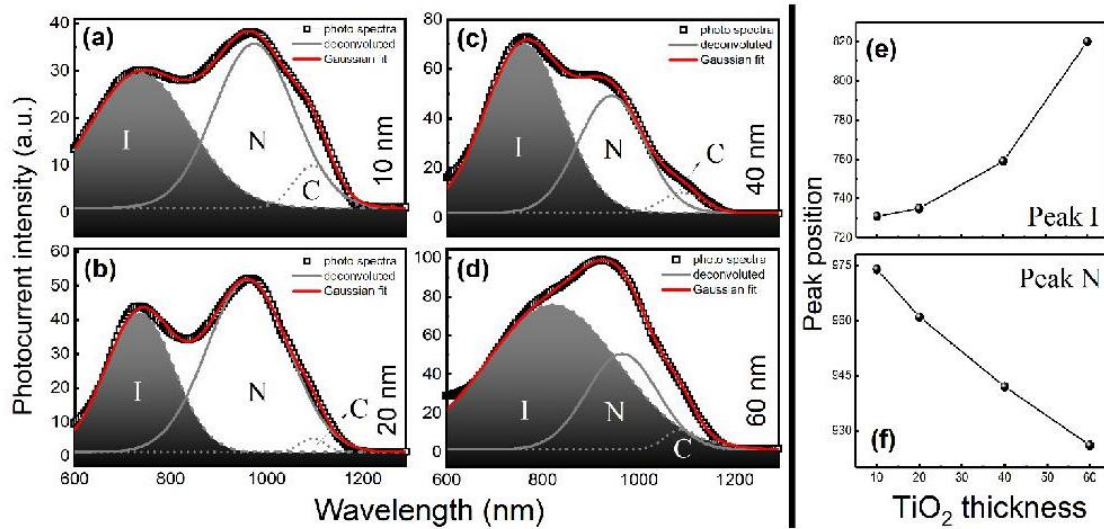


Figure 8. (a)-(d) Photocurrent room temperature spectra of as-grown ($\text{SiO}_2/\text{TiO}_2/\text{SiGe}/\text{TiO}_2$) structures deposited via HiPIMS (HHD-rutile), having TiO_2 thickness (bottom and top) varying from (a) 10 nm, (b) 20 nm, (c) 40 nm, to (d) 60 nm. The shaded area represents the peak I, the intensity of which varies with TiO_2 thickness. (e) and (f) Position of peaks I and N with respect to increasing TiO_2 thickness at SiGe thickness of 20 nm as determined with deconvolution in (a)-(d).

In addition, the realization of a decrease in peak C intensity with increased matrix thicknesses was observed. This is in line with the results of Lepadat *et al.*²⁹, over TiO_2 embedded with Ge nanocrystals, where the peak (approximately position at similar wavelength ~ 1100 nm) is attributed to capacitive coupling i.e. surface photo voltage and gating effect; the intensity of which is effected by the buffer-layer thickness.

4. Conclusion

In summary, $\text{SiO}_2/\text{TiO}_2/\text{SiGe}/\text{TiO}_2$ structures (MLs) were fabricated using combination of dcMS and HiPIMS. The investigation highlights the importance of process optimization in reactive HiPIMS, to obtain desired TiO_2 phase (i.e. either anatase or rutile) in as-grown state and its consequent effect over the photocurrent spectra. It is shown that application of HiPIMS, facilitate formation of crystalline structure without the need of any thermal treatments. TiO_2 films grown by HiPIMS were also investigated using GiXRD analysis as reference. The HiPIMS-prepared MLs exhibited photocurrent intensity of more than 1.7-order magnitude higher than that obtained over dcMS deposited structure annealed at 600 °C for 5 min. Whereas, the as-grown dcMS structure showed no photo-response. Furthermore, a control over the size of SiGe nano-crystallites and increased crystallinity was obtained by HiPIMS discharge, along with a crystalline TiO_2 matrix either in anatase or rutile state (depending on HiPIMS discharge operational parameters). A further work is needed to investigate the effect of HiPIMS deposition parameters, magnetron strength i.e. magnetic confinement (that have a major effect over the ionized flux fraction⁷⁷), and other in-situ

approaches (i.e. substrate heating and biasing). To put in words, we have obtained crystalline structure in as-grown state demonstrating an energy efficient production and higher pay back of these devices, while reducing the manufacturing cost on account of eliminating the need of any thermal treatment budget.

AUTHOR INFORMATION

Corresponding Author

Halldor Gudfinnur Svavarsson

*E-mail: halldorsv@ru.is

Muhammad Taha Sultan

*E-mail: muhammad16@ru.is

Acknowledgements

This work is funded through M-ERA.NET project PhotoNanoP UEFISCDI Contract no. 33/2016, PCE project UEFISCDI Contract no. 122/2017 and by Romanian Ministry of Research and Innovation through NIMP Core Program PN19-03, contract no. 21 N/08.02.2019 and by the Technology Development Fund of the Icelandic Centre for Research, grant no. 159006-0611.

References

- [1] H. Ye, J. Yu, Germanium epitaxy on silicon, *Sci. Technol. Adv. Mater.* 15 (2014) 024601. doi:10.1088/1468-6996/15/2/024601.
- [2] J.N. Aqua, I. Berbezier, L. Favre, T. Frisch, A. Ronda, Growth and self-organization of SiGe nanostructures, *Phys. Rep.* 522 (2013) 59–189. doi:10.1016/j.physrep.2012.09.006.
- [3] M.T. Sultan, A. Manolescu, J.T. Gudmundsson, K. Torfason, G.A. Nemnes, I. Stavarache, C. Logofatu, V.S. Teodorescu, M.L. Ciurea, H.G. Svavarsson, Enhanced photoconductivity of SiGe nanocrystals in SiO₂ driven by mild annealing, *Appl. Surf. Sci.* 469 (2019) 870–878. doi:10.1016/J.APSUSC.2018.11.061.
- [4] A. Slav, C. Palade, I. Stavarache, V.S. Teodorescu, M.L. Ciurea, R. Muller, A. Dinescu, M.T. Sultan, A. Manolescu, J.T. Gudmundsson, H.G. Svavarsson, Influence of preparation conditions on structure and photosensing properties of GeSi/TiO₂ multilayers, in: *2017 Int. Semicond. Conf., IEEE, 2017*: pp. 63–66. doi:10.1109/SMICND.2017.8101154.
- [5] M. L. Ciurea, A –M. Lepadatu, Tuning the Properties of Ge and Si nanocrystals based structures by tailoring the preparation conditions. *Dig. J. Nanomater. Biostructures 2015*, 10 (1), 59–87.
- [6] P.B. Nair, V.B. Justinivictor, G.P. Daniel, K. Joy, K.C. James Raju, D. Devraj Kumar, P.V. Thomas, Optical parameters induced by phase transformation in RF magnetron sputtered TiO₂ nanostructured thin films, *Prog. Nat. Sci. Mater. Int.* 24 (2014) 218–225. doi:10.1016/J.PNSC.2014.05.010.
- [7] F. Cemin, M. Tsukamoto, J. Keraudy, V.G. Antunes, U. Helmersson, F. Alvarez, T. Minea, D. Lundin, Low-energy ion irradiation in HiPIMS to enable anatase TiO₂ selective growth, *J. Phys. D. Appl. Phys.* 51 (2018) 235301. doi:10.1088/1361-6463/aac080.
- [8] K. Sarakinos, J. Alami, M. Wuttig, Process characteristics and film properties upon growth of TiO_x films by high power pulsed magnetron sputtering, *J. Phys. D. Appl. Phys.* 40 (2007) 2108–2114. doi:10.1088/0022-3727/40/7/037.

- [9] P. Löbl, M. Huppertz, D. Mergel, Nucleation and growth in TiO₂ films prepared by sputtering and evaporation, *Thin Solid Films*. 251 (1994) 72–79. doi:10.1016/0040-6090(94)90843-5.
- [10] K. Connelly, A.K. Wahab, H. Idriss, Photoreaction of Au/TiO₂ for hydrogen production from renewables: a review on the synergistic effect between anatase and rutile phases of TiO₂, *Mater. Renew. Sustain. Energy*. 1 (2012) 3. doi:10.1007/s40243-012-0003-9.
- [11] Y. Yamada, Y. Kanemitsu, Determination of electron and hole lifetimes of rutile and anatase TiO₂ single crystals, *Appl. Phys. Lett.* 101 (2012) 133907. doi:10.1063/1.4754831.
- [12] M.D. Wiggins, M.C. Nelson, C.R. Aita, Phase development in sputter deposited titanium dioxide, *J. Vac. Sci. Technol. A Vacuum, Surfaces, Film*. 14 (1996) 772–776. doi:10.1116/1.580387.
- [13] T. Luttrell, S. Halpegamage, J. Tao, A. Kramer, E. Sutter, M. Batzill, Why is anatase a better photocatalyst than rutile? - Model studies on epitaxial TiO₂ films, *Sci. Rep.* 4 (2015) 4043. doi:10.1038/srep04043.
- [14] J. Li, M. Songhe, Q. Liyuan, H. Lu, Optical properties of anatase and rutile TiO₂ studied by GGA+U. *Chinese Phys. B* 2017, 26 (8), 087101. <https://doi.org/10.1088/1674-1056/26/8/087101>.
- [15] D. Rafeian, W. Ogieglo, T. Savenije, R.G.H. Lammertink, Controlled formation of anatase and rutile TiO₂ thin films by reactive magnetron sputtering, *AIP Adv.* 5 (2015) 097168. doi:10.1063/1.4931925.
- [16] G. Valverde-Aguilar, J.A. García-Macedo, V. Rentería-Tapia, M. Aguilar-Franco, Photoconductivity studies on amorphous and crystalline TiO₂ films doped with gold nanoparticles, *Appl. Phys. A*. 103 (2011) 659–663. doi:10.1007/s00339-010-6199-6.
- [17] A. Surpi, T. Kubart, D. Giordani, M. Tosello, G. Mattei, M. Colasuonno, A. Patelli, HiPIMS deposition of TiO_x in an industrial-scale apparatus: Effects of target size and deposition geometry on hysteresis, *Surf. Coatings Technol.* 235 (2013) 714–719. doi:10.1016/j.surfcoat.2013.08.053.
- [18] S. Konstantinidis, J.P. Dauchot, M. Hecq, Titanium oxide thin films deposited by high-power impulse magnetron sputtering, *Thin Solid Films*. 515 (2006) 1182–1186. doi:10.1016/J.TSF.2006.07.089.
- [19] B. Agnarsson, F. Magnus, T.K. Tryggvason, A.S. Ingason, K. Leosson, S. Olafsson, J.T. Gudmundsson, Rutile TiO₂ thin films grown by reactive high power impulse magnetron sputtering, *Thin Solid Films*. 545 (2013) 445–450. doi:10.1016/J.TSF.2013.07.058.
- [20] Q.M. Wang, S.-H. Kwon, K.N. Hui, D.-I. Kim, K.S. Hui, K.H. Kim, Synthesis and properties of crystalline TiO₂ films deposited by a HIPIMS+ technique, *Vacuum*. 89 (2013) 90–95. doi:10.1016/j.vacuum.2011.11.020.
- [21] M. Samuelsson, D. Lundin, J. Jensen, M.A. Raadu, J.T. Gudmundsson, U. Helmersson, On the film density using high power impulse magnetron sputtering, *Surf. Coatings Technol.* 205 (2010) 591–596. doi:10.1016/j.surfcoat.2010.07.041.
- [22] J. Alami, P.O.Å. Persson, D. Music, J.T. Gudmundsson, J. Bohlmark, U. Helmersson, Ion-assisted physical vapor deposition for enhanced film properties on nonflat surfaces, *J. Vac. Sci. Technol. A Vacuum, Surfaces, Film*. 23 (2005) 278–280. doi:10.1116/1.1861049.
- [23] U. Helmersson, M. Lattemann, J. Bohlmark, A.P. Ehiasarian, J.T. Gudmundsson, Ionized physical vapor deposition (IPVD): A review of technology and applications, *Thin Solid Films*. 513 (2006) 1–24. doi:10.1016/J.TSF.2006.03.033.
- [24] D. Lundin, K. Sarakinos, An introduction to thin film processing using high-power impulse magnetron sputtering, *J. Mater. Res.* 27 (2012) 780–792. doi:10.1557/jmr.2012.8.

- [25] J.T. Gudmundsson, The high power impulse magnetron sputtering discharge as an ionized physical vapor deposition tool, *Vacuum*. 84 (2010) 1360–1364. doi:10.1016/j.vacuum.2009.12.022.
- [26] J.T. Gudmundsson, N. Brenning, D. Lundin, U. Helmersson, High power impulse magnetron sputtering discharge, *J. Vac. Sci. Technol. A Vacuum, Surfaces, Film*. 30 (2012) 030801–34. doi:10.1116/1.3691832.
- [27] V. Straňák, M. Quaas, H. Wulff, Z. Hubička, S. Wrehde, M. Tichý, R. Hippler, Formation of TiO_x films produced by high-power pulsed magnetron sputtering, *J. Phys. D. Appl. Phys.* 41 (2008) 055202. doi:10.1088/0022-3727/41/5/055202.
- [28] V. Straňák, M. Čada, M. Quaas, S. Block, R. Bogdanowicz, Š. Kment, H. Wulff, Z. Hubička, C.A. Helm, M. Tichý, R. Hippler, Physical properties of homogeneous TiO₂ films prepared by high power impulse magnetron sputtering as a function of crystallographic phase and nanostructure, *J. Phys. D. Appl. Phys.* 42 (2009) 105204. doi:10.1088/0022-3727/42/10/105204.
- [29] A.-M. Lepadatu, A. Slav, C. Palade, I. Dascalescu, M. Enculescu, S. Iftimie, S. Lazanu, V.S. Teodorescu, M.L. Ciurea, T. Stoica, Dense Ge nanocrystals embedded in TiO₂ with exponentially increased photoconduction by field effect., *Sci. Rep.* 8 (2018) 4898. doi:10.1038/s41598-018-23316-3.
- [30] C.P. Church, E. Muthuswamy, G. Zhai, S.M. Kauzlarich, S.A. Carter, Quantum dot Ge/TiO₂ heterojunction photoconductor fabrication and performance, *Appl. Phys. Lett.* 103 (2013) 223506. doi:10.1063/1.4826916.
- [31] J. Jettanasen, Study of silicon nanoparticles in dielectric oxides obtained by sol-gel route, *J. Exp. Nanosci.* 10 (2015) 1319–1326. doi:10.1080/17458080.2015.1007096.
- [32] A.F. Khan, M. Mehmood, M. Aslam, S.I. Shah, Nanostructured multilayer TiO₂/Ge films with quantum confinement effects for photovoltaic applications., *J. Colloid Interface Sci.* 343 (2010) 271–80. doi:10.1016/j.jcis.2009.11.045.
- [33] A.F. Khan, M. Mehmood, T. Ali, H. Fayaz, Structural and optical studies of nanostructured TiO₂/Ge multi-layer thin films tehsis, *Thin Solid Films*. 536 (2013) 220–228. doi:10.1016/J.TSF.2013.03.058.
- [34] M. Zhang, R. Cai, Y. Zhang, C. Wang, Y. Wang, G.G. Ross, D. Barba, Evolution of microstructural defects with strain effects in germanium nanocrystals synthesized at different annealing temperatures, *Mater. Charact.* 93 (2014) 1–9. doi:10.1016/J.MATCHAR.2014.03.010.
- [35] A -M. Lepadatu, I. Stavarache, T. F. Stoica, M. L. Ciurea, Study of Ge nanoparticles embedded in an amorphous SiO₂ matrix with photoconductive properties. *Dig. J. Nanomater. Biostructures* 2011, 6 (1), 67–73.
- [36] P. Granitzer, K. Rumpf, *Nanostructured Semiconductors*; Rumpf, K., Ed.; Pan Stanford Publishing, 2014. <https://doi.org/10.1201/b15634>.
- [37] I. Stavarache, V.A. Maraloiu, C. Negrila, P. Prepelita, I. Gruia, G. Iordache, Photo-sensitive Ge nanocrystal based films controlled by substrate deposition temperature, *Semicond. Sci. Technol.* 32 (2017) 105003. doi:10.1088/1361-6641/aa8154.
- [38] M.T. Sultan, J. T. Gudmundsson, A. Manolescu, V. S. Teodorescu, M. L. Ciurea, H.G. Svavarsson, Efficacy of annealing and fabrication parameters on photo-response of SiGe in TiO₂ matrix, *Nanotechnology*. 30 (2019) 365604. <https://doi.org/10.1088/1361-6528/ab260e>.
- [39] M.T. Sultan, J.T. Gudmundsson, A. Manolescu, T. Stoica, M.L. Ciurea, H.G. Svavarsson, Enhanced photoconductivity of embedded SiGe nanoparticles by hydrogenation, *Appl.*

- Surf. Sci. 479 (2019) 403–409. doi:10.1016/J.APSUSC.2019.02.096.
- [40] M.T. Sultan, A.V. Maraloiu, I. Stavarache, J.T. Gudmundsson, A. Manolescu, V.S. Teodorescu, M.L. Ciurea, H.G. Svavarsson, Fabrication and Characterization of $\text{Si}_{1-x}\text{Ge}_x$ Nanocrystals in as-Grown and Annealed Structures: A Comparative Study. *Beilstein Arch.* 2019, 201916. [https://doi:10.3762/bxiv.2019.16.v1](https://doi.org/10.3762/bxiv.2019.16.v1).
- [41] E. Bertran, S.N. Sharma, G. Viera, J. Costa, P. St'ahel, P.R. i Cabarrocas, Effect of the nanoparticles on the structure and crystallization of amorphous Silicon thin films produced by rf glow discharge, *J. Mater. Res.* 13 (1998) 2476–2479. doi:10.1557/JMR.1998.0347.
- [42] J. Dasović, P. Dubček, I. Pucić, S. Bernstorff, N. Radić, B. Pivac, The interface quality of Ge nanoparticles grown in thick silica matrix, *Appl. Surf. Sci.* 414 (2017) 1–7. doi:10.1016/J.APSUSC.2017.03.264.
- [43] H.C. Lee, G.Y. Yeom, Y.J. Lee, J.K. Shin, S. Il Baik, Y.W. Kim, Structural and Electrical Analysis of Silicon Thin Films Deposited by Transformer-Coupled-Plasma Chemical-Vapor Deposition, *J. Korean Phy. Soc.* 47 (2005), 277–282.
- [44] A. Kole, P. Chaudhuri, Growth of silicon quantum dots by oxidation of the silicon nanocrystals embedded within silicon carbide matrix, *AIP Adv.* 4 (2014) 107106. doi:10.1063/1.4897378.
- [45] A.L. Patterson, The Scherrer Formula for X-Ray Particle Size Determination, *Phys. Rev.* 56 (1939) 978–982. doi:10.1103/PhysRev.56.978.
- [46] V. Sittinger, A. Pflug, W. Dewald, S. Jung, C. Britze, A. Kaiser, W. Werner, B. Szyszka, G. Bräuer, Rotatable serial co-sputtering of doped titania, *Vacuum.* 114 (2015) 158–161. doi:10.1016/j.vacuum.2014.12.007.
- [47] B. Astinchap, R. Moradian, K. Gholami, Effect of sputtering power on optical properties of prepared TiO_2 thin films by thermal oxidation of sputtered Ti layers, *Mater. Sci. Semicond. Process.* 63 (2017) 169–175. doi:10.1016/j.mssp.2017.02.007.
- [48] J. Čapek, M. Hála, O. Zabeida, J.E. Klemberg-Sapieha, L. Martinu, Steady state discharge optimization in high-power impulse magnetron sputtering through the control of the magnetic field, *J. Appl. Phys.* 111 (2012) 023301. doi:10.1063/1.3673871.
- [49] M.L. Ciurea, I. Stavarache, A.-M. Lepadatu, I. Pasuk, V.S. Teodorescu, Electrical properties related to the structure of GeSi nanostructured films, *Phys. Status Solidi.* 251 (2014) 1340–1346. doi:10.1002/pssb.201350112.
- [50] Y. Yuan, L. Yang, Z. Liu, Q. Chen, High power impulse magnetron sputtering and its applications, *Plasma Sci. Technol.* 20 (2018) 065501. doi:10.1088/2058-6272/aa9e48.
- [51] G. Zatoryb, A. Podhorodecki, J. Misiewicz, J. Cardin, F. Gourbilleau, Correlation between matrix structural order and compressive stress exerted on silicon nanocrystals embedded in silicon-rich silicon oxide, *Nanoscale Res. Lett.* 8 (2013) 40. doi:10.1186/1556-276X-8-40.
- [52] J. Rodríguez, M. Gómez, J. Ederth, G.A. Niklasson, C.G. Granqvist, Thickness dependence of the optical properties of sputter deposited Ti oxide films, *Thin Solid Films.* 365 (2000) 119–125. doi:10.1016/S0040-6090(99)01109-8.
- [53] J. Jia, L. Mu, Y. Lin, X. Zhou, Rutile versus anatase for quantum dot sensitized solar cell, *Electrochim. Acta.* 266 (2018) 103–109. doi:10.1016/J.ELECTACTA.2018.01.186.
- [54] H. Tang, K. Prasad, R. Sanjinès, P.E. Schmid, F. Lévy, Electrical and optical properties of TiO_2 anatase thin films, *J. Appl. Phys.* 75 (1994) 2042–2047. doi:10.1063/1.356306.
- [55] M.I. Khan, K.A. Bhatti, R. Qindeel, H.S. Althobaiti, N. Alonizan, Structural, electrical and optical properties of multilayer TiO_2 thin films deposited by sol–gel spin coating, *Results Phys.* 7 (2017) 1437–1439. doi:10.1016/J.RINP.2017.03.023.
- [56] G. Zatoryb, J. Misiewicz, P.R.J. Wilson, J. Wojcik, P. Mascher, A. Podhorodecki, Stress

- transition from compressive to tensile for silicon nanocrystals embedded in amorphous silica matrix, *Thin Solid Films*. 571 (2014) 18–22. doi:10.1016/J.TSF.2014.09.046.
- [57] J. Zhu, H.-C. Hao, D. Li, M. Lu, Matrix effect on the photoluminescence of Si nanocrystal, *J. Nanoparticle Res.* 14 (2012) 1097. doi:10.1007/s11051-012-1097-9.
- [58] D.A.H. Hanaor, C.C. Sorrell, Review of the anatase to rutile phase transformation, *J. Mater. Sci.* 46 (2011) 855–874. doi:10.1007/s10853-010-5113-0.
- [59] J. Zhang, B. Tian, L. Wang, M. Xing, J. Lei, *Photocatalysis Fundamentals, Materials and applications*, Springer Nature Singapore Pte Ltd. 2018. doi:10.1007/978-981-13-2113-9.
- [60] K. Zakrzewska, Nonstoichiometry in TiO_{2-y} studied by ion beam methods and photoelectron spectroscopy, *Adv. Mater. Sci. Eng.* 2012 (2012) 1–13. doi:10.1155/2012/826873.
- [61] K.V.K. Rao, S.V.N. Naidu, L. Iyengar, Thermal Expansion of Rutile and Anatase, *J. Am. Ceram. Soc.* 53 (1970) 124–126. doi:10.1111/j.1151-2916.1970.tb12051.x.
- [62] D.R. Hummer, P.J. Heaney, J.E. Post, Thermal expansion of anatase and rutile between 300 and 575 K using synchrotron powder X-ray diffraction, *Powder Diffr.* 22 (2007) 352–357. doi:10.1154/1.2790965.
- [63] E. P. Meagher, George A. Lager, Polyhedral thermal expansion in the TiO_2 polymorphs: Refinement of the crystal structures of rutile and brookite at high temperature, *Can. Mineral.* 17 (1979) 77–85. https://ruff-2.geo.arizona.edu/uploads/CM17_77.pdf (accessed March 22, 2019).
- [64] A. Schauer, Thermal expansion of solids and the temperature dependence of lattice vibration frequencies, *Can. J. Phys.* 42 (1964) 1857–1864. doi:10.1139/p64-173.
- [65] Z. Liu, X. Zhang, S. Nishimoto, M. Jin, D.A. Tryk, T. Murakami, A. Fujishima, Anatase TiO_2 Nanoparticles on Rutile TiO_2 Nanorods: A Heterogeneous Nanostructure via Layer-by-Layer Assembly, *Langmuir*. 23 (2007) 10916–10919. doi:10.1021/la7018023.
- [66] B. Bharti, S. Kumar, R. Kumar, Superhydrophilic TiO_2 thin film by nanometer scale surface roughness and dangling bonds, *Appl. Surf. Sci.* 364 (2016) 51–60. doi:10.1016/J.APSUSC.2015.12.108.
- [67] G.C. Vásquez, S. Zh Karazhanov, D. Maestre, A. Cremades, J. Piqueras, S.E. Foss, Oxygen vacancy related distortions in rutile TiO_2 nanoparticles: A combined experimental and theoretical study, *Phys. Rev. B.* 94 (2016) 235209. doi:10.1103/PhysRevB.94.235209.
- [68] H. Li, Y. Guo, J. Robertson, Calculation of TiO_2 surface and subsurface oxygen vacancy by the screened exchange functional, *J. Phys. Chem. C.* 119 (2015) 18160–18166. doi:10.1021/acs.jpcc.5b02430.
- [69] L. Ferraioli, M. Wang, G. Pucker, D. Navarro-Urrios, N. Daldosso, C. Kompocholis, L. Pavesi, Photoluminescence of Silicon nanocrystals in silicon oxide, *J. Nanomater.* 43491 (2007). doi:10.1155/2007/43491.
- [70] D. Barba, F. Martin, C. Dahmoune, G.G. Ross, Effects of oxide layer thickness on Si-nanocrystal photoluminescence intensity in Si⁺-implanted SiO_2/Si systems, *Appl. Phys. Lett.* 89 (2006) 034107. doi:10.1063/1.2234739.
- [71] M. Avella, J. Jimenez, S. Profile, A. Rodríguez, Luminescence in Multilayers of SiGe Nanocrystals Embedded in SiO_2 , *MRS Proceedings* 958. 2007. doi:10.1557/PROC-0958-L04-03.
- [72] R. Guerra, E. Degoli, S. Ossicini, Size, oxidation, and strain in small Si/ SiO_2 nanocrystals, (2010). doi:10.1103/PhysRevB.80.155332.
- [73] A. Mashreghi, Determining the volume thermal expansion coefficient of TiO_2 nanoparticle by molecular dynamics simulation, *Comput. Mater. Sci.* 62 (2012) 60–64.

doi:10.1016/J.COMMATSCI.2012.05.018.

- [74] L. Pavesi, R. Turan, *Silicon Nanocrystals: Fundamentals, Synthesis and Applications*. Wiley-VCH, 2010. <https://doi.org/10.1002/9783527629954.ch1>.
- [75] E. Tuğay, S. İlday, R. Turan, T. G. Finstad, Influence of Ge content and annealing conditions on the PL properties of NC-Si_{1-x}Ge_x embedded in SiO₂ matrix in weak quantum confined regime *J. Lumin.* 155 (2014), 170–9. <https://doi.org/10.1016/j.jlumin.2014.06.012>.
- [76] X.X. Wang, J. G. Zhang, L. Ding, B. W. Cheng, W. K. Ge, J. Z. Yu, Q. M. Wang, Origin and evolution of photoluminescence from Si nanocrystals embedded in a-SiO₂ matrix. *Phys. Rev. B* 72 (2005), 195313. <https://doi.org/10.1103/PhysRevB.72.195313>.
- [77] H. Hajihoseini, M. Čada, Z. Hubička, S. Ünalđı, M.A. Raadu, N. Brenning, J.T. Gudmundsson, D. Lundin, The effect of magnetic field strength and geometry on the deposition rate and ionized flux fraction in the HiPIMS discharge, *Plasma*. 2 (2019) 201–221. doi:10.3390/plasma2020015.



School of Science and Engineering
Reykjavík University
Menntavegur 1
101 Reykjavík, Iceland
Tel. +354 599 6200
Fax +354 599
www.ru.is